Development and Application of Computational Methods for the Prediction of Chiral Phosphoric Acid Catalyst Performance

This dissertation is submitted for the degree of Doctor of Philosophy at the University of Cambridge

by

Jolene Patricia Reid

of

Clare College

August 2017

“Scientific discovery is not yet predictable. If you have an exciting road to follow do not be put off by those who say there is nothing at the end of it; they do not know. Persevere, and enjoy the excitement of exploring the unknown.”

Chatt J. *Platinum Met. Rev.* **1985,** *19,* 126.

Acknowledgements

Firstly, I would like to thank my supervisor, Professor Jonathan Goodman, for his guidance and mentorship over the last four years. His seemingly limitless optimism has proved critical to the development of my work described in this thesis. Among the many lessons I learned from Jonathan's lab, for me the most important was the value of performing smart experiments. In the end, I could not have imagined a better place for my PhD study.

I would like to thank all members of the Goodman group who have worked in the lab during my time. In particular Dr Kristaps Ermanis for his friendship, Python assistance and thorough proof reading of this thesis. To Jonathan Lam and Andy Wedlake, without whom the last couple of years would have been a lot less entertaining. In addition, I would like to acknowledge members of the Paterson group, with whom we share our lab space, in particular, Nelson Lam, for his input at our joint group meetings. The EPSRC is also thanked for funding.

I am grateful to Professor Matthew Cook, who was my advisor when I was an undergraduate student at Queens University, Belfast. The research experience in his group and his support were instrumental for my decision to pursue a career in Organic Chemistry.

I would like to thank my family and friends, for their love, encouragement and support of my scientific and academic goals, which have taken me further and further away from home.

Finally, my husband and best friend, David. I'm forever grateful for all your silent sacrifices.

Declaration

Except as is indicated by the text, this dissertation is a result of my own work and includes nothing, which is the outcome of the collaboration. It has not been submitted, either in whole or in part, for a degree or other qualification at another university. In accordance with the regulations, this thesis does not exceed 60,000 words.

Publications

Some of the PhD work described in this thesis has been published in the following peer-reviewed articles:

"A Practical Guide for Predicting the Stereochemistry of Bifunctional Phosphoric Acid Catalysed Reactions of Imines" **Jolene P. Reid**, Luis Simón and Jonathan M. Goodman* – *Acc. Chem. Res.* **2016,** *49*, 1029-1041.

"Goldilocks Catalysts: Computational Insights into the Role of the 3,3' Substituents on the Selectivity of BINOL-Derived Phosphoric Acid Catalysts" **Jolene P. Reid** and Jonathan M. Goodman* – *J. Am. Chem. Soc.* **2016**, *138*, 7910-7917.

Selecting Chiral BINOL-derived Phosphoric Acid Catalysts: General Model to Identify Steric Features Essential For Enantioselectivity" **Jolene P. Reid** and Jonathan M. Goodman* - *Chem. Eur. J.* **2017**, Accepted.

"*Transfer Hydrogenation of ortho-Hydroxybenzophenone Ketimines Catalysed by BINOL-derived Phosphoric Acid Occurs by a 14-Membered Bifunctional Transition Structure"* **Jolene P. Reid** and Jonathan M. Goodman* - *Org. Biomol. Chem.* **2017**, Accepted.

Table of Contents

Development and Application of Computational Methods for the Prediction of Chiral Phosphoric Acid Catalyst Performance

Jolene Patricia Reid

Abstract

Chiral phosphoric acids are bifunctional catalysts that have the ability to activate electrophiles and nucleophiles through hydrogen bonding, and they have been successful in catalysing highly enantioselective additions of a wide range of nucleophiles to imines. In most literature reports it is not frequently revealed how these catalysts impart enantioselectivity. Thus, the vast majority of time required for reaction development is expended on the optimisation of the catalyst features. The research described here explores the ability of relating computational derived catalyst parameters to enantioselectivity as a means to assess the catalyst features important for enantioinduction. The proposed features are evaluated computationally and summarised into simple qualitative models to understand and predict outcomes of similar reactions.

In Chapter 1, I provide an overview of the progress and challenges in the development of chiral phosphoric acid mediated reactions. I highlight leading computational studies that have enabled a greater understanding of how the catalyst imparts reactivity and selectivity. In general, the studies focus on the most effective catalyst and do not do a detailed investigation into the effects of changing the substituents at the 3,3' positions. Implicating steric effects from reasonably large groups as a key component in imparting enantioselectivity. However, it is clear that they have a more subtle effect. A large group is required but if it is too large poor or unusual results are obtained, making the correct choice of reaction conditions challenging. In Chapter 2, I develop a quantitative assessment of the substituents at the 3,3' positions. I show in Chapters 3 and 4 that I can use rotation barriers in combination with a novel steric parameter, AREA(θ), to correlate enantioselectivity. By exploiting this finding, the catalyst features important for enantioselectivity can be identified, and this is validated by QM/MM hybrid calculations. Summarising these detailed calculations

into a single qualitative model, guides optimal catalyst choice for all seventy-seven literature reactions reporting over 1000 transformations. These mechanistic studies have guided the design of a new catalyst with increased versatility, which is discussed in Chapter 5.

Chapter 6 details my study into the effect of the hydroxyl group on the mechanism of transfer hydrogenation of imines derived from *ortho*-hydroxyacetophenone. I show, using detailed DFT and ONIOM calculations, that transition states of these reactions involve hydrogen bonding from both the hydroxyl group on the imine and the nucleophile's proton to the phosphate catalyst. This mechanistic pathway is lower in energy than the conventional, consistent with the experimentally observed increased rates of reaction compared with imines that are not derived from *ortho*-hydroxybenzophenone. To complement, the high-level calculations have been summarised into a simple accessible qualitative model that predicts the correct sense of stereoinduction for all examples.

In Chapter 7, computational analysis is used to provide insight into the origins of enantioselectivity in chiral phosphoric acid catalysed Friedel-Crafts and Mannich reactions proceeding through monoactivation mechanisms. I show that enantioselectivity arises as a result from minimising steric clashing with the catalyst and despite the increased flexibility for rotation around the catalyst-imine H-bond only one TS is favoured.

The final chapter contains an in-depth look into the stereoelectronic effects altering enantioselectivity in the silver-phosphate mediated spirocyclisation reaction involving aromatic ynones. In this study I show that enantioselectivity is governed by the non-covalent interactions between the aromatic group of the ynone and the 3,3' substituent. I was able to propose synthetic modifications to the substrate used in this reaction, resulting in an improvement in enantioselectivity.

Glossary of Abbreviations and Acronyms

Å	Angstrom (10^{-10} m)
Ar	aromatic group
AREA	a remote environment angle
ASL	atom specification language
B3LYP	Becke exchange with Lee-Yang-Parr correlation
B3LYP-D3	B3LYP with Grimme's D3 dispersion correction
BINOL	1,1'-bi-2-naphthol
Bn	benzyl
Boc	*tert*-butyloxycarbonyl
Bu	butyl group
Bz	benzoyl
CPA	chiral phosphoric acid
DCM	dichloromethane
DFT	density functional theory
DME	dimethoxyethane
dppm	1,1-Bis(diphenylphosphino)methane
ECP	effective core potential
ee	enantiomeric excess
Et	ethyl group
H_8-BINOL	5,5',6,6',7,7',8,8'-octahydro-1,1'-2-naphtol
K	Kelvin
kcal mol^{-1}	kilocalories per mole
kJ mol^{-1}	kilojoules per mole
M06	Minnesota 06 density functional with 27% HF exchange
M06-2X	Minnesota 06 density functional with 54% HF exchange
Me	methyl group
MM	molecular mechanics
MPWB1K	modified Perdew-Wang exchange with Becke's 95 correlation functional optimised for kinetics
Nu	nucleophile
ONIOM	our own n-layered integrated molecular orbital and molecular mechanics
OPLS	optimised potentials for liquid simulations

PCM	polarisable continuum model
PES	potential energy surface
Ph	phenyl group
PhMe	toluene
PMP	*para*-methoxyphenyl
QM	quantum mechanics
RT	room temperature
SCRF	self-consistent reaction field
SPINOL	1,1’-spirobiindane-7,7’-diol
TADDOL	α,α,α',α'-tetraaryl-2,2-disubstituted 1,3-dioxolane-4,5-dimethanol
TBS	*tert*-butyl-dimethylsilyl
THF	tetrahydrofuran
TIPSY	3,3’-Bis(triphenylsilyl)-1,1′-binaphthyl-2,2′-diyl hydrogenphosphate
TMP	trimethoxyphenyl
TMS	trimethylsilyl
TRIP	3,3'-bis(2,4,6-triisopropylphenyl)-1,1'-binaphthyl-2,2'-diyl hydrogenphosphate
TS	transition state(s)
UFF	universal force field
VANOL	3,3′-Diphenyl-2,2′-bi-1-naphthol
VAPOL	2,2′-Diphenyl-(4-biphenanthrol)

Chapter 1

1 Chiral Phosphoric Acids As Catalysts In Asymmetric Organic Reactions

1.1 Introduction

The need for single enantiomer molecules has driven great advances in the field of enantioselective catalysis. In response to demand, a wide variety of asymmetric catalysts have been developed that provide synthetic chemists with the tools to perform numerous organic transformations in an enantioselective fashion.[1-2] Chiral transition metal and Lewis acid catalysts once dominated this thriving field.[3-7] Only over the last decade has the use of organic molecules as catalysts played an increasingly prominent role. Despite historical roots dating back to 1912,[8] the area remained largely unexplored until Barbas and List demonstrated a highly enantioselective intermolecular aldol catalysed by (*S*)-Proline (Figure 1.1).[9]

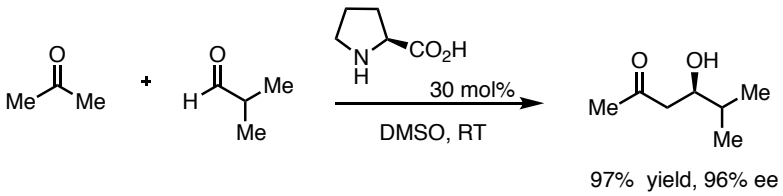

Figure 1.1. Proline catalysed intermolecular aldol reaction.

This and the seminal reports that followed lead to the area of organocatalysis which has expanded to include numerous small organic molecule catalysts that interact with their targets through a range of Lewis acidic,[10-13] basic,[14] and hydrogen bonding[15-16] interactions. The most notable organocatalysts have held persistent interest in the area due to their mechanism of activation being applicable to a range of transformations. In some instances a single catalyst can activate a substrate through distinctly different modes promoting mechanistically disparate reactions.[17] There have been several recent examples of catalysts that demonstrate such sophisticated utility; chiral phosphoric acids[18-19] have, however, emerged to be exceptionally general.

1.2 Chiral Phosphoric Acids as Catalysts

Chiral phosphoric acids are commonly derived from BINOL and their use as catalysts has witnessed impressive development since their introduction in 2004. The disclosure of the first chiral phosphoric acid catalysed Mannich reaction established the conceptual foundations for activation of imines to nucleophilic addition.[18-19] A variety of nucleophiles have shown to participate efficiently, enabling the formation of multiple types of bonds, (C-C, C-O, C-S, C-N, C-P and C-H) in an asymmetric fashion summarised in Figure 1.2.

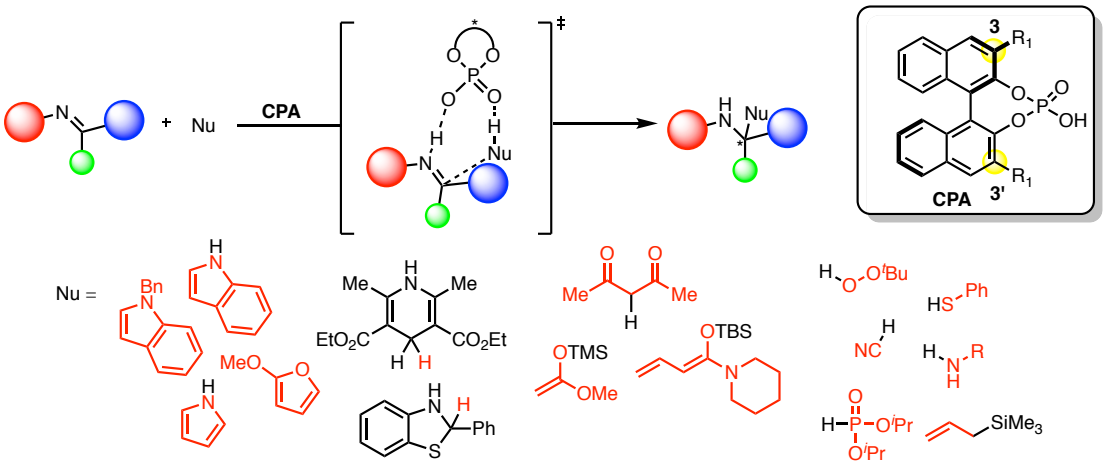

Figure 1.2. Examples of the addition of nucleophilic to imines catalysed by phosphoric acids. Red indicates the functionality added to imine.

Phosphoric acids catalyse these transformations through multiple mechanisms and numerous experimental and computational studies have generated a good mechanistic understanding of the reasons for stereoselectivity. Most proceed through a bifunctional mechanism, in which the electrophile and nucleophile are activated simultaneously, creating a rigid network capable of inducing high enantioselectivity (Figure 1.2). The successful realisation of such a strategy constituted a highly general method of addition of protic nucleophiles to imines. Results from calculations have led to the establishment of simple qualitative models that have found use in predicting the stereochemical outcome for a diverse array of reactions.[20] Despite the predictable nature of the stereocontrol and the plethora of transformations that can be effected by these catalysts, their use in the construction of complex natural products has lagged far behind other organocatalysts.[21] A number of excellent reviews on chiral phosphoric acid catalysis have been published

focussing on the different reactions possible.[22-24] To be consistent with the theme of this thesis, this review will divert attention to key mechanistic studies that led to and provided evidence for the distinct modes of catalyst activation of imines. Theoretical calculations have played a valuable role providing chemists with accurate energies and geometries of key transition states, TS, providing insight into the mechanism often not possible by experiment. Mechanistic investigations have been largely based on the fundamental curiosity of how these catalysts operate. With the seemingly ever-increasing structural variations of the catalysts outlined below, I ask complementary questions. *Why are some catalysts more selective than others? Is it even possible to know with a high degree of certainty what catalyst to choose?* My attempt at answering these questions will be the subject of this thesis.

1.3 Investigations into the Bifunctional Mechanism

In contrast to the rapidly accumulating reports on new methods for asymmetric additions to imines, there were at that time very few, if any, systematic mechanistic studies to elucidate the basis of catalysis and enantioinduction. This was presumably due to the large size of the catalyst combined with the high degree of conformational flexibility making it difficult to study the key steps of the reactions computationally. This section will detail the leading computational investigations into the bifunctional mechanism focussing on the general challenges and strategies in this field.

1.3.1 Phosphoric acid catalysed transfer hydrogenation

In 2007, our group studied the asymmetric reduction of imines by Hantzsch esters catalysed by BINOL-derived chiral phosphoric acids (Figure 1.3).[25] At that time there were two plausible mechanisms (Figure 1.4). The first, *Mechanism A*, involves activation of the imine through a single hydrogen bond, in which the Hantzsch ester approach should be preferred on one face. An alternative, *Mechanism B*, involves the activation of both the electrophile and the nucleophile by the catalyst. Prior experimental investigations on the Mannich,[26] aza-ene,[27] Friedel-Crafts[28] and hydrophosphonylation[29] reactions have suggested a similar mechanism could be in operation. Goodman *et al.* expressed a preference for *Mechanism B*, as the substrate bound to the catalyst *via* a single hydrogen bond may be too flexible to account for the high enantioselectivity. Despite this, there was experimental evidence based on X-ray diffraction studies of imine-catalyst complex in support of *Mechanism A*. Terada *et*

al. also suggested that a similar mechanism to *A* could be in operation in the Mannich reaction.[30]

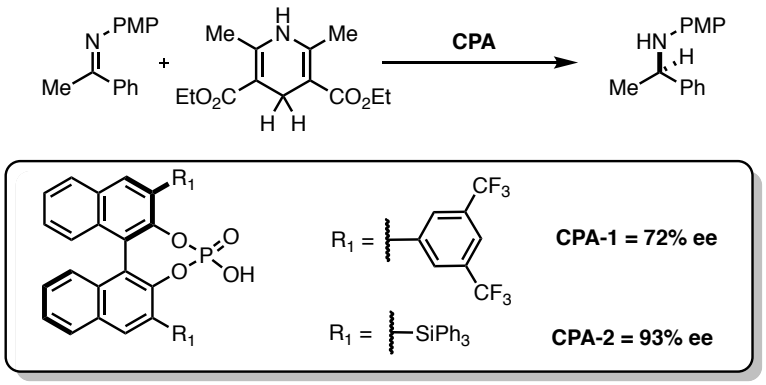

Figure 1.3. BINOL-phosphoric acid catalysed transfer hydrogenation. The MacMillan[31] synthetic protocol differs from the Rueping[32] approach in that the imines were not preformed. The overall transformation, however, is the same.

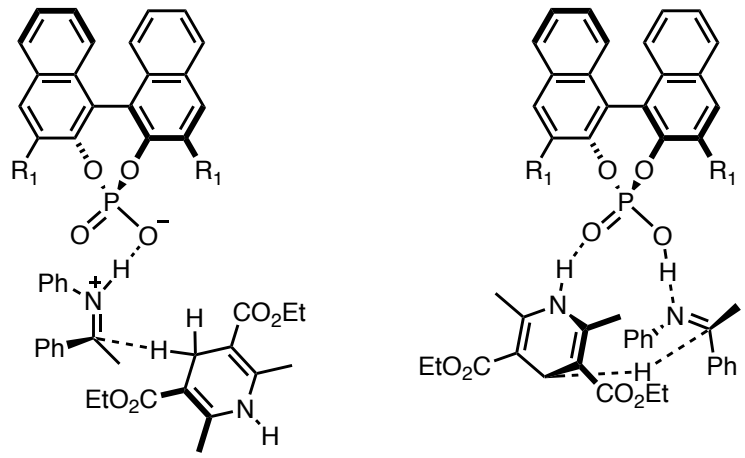

Mechanism A ***Mechanism B***

Figure 1.4. Mechanistic proposals for the transfer hydrogenation reaction.

The theoretical investigation began using a simplified model, 1,3-butadiene-1,4-diol-phosphoric acid as the catalyst, calculated which of the mechanisms was most likely using DFT (Figure 1.5). The study revealed four unique transition states according to *Mechanism B*, evenly divided between *E* and *Z* configurations of the imine. Due to the open, flexible nature of *Mechanism A*, twelve transition states were found, once again evenly divided between *E* and *Z* imine configurations. The relative energies of these competing transition states showed that *Mechanism A* was strongly disfavoured relative to *Mechanism B*, where the hydrogen atoms are transferred between reactants and catalyst in a concerted fashion. Another possible mode of activation involves protonation of imine and a single interaction from the phosphate catalyst with NH of the Hantzsch ester; *Mechanism C*. As with *A*, *C* was strongly disfavoured relative to *B*. The transition structures in which the imine has a *Z* configuration are lower in energy compared to *E*. Although calculations show that the *E*–imine ground state is more stable by 2.9 kcal mol^{-1}, a fast *E/Z* equilibration is expected and so the reaction should proceed through the lowest transition state pathway, following the Curtin-Hammett principle. Mechanisms have been reported for the acid catalysed *E/Z* isomerisation of imines, including protonation-rotation and addition-rotation-elimination.[33] Lack of resonance stabilization and greater steric interactions between the phenyl and methyl groups in the imine all contribute to the destabilisation of the *E* transition state. Rueping constructed a model based on a X-ray crystal structure of the phosphoric acid catalyst. In this model he placed the imine in a *Z* configuration and the nucleophile approached from the less hindered face, reproducing the sense of stereoinduction observed experimentally.

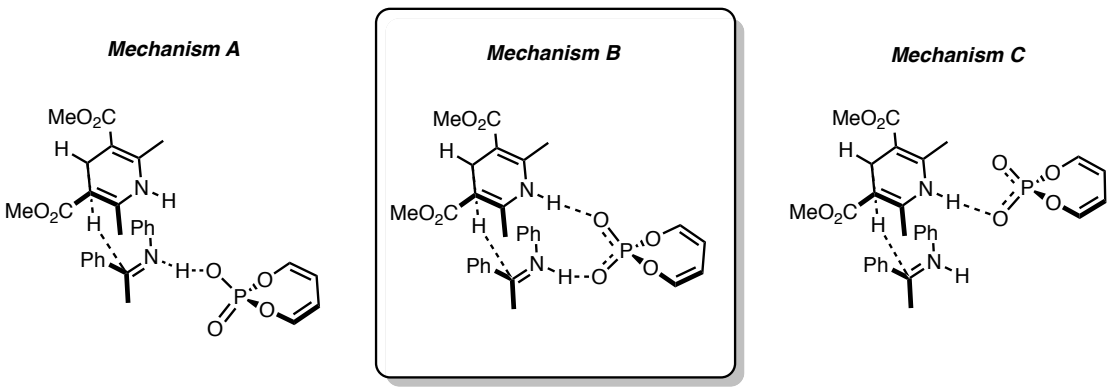

Figure 1.5. Lowest energy transition states for the model catalyst.

To probe the origins of stereoselectivity transition states using the full catalyst system were located. To reduce computational time slightly, simpler molecules were used as substrates in the calculations; para-methoxyphenyl (PMP) group was replaced by a phenyl, and the dimethyl Hantzsch ester was used instead of the diethyl counterpart. In Simón and Goodman's investigation they performed high-level two layer ONIOM[34] calculations using the Gaussian package.[35] Our group has successfully investigated the enantiodetermining step of many phosphoric acid catalysed reactions using this method.[25,36-41] These calculations demonstrated that molecular mechanics, despite being computationally very cheap, was sufficiently accurate to describe the steric environment of the BINOL scaffold; the chemically relevant part, the bond breaking and making, was investigated using QM methods (Figure 1.6). A benchmarking process determined UFF offered a better description of the rotational barrier of the biphenyl when compared to some semiempirical methods, so it reproduces well the position of the bulky groups attached to the BINOL. The UFF description of conformational energetics is typically quite poor,[42] however, when used to study a rigid catalyst backbone and flanking groups this is not as important as the force field's description of non-bonding interactions between the catalyst's aromatic groups and the two substrates. This can lead to greater accuracy than uncorrected DFT calculations. The failures of popular density functionals, including B3LYP,[43-44] to describe dispersion effectively are well documented[45] and this has the result that the prediction of critical binding energies is too small in many reactions. The Minnesota meta-GGA functionals developed by Truhlar,[46-47] have been parameterized to include dispersion effects and their use has become routine in the study of dispersion dominated systems. Dispersion-corrected DFT is another method by which dispersion effects are modelled. Functionals such as B3LYP-D3, make use of a pre-existing functional but include an add-on energy term to account for dispersion, a method made popular by Grimme.[48] In this study, geometry optimization with ONIOM(B3LYP/6-31G*:UFF) followed by single-point calculations (MPWB1K/6-31G**) in toluene with polarizable continuum model (PCM) was performed. By combining MM and QM, the speed of the calculations is dramatically increased without compromising the precision for this many-atom system. The additional single point calculation is required to accurately describe the multiple interactions leading to the overall catalytic effect. Applying this energy correction allows improved comparisons between calculation and experiment. Solvation often plays a crucial role in organic reactions and computationally, I can model solvation in one of two ways. One option is employing an explicit model, in which I include explicit solvent molecules within the systems that I am optimising. Although more accurate if employed with appropriate conformational sampling, this can prove to be computationally very expensive. It

is much more commonplace to use an implicit solvation model. One type applies a homogenous dielectric across the system; this continuum averages the solvent effect making it much more computationally feasible than modelling individual molecules.[49] The self-consistent reaction field (SCRF) method is often used, where a cavity is defined in which the system being solvated is placed. The free energy of solvation is computed as the sum of four terms, ΔG_{cavity} the free energy cost of creating the cavity, and multiple terms to describe the interactions between the solvent and solute; $\Delta G_{dispersion}$, $\Delta G_{repulsion}$ and $\Delta G_{electrostatic}$. Numerous variations of these continuum models exist; the most popular is the PCM in which the continuum is polarizable and will be used in this thesis.[50]

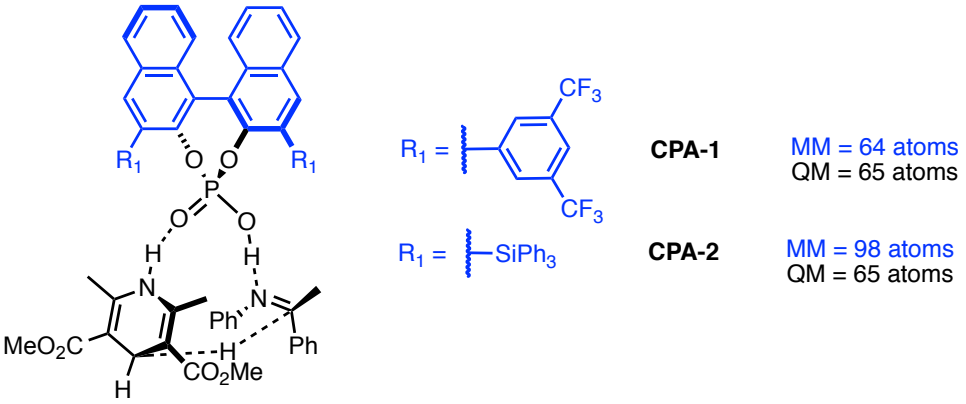

Figure 1.6. ONIOM partitioning in the phosphoric acid catalysed transfer hydrogenation. Blue indicates atoms treated with MM, black atoms indicated atoms treated with QM methods.

Computational investigations described in this thesis uses a similarly structured protocol of combining calculations at different levels of theory with Monte Carlo[51] searching algorithms as a trade-off between precision and speed. My TS searching protocol proceeds as follows; firstly we use chemical intuition to create a candidate structure, keeping key bond distances constrained in the molecule(s) of interest, I then use a Monte Carlo conformational searching program, in line with MM optimisations to randomly sample dihedral angles. Due to the approximate nature of the low-level method at this stage of the sampling it is not sufficient to rely on the lowest energy structure generated. Instead, an energy limit is specified, typically a 10 kJ mol^{-1} cut-off, structures below are re-optimised using a high-level method. In order to locate the stationary point, I use the guess geometry generated, and either using ONIOM(B3LYP/6-31G**:UFF) or full DFT(B3LYP/6-31G**) to perform constrained geometry optimisations followed by TS optimisations with the use of the Berny algorithm. [52]

Unfortunately, there are no easy ways to locate a TS and finding one is complicated since I need the single coordinate for which the associated force constant is negative. TS geometries are much more sensitive to the initial guess geometry provided for the calculation than for the location of ground states. If the guess is not accurate enough the technique will not work. A second method through which I can generate accurate guess geometries is by running a PES scan, which can be used to fix and optimise geometries across a broad range of bond distances. The geometry, which results in the highest energy, is the most accurate initial guess geometry for a TS optimisation. Such a method can be time-consuming and should only be used in instances when the first, fails. If successful this, in most cases, provides a TS with a reliable geometry. In order to increase the accuracy of the energy, a single point energy calculation is performed on the resulting structures using a higher level of theory, typically M06-2X/6-31G** and used to correct that obtained from the ONIOM calculation. I can now compare the TS leading to competing products, to obtain $\Delta\Delta G^{\ddagger}$ values with which I can determine the selectivities of various reactions. If I have a system for which non-degenerate conformers may exist, I can evaluate their relative population using Boltzmann analysis, which may result in improved comparisons between experiment and theory. Since the relationship between the rate constant and calculated selectivities with Gibbs free energy is exponential, minor errors in computed energies can lead to major errors in replicating experimental ee. The effects of error in calculated energies are most pronounced when the selectivity of the system is low, and less when systems are expected to exhibit high levels of enantioselectivity. If calculation does not compare favourably with experiment, problems may have arisen from conformational issues from insufficient sampling and the conformer energy window should be increased. Alternatively, the functional in the QM layer should be changed for one that accounts for dispersion. However employing a higher level of theory will be computationally more expensive and so re-optimisation of the key TS should be considered in the first instance. Finally, as a last resort the proposed mechanism may not be in operation and will need to be re-evaluated with the simplest model catalyst. This approach is outlined in Figure 1.7. All steps are operated by hand; despite the increasing popularity of automating TS searching through computer algorithms,[53] that process, however, is not appreciably faster.

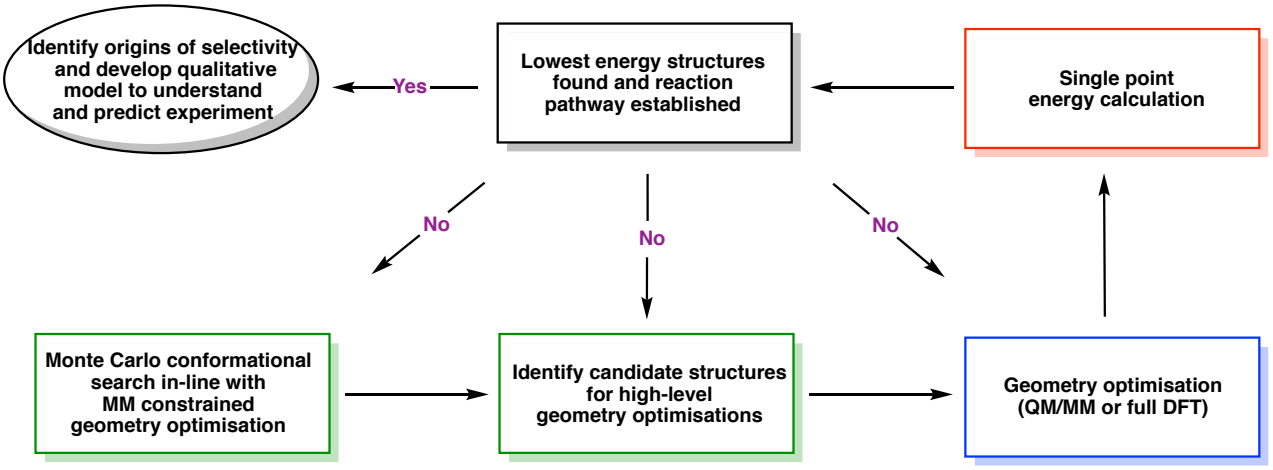

Figure 1.7. An illustration of my approach used for TS conformational searching. The steps highlighted in colour indicate the different computer programs used; green represents Macromodel,[54] blue, Gaussian[35] and red, Jaguar.[55]

Computations of the full catalyst systems have led to the development of the model depicted in Figure 1.8. This model is based on the projection of the catalyst such that the two BINOL oxygen atoms are in the plane of the paper. The free oxygen atoms are above and below, each having bulky substituents on either side. Alternatively, the chiral scaffold can be modelled by a quadrant diagram, in which quadrants II and III are equivalently hindered. The reagents reside in the empty quadrants. Such a model originally proposed by Terada[30] and Himo[56] has become popular to explain the stereoselectivities of numerous phosphoric acid catalysed reactions.

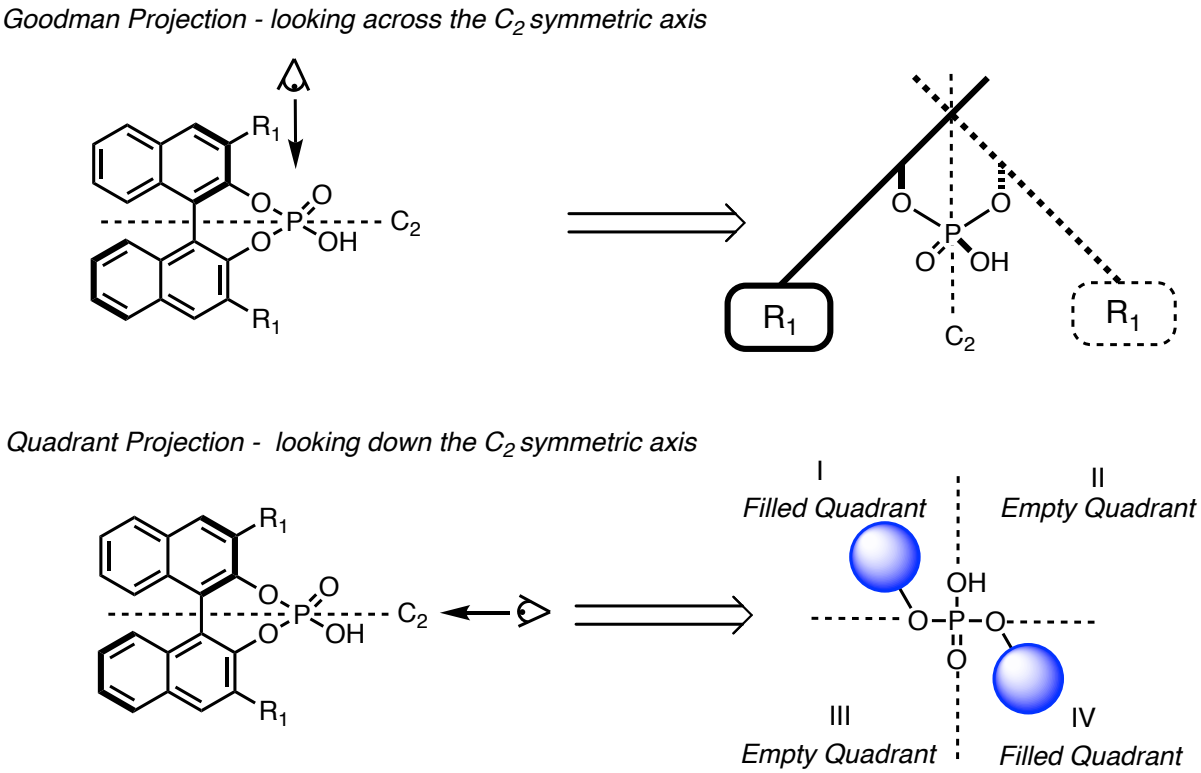

Figure 1.8. Alternative views of the phosphoric acid catalyst.

The catalyst binds to the substrate *via* the catalyst's hydroxyl group and there is a second interaction from the phosphoryl oxygen to the nucleophiles proton. The catalyst therefore simultaneously activates both the electrophile and the nucleophile. The C_2 symmetry of the phosphate anion allows us to draw the imine at the front of the diagram without loss in generality. The *N*-substituent can be directed away from the front of the 3,3' which I label *Type I* or towards the 3,3' which I label *Type II*. Additionally, the imine can exist as the *E* or *Z* stereoisomers, which is defined based on steric size. In each case the nucleophile is delivered from behind (Figure 1.9).

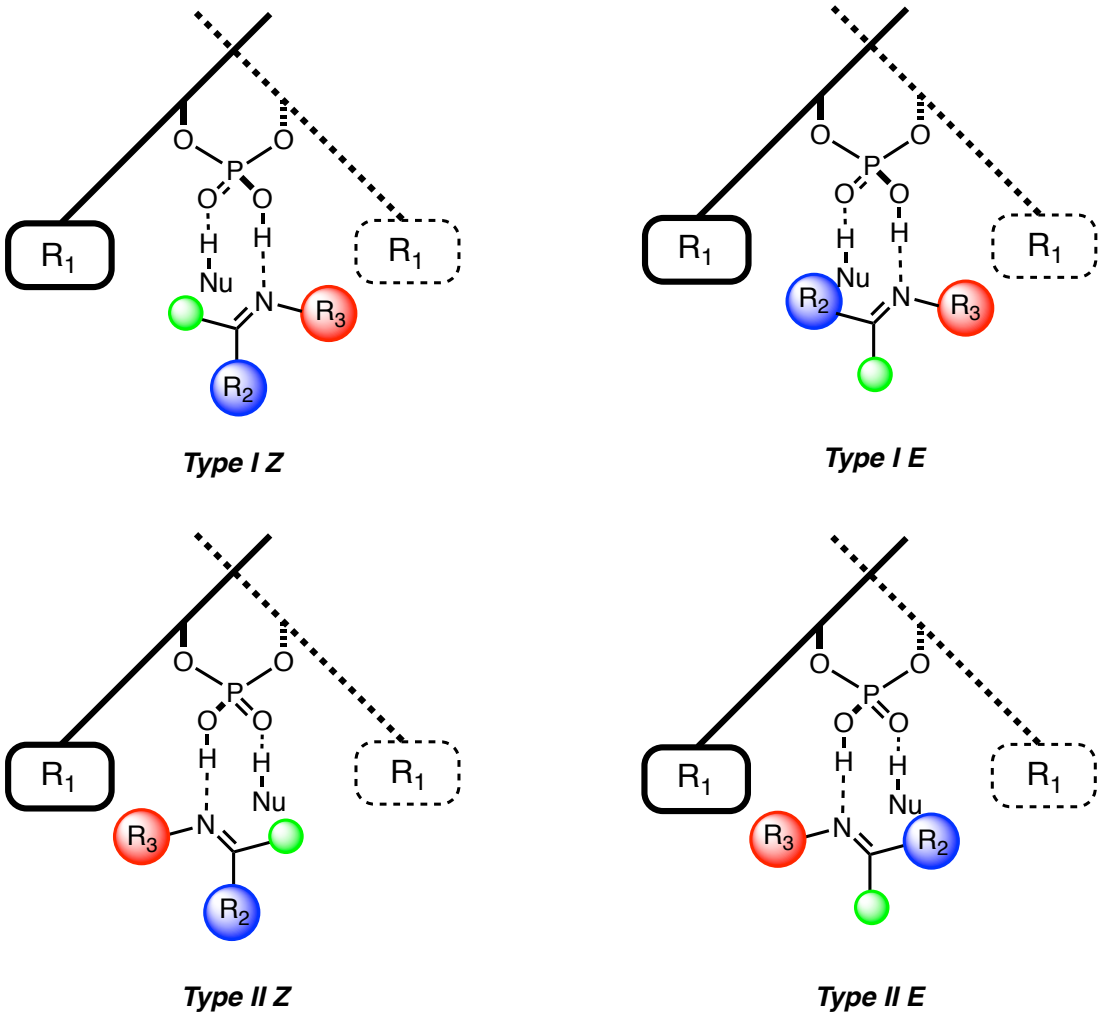

Figure 1.9. Transition state models for the prediction of stereoselectivity.

Both catalysts, **CPA-1** and **CPA-2** (Figure 1.3) favoured a *Type I Z* pathway and several interactions account for such a preference. The unfavourable steric clash between the large phenyl substituent and the 3,3' disfavours the *E* transition state relative to the *Z*. Similar steric interactions between the N-substituent and the 3,3' group disfavour *Type II* relative to *Type I.* The calculations also capture the increase in stereoselectivity observed when Macmillan's catalyst was employed. Relative populations of transition states were predicted at the temperature they were performed from electronic energy differences and based on Boltzmann distribution analysis. The computed enantiomeric excess (ee) for Rueping's catalyst was 70% ee and 97% ee for Macmillan's, both of which are very close to the experimental values of 72% ee and 93% ee. List and co-workers reported a similar protocol to Rueping's.[57] Improved enantioselectivities were reported when TRIP was employed as the catalyst. Although the precise mechanism was unclear, the Rueping group expanded the

scope of the transfer hydrogenation to quinolones.[58] In such a substrate only the *Z* imine configuration could exist. This produced the same sense of stereoinduction as with the transfer hydrogenation reaction, which provides further evidence of the participation of a *Z* imine in the transition state, reinforcing Rueping's original surmise. Himo *et al.* also observed, through full DFT calculations at the B3LYP/6-31G* level utilising a biphenol model catalyst, the chiral phosphate acts as a bifunctional catalyst in their theoretical study of the transfer hydrogenation reaction of phenyl ketimines.[56] Expressing the importance of *E* and *Z* imine stereoisomers for the stereochemical induction, the group determined that the more compact *Z* iminium transition state was energetically more reasonable than the *E*. Yamanaka *et al.* have reached similar conclusions in their theoretical investigation into the mechanism of transfer hydrogenation of ketimines by benzothiazoline.[59] In their studies they also investigated the substituent effect of the phosphoric acid. Through calculating the diastereomeric transition state structures for each of the catalysts it was determined that the larger substituent enforces stereoselectivity. The 4.9 kcal mol^{-1} energy difference between the *Type I Z* and *Type II Z* in the TRIP catalysed process is reduced to 1.5 kcal mol^{-1} with the 9-anthryl derived catalyst reproducing the trend observed experimentally. Shortly after the emergence of chiral phosphoric acid catalysed transfer hydrogenations, the List group sought to expand this further with their investigations of the asymmetric reductive amination of aldehydes *via* dynamic kinetic resolution.[60] A crucial practical requirement was the hydrogenation would be faster for one imine enantiomer than the other. Under reductive amination conditions rapid racemisation of the imine would occur through imine/enamine tautomerisation, setting up a dynamic kinetic resolution. Using this system, good to excellent enantioselectivities were achieved with a range of substrates. Detailed calculations by Himo have investigated the origins of enantioselectivity, in which they determine that the reaction proceeds through the *S*-*E*-imine.[61]

1.3.2 Phosphoric acid catalysed Strecker reaction

Our discoveries about the Hantzsch ester hydrogenation lead us to re-examine the related Strecker reactions reported by Rueping (Figure 1.10). [62 - 63] Both imines undergo stereoselective cyanide addition to afford the corresponding α-aminonitriles in good to excellent enantiomeric excess. The reaction of ketimines lead to lower levels of selectivity and modification of the 3,3' substituents did not lead to an improvement. Intriguingly, the reaction of imine **1** produces the opposite sense of stereoinduction than observed with the transfer hydrogenation study (Figure 1.3).[25] Recognizing this, the authors constructed a model based on the X-ray crystal structure of the phosphoric acid, in which the imine was in the *E* conformation and the nucleophile approached from the less hindered face. The configuration of the stereogenic center in **4** was not determined.

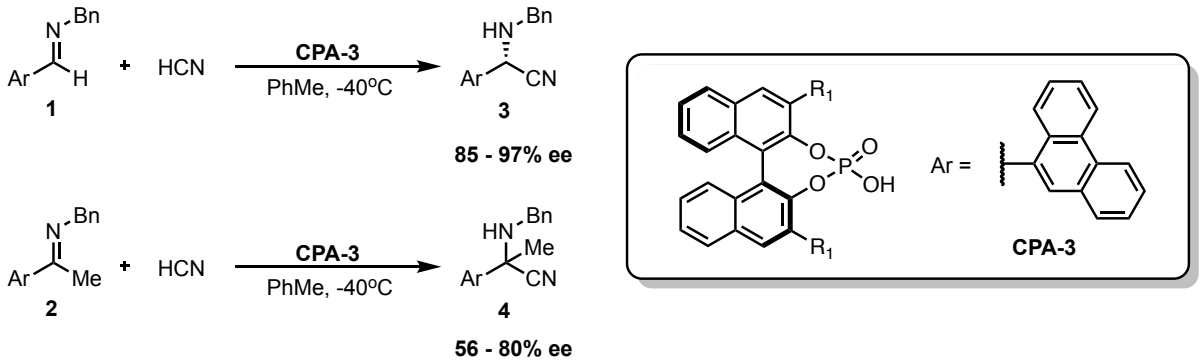

Figure 1.10. Examples of phosphoric acid catalysed Strecker reactions reported by Rueping.[62-63]

Rueping proposed a stepwise mechanism, in which the phosphoric acid catalyst first protonates the imine, activating it towards nucleophilic attack by the hydrogen cyanide. Recovering the proton from the protonated nucleophile then regenerates the phosphoric acid. The mechanism could also proceed through simultaneous hydrogen bonding interactions to both electrophile and nucleophile analogous to Goodman's studies with the transfer hydrogenation of imines.[25] The preferred reaction pathway was determined using the model phosphoric acid as before. Four different pathways were considered, summarised in Figure 1.11.[36] Transition states in which the catalyst establishes a single interaction with HCN leads to *Mechanism D*. The catalyst can establish two points of contact to the reactants leading to *Mechanism E*. This would afford an alkylisocyanide that could rearrange to form the product. [64] These transition states were calculated to be disfavoured relative to *Mechanism F* in which the catalyst binds to hydrogen isocyanide through the phosphoryl oxygen and a second interaction from the Brønsted acidic site to the imine. This analysis

would suggest that the isomerisation of hydrogen cyanide is faster than the addition to the imine. The calculated energy barrier for isomerization catalysed by the phosphoric acid is 23.5 kcal mol^{-1}. Amines generated in the reaction may also participate in this process. The energy barrier mediated by ammonia was calculated to be 19.9 kcal mol^{-1}. The energy barrier for isomerisation is smaller than any of the reactions involving hydrogen cyanide suggesting a rapid isomerisation followed by addition. HCN attacking through the carbon rather than the nitrogen leads to *Mechanism G*. The *Z* transition state corresponding to *Mechanism G* was never located; attempted geometry optimisation led to rearrangement to the isomeric *Mechanism F Z* TS. As with the transfer hydrogenation of phenyl ketimines, the model studies showed a preference for a *Z* transition state.

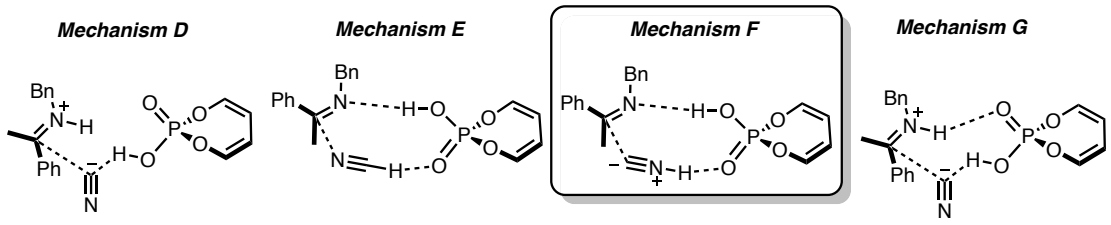

Figure 1.11. Calculated lowest energy transition states for the model catalyst. The imine stereoisomer depicted was calculated to be lower in energy for this mechanism.

The models depicted in Figure 1.9 are used to rationalise the stereoselectivities. In line with the model studies *N*-benzyl ketimines proceeded through a *Type I Z* transition state. Relative populations of transition states were predicted at 298 K from electronic energy differences and based on the Boltzmann distribution analysis. The calculation suggests that the *R* product should be formed in 58% enantiomeric excess in accordance with experiment, 56% ee, although the absolute configuration was not determined. For benzaldehyde-derived benzyl imines the reaction proceeds *via Type I E* pathway, agreeing with Rueping's original conformational analysis proposed interaction of the phosphate anion and the iminium ion. Although *Type I Z* transition states are more compact, the energy required to rotate the phenyl group is greater than the energy of the steric interactions with the 3,3' substituents.

1.3.3 Phosphoric acid catalysed Friedel-Crafts reaction

The bifunctional mechanism can also be applied to the Friedel-Crafts reaction as proposed by Zhou, supported by experimental studies.[28] The group noted that protecting the indole led to no reaction, supporting the importance of a productive binding site to the catalyst *via* a hydrogen bond to this position. Indeed, such a strategy has become a standard experimental

test of the bifunctional mechanism. In each of the reactions studied so far, the nucleophile has been symmetrical, unlike indole. Focusing their efforts on two literature examples reported by Zhou[28] and You[65] (Figure 1.12), Goodman expanded the model (Figure 1.9) to account for the stereoselective outcome of such reactions.[37] There are sixteen reasonable diastereomeric transition states for these reactions, resulting from *Type I* or *Type II* pathways, four different arrangements of the imine and two orientations of the indole. The model studies allowed reduction of this number to eight, as the energy differences between the *E* and *Z* configurations are so large that not even the catalysts steric interactions could change this preference.

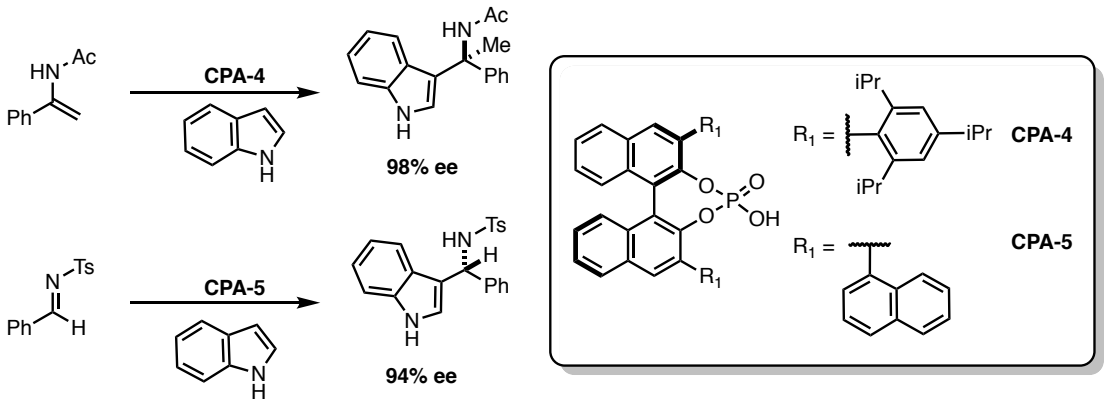

Figure 1.12. Friedel-Crafts reactions of indole and imines reported by the groups of Zhou[28] and You[65].

In both reactions only four of the transition states explored computationally are significant for the prediction of stereoselectivity. There were two possible arrangements of imines, *Type I* and *Type II* and also two possible arrangements of the nucleophile, *exo* and *endo*. In the lowest energy transition state structures, the large indole is directed to the side of the catalyst that is not occupied by the bulky catalyst group, minimising steric interactions. The lowest TS corresponds to a *Type II* pathway. In this conformation the acyl group is directed towards the 3,3' but the steric interactions are reduced as the imine tilts. This allows the largest substituent, the phenyl group, to be placed furthest from the bulk of the 3,3' substituents. Larger N-substituents adopt a similar tilted disposition, but the interactions with the 3,3' substituent and this larger group are much more costly. As shown in Figure 1.13 the *Type I* pathway with tosyl-imines is now highly favoured. In agreement with experiments, a reversal in stereochemistry is expected.

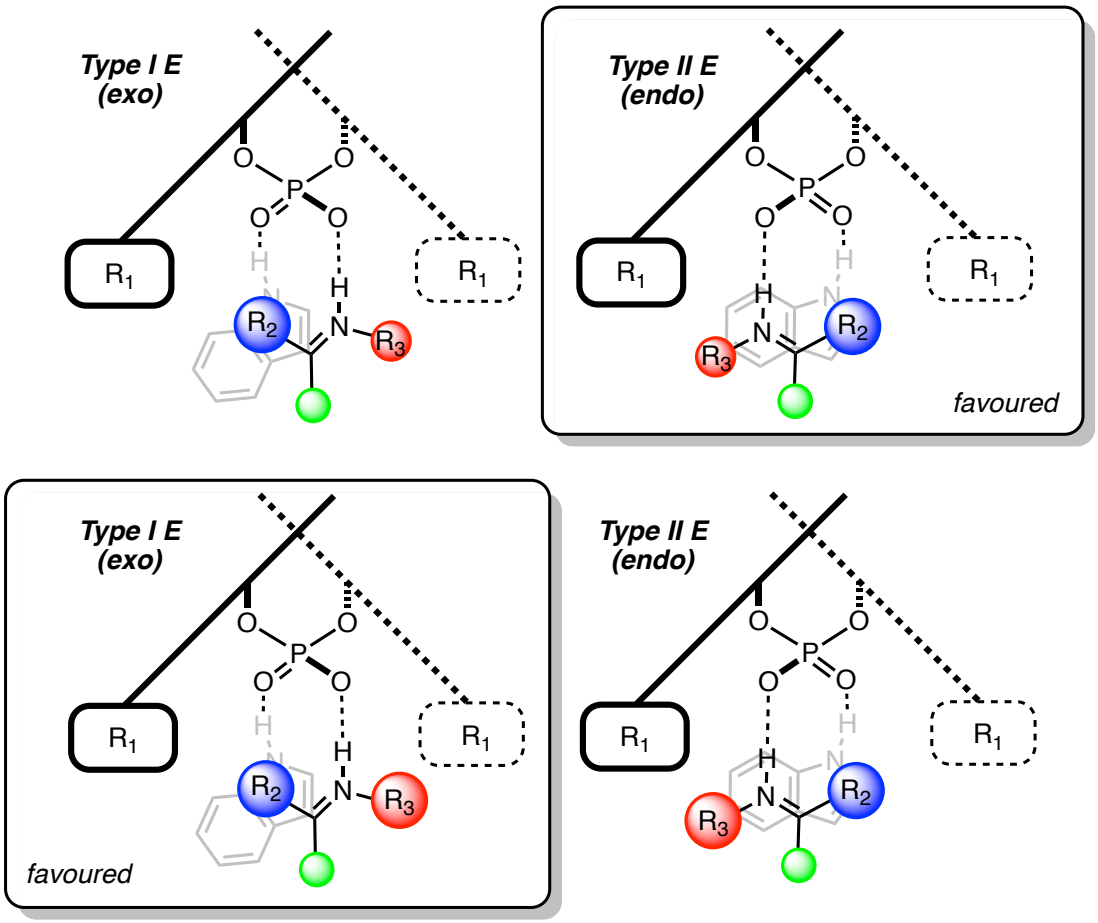

Figure 1.13. Models to predict the enantioselectivity in the Friedel-Crafts reaction of indoles to acyl ketimines (top) and tosyl aldimines (bottom).

Although not directly related, a recent study by Gschwind *et al.* on the conformational preferences of binary complexes between ketimines and TRIP showed by NMR studies that the interconversion between *Type I* and *Type II* conformations can occur by two distinct mechanisms, rotation (oxygen on catalyst that participates in H-bonding is maintained) or tilting (oxygen on catalyst that participates in H-bonding is swapped).[66] The more compact structure of *Z* imines allows operation of both. However, the more extended structure of the *E* restricts this to only a tilting mechanism. The group did not do an extensive investigation into the effect of the 3,3' group on the dynamic movement of the imine inside the catalyst cavity. A larger substituent at the 3,3' position, such as $SiPh_3$, may restrict the *Z* imine's mechanism of interconversion to tilting only.

1.3.4 Phosphoric acid catalysed hydrophophonylation

The hydrophosphonylation of imines was an early example of phosphoric acid catalysed addition of a nucleophile to an imine.[29] This reaction has been the subject of a number of computational studies,[67-69] and each determined that a concerted mechanism was most likely. Experiments also shed light on the mechanism. Replacement of the acidic hydrogen of the nucleophile by an alkyl group eliminates the second point of attachment to the catalyst, and so the product of the reaction was found to be almost racemic, highlighting the importance of a second binding site. Calculations by Shi *et al.* show that acid catalysis is necessary to facilitate phosphonate-phosphite tautomerisation.[69] The pathway involving proton transfer from the phosphoric acid has a lower free energy of activation (31.9 kcal mol^{-1}) than those where the proton is transferred from another molecule of phosphonate. Large substituents at the 3,3' position were important for high stereoselectivities. Steric hindrance between the catalyst and the N-substituent on the imine disfavours the *Type II E* pathway, which accounts for the difference in energy between the diastereomeric transition states, calculated by Shi and Akiyama. In agreement with experiments, similar enantiomeric excesses are expected for the reaction catalysed by catalyst entries 2 and 3 (Figure 1.14). Experimentally Akiyama uncovered the importance of large substituents on the phosphonate. Calculations by Yamanaka trace this back to increased steric repulsion between the isopropyl groups and the catalyst substituents in the competing diastereomeric transition state.

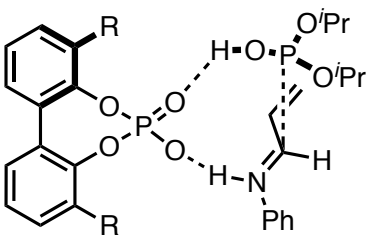

TSA

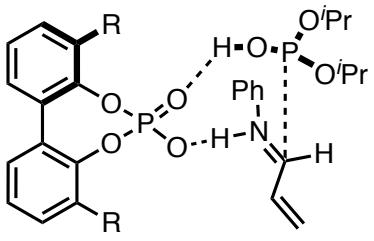

TSB

Entry	R Substituent	$\Delta E^{\ddagger}_{rel}$ **TSA**	$\Delta E^{\ddagger}_{rel}$ **TSB**	ee(%)
1	H	0	+1.0	11
2	Ph	0	+3.2	30
3	4-$NO_2C_6H_4$	0	+3.4	30
4	4-$CF_3C_6H_4$	0	+3.9	33
5	3,5-$(CF_3)_2$-C_6H_3	0	+4.3	84
6	9-Anthryl	0	+0.1	26

Figure 1.14. Effect of the 3,3' substituent on enantioselectivity.

1.4 Alternative Modes of Activation

Most reactions involving nucleophilic addition to imines proceed *via* a bifunctional mechanism involving the activation of both the electrophile and the nucleophile by the catalyst. Such a model, in which the catalyst binds to the nucleophile through its phosphoryl oxygen, requires an acidic proton for such an interaction. Alternatively, if a site of attachment is absent the reaction can proceed *via* dual or mono activation mechanisms. Dual activation involves two contacts either from substrate to catalyst or from catalyst to substrate. Akiyama's Mannich reaction involving silyl enol ethers typifies an example of a reaction proceeding through such a mode of activation.[18] Intriguingly, the free hydroxyl group is absolutely necessary for efficient stereoinduction confirmed experimentally. On the basis of this, Akiyama *et al.* proposed two possible pathways: monocoordination and dicoordination (Figure 1.15). Both involve activation of the imine by protonation, and a second interaction between the free hydroxyl group and the catalyst**.** Using (*R*)-BIPOL as a model catalyst, the lowest energy pathway was calculated to be the dicoordination.[70]

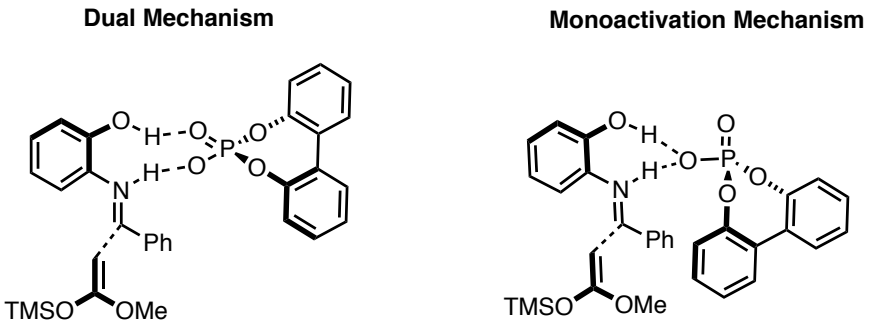

Figure 1.15. Mechanistic proposals for the Mannich reaction.

The computational study has also provided insight into the origin of stereoinduction. The nucleophile attacks the imine preferentially on the *Re*-face, due to steric repulsion between the incoming nucleophile and the 3,3' substituent in the *Si*-face attack. In addition, the *Re*-face features a slipped parallel arrangement of the two aryl groups, with an Ar-Ar separation of 3.86 Å, typical for π-stacking. This stabilizing electrostatic interaction also contributes to the lowering transition state structure and offers an explanation into why 4-nitrophenyl substituted catalysts offer higher enantioselectivies than others (Figure 1.16).

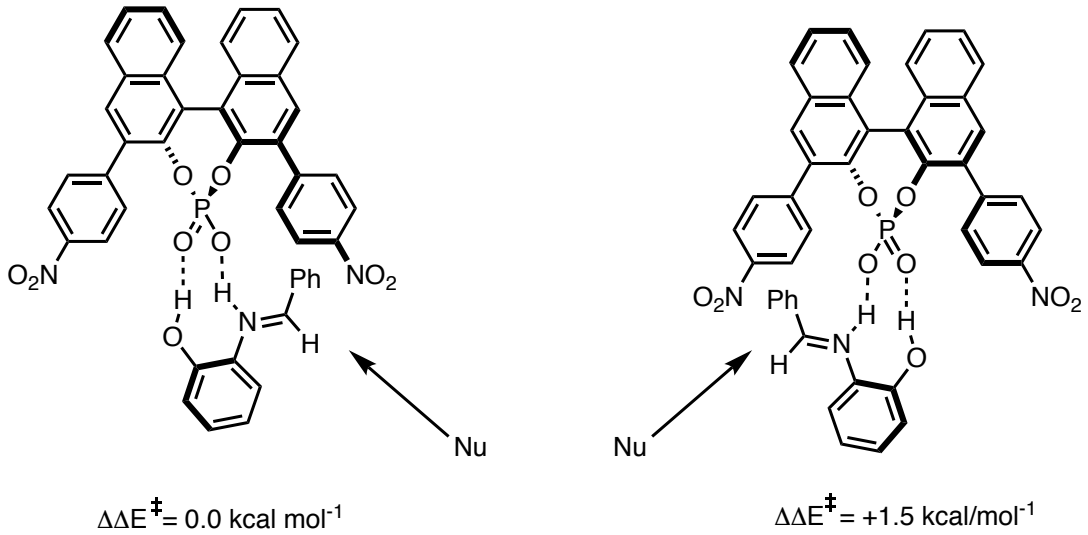

Figure 1.16. Calculated transition states for the origin of stereoselectivity in the Mannich reaction.

Further investigations have demonstrated that this mode of activation is general to 2-hydroxyphenyl imines with non-protic nucleophiles. The Akiyama model can be expanded to include aza-Diels-Alder[71-72] and vinylogous Mannich reactions.[73]

Additional mono activation mechanisms have been proposed. However, in each reaction studied so far, [36,38-41,56,70] transition states involving a single interaction to the catalyst are higher in energy than those involving double coordination. If the reactants lack a second site of interaction, such a mode of activation seems reasonable. Despite the risks of the strategy, numerous reactions involving reactants in which a second binding to the catalyst seems mechanistically improbable have shown to be highly enantioselective.[74-83] These examples provide an interesting mechanistic question in that reactions proceeding through single point binding pathways provide high levels of π facial discrimination. This offers the possibility of expanding the broad potential applications of phosphoric acids in asymmetric catalysis.

1.5 Overview of Reaction Features

Since the initial reports describing chiral phosphoric acids as catalysts, progress in this field has been rapid, and much of their success has been accredited to the ease of modulation of the catalyst properties. Breakthroughs in this area have been largely driven by the discovery of new catalysts. Notable examples, which have served to continually increase the scope and to render the reactions more efficient, include TRIP, TIPSY and 9-anthryl derived chiral phosphoric acids. Despite the plethora of systems currently available, only a relatively limited group has witnessed extensive application. This reflects on a combination of the selectivity, availability and reaction scope of the catalyst. Catalysts based on BINOL have been extensively used. These were first described by Terada and Akiyama in 2004. Since then further work has led to the development of a versatile family of structurally related catalysts that have found use in acting as but not limited to Brønsted acid catalysts, for most notably nucleophilic additions to imines,[20] allylboration[84 - 86] and propargylation of aldehydes,[87] nucleophilic addition into oxetanes[88-92] and pericyclic reactions.[93-96] The optimal catalyst and other reaction parameters can vary for different substrate combinations, contributing to the difficulty in selecting the best conditions. It is my contention that the mechanism in operation directly impinges on the choice of reaction conditions. As such, through understanding the mechanism the chemist will be able to more easily select the most efficacious conditions for a given substrate combination. There are a number of thorough reviews describing the advancement of the field,[97] applications[98] and mechanistic aspects.[20, 99] A current understanding and a synthetic practical guide to the use of these catalysts are lacking. It is the unifying goal of my research to provide that and I hope it culminates in an understanding why certain catalyst function well and from which lessons may be learned for future catalyst designs. Ultimately the achievements I envision would accelerate my capacity to synthesise more complex molecules with these catalysts. In this section I will specifically focus on the key reaction features for modulation and effect of such, mechanistic studies will be highlighted that explain the effect of the structural perturbation.

1.5.1 Key Variables

The selection of the key structural parameters of the catalyst is typically determined by both the structure of the imine and the nucleophile. In most cases, the optimal catalyst for one combination of reactants does not necessarily translate to another. Therefore, the optimization of reaction conditions can often be laborious and frustrating, as simple modifications to either the catalyst or the reactants can have a profound effect on the reaction outcome (Figure 1.17).

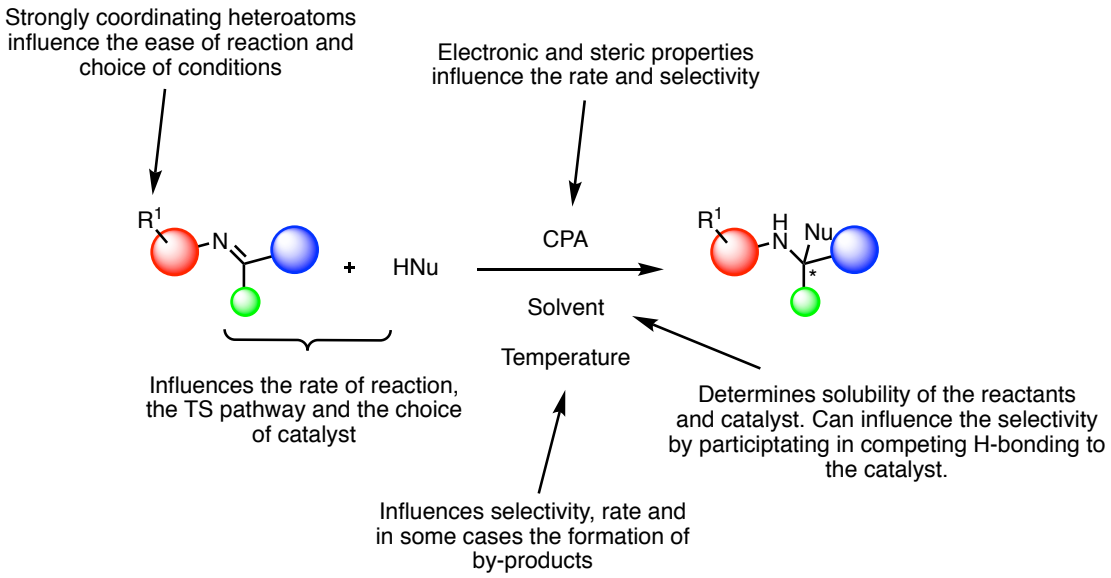

Figure 1.17. Factors influencing a typical chiral phosphoric acid catalysed reaction.

Despite the large scope for reaction modularity, one of the most important determinants of the success of any given reaction is the structure of the substituent at the 3,3' positions Figure 1.18).

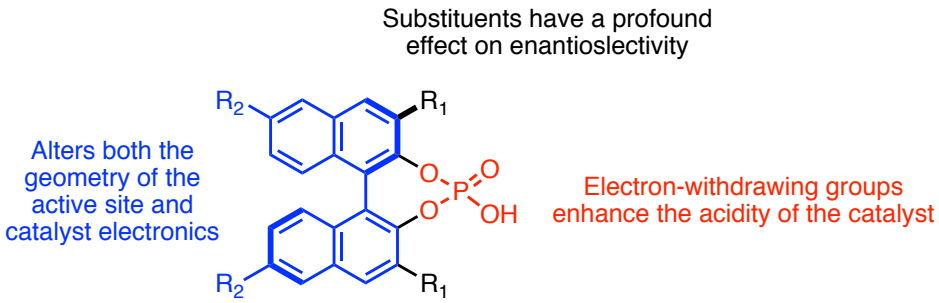

Figure 1.18. Important structural features of chiral phosphoric acids.

1.5.2 Chiral Environment

The stereochemical outcome in each reaction is controlled by the orientation of the substrates within the catalysts chiral cavity, created by the rigid backbone and constrained by the 3,3' substituents. Synthetic modulation of these features can effectively tune the shape of the chiral pocket. The first reports made use of 4-(β-naphthyl)C_6H_4 and 4-$NO_2C_6H_4$ derived BINOL phosphoric acids for Mannich reactions,[18-19] since, these catalysts have found limited application in the development of methodology. Subsequently, several structural variants have been reported as a result of the modularity afforded by the synthetic route and it has been found empirically that selectivity varies widely. Figure 1.19 shows the basic design of the most popular catalysts.

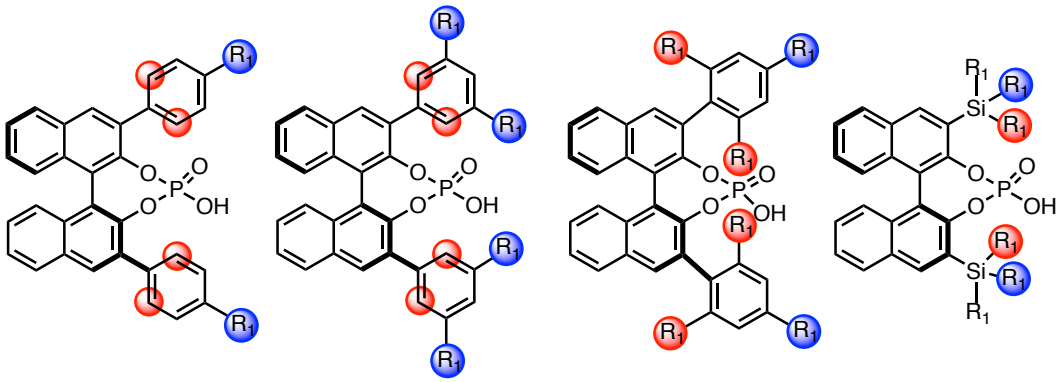

Figure 1.19. Commonly used phosphoric acid structures. Red substituents are close to the catalyst active site and blue substituents further away. For silyl derived 3,3' groups with identical R_1 substituents (see example on far right) the substituent that points up and towards is described as proximal sterics, down and back, remote.

Derived from BINOL, most have an aromatic ring at the 3,3' position, which can be further functionalised. The original studies made use of substitution at the 4- and the 3,5-positions, allowing modulation of remote sterics, highlighted in blue. Later 2,4,6 tri-substitution became prominent, which allows placing large groups proximal and remote from the phosphoric acid. A major breakthrough came with the discovery of TRIP, developed by List,[100] which has isopropyl groups at the 2,4,6 positions of the aromatic ring, this catalyst is by far the most versatile and selective known to date. Less frequently seen are alkyl and silyl derived 3,3' substituents, the most successful catalyst of this class is known as TIPSY, which places large triphenylsilane groups in the 3,3' positions, developed by MacMillan.[31] These catalysts are air stable, easily handled crystalline solids and a number are commercially available. Although no catalyst is optimal for all combination of reactants, large substituents are

required for high stereoselectivity. For more difficult cases, the catalyst structure can be fine-tuned for the application. Whilst most substituents can be introduced by a Suzuki cross coupling, appending sterically demanding groups may require a Kumada coupling. Substituents can also be introduced at 6 and 6' positions, a feature that has been recently exploited in an innovative procedure to immobilize TRIP on polystyrene and shown to be enantioselective in the asymmetric allylboration of aldehydes.[101] The success of BINOL-derived phosphoric acids prompted the development of catalysts with alternative backbones, with the aim of modifying the geometry of the active site and these can also provide selective catalysts for important transformations (Figure 1.20). The partially hydrogenated BINOL backbone has proved superior but only for certain examples.[102] Akiyama introduced TADDOL-derived Brønsted acids driven on the basis of practical considerations; TADDOL can be derived from tartaric acid, one of the least expensive chiral starting materials with two-fold symmetry. Unfortunately, these catalysts failed to promote highly enantioselective transformations.[103] VAPOL and VANOL both introduced by Antilla have had limited success.[104] List has demonstrated SPINOL as an efficient alternative to BINOL and can provide in some limited cases superior but in general comparable enantioselectivies to BINOL.[105] Gong, Du and others have designed more exotic backbones to include multiple axes of symmetry and catalyst sites. Neither provides distinct advantages over the standard.[106-108]

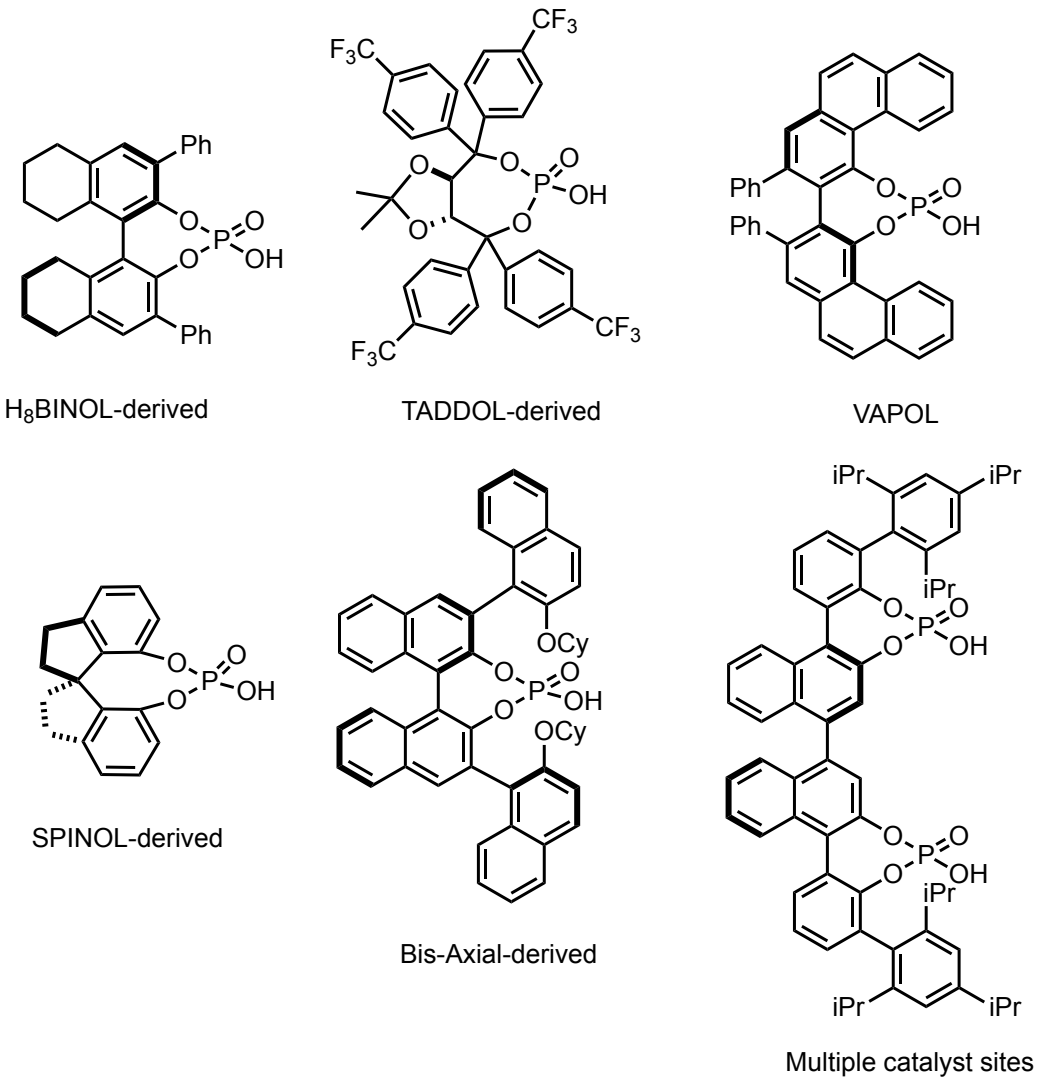

Figure 1.20. Various backbone modifications.

The List group noted that on studying reactions of small aliphatic substrates that do not possess sterically demanding groups, BINOL-derived systems only proceed with moderate enantioselectivities. Postulating that this was due to the inability of the current design of chiral phosphoric acids to provide a compact microenvironment for enantiodescrimination (Figure 1.21), List *et al*. focused their attention on a new design incorporating a highly sterically congested active site (Figure 1.22).

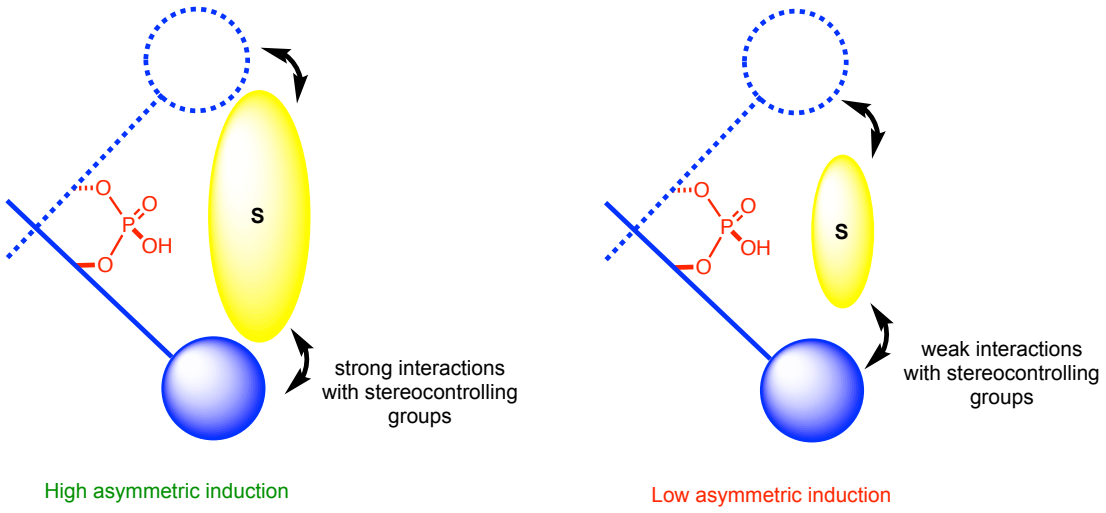

Figure 1.21. Limitations of chiral phosphoric acids with small molecules.

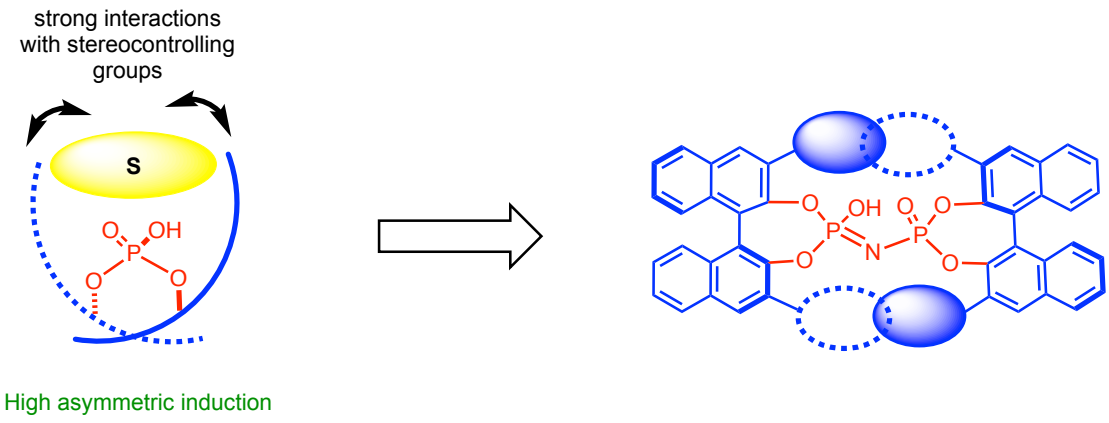

Figure 1.22. Confined C_2-symmetric imidodiphosphoric acids.

Imidodiphosphoric acids, (Figure 1.22) were found to be a suitable motif and shown to be highly effective in asymmetric acetalisations[109] and oxidation of thiols[110] which both were beyond the ability of known chiral phosphoric acids. Imidodiphosphoric acids have become an attractive alternative when traditional BINOL-derived catalysts fail to give high selectivity. [111] Simón and Paton have computationally studied the mechanism of spiroacetalization of enol ethers promoted by these confined catalysts.[112] They show that despite the confinement and increased steric demands of the catalyst, the main source of chiral discrimination can be traced back to the enforced orientation of the H-bonding interactions between catalyst and substrate. Steric effects become more important with increasing size of the reactants as shown by Sunoj and Jindal.[113]

The synthetic literature contains many examples of asymmetric reactions whose stereoselectivities changed unexpectedly through simple catalyst modification. [114] Investigations by Gong *et al.* have shown the importance of catalyst structure on reaction pathway. ONIOM calculations showed that the lowest transition state pathway was not consistent during the catalyst screen while studying the Bignelli reaction (Figure 1.23).[115] An archetypal example of this mechanistic phenomena is observed when **CPA-6** was employed, the reaction proceeded *via* a *Type II E* pathway, employing the larger catalyst **CPA-2** lead to a *Type I E* pathway being favoured. Based on calculations the authors suggest that the reversal originated from the strengths of the H-bonds.

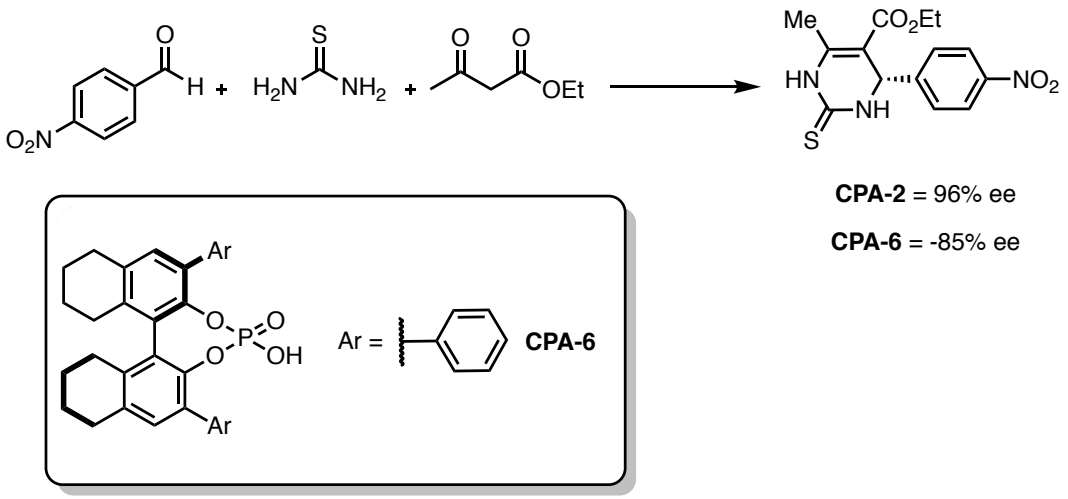

Figure 1.23. Reversal stereochemical induction for the Bignelli reaction.

Terada also noted a similar reversal in the Friedel-Crafts reaction of aldimines with TBS protected indole. Based on DFT optimised ground state geometries of the catalysts (B3LYP/6-31G**) he rationalised the reversal in stereoinduction was due to the difference in accessibility of the reactants to the acidic site (Figure 1.24). [116]

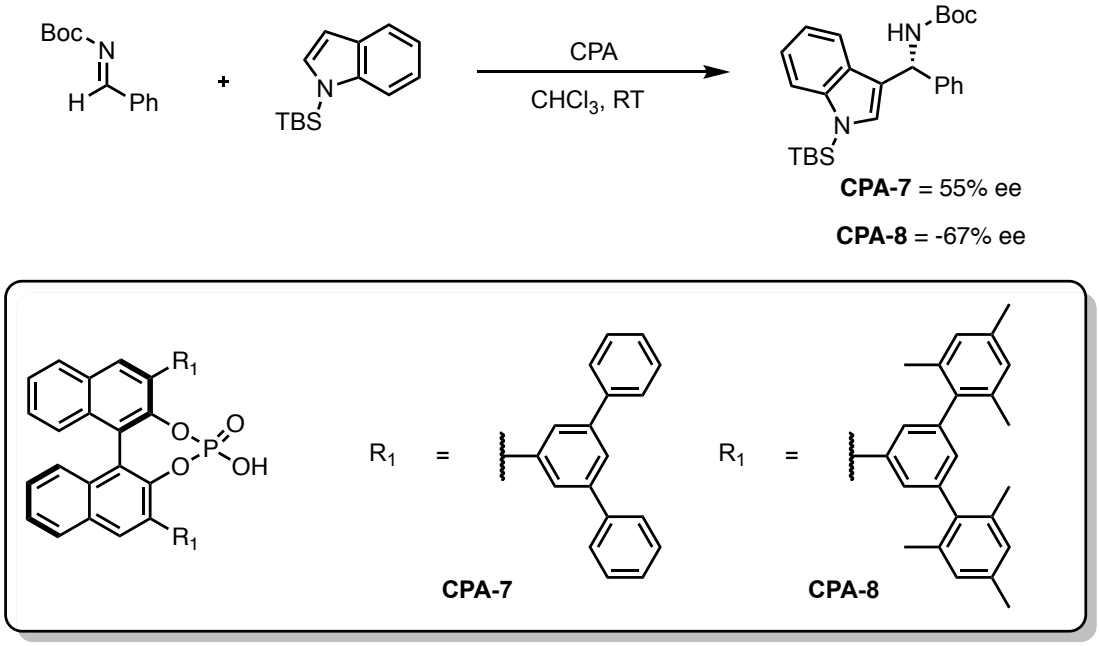

Figure 1.24. Reversal stereochemical induction for the Friedel-Crafts reaction.

Despite the importance of the substituent structure at the 3,3' positions there been relatively few investigations into the effect of catalyst structure on enantioselectivity. Current approaches to catalyst selection is driven on the basis of empirical observations; studies by Wheeler,[117] Sigman,[118] Tantillo[119] and Sunoj[120] have suggested non-covalent interactions as possible determinants of selectivity.

1.5.3 Catalyst Active Site

Initial studies on chiral phosphoric acids as catalysts were carried out predominantly with imines as electrophiles. The realization that incorporating electron-withdrawing groups at the catalyst site can activate difficult substrates has been decisive in the utilisation of carbonyl compounds to be engaged in a variety of reactions.[121-123] N-trifyl phosphoramide catalyst systems are the most popular, first introduced by Yamamoto,[124] allows reactions of electron-poor, electron-rich and neutral compounds to be achieved with high efficiency.[125-127] Often

the higher acidity of the chiral N-triflyl phosphoramides is crucial for the success of the reaction. Later Cheon and Yamamoto also introduced thio- and seleno- derivatives for the protonation of enol silanes (Figure 1.25).[128]

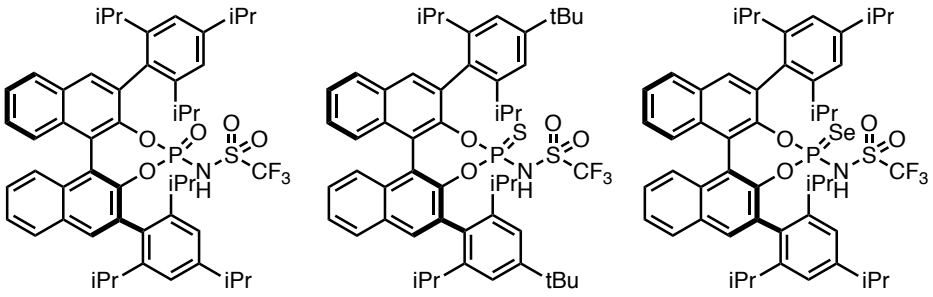

Figure 1.25. *N*-triflyl phosphoramides and derivatives**.**

Following later developments in catalyst design, synthetic work demonstrated that both phosphordiamidic[129] and dithiophosphoric[130] acids as highly active catalysts. In both cases only low levels of enantioselectivity were achieved. Phosphoric acid catalysts based on BINOL, although followed by several different acidic motives, are by far the most successful catalysts. With exception of Yamamoto's catalyst, all other stronger Brønsted acid motifs are very reaction specific. Given the wide range of catalysts with different acidities and importance of pKa on activity, experimental[131-132] and computational[133] methods aimed at developing an accessible acidity scale. The efficiency of any process varies between substrates and employing a strongly acidic catalyst can have a beneficial effect. However, this method is not always effective as a result of the issues faced by introducing larger substituents at the active site. In some instances this can result in a dramatic drop in enantioslectivity as shown by Antilla[87] and subsequently studied by our group.[134] Our group showed that the increased steric demands at the phosphorous reduces the steric effect of the 3,3' groups. Noting this, there is often an interaction between the demands at the phosphorus and the 3,3' substituents and the observations with phosphoric acids are not directly transferable to N-trifyl phosphoramides. The development of stronger Brønsted acids has been a strongly researched area and still continues to be today.

1.5.4 Structure of the Reactants

The structures of both the electrophile and the nucleophile weigh substantially on the choice of reaction conditions. Whether an imine or a stable precursor is employed can have a large effect on the reaction conditions required. Enamides and carbonyl compounds are typically used for the *in-situ* generation of imines and have distinct properties with respect to ease of formation. Enamides may require an acidic co-catalyst to facilitate tautomerisation and condensation reactions need a drying agent, with both requiring moderate to high temperatures. Similarly, nucleophiles can possess widely differing nucleophilicity as well as variable steric properties and, therefore, require different catalysts and reaction conditions. The models for stereoselectivity depicted in Figure 1.9 not only predict the stereoselectivity of the reactions described above, but can also be used to rationalise the stereochemical outcome of many nucleophilic additions to imines. Combining all possible considerations, a total of four possible transition state pathways are formulated and, as demonstrated above, not all reactions proceed *via* the same one. Through detailed DFT calculations and literature results, our group has generalised and summarised which effects dictate the favoured reaction pathway allowing the model to become a powerful predictive tool. In general most reactions proceed *via Type I E* pathways. However, this preference can be modulated by the sterics of the reactants. In the next section I discuss our guiding principles to reaction pathway classification and give an overview of reactions for which it is useful.

1.5.4.1 Electrophile: *E* or *Z* Transition State

E imines are generally more stable than *Z* imines and this energy difference is maintained in the transition state structure. Consequently, aldimines have a larger energy difference between the *E* and *Z* forms and so proceed *via E* transition state pathways. Ketimines have a smaller energy difference between *E* and *Z* forms and both pathways are possible. While acyclic substrates can freely equilibrate, cyclic substrates are locked in a *Z* configuration and can only proceed *via Z* pathways. Based on this observation Simón and Goodman has suggested that structure of the starting material is used to provide the stereochemical information in the transition state. Building on this hypothesis, Goodman later proved based on a thorough study of eighteen substrates and three different reactions that aldimine transition state structures are always *E.* Methyl ketimine transition state structures are usually *Z,* unless the mean imine/iminium *E* structures are preferred to *Z* structures by more than 3 kcal mol^{-1}.[38] This guideline allows a prediction of the preferred transition state to be made from analysis of the ground state preference of the imine, which is generally much

easier to calculate or to estimate. The simple model is able to capture a number of results that are neither intuitive nor predictable. In 2009 Antilla *et al.* reported the transfer hydrogenation of enamides.[135] The stereochemical outcome is consistent with a *Type I E* pathway except for two examples. One of which was the reduction of (2-methoxyphenyl)methyl ketone derivative. The major compound has the opposite stereochemistry and lower enantiomeric excess (ee) than if the acetophenone derived enamide was reduced. It is not altogether clear why such a small structural modification could lead to such a dramatic change in result. On the basis of this, ONIOM calculations were performed, considering all possible pathways and found that the preferred pathway changed from *Type I E* to *Z*.[38] Such a change was captured with the simple ground state calculations. The high energy difference between the *E/Z* imine and its protonated counterpart for **5** suggests that *E* selectivity will be good and the dramatically reduced preference for *E* suggests that *E/Z* selectivity will be poor (Figure 1.26). Further examples are shown in Figures 1.26 and 1.27 in support of the mechanistic analysis.

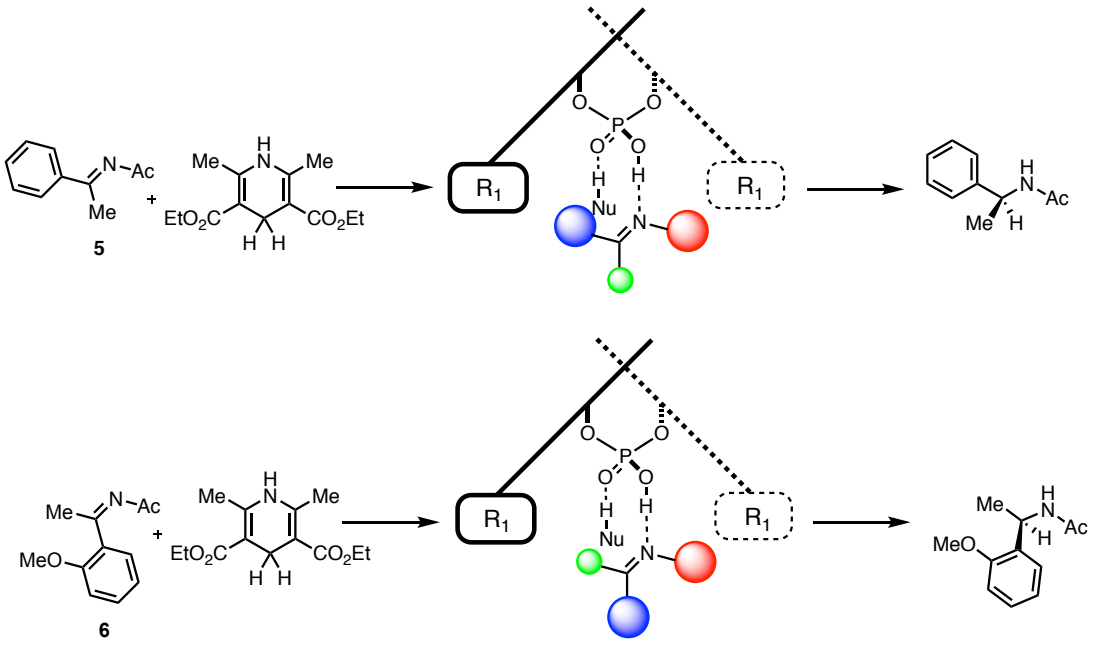

Imine relative energies		Iminium relative enegies	
E-**5**	0 kcal/mol	*E*-**5**	0 kcal/mol
Z-**5**	+4.0 kcal/mol	*Z*-**5**	+4.9 kcal/mol
E-**6**	0 kcal/mol	*E*-**6**	0 kcal/mol
Z-**6**	+0.2 kcal/mol	*Z*-**6**	+3.4 kcal/mol

Figure 1.26. Prediction of reaction pathway based on the assumption that the transition state geometry is between that of the imine and iminium.

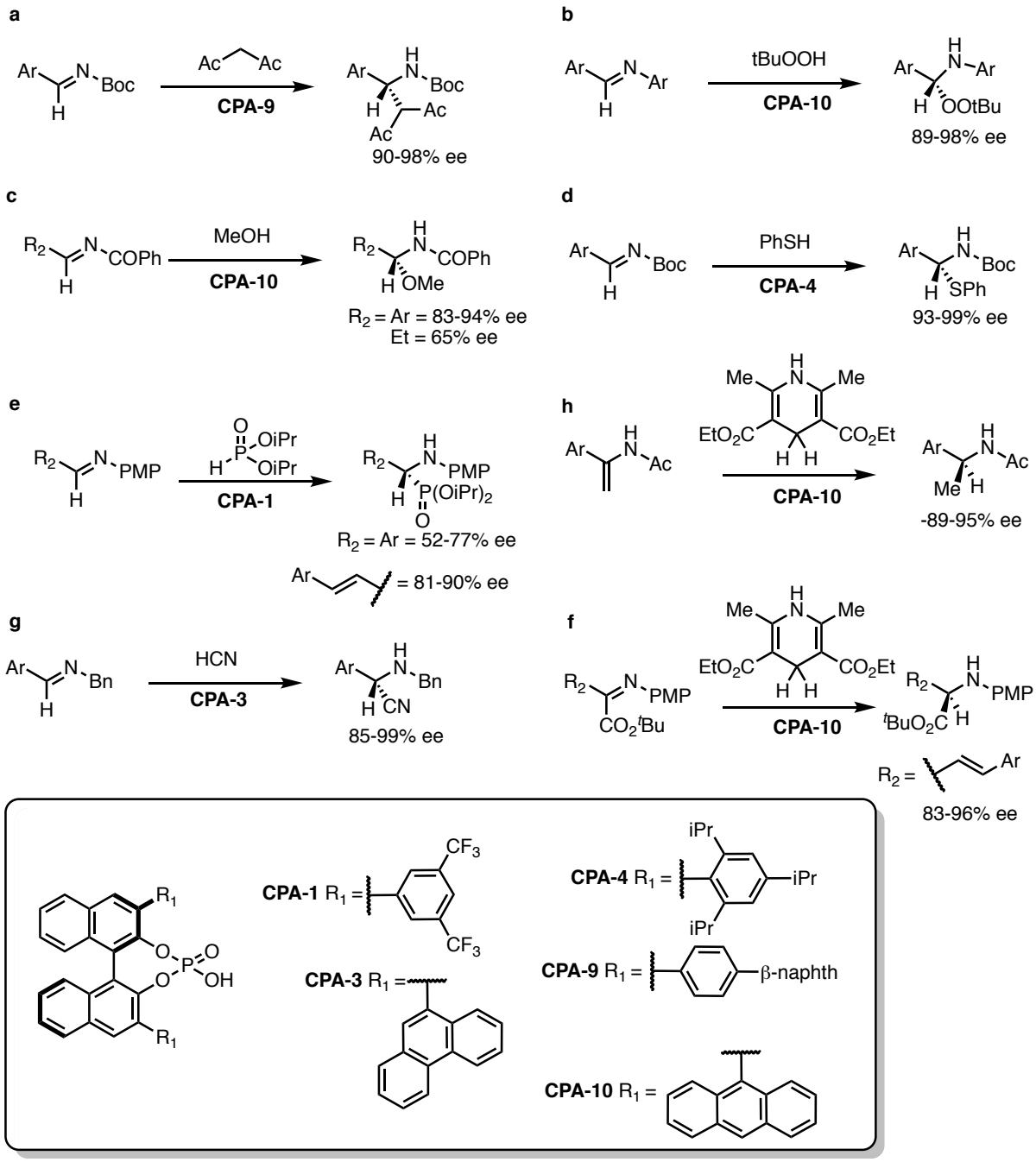

Figure 1.27. Summary of reactions that proceed *via E* pathways.[19,29,62,114b,135,136 -138]

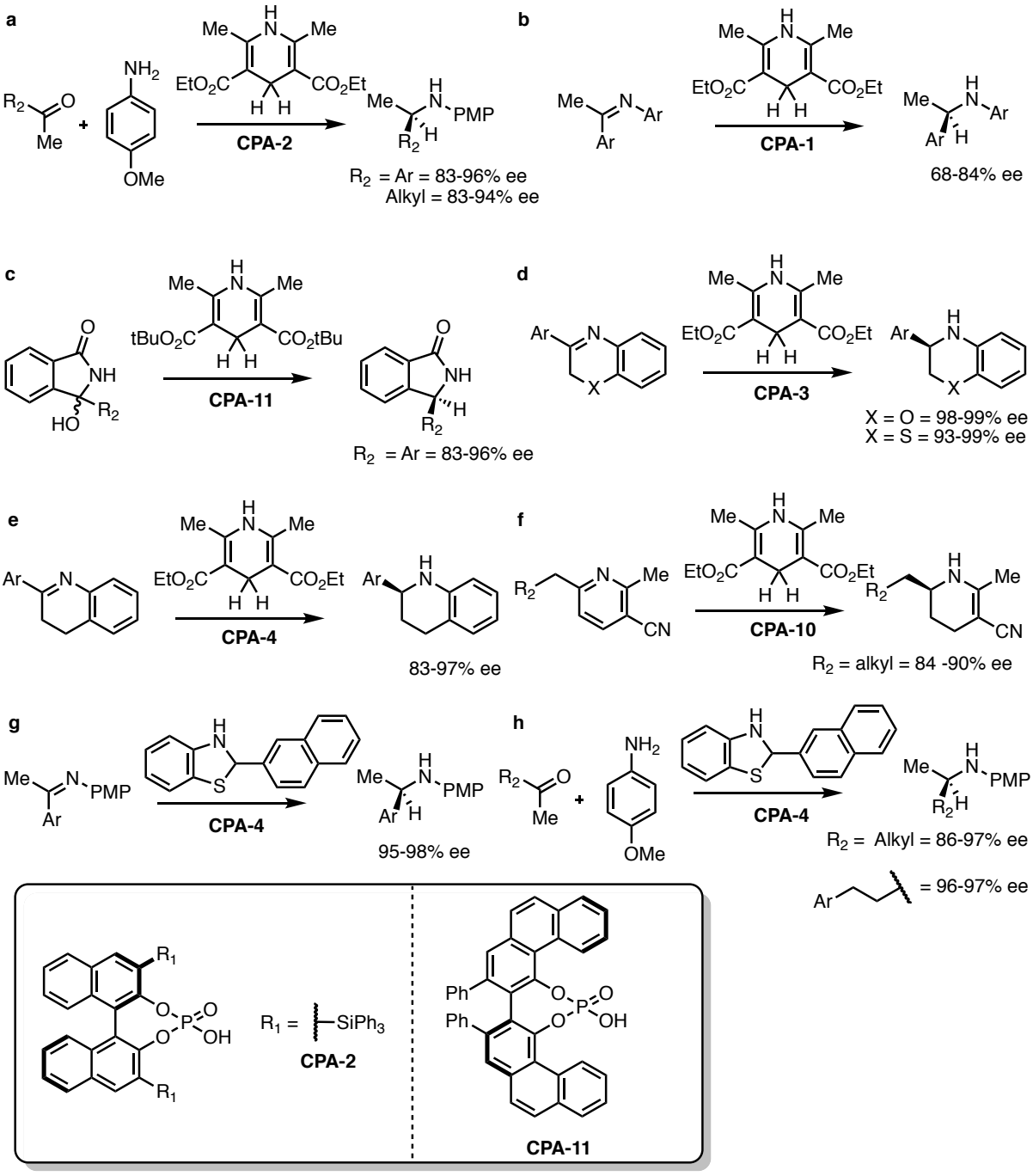

Figure 1.28. Examples of reactions that proceed *via Z* pathways.[31-32,58,139-144]

1.5.4.2 Nucleophile: *Type I* or *Type II* Transition State

For most nucleophiles, such as HCN and the Hantzsch ester, the H-bond, which holds the nucleophile to the catalyst, is in line with nucleophilic site. In some cases, however, the bond may be displaced to one side. This can promote a *Type II* process, but only if it is reinforced by a small N-imine and a large coplanar substituent. Indoles, enamides and enols fall into this category and some examples are shown in Figures 1.29 and 1.30. Due to the greater steric accessibility enols and enamides almost always proceed *via Type II* pathways. Indoles can proceed by either and the pathway choice is heavily influenced by the size of the N-substituent.

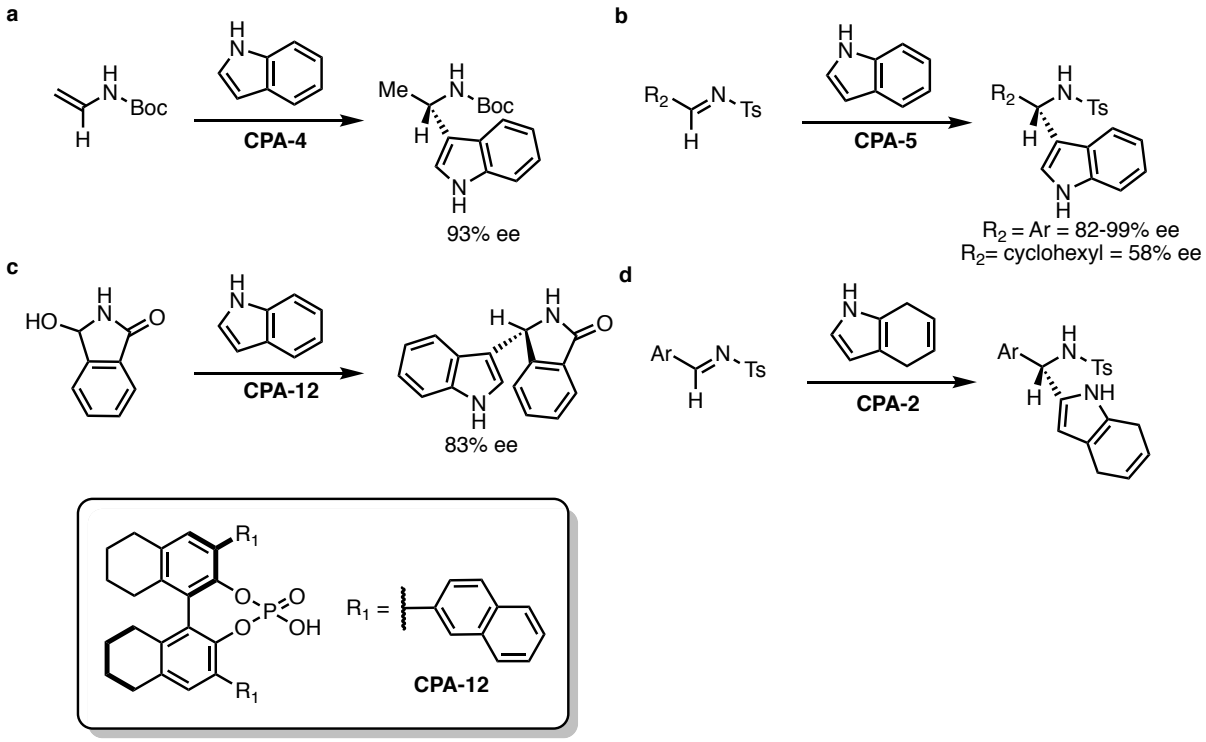

Figure 1.29. Reactions that proceed *via Type I* pathways with displaced nucleophiles.[65,145-147]

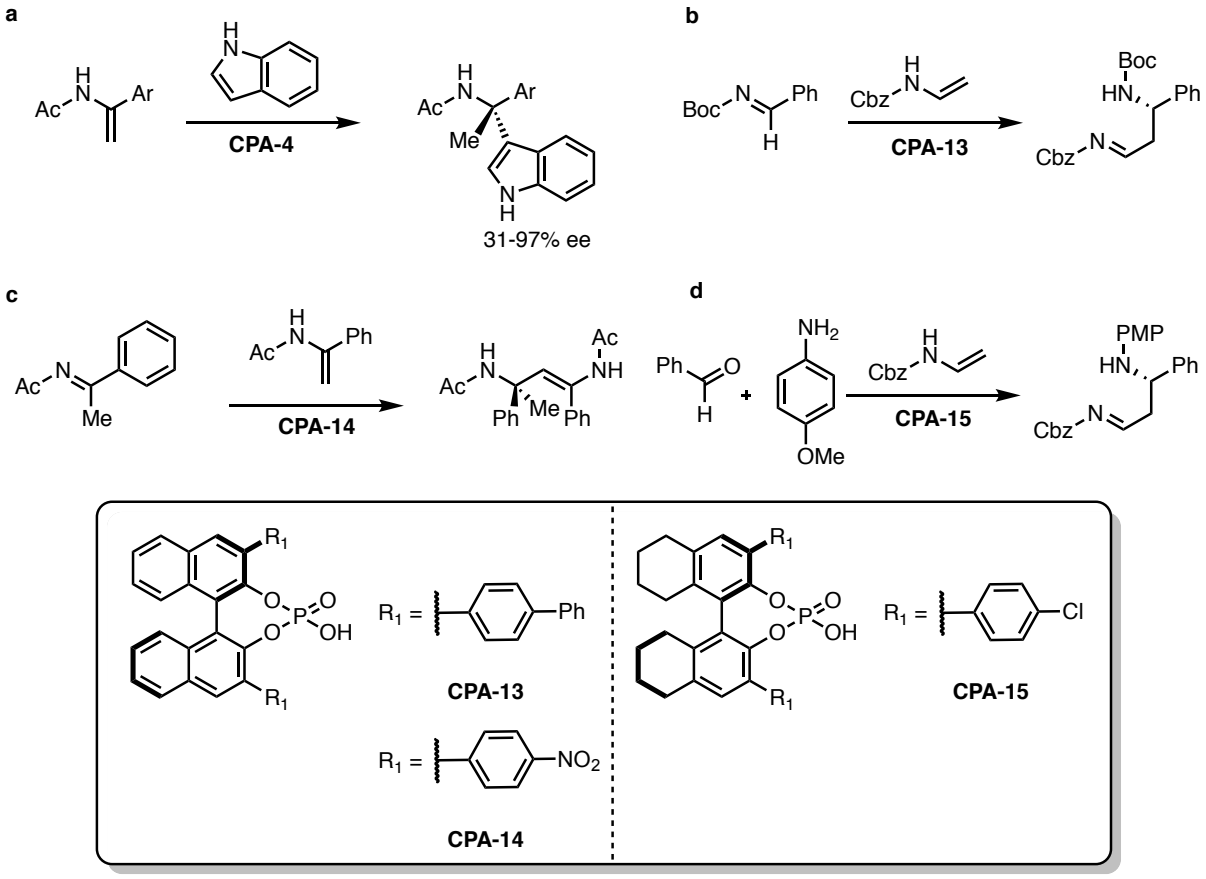

Figure 1.30. Examples of reactions that proceed *via Type II* pathways.[28,148-150]

1.5.4.3 Qualitative Model for TS pathway choice

Based on theoretical studies and the literature results, Goodman *et al.* have summarised the factors that contribute to the reaction pathway in Figure 1.31. The reactants follow either the right hand or left hand pathways, and the choice is controlled by the four factors listed: R_3 size, R_2 size, nucleophile type and imine configuration. The underlying feature of the pathways is the desire for the reactants to minimise steric interactions with the 3,3' substituents. It is, therefore, unsurprising that large *N*-imine substituents (R_3 in Figure 1.31) favour *Type I* processes and small substituents bias towards *Type II*. Similarly, a large group on the other end of the imine (R_2) would also avoid the 3,3' substituents and so a large R_2 favours *Type II*. The nature of the nucleophile is also very important: displaced nucleophiles, such as indole, favour *Type II* processes. A *Z* transition state makes it possible to place two large groups away from the majority of the steric bulk. However, to proceed through such a pathway the configuration will need to be accessible. The energy difference for the *E* and *Z* imine ground states can be used to estimate how likely a *Z* transition state will be. An energy

difference of less than 3 kcal mol^{-1} in favour of the *E* ground state suggests that a *Z* preference is possible.

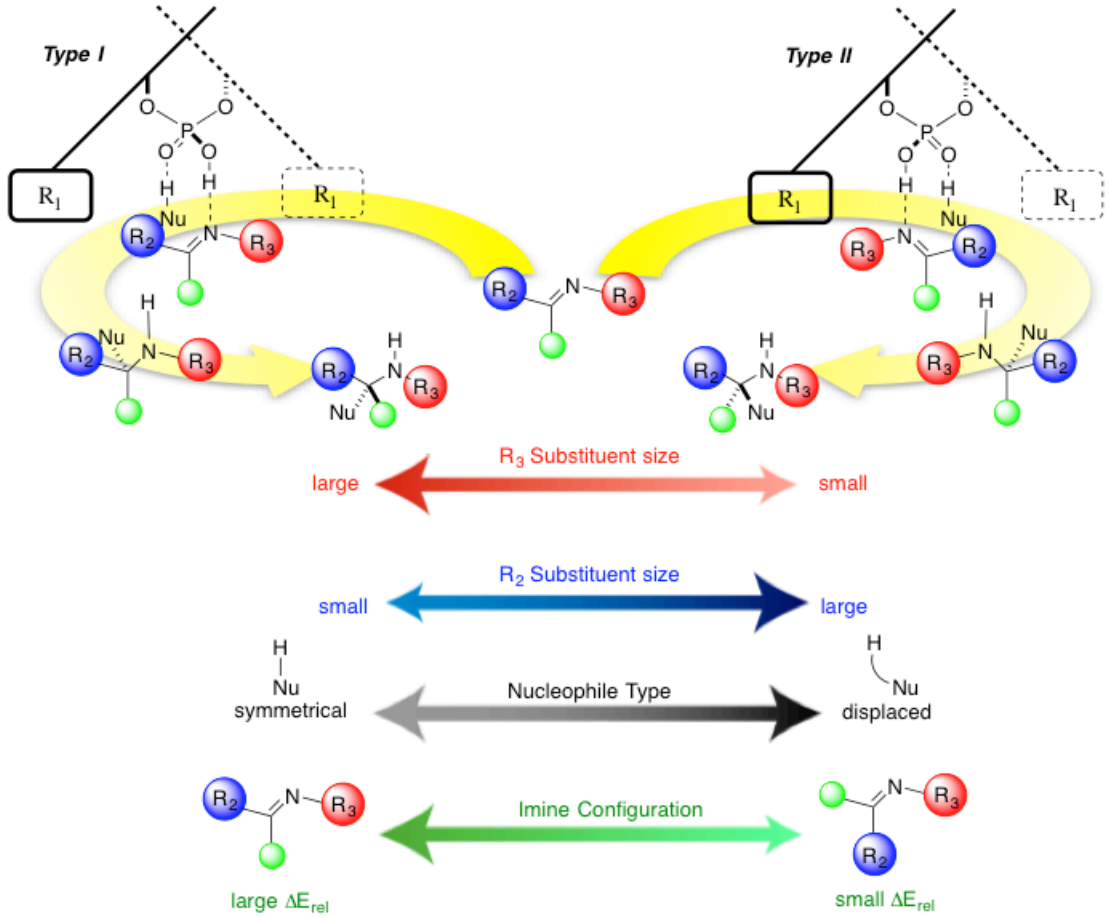

Figure 1.31. Reaction pathway spectrum: the effects of various features on the stereoselective outcome are shown.

1.6 Summary

Computational methods have become increasingly useful for modelling catalytic reactions. Such methods have evolved to provide new understanding of experimental results, with detailed insights into mechanisms and origins of stereoinduction. However, for many-atom systems, it was impractical to study reactions by very accurate methods until it became possible to use ONIOM approaches. Rationalising the outcome and enantiomeric excesses of these complex reactions is now feasible. Summarising the calculations into a simple qualitative model, Figure 1.31, represents a powerful tool for predicting the stereochemical

outcome of phosphoric acid catalysed nucleophilic additions to imines and is a quick and easy method for the prediction of reaction pathway and stereoselectivity.

At this stage, there are no guidelines for optimisation available. The exact choice of the conditions will depend to a large extent on both the structure of the reactants, catalyst as well as the goals of the optimisation; increase in yield, selectivity, rate, lower catalyst loadings or generality. When attempting to improve a set of reaction conditions, a number of simple changes can be effective. The bulk of the catalyst can be reduced or increased. A change to a non-polar solvent can bring improvements to the reaction whilst maintaining substrate solubility. Poor selectivity can reveal the presence of excess moisture. This can be minimised by thorough drying of reagents and the addition of activated molecular sieves to the reaction mixture. Switching to a more acidic catalyst can be helpful in activating less basic electrophiles.

Chiral phosphoric acids have undergone considerable development since their discovery. Much of the progress has been driven by innovations in design rather than attention to optimizing reaction conditions. The reactions usually require quite high catalyst loadings (5-20 mol%). In general, catalysts based on the 2,4,6-substitution pattern are the most efficient. Individual reaction combinations may necessitate a different catalyst as a result of the structural peculiarities of nucleophile and electrophile. I hope in future to supply better insights into selection of reaction conditions: in particular, the choice of catalyst for a given process, and the rationale for further optimisation.

In summary, chiral phosphoric acid catalysis is a growing area with many opportunities. Nucleophilic additions to imines have been most explored. However, for many reactions, we do not yet know the influence of catalyst structure on enantioselectivity. This makes strategic choice of catalyst very difficult and hinders hypothesis driven catalyst design. The following chapters detail my explorations into studying the 3,3' effect.

Chapter 2

2 Development of Phosphoric Acid Steric Descriptors

2.1 Background

The field of asymmetric catalysts has relied on empiricism to develop catalysts and this is particularly true for chiral phosphoric acids. The number of methodologies employing these catalysts increases at a rapid rate. However, the number of tools available to probe the origin of enantioselectivity in reactions has remained static. If these reactions are to be applied broadly in organic synthesis, additional studies must be done beyond the scope of the initial report. In general, chemists are not willing to explore recently reported reactions where considerable synthetic effort is required to generate materials and the results are not certain. In this short section I will highlight two current approaches to streamline and quantify catalyst performance. These studies have been instrumental in the development of my current experiment-correlation-calculation based approach for understanding, selecting and designing chiral phosphoric acid catalysts and require a mention prior to introduction of my results. This chapter also compares and reviews steric based parameters common in quantitative structure activity relationships and how they have been applied to asymmetric catalysis.

2.1.1 Current Methods for Predicting and Optimising Chiral Catalyst Performance

The discovery of catalysts that effectively facilitate organic transformations in a stereocontrolled fashion is central to synthetic organic chemistry. Selectivity in chemical reactions is a matter of distinguishing between pathways of small energy differences in their energy barriers. Ranging from 0 to approximately 3 kcal mol^{-1} from reactions affording no selectivity to high levels of >99:1, no more than the energy required to rotate the carbon-carbon bond in ethane. Controlling and identifying the origin of the small energy differences that afford selectivity has, historically, been a challenge and predominantly characterised by empiricism.

One of the current goals in asymmetric catalysis is to provide a degree of predictability to enantioselectivity outcomes, which not only holds considerable potential in applying asymmetric reactions in synthetic chemistry but also represents a powerful tool in designing and optimising chiral catalysts. Traditionally, asymmetric catalysts have been developed by trial and error approaches. Generally new reactions and catalysts are discovered through systematic screens of known privileged catalysts. Once a lead has been identified, it is optimized, a process driven on the basis of experimental observations, often time consuming and difficult. Increasing emphasis is being placed on predictive computational strategies in which the free energy differences between the pathways leading to opposite enantiomers are calculated, often with positive results.[151-152] However, this requires both calculating every possible substrate-catalyst combination and having a precise knowledge of the mechanism, which may not be available or easy to determine. The key to accurately predicting enantioselectivity computationally lies in the ability to precisely model the key interactions in competing diastereomeric transition states. As computational methods advance in their ability to model complex interactions accurately, the prediction of enantioselectivity completely *in silico* will be more of a reality, leading catalyst design rather than assisting.[153] Another approach recently promoted by Sigman, focuses on developing mathematical relationships between catalyst and substrate parameters to enantioselectivity, allowing quantitative prediction of the level of stereoinduction.[154] The synthetic effort required to generate libraries capable of interrogating simple systems is significant and each reaction type requires a different quantitative model. In addition, this method often does not provide a clear physical meaning why certain catalyst features are important for a particular reaction. Neither method allows for general design principles to be developed, which are indispensable guides when planning syntheses. In this context I recognised an improved

methodology was needed to investigate and understand how asymmetric catalysts shape the potential energy surface to achieve the desired reaction outcome.

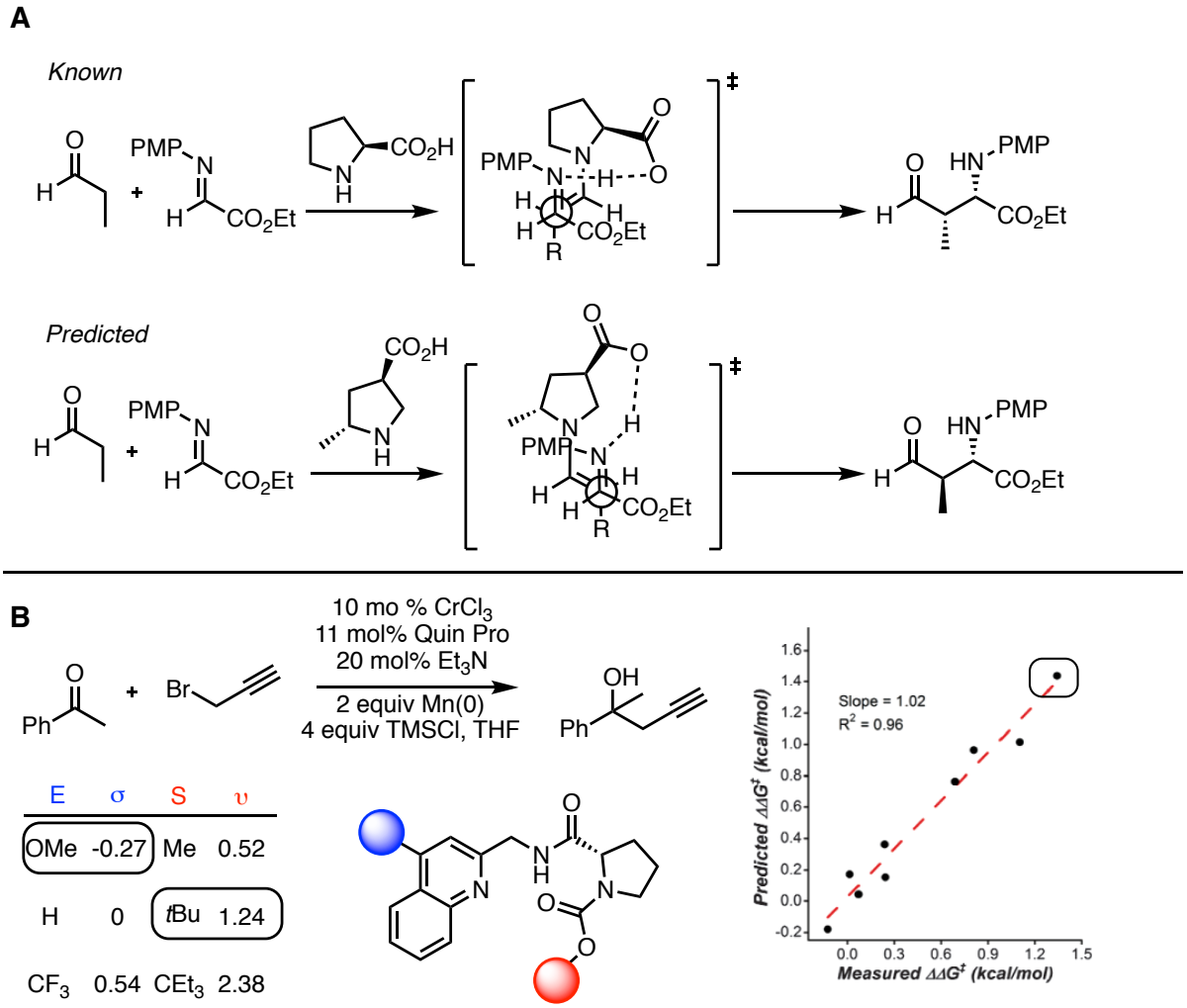

Figure 2.1. Current approaches to predicting enantioselective outcomes in asymmetric catalysis. (A) Computational approach – computing selectivites for each individual catalyst for a reaction in which the mechanism is known. (B) Correlate structural parameters to enantioselectivity outcomes. Hammett values are employed as the electronic (E) parameter and Charton values as the steric (S) parameter.

2.1.2 Developing a New Method for Predicting Chiral Catalyst Performance

Our group has had long-term interest in the mechanism and use of chiral phosphoric acids for a range of Brønsted acid mediated reactions, covered in Chapter 1.[20] However, despite the numerous computational and experimental studies dedicated to this important area of catalysis by our group and others, the selectivity trends with different catalysts are not well understood and this deters strategic selection of catalyst by synthetic chemists. Substituents at the 3,3' on the binaphthol ring are central to the selectivity, and different groups are optimal for different applications. Generally, large steric bulk is required for high enantioselectivity. However, if they are too large this may stop reactions altogether,[155] or, in some cases,[114] reverse the sense of stereoinduction. Thus, the vast majority of time required for reaction development is expended on optimization of this vital parameter. Such a campaign can be highly frustrating, as simple modifications to reaction parameters can have a profound impact on enantioselectivity. In general, the primary reasons for the different catalyst performance are often not frequently revealed. Hence, the ability to rationally select a catalyst to achieve a desired selectivity is practically important. Presently, predicting how effective a catalyst will be in a specific reaction is an impossible task.

On the basis of these observations a question was identified "*Why are some catalysts more selective than others, but only for certain reactions?"* A purely computational approach to this question would be intrinsically time consuming (approach A, Figure 2.1). An alternative approach is to discover relationships between catalyst descriptors and enantioselectivity (approach B, Figure 2.1). I believed that a merger of the two would be an attractive platform for providing significant mechanistic insight into the reasons for selectivity differences with varying 3,3' substituent structures providing the basis to suggest new catalysts. This method would allow exploration of the molecular features affecting the TS without making any assumptions about the mechanism. Specifically I planned to relate catalyst parameters to reaction enantioselectivity values obtained from the synthetic literature.[156-157] The resulting relationship would describe how changing the catalyst affected the enantioselectivity and therefore the TS of the enantiodetermining step, guiding mechanistic hypotheses which would then be verified or discredited by high-level ONIOM calculations. Simple qualitative models would then be constructed to understand and predict experiment. These program goals are described in the six-step workflow depicted in Figure 2.2. Consequently, a significant goal is to design steric descriptors as repulsive steric interactions are widely invoked within asymmetric catalysis, with these molecules, as a rationale for chirality transfer.

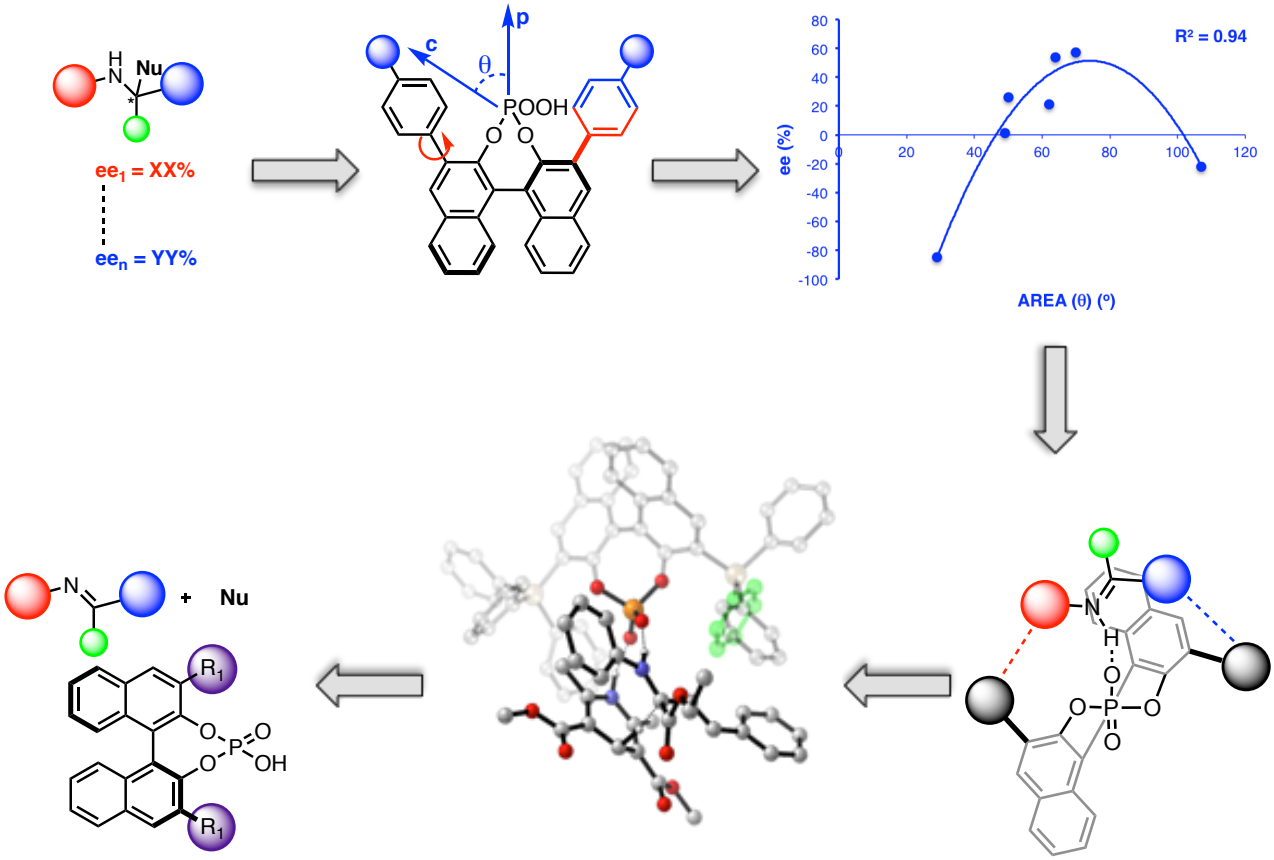

Figure 2.2. Overview of program goals. Steps 1-3 plan to use correlations between experimental data and computationally derived structural descriptors to study the effect of the catalyst on enantioselectivity. Steps 4 and 5 identify and validate the stereocontrolling catalyst features. Simple qualitative models are generated and applied to similar reactions to understand and predict experiment.

2.1.3 Steric Parameters in the Analysis of Asymmetric Catalytic Reactions

Attempts to quantify steric hindrance in organic chemistry began in the early 20th century. Once it was generally established that steric hindrance could affect reaction rate, these steric effects began to be examined in depth.[158] Taft's work in the area was pivotal as he recognised the need to separate electronic effects from sterics.[159] Since then, steric effects have been subjected to several different parameterizations. The variety of methods through which these steric parameters have been obtained can lead to uncertainty regarding how and when to apply them.

Taft's parameters, developed in the 1950s, were experimentally derived from the variation in rate of acid catalysed hydrolysis of esters.[160] Taft's original experimental results have been manipulated and redefined in many studies, resulting in various sets of Taft based steric parameters.[161-165] Of particular note, Charton correlated Taft's experimentally measured rates to the minimum van der Waals radii of the substituents, creating a set of computational derived parameters. Several other steric parameters have been developed since then including A-values,[166] and interference values (barriers to rotation),[167-168] which will be discussed later. The Tolman cone angle has had a wide impact on organometallic chemistry.[169-170] Tolman and subsequently others have measured the projected cone angle of phosphines from a metal centre and remains the standard parameter for measuring ligand size. Molecular volume based parameters have also been developed. The steric properties of NHCs can be quantified using the buried volume parameter described by Nolan, which refers to the percentage of a sphere occupied by the ligand when coordinated to a metal centre.[171]

Several sets of experimentally based parameters have existed for years, but there has been little effort to correlate them to enantioselectivity until the Sigman group became interested in correlating steric effects to enantioselectivity values in the NHK reaction.[172] Applying these parameters has been successful, but there are limitations, particularly as the mechanistic scenarios diverge significantly from the situation they were first derived from. Moreover, situations where subtle connections among several parameters may operate further exposed the ineffectiveness of the parameters.

The Sigman group had limited success at applying Charton parameters to enantioselective outcomes. In a few cases, predictive models could be developed,[172-173] but in others application was flawed producing distinct “breaks” in trends.[156] This lead to the development of more sophisticated steric parameters for the analysis of reaction outcomes, in particular the application of multiple parameters to describe the steric profile of a single substituent known as Sterimol created by Verloop.[174] Sterimol parameters contain three subparameters: two width (B_1, minimum and B_5, maximum width), which are measured orthogonal to the primary bond axis and a length parameter (L), which is measured along the primary bond axis. Application of Sterimol parameters have proven to be robust allowing predictive models to be constructed in line with additional electronic terms for many asymmetric catalytic reactions. [175-183] These steric parameters have been summarised into Figure 2.3. The success of the Sterimol parameters in describing the steric effects in mechanistically disparate reactions has been accredited to the fact that it describes substituents that are intrinsic to the group rather than to a reaction outcome i.e. reaction rates, position of equilibrium of axial and equatorial conformers. Considering this, deriving steric parameters from the catalyst itself may lead to more meaningful correlations rather than application of a predetermined universal descriptor.

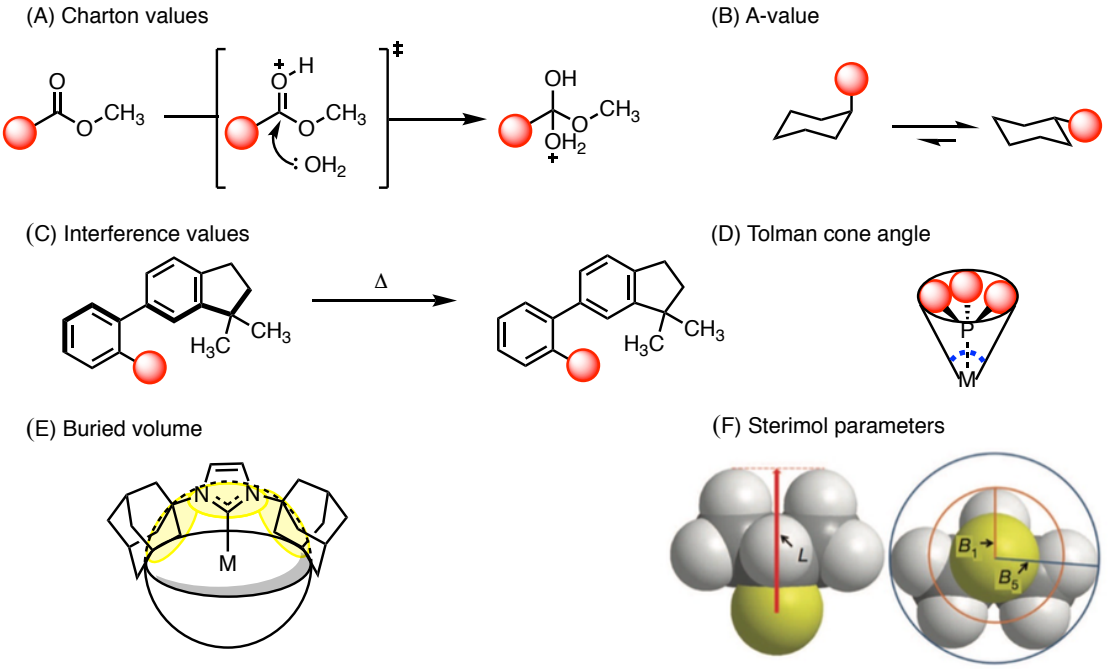

Figure 2.3. Summary of steric parameters.

2.2 Quantification of Proximal and Remote Chiral Phosphoric Acid Sterics

A key aspect in developing correlations is identifying appropriate parameters to connect changes in structure with selectivity. The identification of descriptors is facilitated by the observation that the reactions are, in general, very sensitive to catalyst steric bulk. In most cases it is required for high selectivity. However, excessive bulk can lead to unusual or poor results. The examples of substrates for the chiral phosphoric acid catalysed transfer hydrogenation of imines using Hantzsch esters in Figure 2.4 demonstrate how a subtle steric effect can have a pronounced influence on enantioselectivity.[31,104,114b,141] The catalyst series reveals that the physically larger 3,3' substituent doesn't necessarily yield high enantioselectivities and minor modifications to substrates can have a profound effect on catalyst choice. This highlights the difficulty in choosing the correct catalyst for a particular reaction and implies that the mechanism of asymmetric induction is not robust to changes in the system.

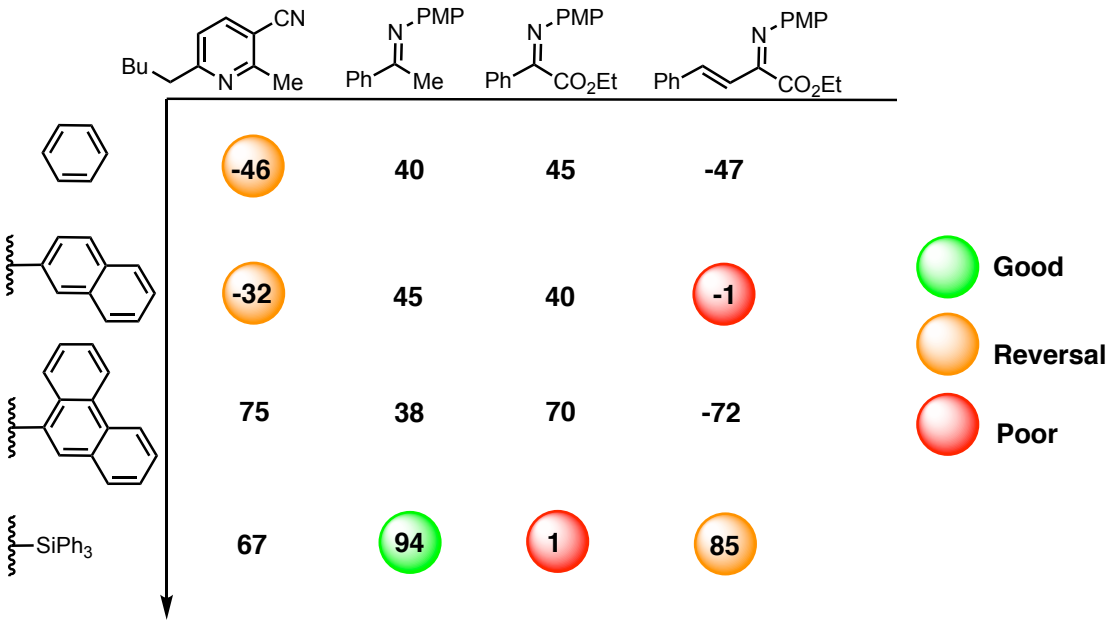

Figure 2.4. Effect of catalyst 3,3' substituent structure on the transfer hydrogenation of various imines. A consistent enantiomer of the catalyst was used for each substrate to allow comparisons to be made.

On the basis of this, I began to examine methods in which the sterics of the 3,3' substituents could be described numerically. I first investigated the use of A-values and the rotation barrier for a phenyl group as steric descriptors. These parameters were selected due to their wide applicability and they can easily be derived from computational methods, ensuring values would be available and consistent for all groups of interest. A-values are derived from a conformational study on the equilibrium position of ring flipping in monosubstituted cyclohexane rings. The destabilization of the axial conformation is due to 1,3 diaxial interactions. Rotational barriers for a phenyl group are derived from the energy required for rotation around the central C-C bond. The interaction between the R groups and the hydrogens on the opposing aryl ring are responsible for the destabilization of the eclipsed conformation (Figure 2.5).

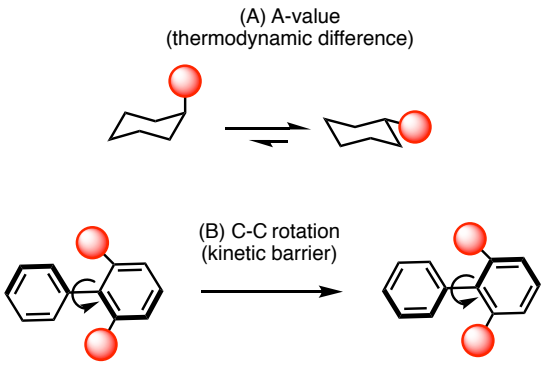

3, 3' Group	Computed A-Value (A)	Rotation Barrier (B)
H	0.00	0.00
$CHPh_2$	1.76	1.13
$SiPh_3$	4.85	1.35
Ph	4.39	2.05
1-naphth	4.07	13.63
2-naphth	4.35	2.13
9-anthryl	14.40	28.31
9-phenanthryl	4.09	14.45
$4\text{-}PhC_6H_4$	4.35	2.01
$4\text{-}^tBuC_6H_4$	4.37	2.02
$3,5\text{-}(Ph)_2C_6H_3$	4.21	2.21
$3,5\text{-}(CF_3)_2C_6H_3$	4.03	2.02
$2,4,6\text{-}(Me)_3C_6H_2$	15.97	21.58
$2,4,6\text{-}(^iPr)_3C_6H_2$	26.33	28.40

Figure 2.5. Steric parameters calculated using OPLS-2005 force field,[184-186] in MacroModel. All energies in kcal mol^{-1}.

Figure 2.5 gives the approximate values of the energy difference between the equatorial position and the axial and the energy required to rotate a phenyl group. For the groups, both the equatorial preference and the energy for rotation increases with size, although increasing the steric demands remote from the cyclohexane and phenyl ring is unimportant – only proximal sterics are assessed by these measures.

The treatment of naphthalene like substituents varies between the A-values and rotation barrier; the computed A-value underestimates the sterics of these particular groups. To analyze the potential flaw in application the basis of the A-value parameters must be revisited. A-values are derived from the difference in energy of axial and equatorial conformations, weighted through Boltzmann distribution based on the OPLS_2005 FF energies. Considering the free rotation around the cyclohexyl and the 3,3' substituent bond, the bond can rotate the large substituent away from the cyclohexyl ring and therefore minimize the 1,3-diaxial interactions that destabilize the axial conformation (Figure 2.6). The high-energy axial conformations experiencing significant steric interactions are weighted considerably less and so don't affect the energy of the axial conformer to an appreciable extent. Rotational barriers on the other hand are deduced from scanning the dihedral angle between the phenyl and the 3,3' substituent, enabling calculation of the energy of multiple conformations around the primary bond, allowing for different points of interaction. The rotational barriers are close approximations to the conformationally restricted size of the 3,3' group, representing steric interactions that are physically relevant and so are expected to correlate better to experiment.

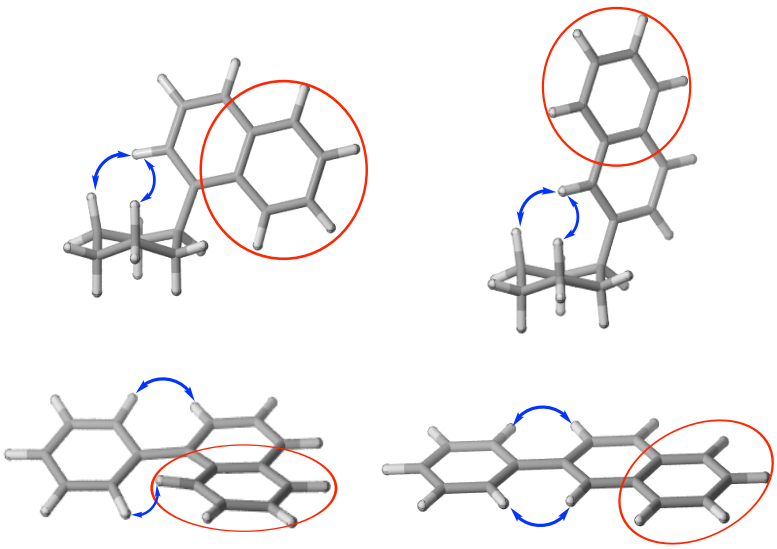

Figure 2.6. The effect of 1-naphthyl and 2-naphthyl on A-values and rotation barriers.

As expected, A-values and rotation barriers were both connected with stereoselectivity, but, as also expected, it is clear they are not describing the entire steric environment of the 3,3' group and rotation barriers correlate better. The general correspondence between A-values and rotation barrier implies they are both measuring similar properties. The steric bulk remote from the phosphoric acid active site is not being taken into account by the A-value or

the rotational barrier and is a key structural feature affecting the TS and the enantioselectivity. For example, aromatic rings with hydrogen in the 2,6 positions all have similar A-values (approximately 4.2) and similar rotation barriers (about 2.0). Changing the substituents at the 3,4,5 positions does not affect the proximal steric effect but does change the enantioselectivity. So when I compare this to experiment, I observed a vertical line of points in which the A-value (4.2) and rotation barrier (2.0) is not changing but the enantioselectivity is (Figure 2.7).

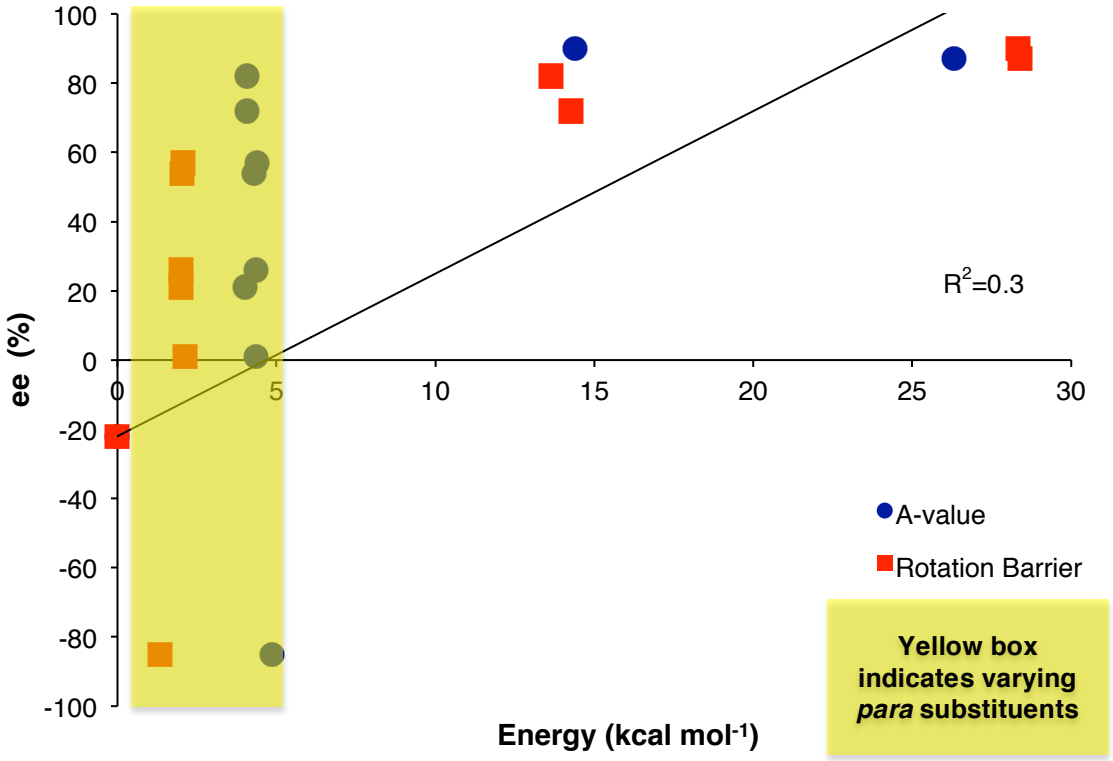

Figure 2.7. Proximal steric parameters evaluated in this study, literature example reported by You *et al.*[114b]

I therefore sought to develop an alternative steric parameter to describe the remote steric demands of the substituents. Conformational analysis of the chiral phosphoric acid shows the distinctive feature that the active site is deep inside a chiral cone created by the BINOL and constrained by the 3,3' substituents. Increasing steric demands remote from the phosphoric acid decreased the empty cone of space inside the chiral cavity. Based on this, I define A Remote Environment Angle, AREA(θ),[41] as the smallest angle (in degrees) between the vector from the center of the phosphorous atom to the midpoint of the binaphthol oxygens (Figure 2.8).

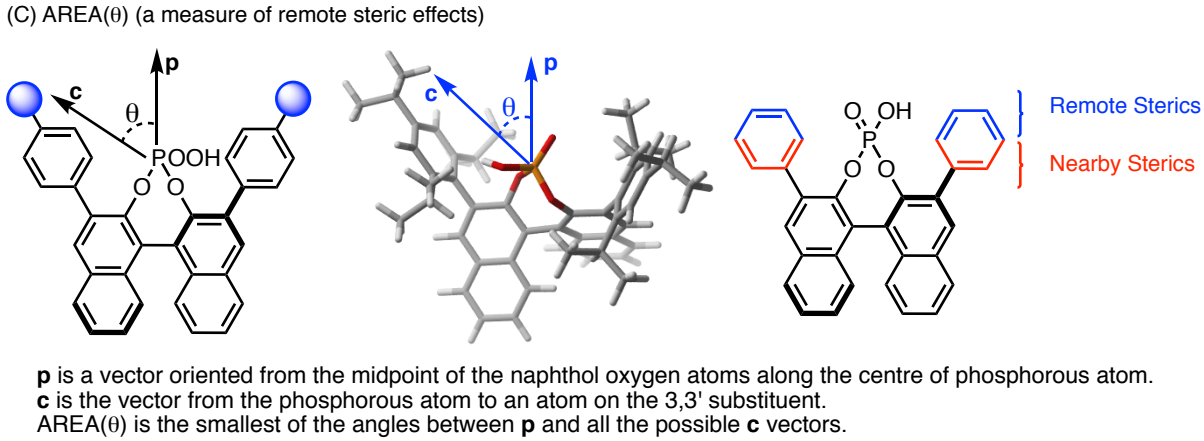

Figure 2.8. (C), AREA(θ), measures steric effects distant from the phosphoric acid moiety. 3D structure of (*S*)-TRIP is shown in a wire frame model as an example. I used the value for AREA(θ) from the global minimum, as the value did not vary by more than a degree when conformations within 10 kJ mol^{-1} were considered. Steric parameters (A) and (B) measure proximal sterics only.

Substituents which crowd access to the phosphoric acid, such as 4-tert-butyl-benzene, AREA(49), have smaller AREA values than less sterically demanding substituents, such as phenyl, AREA(70), even though the rotation barrier is identical. TRIP has a much larger rotation barrier than $SiPh_3$ but is less sterically demanding away from the phosphoric acid: AREA(51) vs AREA(29) (Figure 2.9). Computation of this parameter is straightforward and I have written a Python script to ensure that this parameter can be derived efficiently for the largest of catalyst structures.

3, 3' Group	AREA(θ) (C)
H	107
Ph	70
3,5-$(CF_3)_2C_6H_3$	62
1-naphth	62
9-anthryl	61
2,4,6-$(Me)_3C_6H_2$	61
2,4,6-$(^iPr)_3C_6H_2$	51
4-PhC_6H_4	50
4-$^tBuC_6H_4$	49
2-naphth	49
9-phenanthryl	48
$CHPh_2$	47
3,5-$(Ph)_2C_6H_3$	36
$SiPh_3$	29

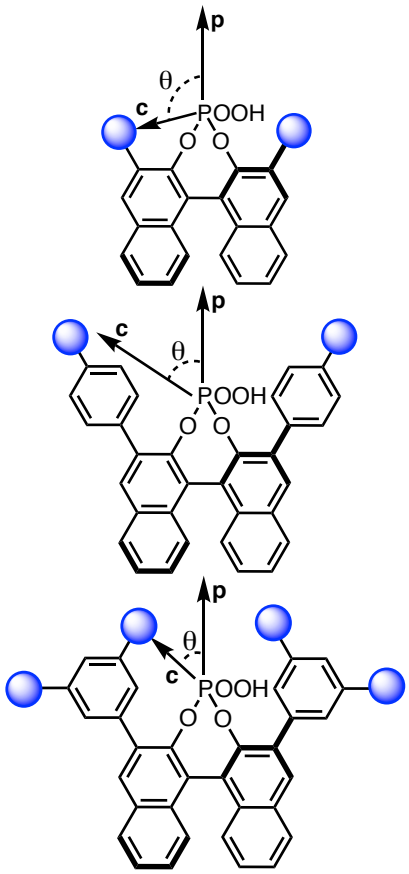

Figure 2.9. Variation in AREA(θ) with 3, 3' substituent. Increasing the size of the remote substituents decreases AREA(θ).

On comparing a series of catalyst structures for the Mannich reaction,[19] it was found that the correlation provides a good fit to the experimental data and more importantly it exposes a new relationship that could not be described with proximal sterics alone (Figure 2.10). From this brief examination, it is clear that inclusion of both parameters could describe the steric profile of the 3,3 substituents adequately.

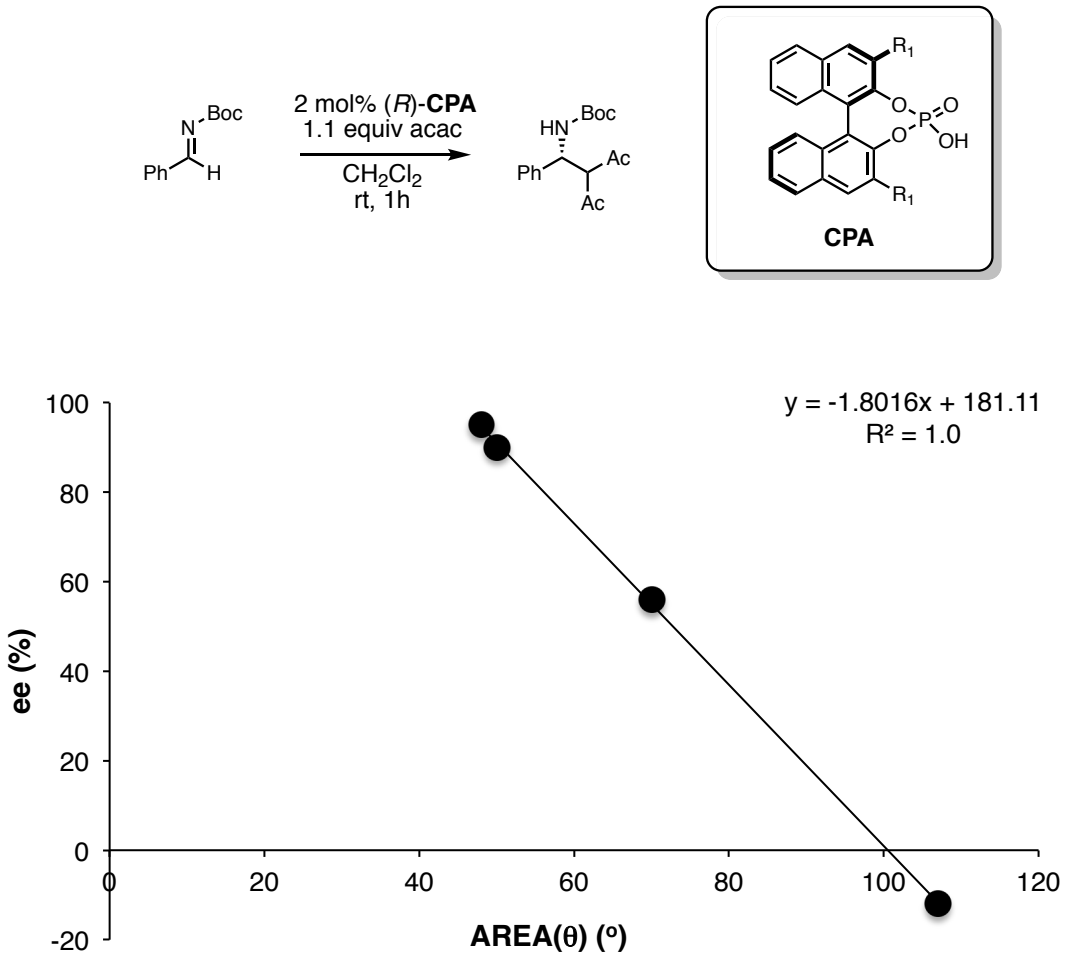

Figure 2.10. Ligand AREA(θ) parameter provides a linear relationship with enantioselectivity in Terada's Mannich reaction.

Despite the different chiral phosphoric acid structural modifications and the wide variation between them, as outlined in Chapter 1, it appears that AREA(θ) could be an unifying physical organic parameter that could explain enantioselectivity trends across the series of BINOL, BIPOL, SPINOL, H_8-BINOL and N-trifyl phosphoramides (Figure 2.11).

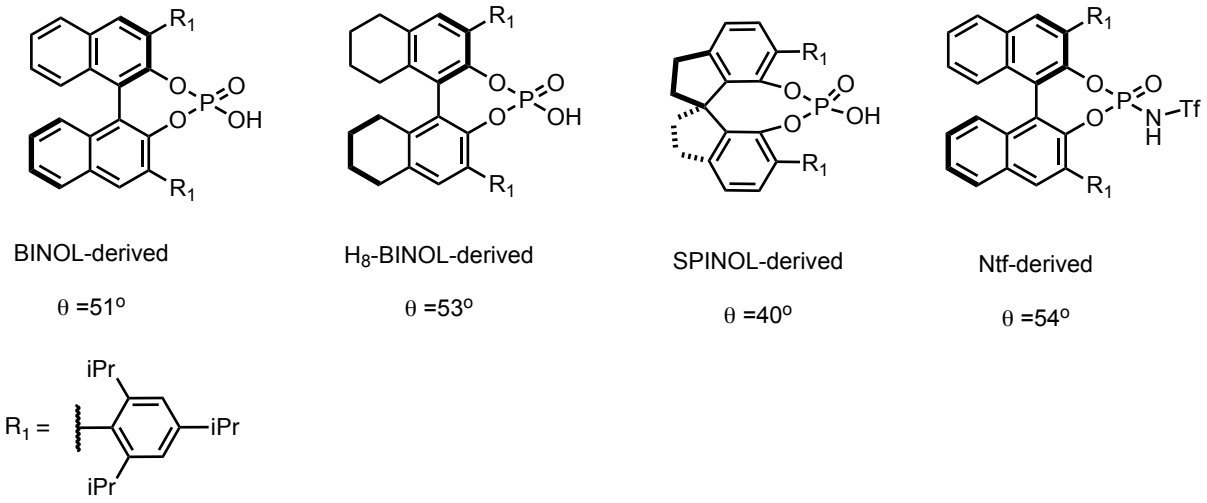

Figure 2.11. Comparison of the effect of changing the catalyst backbone and sterics on the phosphorous atom on the AREA(θ) parameter.

Figure 2.11 shows the effect on keeping the 3,3' groups consistent but changing either the backbone or the sterics at the phosphorous. This demonstrates that such modifications can have a profound effect on the chiral space. This could help guide mechanistic studies on understanding the effect of hydrogenation of the rear aromatic rings, which has often been attributed to an electronic difference or reducing the proximal steric effects.[187] Similarly, the increase of steric bulk at the phosphorus has been thought to affect only the proximal steric profile to an appreciable extent, but I can now conclude that this does indeed affect the remote sterics as well, albeit to a lesser extent.[134] Changing the backbone from BINOL to SPINOL has a dramatic effect on AREA(θ) and this should translate to experiment. For instance, in 2016, Sun and co-workers described the oxetane desymmetrization using HCl as the *in-situ* generated nucleophile.[92] SPINOL-derived catalysts were found to be more selective (Figure 2.12) than commonly used BINOL-derived chiral phosphoric acids. Changing the backbone of TRIP from BINOL to SPINOL lead to a large increase in

enantioselectivity and this can be attributed to changing the remote sterics of the catalyst, highlighted by AREA(θ) and computationally verified by Houk *et al.*[188]

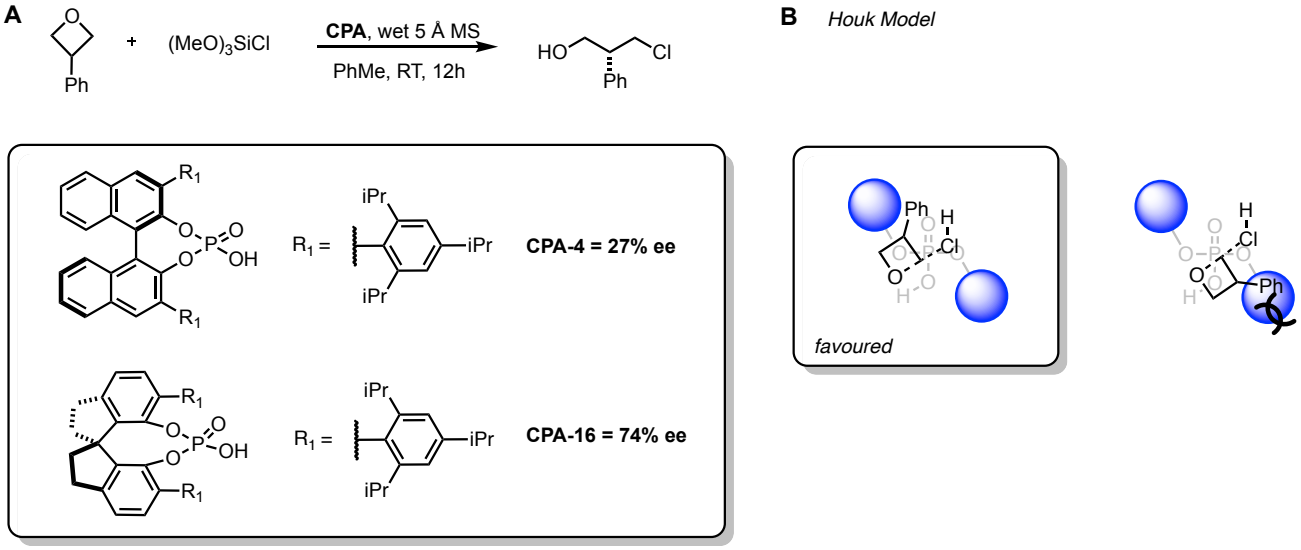

Figure 2.12. Using AREA(θ) to determine the effect of changing the catalyst backbone on enantioselectivity. (A) Desymmetrisation of oxetanes in which higher enantioselectivities are obtained with smaller AREA(θ) catalysts. (B) Houk model for stereoselectivity confirms that, increasing the sterics remote from the phosphoric acid increases the steric interactions between the phenyl oxetane substituent and the catalyst. This bad interaction disfavours the pathway leading to the competing product, leading to higher levels of enantioselectivity.

Smaller modifications such as hydrogenation of the rear aromatic rings of BINOL are expected to lead to minor modifications in product enantioselectivity as shown by List.[189] In a similar manner, I expect that such modifications affect different 3,3' substituted catalysts in different ways. For instance, although changing the backbone of TRIP from BINOL to H_8-BINOL has a small effect on AREA(θ), there may be others where this effect is more pronounced. The reactions conducted by Gong *et al.* investigating the Mannich reaction demonstrate this (Figure 2.13).[26] For the 4-FC_6H_4 BINOL-derived phosphoric acid, hydrogenation of the rear aromatic rings has a negligible effect on chiral space and enantioselectivity. However, the same modification increases the enantioselective effect of the phenyl substituted catalyst and this is captured by the larger change in AREA(θ) values. Interestingly, the magnitude and the direction of enantioselectivity changes are also captured. Changing **CPA-17** for **CPA-19** increases AREA(θ) and the enantioselectivity is decreased. For the other, **CPA-6**, the AREA(θ) is decreased and the catalyst is more selective. Such powerful trends would be almost impossible to capture by calculation as

such differences in enantioselectivity would correspond to very small energy differences which are much less than the average error.

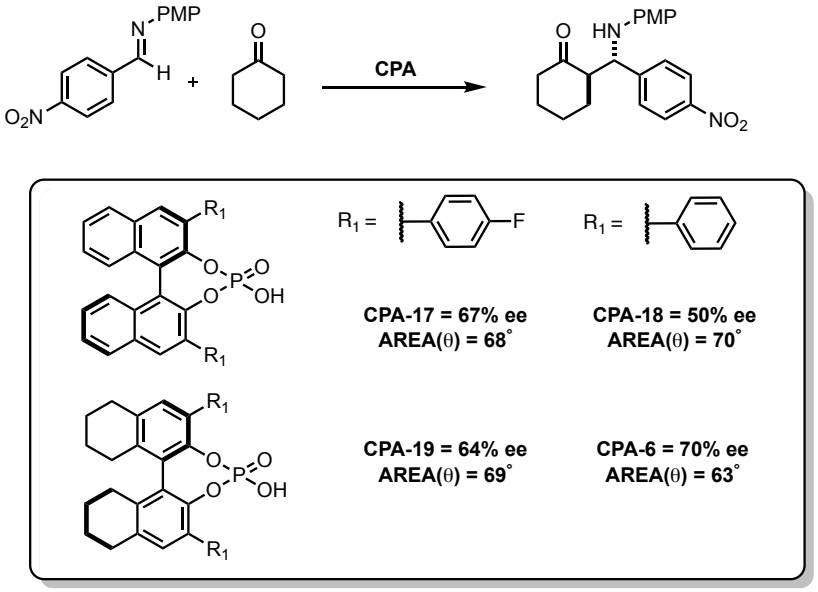

Figure 2.13. Effect of changing the catalyst backbone on AREA(θ) and enantioselectivity for the Mannich reaction.

These examples show that AREA(θ) is an effective parameter choice. Models could be built around this single descriptor, with other parameters added as correction terms: one for the increased bulk around the phosphorus and a second for increased steric profile of the rear aromatic rings. This should make it possible to model the catalysts collectively.

The Sigman group have also investigated the effect of the 3,3' substituent on guiding asymmetric induction. In their investigations on the chiral phosphate catalysed fluorination of allylic alcohols the torsional angle between the substituent and the binaphthyl backbone was employed as the steric decriptor.[181] Comparison of the steric values does not differ significantly between the dihedral angle and the rotation barrier (Figure 2.14). Examining the larger substituents, the mismatch between the two sets of parameters becomes more apparent. At first glance it appears as if the rotation barrier may be a better descriptor in isolation. The rotation barrier appears to capture the increase in steric bulk from 3,3' = H to an aromatic substituent that has hydrogens at the 2 and 6 positions. Additionally the dihedral angle appears to overestimate the nearby steric effects of 2,6-$(iPr)_2C_6H_3$ substituted catalysts.

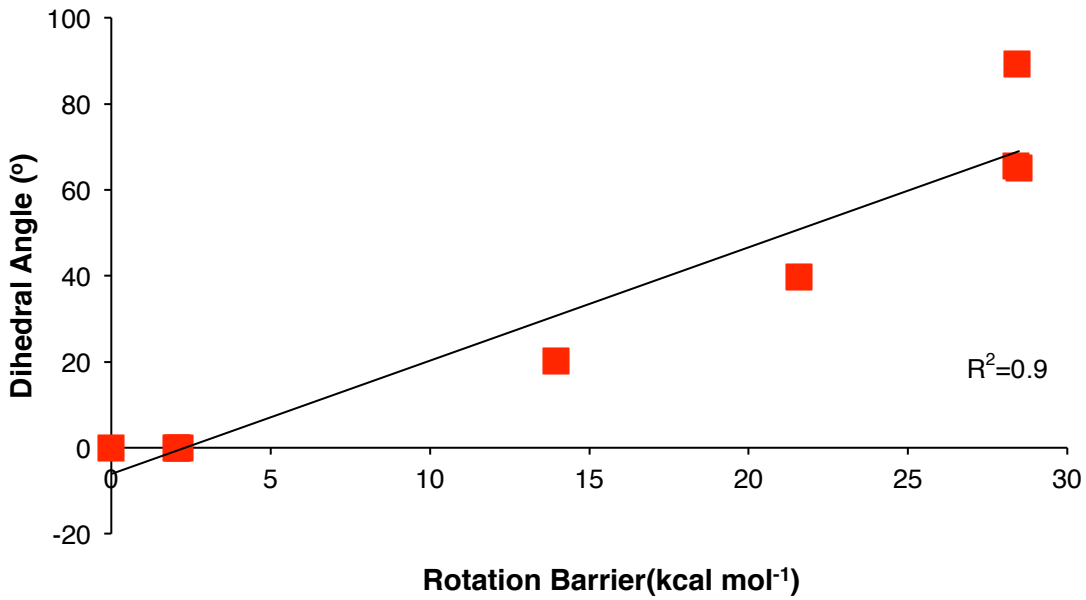

Figure 2.14. Comparison of proximal steric parameters; rotation barrier and the dihedral angle between the BINOL backbone and the 3,3' substituent.

2.3 Development of a Unified Steric Descriptor

To simplify data analysis, I sought to develop a complete steric description of the 3,3' substituents, unifying proximal and remote sterics into a single parameter. I hoped that the molecular volume of the catalyst cavity could reflect the steric profile of the 3,3' group. In the simplest terms the molecular volume would increase with increasing size of both proximal and remote sterics on the 3,3' substituents. The chiral catalyst volume value is calculated on the basis of the volume created by the 3,3' substituents in an abstract 3D array of point probes that is centered on the phosphorous atom and calculated using a Python program (further details in the appendix). Disappointingly, correlations to enantioselectivity revealed a rather poorly defined relationship (Figure 2.15). To assess whether calculation or application of the parameter was flawed, we calculated the solvent accessible surface area which despite the difference in definition measures the same general steric property, the size of the 3,3' group (Figure 2.16). I found that application of this feature resulted in no correlation. I can conclude that two parameters were required to describe the sterics of the 3,3' positions. This point would later prove to be a significant observation for the underlying physical reasons for enantioselectivity. *Could the proximal and remote sterics be playing two different roles in determining enantioselectivity?*

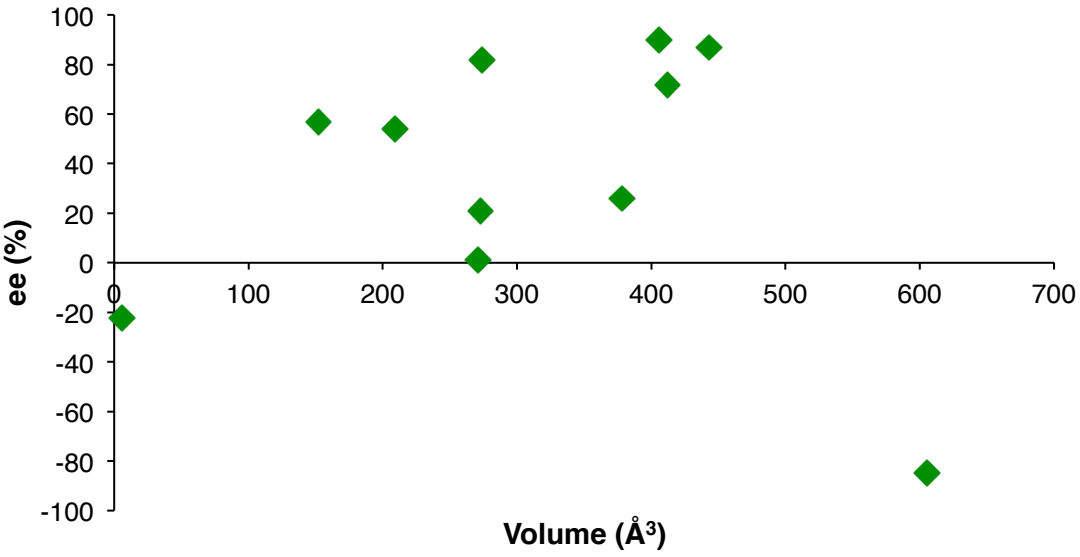

Figure 2.15. Evaluation of the chiral cavity volume parameter; literature example reported by You *et al.*[114b] This reaction was selected primarily because both proximal and remote sterics affect the enantioselectivity.

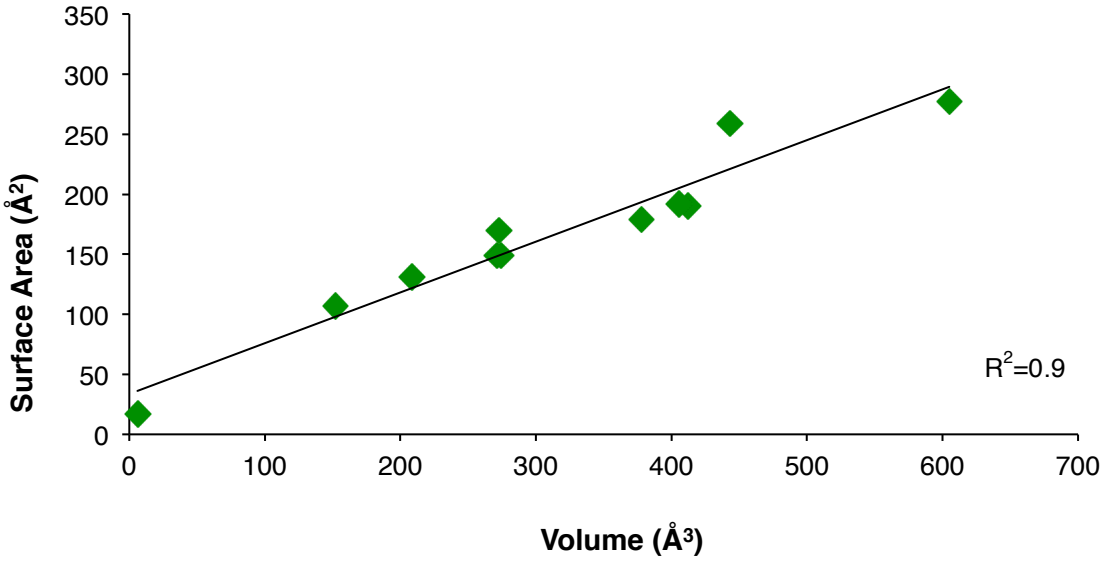

Figure 2.16. Comparison of surface area and volume steric parameters.

2.4 Conclusions

In conclusion, the steric features of the 3,3' groups on the phosphoric acid that determine stereochemical induction have been investigated. Analysis of these factors relied on using a variety of computational techniques including the development of novel software for the calculation of steric parameters. Product selectivity in these reactions is dependent on both sterics distant from the active site, quantified by the ligand AREA(θ) and proximal sterics, quantified by the rotation barrier. By comparing the ligand AREA(θ) parameter with catalysts varying at the backbone and steric bulk at the phosphorus centre I show that these features can have a dramatic effect on the distant sterics offering new mechanistic insights into the reasons for differing selectivity with the same group at the 3,3'. In addition the steric profile of the 3,3' cannot be parameterised by a single cumulative value suggesting that proximal and remote sterics play different roles on stereoinduction, an important observation in its own right.

As I continue to explore the application of these steric descriptors, we hope to be able to develop a consistent understanding into the stereochemical role of the 3,3' groups and use this to guide catalyst selection and design.

Chapter 3

3 Stereochemical Role of 3,3' Groups: Symmetrical Nucleophiles

3.1 Background and Methods

Chiral phosphoric acids have become popular catalysts and the nucleophilic addition to imines is represented in seventy-seven literature reports consisting of over 1000 transformations. This synthetic work went on to become the subject of computational studies, through which the catalyst has been shown to bind to the imine and nucleophile through hydrogen bonding, simultaneously activating both. This has led to the widespread adoption of the Goodman model for stereoselectivity.[20]

The amine architecture is a popular natural product motif and despite notable work, the use of chiral phosphoric acids in complex syntheses is relatively low. Gong,[190] Hiemstra[191] and Antilla[192] have demonstrated the potential to use these catalysts with a clear synthetic purpose (Figure 3.1). Many excellent methodologies exist, even with this precedent; applications are generally limited to the idealized reactions initially reported. Minor structural modifications to the reactant combination and the catalyst can have a profound effect on enantioselectivity outcomes, making it difficult to determine the reaction conditions necessary without a significant empirical screening campaign.

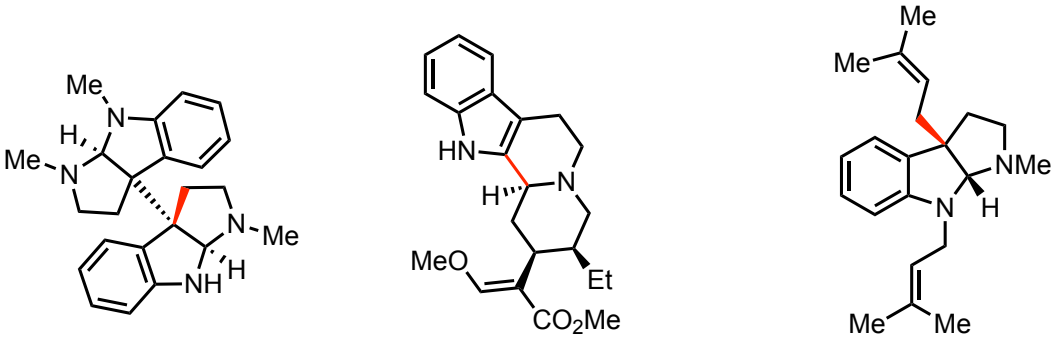

(+)-folicanthine (-)-corynantheidine (-)-debromoflustramine B

Figure 3.1. Examples of natural products constructed using steps, highlighted in red, utilizing chiral phosphoric acids.

Investigations into the effect of the 3,3' groups on stereoselectivity are relatively scarce and the ability to rationally choose a catalyst remains difficult and necessary. A principal challenge lies with the large structural diversity at the 3,3' position coupled with the wide variation in reaction pathway choice (*Type I* vs. *Type II*, *E* vs. *Z*). On the basis of this I aimed to develop a qualitative model that chooses the correct catalyst based on the structure of the reaction combination using the methodology described in Chapter 2. I envisioned that the same reasons for enantioselectivity with one reaction could be applied to another if the imine conformation remained consistent between the TS leading to competing products. With this idea I would analyse reactions involving symmetrical nucleophiles (H-bond that binds to the catalyst in line with nucleophilic site), which are almost always *Type I*, and displaced nucleophiles (nucleophile carbon not in line with the H-bond that binds to the catalyst), which are usually *Type II*, separately (Figure 3.2).

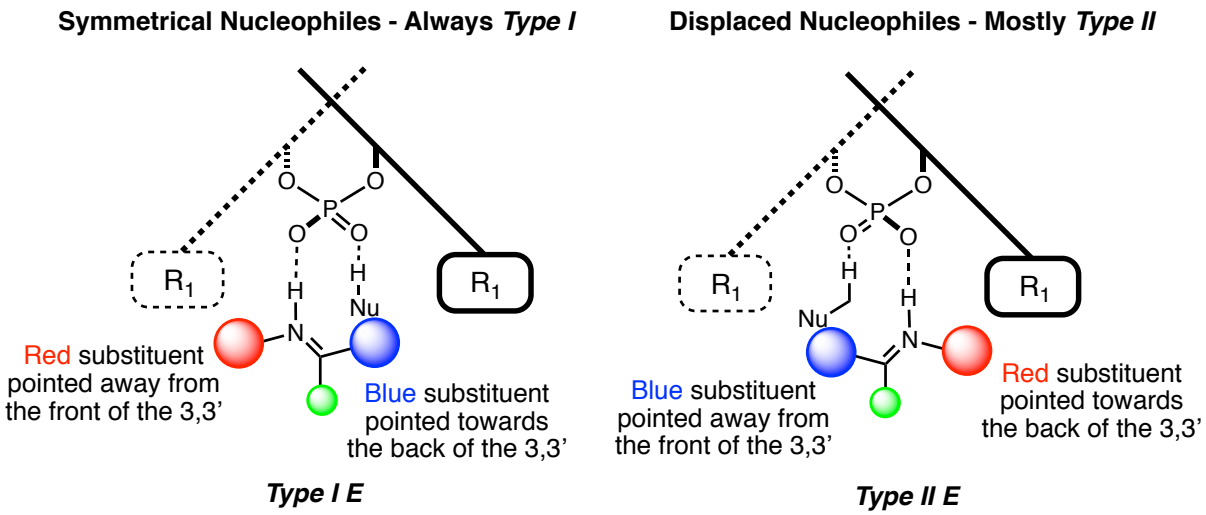

Figure 3.2. Different imine orientations within the chiral catalyst cavity as a function of nucleophile type.

The correlation found between enantioselectivity, rotation barriers and a new measure, AREA(θ) shown in Chapter 2 demonstrated that such measures could be used to identify and provide mechanistic insights into the features required for enantioselectivity. To fully explore the applications of these measures, I undertook computational analysis of three model reactions with varying reactant combinations spanning a range of catalysts with different 3,3' substituents. I was able to provide unprecedented levels of chemical insight into the reasons for high levels of enantioselectivity leading to the development of a simple

qualitative model, which is consistent for all reactions involving imines and symmetrical nucleophiles.[41]

For the QM/MM hybrid calculations on the full catalyst and reagent system, transition states were located first, by a conformational search in MacroModel (version 9.9)[54] using the OPLS-2005 force field.[184-186] Selected conformers within 10 kJ mol^{-1} of the minimum were optimized using the ONIOM method implemented in Gaussian 09 (revision D.01).[35] The B3LYP density functional,[43-44] and split-valence polarized 6-31G** basis set,[193-194] were used for the high-layer, and the force field UFF,[195] was used for the low-layer unless stated otherwise. The reactants and the phosphoric acid moiety of the catalyst were included in the high-layer, and the remaining regions of the catalyst were treated as the low-layer. This method has previously been shown to give excellent results when used to describe reactions catalysed by chiral phosphoric acids.[37-41] The position of the partition within the catalyst was chosen as the phosphoric acid binds directly to the reagents, whereas the remaining catalyst acts as steric bulk and can be adequately described by molecular mechanics. All calculations were performed with the (*S*)-catalyst for model consistency with the connectivity shown in the reaction scheme. I use the Kekulé bonding structure for all catalysts ensuring that the connectivity in the catalyst backbone is consistent between the structures allowing for accurate energy and geometry comparisons. Single point energy calculations were performed on the resulting structures using M06-2X density functional,[46] and the 6-31G** basis set, using non-default convergence criteria (fine grid density, ultrafine accuracy level) as implemented in the Jaguar program (version 7.9).[55] This energy was used to correct the gas-phase energy derived from the ONIOM calculations. Free energies in solution were derived from structures optimized in the gas phase at the ONIOM (B3LYP/6-31G**:UFF), level of theory by means of a single point calculation using M06-2X/6-31G** with the polarizable continuum model (PCM) as implemented in the Jaguar program (version 7.9), using diethyl ether (probe radius = 2.60 Å) for the transfer hydrogenation study of acyclic imines, benzene (probe radius = 2.33 Å) for the transfer hydrogenation of cyclic imines and xylene (probe radius = 2.76 Å) for the phosphorylation of imines, as the solvent.[50] These values were used to correct the Gibbs free energy derived from the ONIOM calculations. The quantitative parameters were calculated as described previously in Chapter 2. Structures are illustrated using CYLview.[196]

3.2 Transfer Hydrogenation of Acyclic Imines

In 2008, You *et al.* reported an efficient method for the reduction of α,β-imino esters using Hantzsch esters catalysed by BINOL-derived phosphoric acids to afford the corresponding imines in excellent yields and enantioselectivities.[114b] Experimentally You *et al.* found that changing the 3,3' groups from 2,4,6-triisopropylphenyl (medium AREA(θ)) to $SiPh_3$ (small AREA(θ)) inverted the sense of stereoinduction (Figure 3.3). However, it is not clear how the 3,3' group induces such a strong reversal. In addition large proximal sterics were found to be necessary for efficient enantioinduction (compare entries 7 and 8).

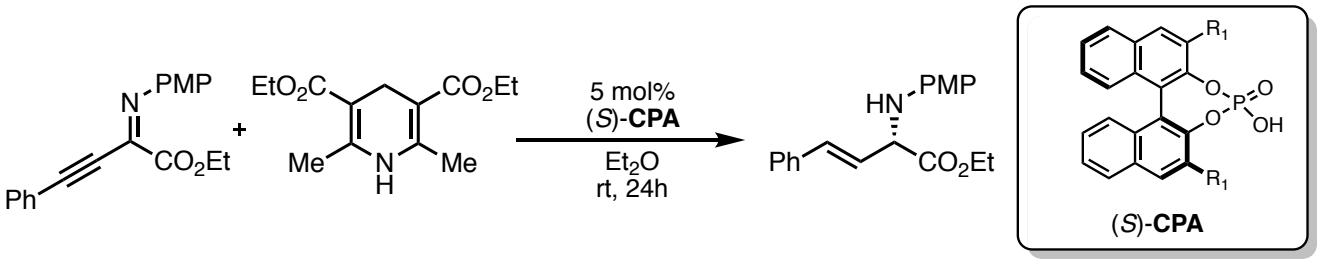

Entry	Catalyst R_1	AREA(θ)	Rotation Barrier (kcal mol^{-1})	ee (%)	Mechanism
1	H	107	0.00	-22	*Type II E*
2	Ph	70	2.05	57	*Type I E*
3	4-$NO_2C_6H_4$	64	2.03	54	*Type I E*
4	1-naphth	62	13.63	82	*Type I E*
5	3,5-$(CF_3)_2C_6H_3$	62	2.02	21	*Type I E*
6	9-anthryl	61	28.31	90	*Type I E*
7	***2,4,6-(^{i}Pr)$_3$C$_6$H$_2$***	***51***	***28.40***	***87***	***Type I E***
8	***4-PhC$_6$H$_4$***	***50***	***2.01***	***26***	***Type I E***
9	2-naphth	49	2.13	<1	*Type I E*
10	9-phenanthryl	48	14.45	72	*Type I E*
11	***SiPh$_3$***	***29***	***1.35***	***-85***	***Type I Z***

Figure 3.3. "Break" in linearity obtained for You's transfer hydrogenation.

Accounting for all the data, enantioselectivity increases with increasing AREA(θ) until a point, stops and then changes to a decline. In classical physical organic chemistry, distinct shifts in mechanism are revealed through changes in slope of univariate correlations, an approach famously depicted by so-called "breaks" in Hammett plots.[197-199] Similarly to Hammett plots, I interpreted this "break" in linearity as an unexpected feature change in the

enantiodetermining step. To probe this feature I decided to investigate the change in mechanism computationally using high-level ONIOM calculations, which we have previously applied to similar systems.[25] Slightly simplified molecules were used in the calculations: the PMP group was replaced by a Ph; the dimethyl Hantzsch ester was used instead of the diethyl counterpart. The imine can orient itself with respect to the catalyst in one of two ways. Noting that the C_2 symmetry of the phosphate anion allows us to draw the imine at the front of the diagram without loss of generality, the *N*-substituent, can be directed away from the front 3,3' group, which I call *Type I*, or towards the 3,3' groups, which I call *Type II*. Additionally, the imine can exist as either the *E* or *Z* stereoisomer; I define *E* or *Z* based on steric size. Combining these considerations, four unique TS for the transfer hydrogenation reaction are formulated. The possible transition states and the products they afford are given below (Figure 3.4).

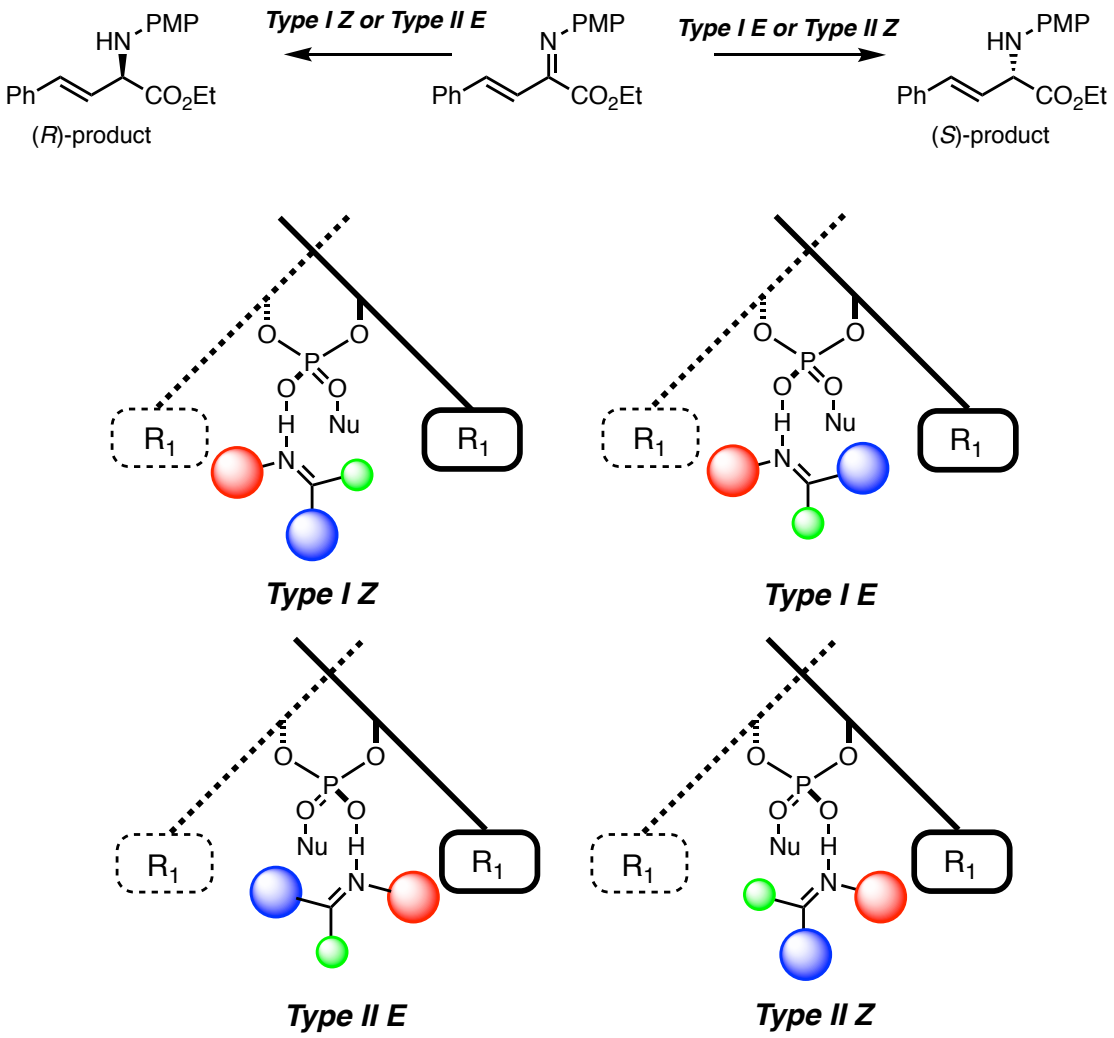

Figure 3.4. Transition state models for the prediction of enantioselective outcome.

Transition state calculations were performed as described above on the TRIP and the $SiPh_3$ derived catalysts. The results are summarised in Table 3.1, Figures 3.5 and 3.6 below. For the TRIP catalysed reaction the lowest calculated transition state is **TS2-*E*** (*Type I E*), which is in good agreement with the experimentally observed outcome (computed ee 99%). For the $SiPh_3$ derived phosphoric acid catalysed reaction the lowest energy transition state is **TS4-*Z*** (*Type I Z*), which accounts for the experimentally observed reversal in stereoinduction. Although the calculated energy values are lower than compared to experiment (computed ee -40%), qualitative trends are accurately predicted. The ONIOM (M06-2X/6-31G**:UFF) method indicates that the discrepancy between calculations and experiment traces back to the B3LYP component of the optimisation. ONIOM (M06-2X/6-31G**:UFF) gave a larger preference for the *Type I Z* pathway than ONIOM (B3LYP/6-31G**:UFF). The energy difference between **TS4-*Z*** and **TS4-*E*** re-evaluated using ONIOM (M06-2X/6-31G**:UFF) was calculated to be 2.9 kcal mol^{-1}. Although the B3LYP geometries are generally found to be reliable,[200] this example was a difficult case. Table 3.1 provides a comparison of energy differences between the TS in Figure 3.5 and Figure 3.6 computed using both ONIOM methods. The combination of calculations and experimental data provides compelling evidence that the imine stereoisomer involved in the transition state changes within a catalyst screen. For both catalysts, the *Type II* pathways were higher in energy due to the additional steric interactions and the directly competing one was that of the opposite imine conformation. Catalysts with very large AREA(θ) have little proximal bulk, and these substituents cannot differentiate between *Type I* and *Type II* pathways. In these cases low enantioselectivities are obtained and either pathway can be slightly favoured (Figure 3.3). Visual inspection of the *Type II* TS for the TRIP-catalysed reactions show the *N*-substituent is directed towards the proximal isopropyl groups, having little interaction with the one remote from the phosphoric acid moiety. This implies that the bulk proximal to the phosphoric acid moiety controls *Type I* vs. *Type II* selectivity. This serves to explain the discrepancies in selectivity between catalysts with similar distal bulk, which I quantify using AREA(θ), but varying proximal bulk (Figure 3.3, entries 7 and 8). This physical factor is not explicitly accounted for by the ligand AREA(θ) but can be described by a proximal bulk steric parameter, such as the rotation barrier (although both proximal bulk steric parameters seem to underestimate the nearby steric effects of $SiPh_3$). The reversal in lowest TS observation can be rationalised by my qualitative model Figure 3.7: facilitating the reaction in a medium catalyst cavity results in the *E* conformation being favoured; this conformation reduces the internal substrate steric interactions present in the *Z* conformation. However, as the catalyst cavity decreases the interaction between the R groups and the 3,3' groups becomes more

energetically costly than the internal steric repulsion and so the *Z* transition state is favoured. The imine R groups are directed towards the bulk distant from the catalyst. It is this interaction that controls which stereoisomer of the imine is present in the TS.

Table 3.1. Comparison of the relative energies derived from both ONIOM methods. All energies in kcal mol^{-1}.

	ONIOM (B3LYP/6-31G**:UFF)		ONIOM (M06-2X/6-31G**:UFF)	
$\Delta\Delta G^{\ddagger}$	$\Delta\Delta G^{\ddagger}$	$\Delta\Delta G_{sol}{}^{\ddagger}$	$\Delta\Delta G^{\ddagger}$	$\Delta\Delta G_{sol}{}^{\ddagger}$
TS2-*E*	0	0	0	0
TS2-*Z*	+3.2	+3.5	+4.6	+5.0
TS1-*Z*	+8.6	+10.3	+10.4	+12.1
TS1-*E*	+9.5	+9.0	+15.6	+15.8
TS4-*Z*	0	0	0	0
TS4-*E*	+0.5	-0.7	+2.9	+1.7
TS3-*Z*	+8.2	+8.0	+5.5	+6.1
TS3-*E*	+10.8	+9.9	+7.2	+6.6

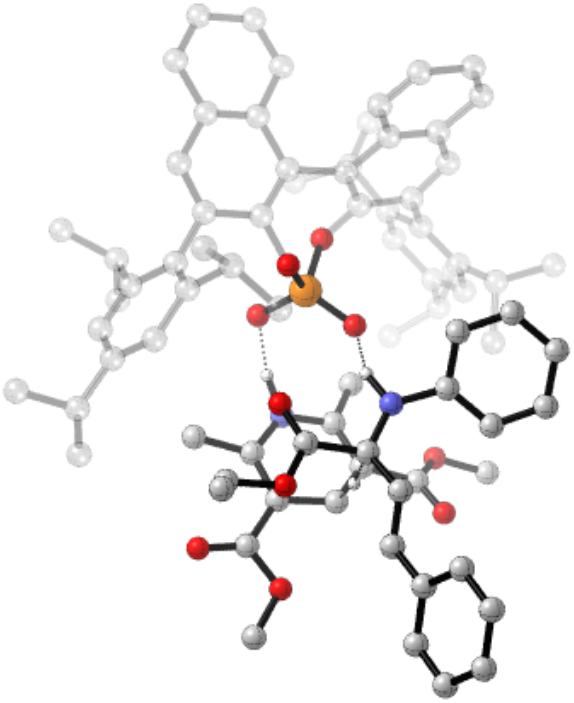

TS1-*Z*: $\Delta\Delta G^{\ddagger}$ = +8.6 kcal mol^{-1}, $\Delta\Delta G_{sol}^{\ddagger}$ = +10.3 kcal mol^{-1}

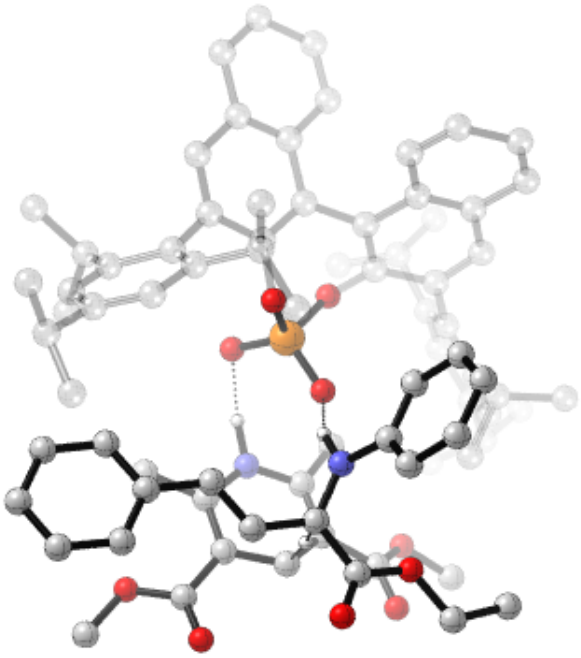

TS1-*E*: $\Delta\Delta G^{\ddagger}$ = +9.5 kcal mol^{-1}, $\Delta\Delta G_{sol}^{\ddagger}$ = +9.0 kcal mol^{-1}

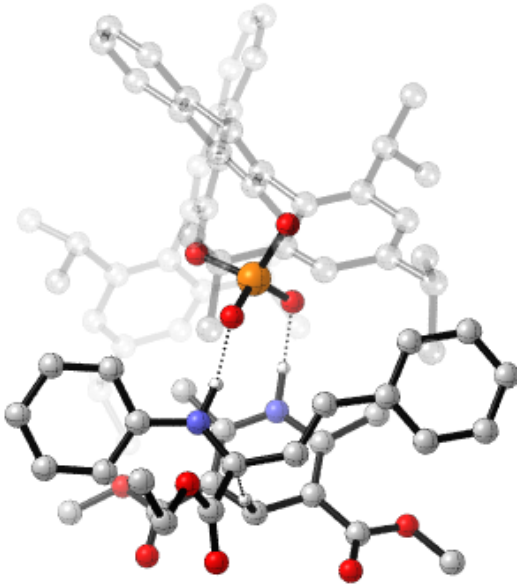

TS2-*E*: $\Delta\Delta G^{\ddagger}$ = 0 kcal mol^{-1}, $\Delta\Delta G_{sol}^{\ddagger}$ = 0 kcal mol^{-1}

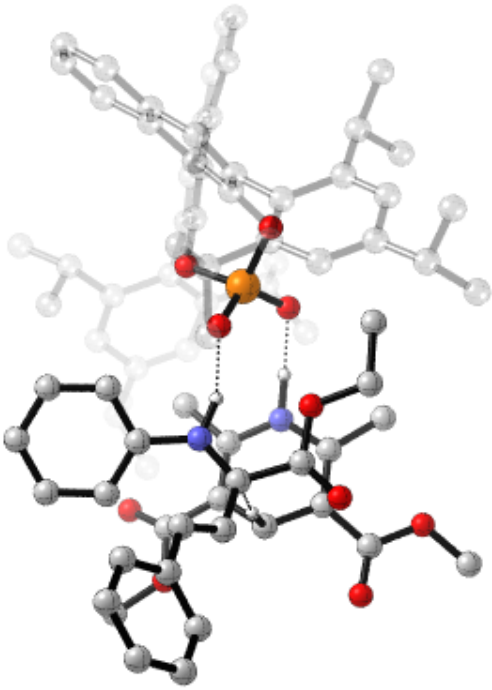

TS2-*Z*: $\Delta\Delta G^{\ddagger}$ = +3.2 kcal mol^{-1}, $\Delta\Delta G_{sol}^{\ddagger}$ = +3.5 kcal mol^{-1}

Figure 3.5. Competing TS for the TRIP catalysed transfer hydrogenation reaction. ONIOM (B3LYP/6-31G**: UFF), single-point energy M06-2X/6-31G**. Grayed-out regions were treated with UFF, and the full-colour regions were treated B3LYP/6-31G**.

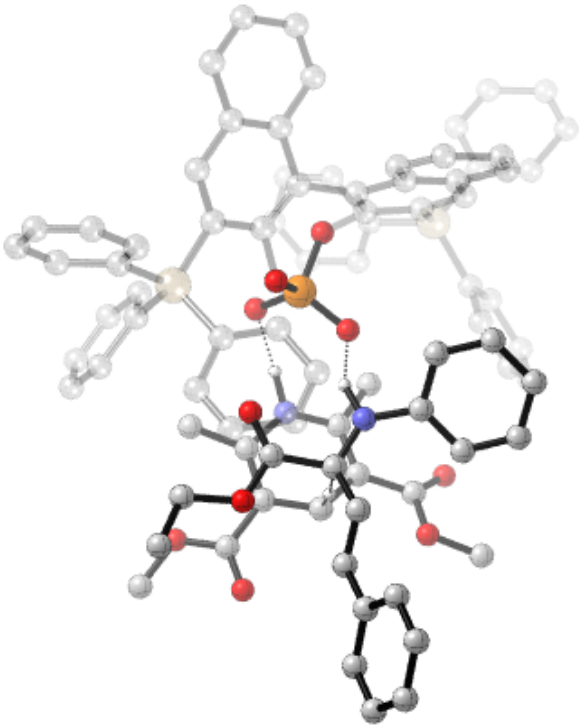

TS3-*Z*: $\Delta\Delta G^{\ddagger}$ = +8.2 kcal mol^{-1}, $\Delta\Delta G_{sol}^{\ddagger}$ = +8.0 kcal mol^{-1}

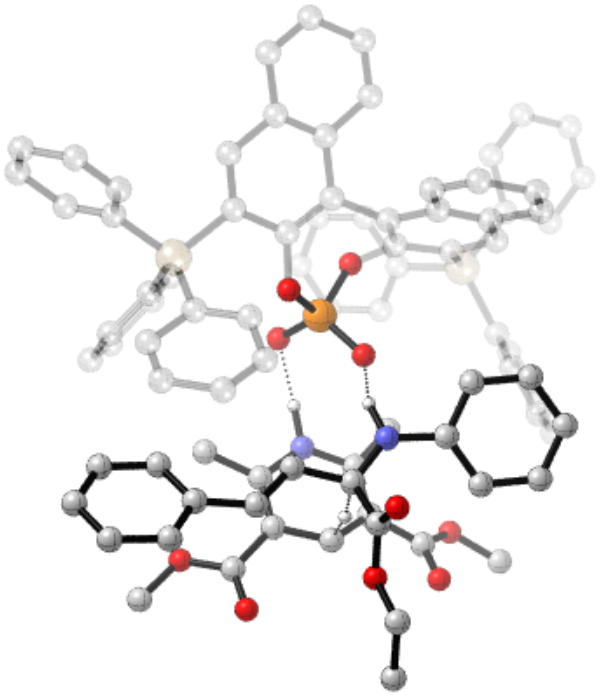

TS3-*E*: $\Delta\Delta G^{\ddagger}$ = +10.8 kcal mol^{-1}, $\Delta\Delta G_{sol}^{\ddagger}$ = +9.9 kcal mol^{-1}

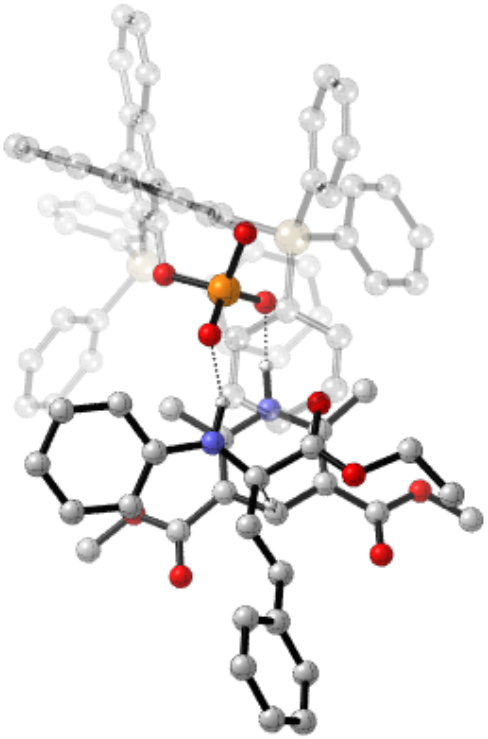

TS4-*Z*: $\Delta\Delta G^{\ddagger}$ = 0 kcal mol^{-1}, $\Delta\Delta G_{sol}^{\ddagger}$ = 0 kcal mol^{-1}

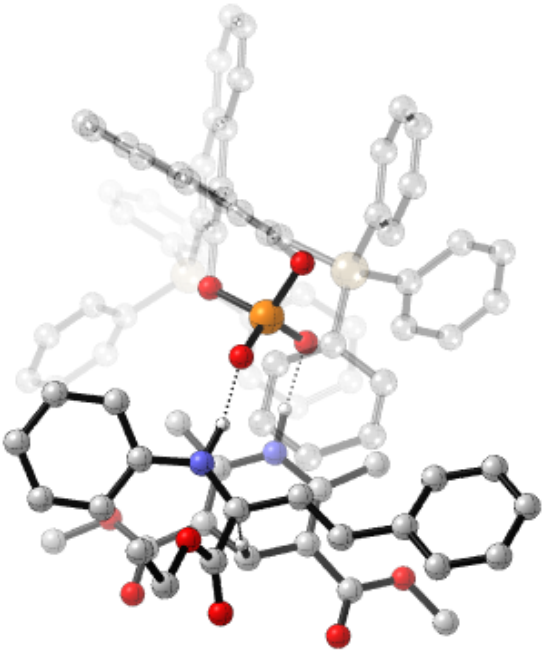

TS4-*E*: $\Delta\Delta G^{\ddagger}$ = +0.5 kcal mol^{-1}, $\Delta\Delta G_{sol}^{\ddagger}$ = -0.7 kcal mol^{-1}

Figure 3.6. Competing TS for the $SiPh_3$ catalysed transfer hydrogenation reaction. ONIOM (B3LYP/6-31G**: UFF), single-point energy M06-2X/6-31G**. Grayed-out regions were treated with UFF, and the full-colour regions were treated B3LYP/6-31G**.

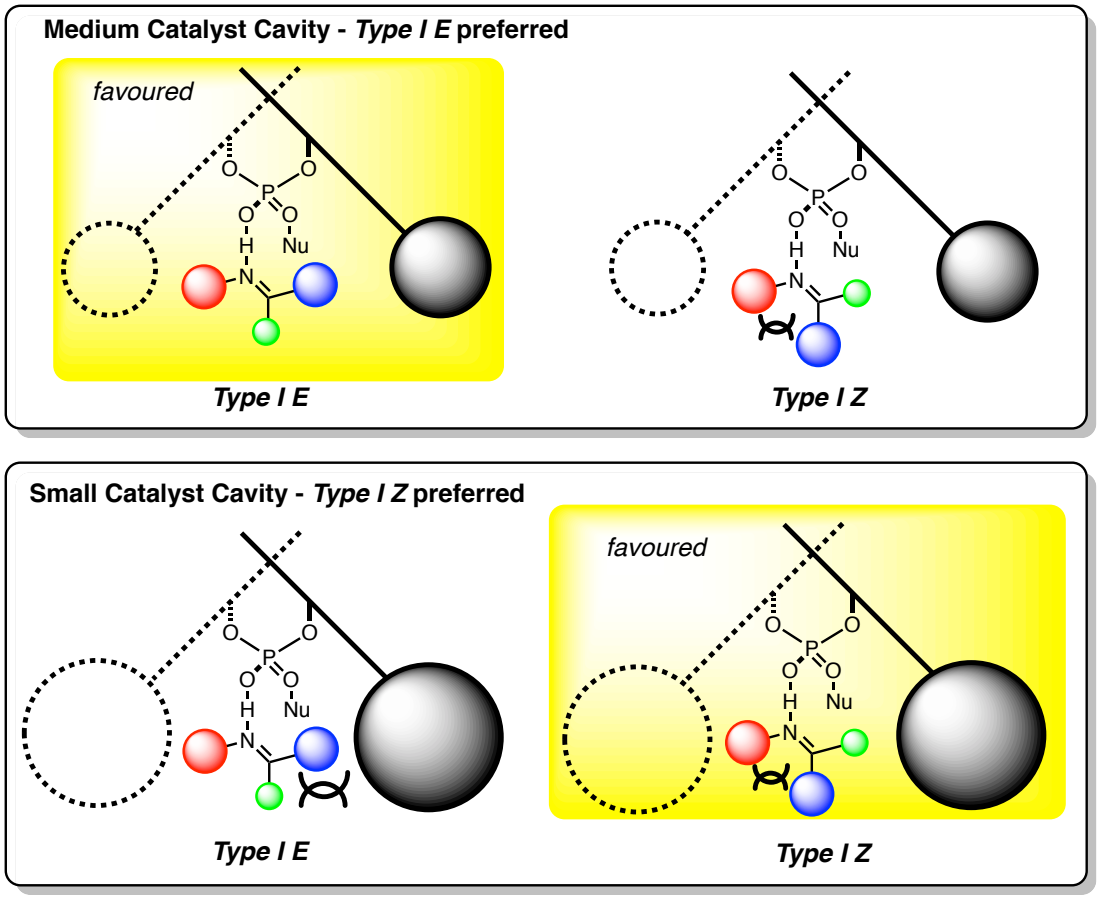

Figure 3.7. Qualitative model describing the preference for *Z* transition state with small ligand angle catalysts. In the *E* configuration the largest R groups are coplanar and so internal steric interactions are minimized. The *Z* imine conformation allows placing two groups distant from the majority of the catalyst bulk, but this is offset by their proximity to each other.

This model implies that similar reactions proceeding *via Type I E* pathways will not be suitable for a reaction catalysed by small ligand AREA(θ) catalysts. Such catalysts bias the reaction towards a *Z* transition state leading to little stereoinduction. An optimal catalyst for such a reaction would be one that is neither too big (raises *E* relative to *Z*) nor one that is too small (cannot differentiate between *Type I* or *Type II*) but somewhere in between. In examples, where small ligand AREA(θ) catalysts proceed with high levels of enantioselectivity the favoured pathway would be a *Type I Z*. Examples where this general trend is observed are given in Table 3.2. However, without detailed mechanistic investigations only a correlation can be established.

Table 3.2. Examples of nucleophilic additions to imines catalysed by chiral phosphoric acids. For each catalyst classification, I have chosen to compare the best performer from the catalyst screen of a model substrate under the same reaction conditions.

Reaction	Mechanism	AREA(θ) > 70 (%ee)	medium AREA(θ) (%ee)	AREA(θ) < 36 (%ee)
addition of diazophosphonates[201]	*Type I E*	0	94	27
addition of diazoacetimides[202]	*Type I E*	-	80	30
Strecker reaction[62]	*Type I E*	-	93	0
addition of alcohols[137]	*Type I E*	-	94	52
addition of thiols[138]	*Type I E*	-	91	11
peroxidation of imines[136]	*Type I E*	-	84	3
reduction of alkynyl esters[114b]	*Type I E/Z*	-22	90	-85
reductive amination[144]	*Type I Z*	6	97	90
reductive amination[31]	*Type I Z*	7	65	87
reduction of N-Ar imines[142]	*Type I Z*	11	92	84

3.3 Transfer Hydrogenation of Cyclic Imines

Acyclic imines can equilibrate between the *E* and *Z* forms but cyclic imines are fixed in a *Z* configuration. The model (Figure 3.7) suggests that in reactions involving such substrates, only proximal sterics will affect the enantioselectivity to an appreciable extent. This is shown in the transfer hydrogenation reaction of pyridines catalysed by BINOL-derived chiral phosphoric acids reported by Rueping *et al.* (Figure 3.8).[141] The examination of both rotation barrier and AREA(θ) as a function of enantioselectivity indicates that, enantioselectivity is almost independent of AREA(θ) but is proportional to rotation barrier. For instance, substituents that crowd access to the phosphoric acid such as 4-PhC_6H_4, AREA(50), have smaller AREA(θ) values than less sterically demanding substituents such as phenyl, AREA(70), even though the rotational barrier is identical and the ee's are similar (-44% vs -46%).

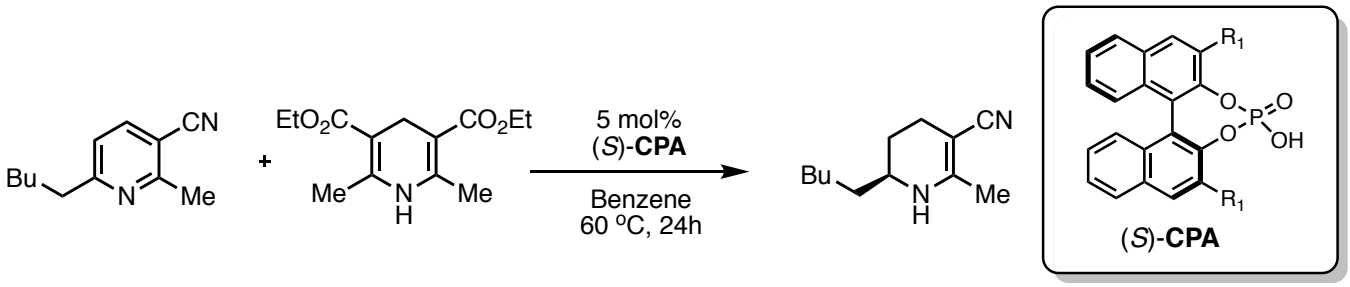

Entry	Catalyst R_1	AREA(θ)	Rotation Barrier (kcal mol^{-1})	ee (%)	Mechanism
1	4-PhC_6H_4	50	2.01	-44	*Type II*
2	3,5-$(CF_3)_2C_6H_4$	62	2.02	-36	*Type II*
3	***Ph***	***70***	***2.05***	***-46***	***Type II***
4	2-naphth	49	2.13	-32	*Type II*
5	3,5-(^{t}Bu)$_2$-4-$OMeC_6H_3$	35	2.51	-56	*Type II*
6	1-naphth	62	13.43	35	*Type I*
7	9-phenanthryl	48	14.25	75	*Type I*
8	***9-anthryl***	***61***	***26.53***	***89***	***Type I***

Figure 3.8. Catalyst screening results for Rueping's transfer hydrogenation reaction. *Type I* and *Type II* are explained in Figure 3.2. Only BINOL derived catalyst are included to simplify analysis.

It may appear, however, that the rotation barrier could overestimate the proximal steric effect of the 1-naphthyl derived phosphoric acid. A second explanation for this failure of the steric description could represent the electronic feature as a significant influence on enantioselectivity. Assuming the reaction proceeds *via* a 1,4-addition followed by tautomerisation to afford the imine, which is then further reduced, as proposed by Rueping *et al.* I computationally studied the enantiodetermining step (Figure 3.9). Detailed geometric and energetic information of the TS structures for the 9-anthryl and phenyl derived phosphoric acids were obtained using the ONIOM method described. In my calculations, I simplify both the cyclic substrate, the *n*-pentyl group is replaced by a *n*-butyl. Such a small structural modification has been experimentally determined not to affect the enantioselectivity to an appreciable extent and the Hantzsch ester, dimethyl is used instead of its diethyl counterpart. Further truncation of the imine alkyl substituent lead to systematic errors between calculations and experiment.

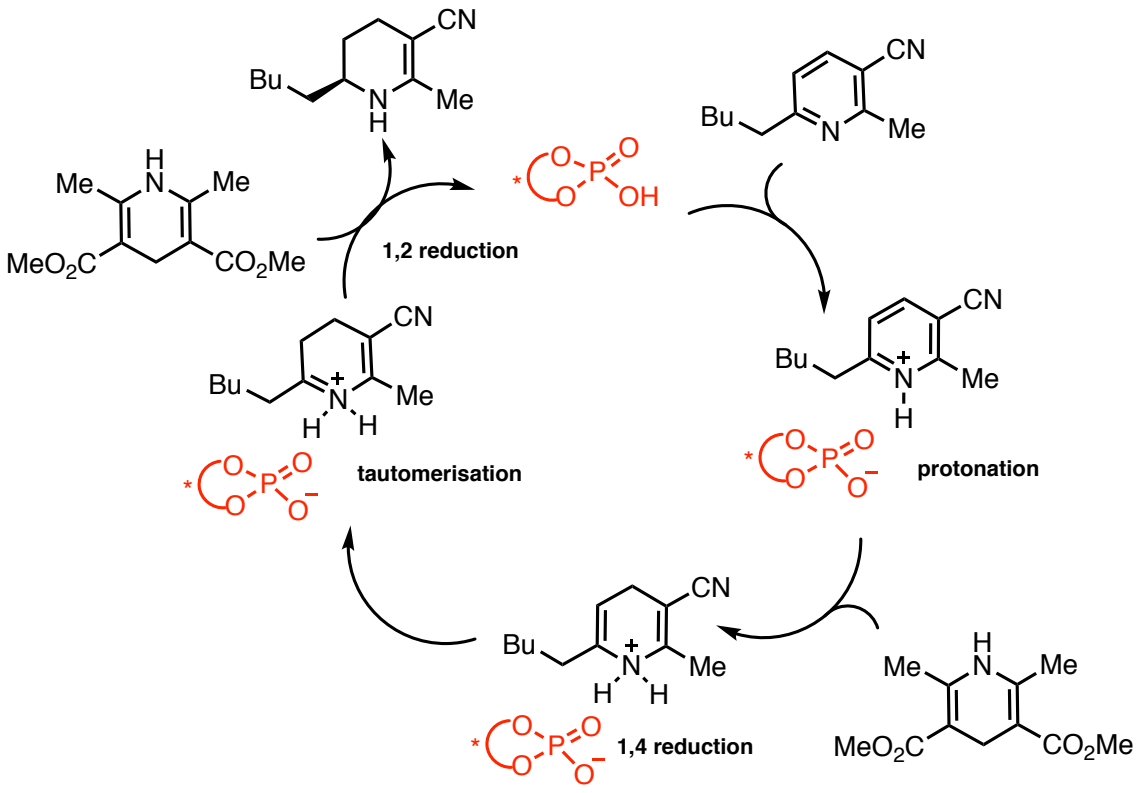

Figure 3.9. Proposed mechanism for the phosphoric acid catalysed reduction of pyridines. The Hantzsch ester and pyridine are both activated by the chiral phosphoric acid catalyst.

For the phenyl-derived phosphoric acid catalysed reaction the lowest calculated transition state is **TS5** (*Type II*), which is in good agreement with the experimentally observed outcome. For the 9-anthryl-derived phosphoric acid catalysed reaction the lowest energy transition state is **TS7** (*Type I*), which accounts for the experimentally observed reversal in stereoinduction. The results are summarized in Figure 3.10, below. Although the calculated energy values are overestimated than compared to experiment (computed ee -99%), the reproduction of qualitative trends is accurately predicted. The ONIOM (M06-2X/6-31G**:UFF) method indicates that the discrepancy between calculation and experiment traces back to the B3LYP component of the optimization in line with my findings from the transfer hydrogenation study in section 3.2. ONIOM (M06-2X/6-31G**:UFF) gave a smaller preference for the *Type II* pathway than ONIOM (B3LYP/6-31G**:UFF). The energy difference between **TS5** and **TS6** re-evaluated using ONIOM (M06-2X/6-31G**:UFF), Table 3.3, was calculated to be 0.7 kcal mol^{-1} (computed ee -48%). Both *Type I* and *Type II* reaction pathways followed different arrangements on comparing the catalysts. On analysing the TS pathways with varying 3,3' substituent the most important difference is the absolute location of the reagents with respect to the 3,3' substituents. In **TS6** (*Type II*) small proximal bulk creates a large cone of empty space at the front right hand side of the catalyst which can accommodate the cyclic imine, the butyl substituent is pointed away from the front of the 3,3' and the Hantzsch ester experiences little steric hindrance from the catalyst. A similar lack of steric interactions between imine and catalyst is present in **TS5** (*Type I*) but due to the increased steric interactions between the phenyl catalyst substituent and the Hantzsch ester leads to a preference for **TS6**. Increasing the proximal catalyst sterics increases the steric interactions between the cyclic imine and the 3,3' group forcing the imine to adopt a tilted disposition, **TS8**. The increased steric interactions destabilises the *Type II* pathway relative to *Type I*, which allows placing most of the substrate steric bulk furthest away from the catalyst. The catalyst entries 6 and 7 (Figure 3.8) present similar proximal steric environments but yet the enantioselectivities are very different. I explored a potential source of this systematic error and the results are summarised in Figure 3.11. On calculation of the TS using these additional two catalysts I found that ONIOM (M06-2X/6-31G**: UFF) leads to consistent agreement between experiment and calculation. Table 3.3 shows an energy comparison of both ONIOM methods with all four catalysts tested. Comparing both ONIOM methods by superposition using the ASL feature in Macromodel calculated the RMSD to be less than 0.2 Å for most TS structures. A larger variation was calculated for the 9-phenanthryl *Type II* TS with an RMSD of 0.5 Å. Despite this structural change the energy difference between the TS leading to competing products catalysed by 9-phenanthryl

derived phosphoric acid remained consistent between the methods. Further inspection of the structural features showed that for **TS10** in order to bind the substrate the P-OH bond angle has been widened to 147°, far from the ideal. This suggests that the reagents are a less ideal fit for the binding pocket of the catalyst. Despite these deviations, the energy difference between the TS leading to competing products is only 0.2 kcal mol^{-1}, which suggests there are stronger stabilising interactions between the substrate and catalyst. I calculated the reduced density to assess the non-covalent interactions between reactants and catalyst. All TS using both catalysts show similar features, multiple CH-π interactions between reagents, the 3,3' group and the BINOL backbone. **TS12,** shows the alkyl chain rotated away from catalyst; **TS10** shows it rotated towards the catalyst, reminiscent of the *Type I* TS. The alkyl group when in close proximity can establish CH-O bonds to the phosphate stabilising the fleeting negative charge. The distances between the hydrogens of the alkyl group and the oxygen of the phosphate are shorter in **TS10** (2.39 Å, 2.46 Å and 2.64 Å) compared to **TS12** (2.44 Å, 2.52 Å and 2.74 Å) shown in Figure 3.12. **TS12** has the shortest hydrogen bond length between the substrate and catalyst. This can promote a stronger attractive interaction between the substrate and phenanthryl group as indicated by a NCI plot, but the alkyl group now has to rotate away from the catalyst to adopt the appropriate geometry. In summary the discrepancy between the computed catalyst parameters and enantioselectivity is a result of an electronic effect. The *Type II* TS using the 1-naphthyl catalyst is lower in energy than expected because of greater stabilisation of the developing negative charge on the catalyst by the alkyl group. The alkyl group of the substrate in the *Type II* TS pathway using the phenanthryl catalyst is rotated away from the phosphate, causing the distances between the hydrogens of the alkyl group and the phosphate to be longer. It is clear that this electronic effect is substrate specific and in most cases, of the two stereocontrol elements, the enantioselectivity is primarily steric in origin and the steric model works exceptionally well (Table 3.4). The counter-intuitive inferior enantioselectivity obtained with 1-napthtyl derived phosphoric acid underscores the importance of systematic electronic-tuning of these catalysts and the possible incorporation of an electronic parameter into the correlation analysis.

.

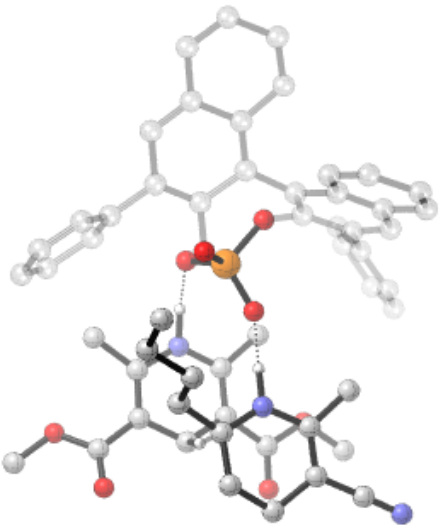

TS5: $\Delta\Delta G^{\ddagger} = 0$ kcal mol^{-1}, $\Delta\Delta G_{sol}^{\ddagger} = 0$ kcal mol^{-1}

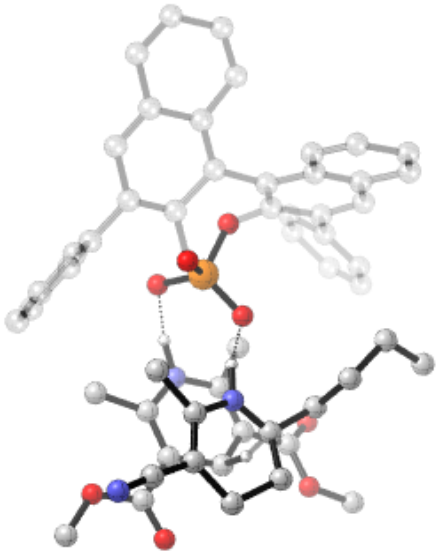

TS6: $\Delta\Delta G^{\ddagger} = +3.5$ kcal mol^{-1}, $\Delta\Delta G_{sol}^{\ddagger} = +3.9$ kcal mol^{-1}

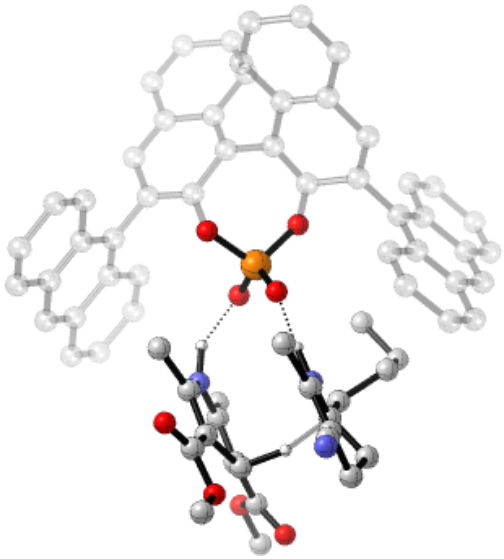

TS7: $\Delta\Delta G^{\ddagger} = 0$ kcal mol^{-1}, $\Delta\Delta G_{sol}^{\ddagger} = 0$ kcal mol^{-1}

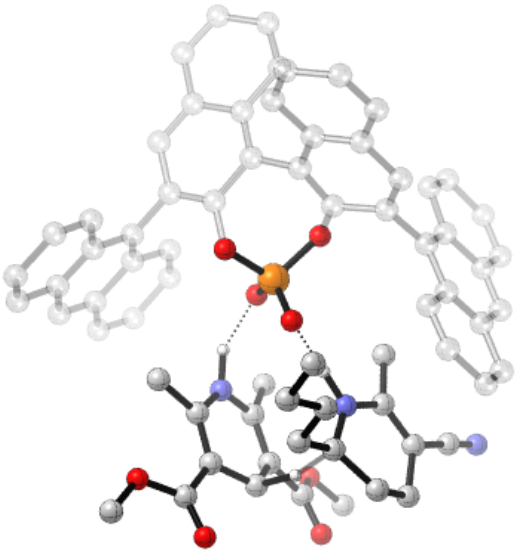

TS8: $\Delta\Delta G^{\ddagger} = +3.5$ kcal mol^{-1}, $\Delta\Delta G_{sol}^{\ddagger} = +3.6$ kcal mol^{-1}

Figure 3.10. Competing TS for the 9-anthryl and phenyl derived phosphoric acid catalysed transfer hydrogenation reaction of cyclic imines. ONIOM (B3LYP/6-31G**: UFF), single-point energy M06-2X/6-31G**. Grayed-out regions were treated with UFF, and the full-colour regions were treated B3LYP/6-31G**.

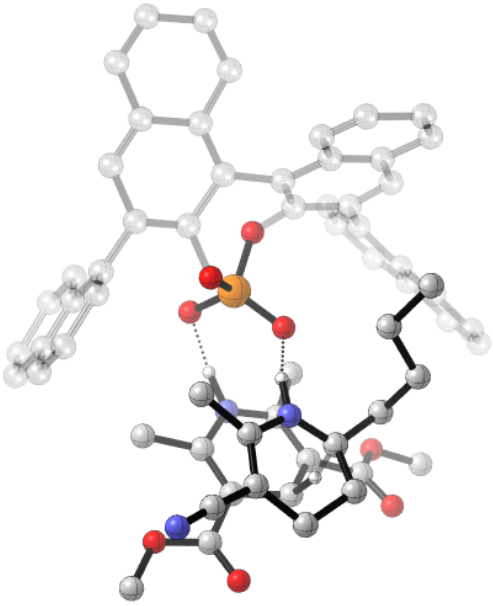

TS9: $\Delta\Delta G^{\ddagger} = 0$ kcal mol^{-1}, $\Delta\Delta G_{sol}^{\ddagger} = 0$ kcal mol^{-1}

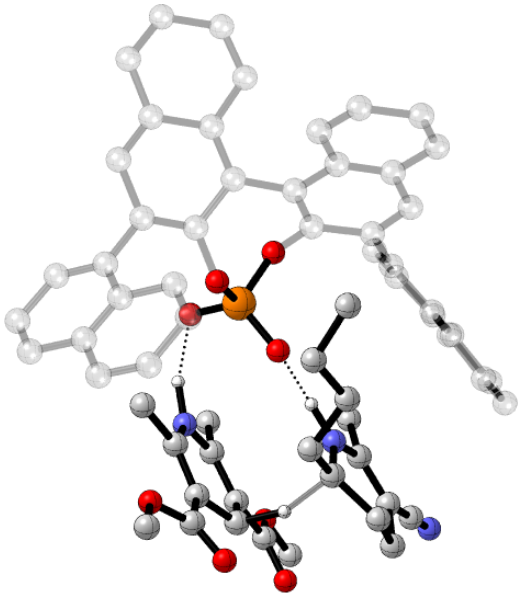

TS10: $\Delta\Delta G^{\ddagger} = 0$ kcal mol^{-1}, $\Delta\Delta G_{sol}^{\ddagger} = +0.8$ kcal mol^{-1}

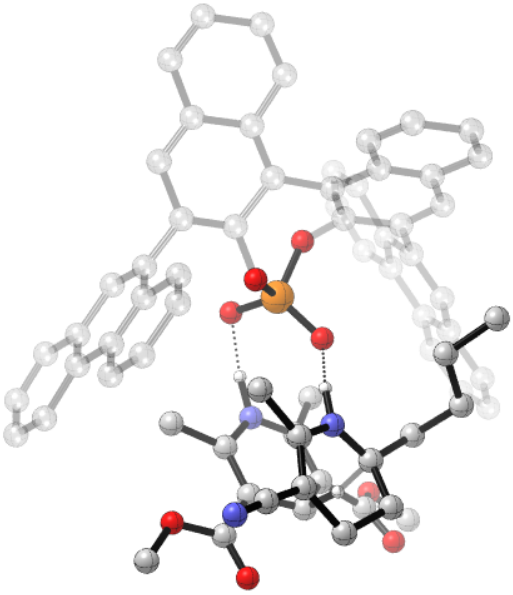

TS11: $\Delta\Delta G^{\ddagger} = 0$ kcal mol^{-1}, $\Delta\Delta G_{sol}^{\ddagger} = 0$ kcal mol^{-1}

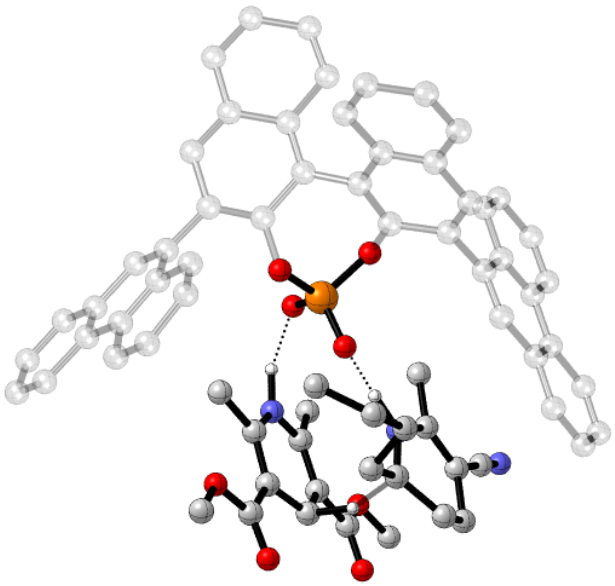

TS12: $\Delta\Delta G^{\ddagger} = +0.6$ kcal mol^{-1}, $\Delta\Delta G_{sol}^{\ddagger} = +1.0$ kcal mol^{-1}

Figure 3.11. Competing TS for the 1-naphthyl and 9-phenanthryl derived phosphoric acid catalysed transfer hydrogenation reaction of cyclic imines. ONIOM (B3LYP/6-31G**: UFF), single-point energy M06-2X/6-31G**. Grayed-out regions were treated with UFF, and the full-colour regions were treated B3LYP/6-31G**.

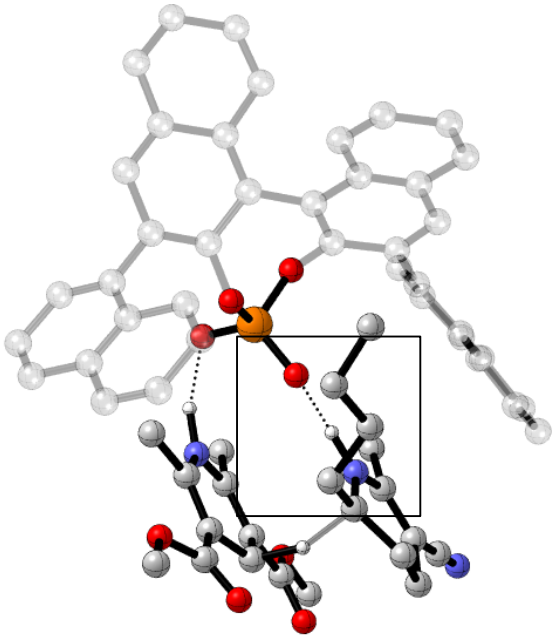

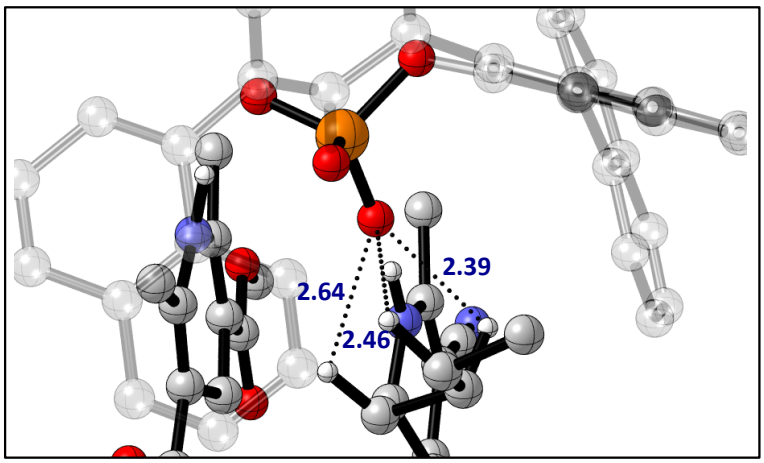

TS10

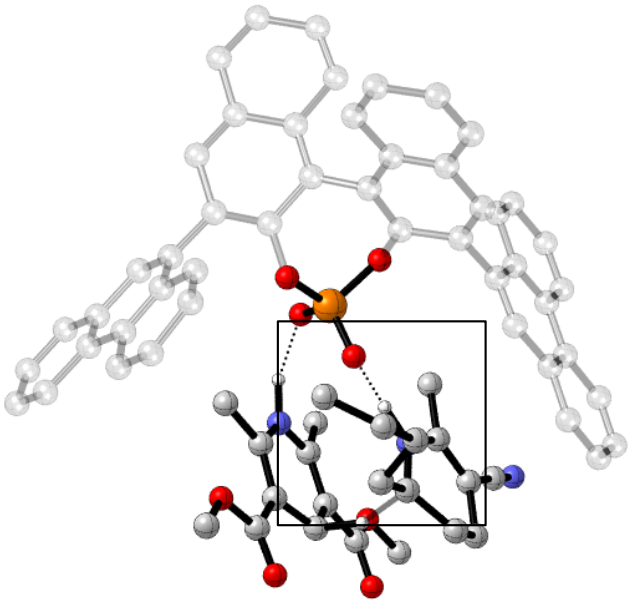

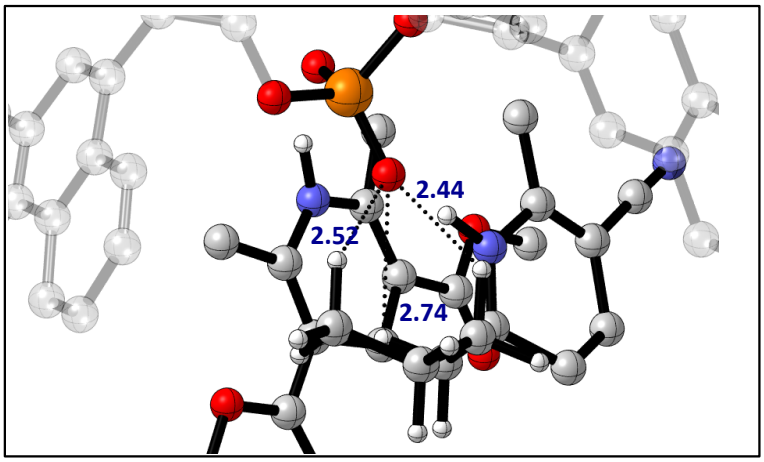

TS12

Figure 3.12. ONIOM (B3LYP/6-31G**: UFF) *Type II* TS structures using both the 1-naphth (top) and 9-phenanthryl (bottom) derived phosphoric acid catalysed transfer hydrogenation reaction of cyclic imines.

Table 3.3. Comparison of the relative energies derived from both ONIOM methods. All energies in kcal mol^{-1} relative to *Type I.*

	ONIOM (B3LYP/6-31G**:UFF)		ONIOM (M06-2X/6-31G**:UFF)	
Mechanism (Catalyst)	$\Delta\Delta G^{\ddagger}$	$\Delta\Delta G_{sol}{}^{\ddagger}$	$\Delta\Delta G^{\ddagger}$	$\Delta\Delta G_{sol}{}^{\ddagger}$
Type I (Ph), **TS6**	0	0	0	0
Type II (Ph), **TS5**	-3.5	-3.9	-0.7	-1.6
Type I (9-anthryl), **TS7**	0	0	0	0
Type II (9-anthryl), **TS8**	+3.5	+3.6	+3.6	+3.9
Type I (9-phenanthryl), **TS11**	0	0	0	0
Type II (9-phenanthryl), **TS12**	+0.6	+1.0	+1.1	+0.8
Type I (1-naphthyl), **TS9**	0	0	0	0
Type II (1-naphthyl), **TS10**	0	+0.8	+0.5	-0.2

Table 3.4. Examples of cyclic imines reduced by Hantzsch ester catalysed by chiral phosphoric acids. All energies in kcal mol^{-1}. For each catalyst classification, I have chosen to compare the best performer from the catalyst screen of a model substrate under the same reaction conditions.

Substrate	Rotation Barrier <3 (ee%)	Medium Rotation Barrier (ee%)	Rotation Barrier >26 (ee%)
Benzoxazine[203]	36	81	94
Indoles[204]	42	72	97
Quinoxalines[205]	10	64	90
3-(Trifluoromethyl)quinolones[206]	-35	72	97

Based on these investigations I hypothesized that increasing the steric profile at the 2 and 6 positions of the aromatic ring would lead to a catalyst displaying superior enantioselectivity. To test this, calculations were performed on 9-anthryl, and a 2,6-^{t}Bu catalyst with a truncated imine substrate. The calculations suggest that 9-anthryl derived phosphoric acid will be moderately selective for the reduction of this particular pyridine substrate. The imine now experiences very little steric repulsion from the large 9-anthryl substituents in the *Type II* pathway lowering the energy of this relative to the *Type I*. Moving to the 2,6-^{t}Bu catalyst leads to a large increase in energy between the pathways leading to competing products. This is a consequence of increased steric repulsion between the imine and the large *t*-Bu groups. The beneficial effect of large proximal substituents on the catalyst demonstrates once again the generality of the model. The calculations suggest that a large group on the carbon atom that is being reduced is a necessity for high levels of enantioinduction with commercial catalysts. Such high substrate specificity limits the potential applications of this method to the construction of a small set of cyclic substrates. In this regard, the 2,6-^{t}Bu catalyst has shown great promise to achieve high selectivity with challenging substrates but the difficult synthesis may prevent this catalyst from being useful.[207]

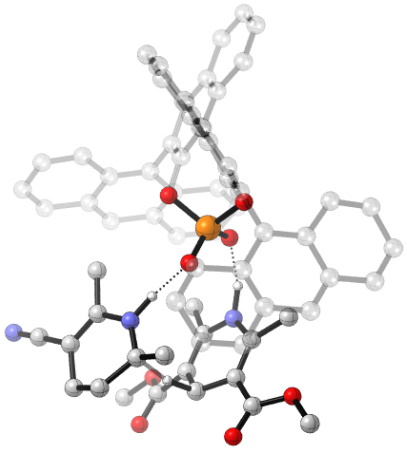

TS13: $\Delta\Delta G^{\ddagger} = 0$ kcal mol^{-1}, $\Delta\Delta G_{sol}^{\ddagger} = 0$ kcal mol^{-1}

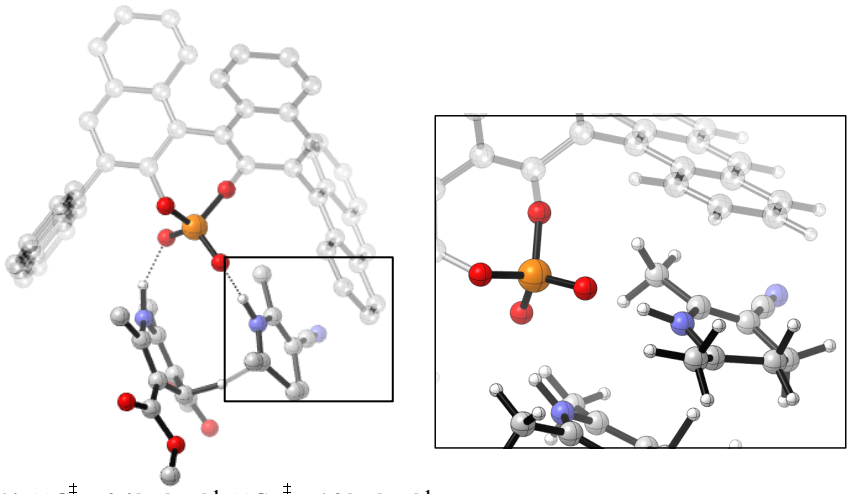

TS14: $\Delta\Delta G^{\ddagger} = +0.6$ kcal mol^{-1}, $\Delta\Delta G_{sol}^{\ddagger} = -1.9$ kcal mol^{-1}

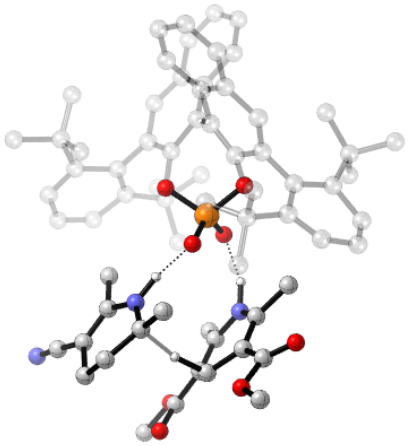

TS15: $\Delta\Delta G^{\ddagger} = 0$ kcal mol^{-1}, $\Delta\Delta G_{sol}^{\ddagger} = 0$ kcal mol^{-1}

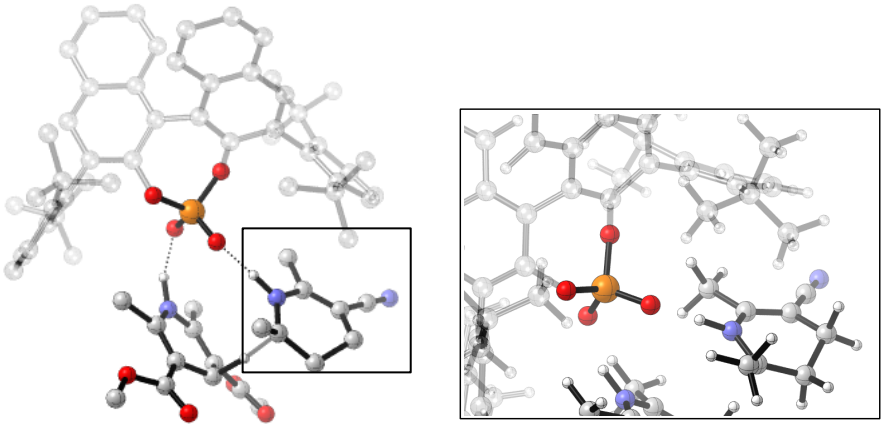

TS16: $\Delta\Delta G^{\ddagger} = +2.5$ kcal mol^{-1}, $\Delta\Delta G_{sol}^{\ddagger} = +2.5$ kcal mol^{-1}

Figure 3.13. Competing TS for the 9-anthryl and 2,6-tBu derived phosphoric acid catalysed transfer hydrogenation reaction of cyclic imines. ONIOM (B3LYP/6-31G**: UFF), single-point energy M06-2X/6-31G**. Grayed-out regions were treated with UFF, and the full-colour regions were treated B3LYP/6-31G**.

3.4 Hydrophosphonation of Acyclic Imines

As previously stated my goal was to create a model capable of directing catalyst selection, and therefore reduce time-consuming empirical screening processes. To assess the potential of this model on a challenging reaction, I explored the hydrophosphorylation of imines.[29] The title reaction was an early example of a transformation catalysed by phosphoric acids. At that time little was known about the requirements for high enantioselectivity as such highly selective and versatile catalysts were scarce. Despite this Akiyama *et al.* showed α-amino phosphonates could be obtained in moderate selectivities using a chiral phosphoric acid catalyst, **CPA-1** (Figure 3.14). The authors suggested the reaction proceeds *via* a *Type I E* TS pathway and based on thorough mechanistic work I believed that the enantioselectivty of the transformation could be further improved by manipulating the substituent structure at the 3,3' position. I hypothesized based on the model (Figure 3.7) that TRIP would be a suitable catalyst. To test this theory, TS were located with both catalysts and the relative energies compared. Consistent with expectation, the energy differences between the pathways leading to competing products increased with the TRIP catalyst. The results of the computational study are summarised in Figures 3.15 and 3.16.

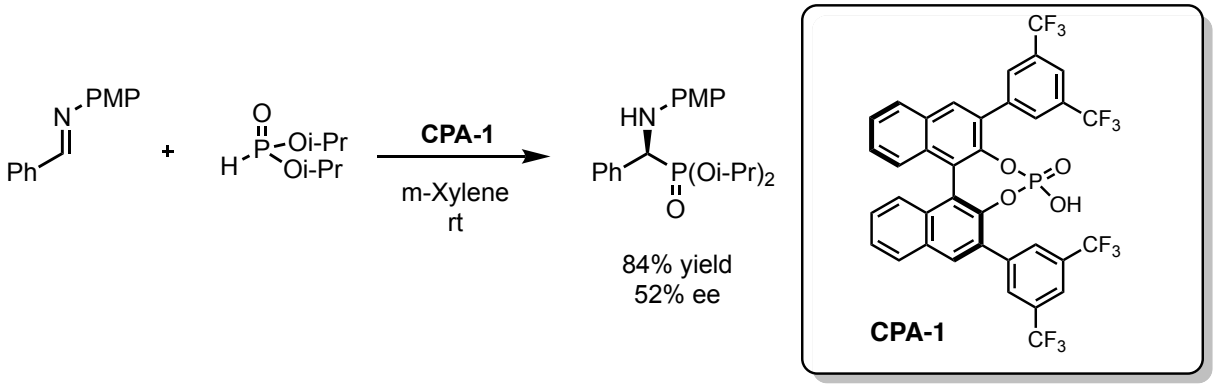

Figure 3.14. Moderate enantioselectivity obtained with Akiyama's hydrophosphonation using **CPA-1**.

For the 3,5-$CF_3C_6H_3$ derived phosphoric acid, **CPA-1**, catalysed reaction the lowest calculated transition state is **TS18-*E*** (*Type I E*), which is in good agreement with the experimentally observed outcome (computed ee 56%). The *Z* pathways were higher in energy due to the internal substrate steric interactions and the directly competing one was that of the alternative imine orientation, *Type II E*. The reduced steric profile of the nucleophile and the 3,3' substituents allows the imine to be placed parallel to the 3,3' groups. This tilted disposition of the imine greatly reduces the steric interactions with the catalyst lowering the energy of the *Type II E* pathway, accounting for the small energy difference, 0.9 kcal mol^{-1}, between the competing pathways. Increasing the steric bulk of the 3,3' groups increases the steric interactions between the reagents. The nucleophile adopts a different position within the catalyst cavity and this shifting distorts the parallel arrangement of the imine leading to greater steric interactions between the catalyst, resulting in, raising the energy of the *Type II E* pathway relative to the *Type I E* (Figure 3.16).

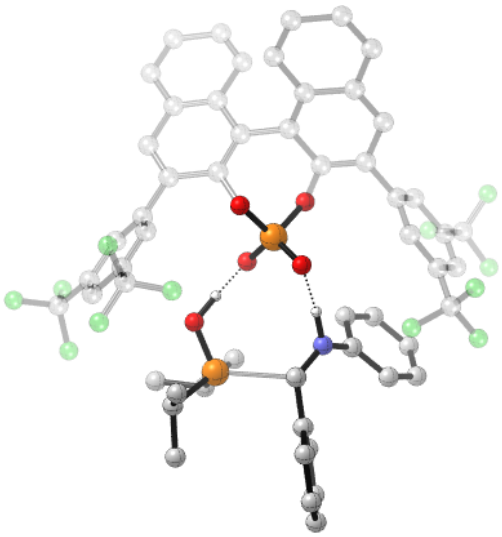

TS17-*Z*: $\Delta\Delta G^{\ddagger}$= +4.8 kcal mol^{-1}, $\Delta\Delta G_{sol}^{\ddagger}$= +3.5 kcal mol^{-1}

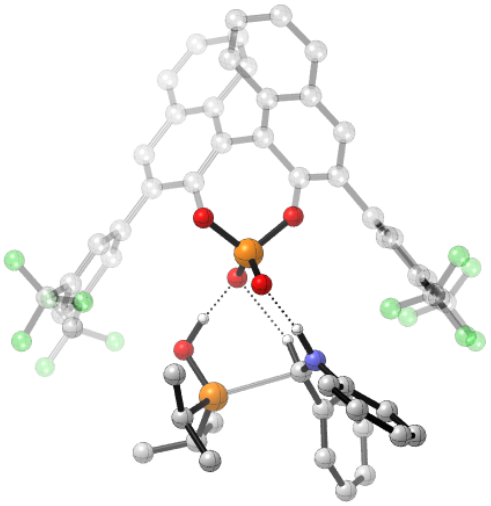

TS18-*Z*: $\Delta\Delta G^{\ddagger}$= +4.8 kcal mol^{-1}, $\Delta\Delta G_{sol}^{\ddagger}$= +3.6 kcal mol^{-1}

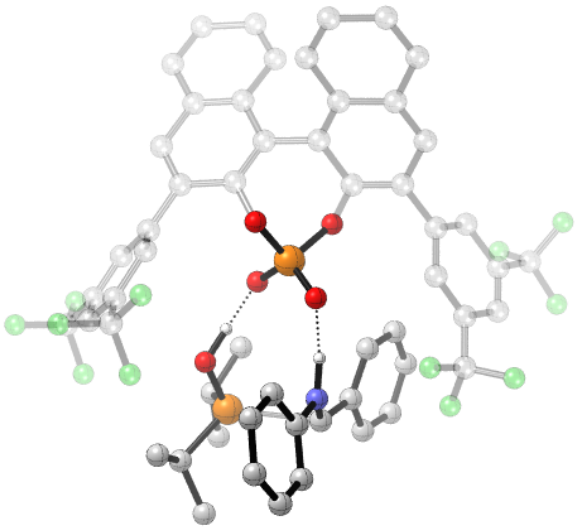

TS18-*E*: $\Delta\Delta G^{\ddagger}$= 0 kcal mol^{-1}, $\Delta\Delta G_{sol}^{\ddagger}$= 0 kcal mol^{-1}

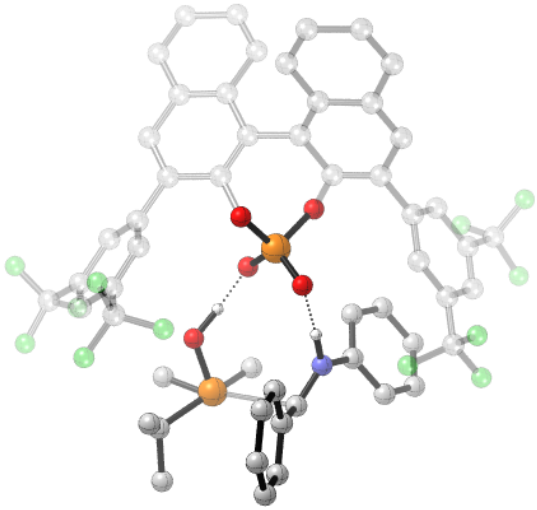

TS17-*E*: $\Delta\Delta G^{\ddagger}$= +0.9 kcal mol^{-1}, $\Delta\Delta G_{sol}^{\ddagger}$= +0.1 kcal mol^{-1}

Figure 3.15. Competing TS for 3,5-$CF_3C_6H_4$ derived phosphoric acid catalysed phosphorylation of imines. ONIOM (B3LYP/6-31G**: UFF), single-point energy M06-2X/6-31G**. Grayed-out regions were treated with UFF, and the full-colour regions were treated B3LYP/6-31G**.

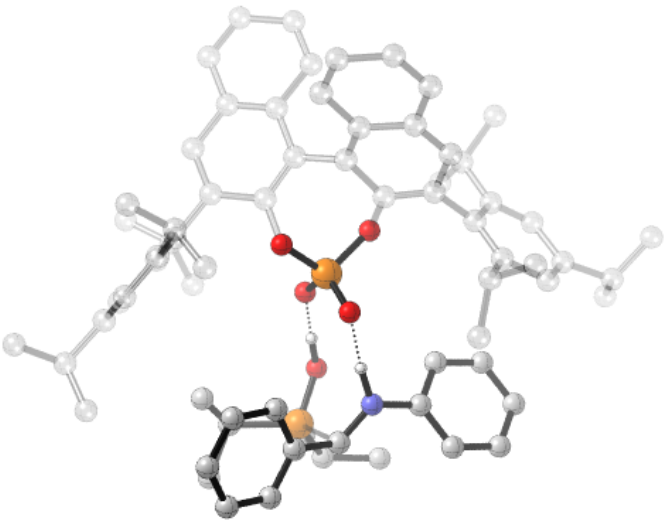

TS19-*E*: $\Delta\Delta G^{\ddagger}$ = +3.3 kcal mol^{-1}, $\Delta\Delta G_{sol}^{\ddagger}$ = +3.4 kcal mol^{-1}

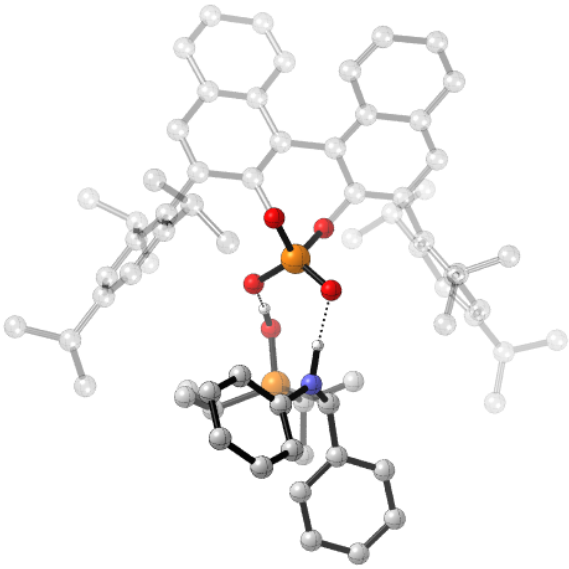

TS20-*Z*: $\Delta\Delta G^{\ddagger}$ = +4.7 kcal mol^{-1}, $\Delta\Delta G_{sol}^{\ddagger}$ = +4.4 kcal mol^{-1}

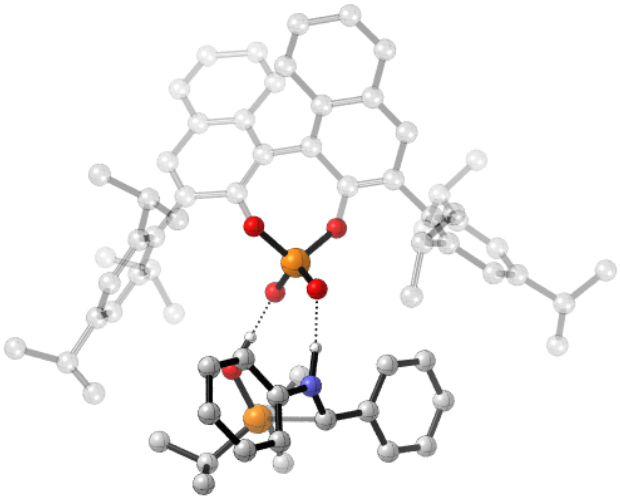

TS20-*E*: $\Delta\Delta G^{\ddagger}$ = 0 kcal mol^{-1}, $\Delta\Delta G_{sol}^{\ddagger}$ = 0 kcal mol^{-1}

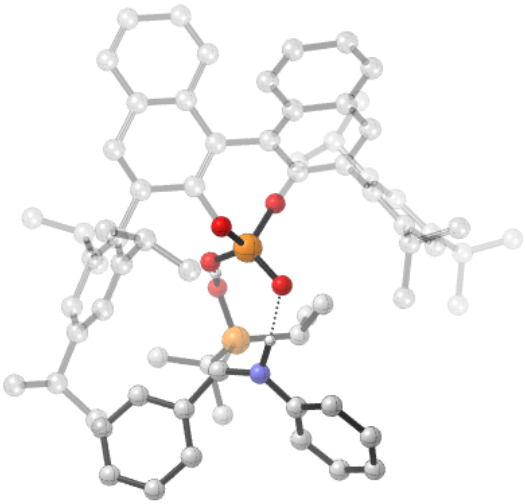

TS19-*Z*: $\Delta\Delta G^{\ddagger}$ = +2.8 kcal mol^{-1}, $\Delta\Delta G_{sol}^{\ddagger}$ = +2.2 kcal mol^{-1}

Figure 3.16. Competing TS for the TRIP phosphorylation of imines. ONIOM (B3LYP/6-31G**: UFF), single-point energy M06-2X/6-31G**. Grayed-out regions were treated with UFF, and the full-colour regions were treated B3LYP/6-31G**.

3.5 Conclusions

In conclusion, by applying the quantitative steric parameters developed in Chapter 2 I can now easily determine the effect of catalyst 3,3' substituent structure on enantioselectivity. Reactions involving acyclic imines and symmetrical nucleophiles show a heavy dependence on both remote and proximal sterics The correct catalyst for a reaction of such, is one that has large proximal sterics and medium AREA(θ).

Since cyclic imines can only exist in the *Z* configuration only proximal sterics should affect the level of enantioinduction to an appreciable extent. While the lack of enantioselectivity dependence on rotation barrier with the 1-naphthyl derived phosphoric acid indicates a more complicated relationship of catalyst and substrate structure with enantioselectivity than my initial hypothesis. In general, the steric model works exceptionally well showing the optimal catalyst is one that has proximally large sterics. Based on these observations, increasing the steric profile of the substituents proximal to the phosphoric acid, such as 2,6-^{t}Bu, offer promising possibilities for extending the scope of this reaction class.

Chapter 4

4 Stereochemical Role of 3,3' groups: Displaced Nucleophiles

4.1 Background and Methods

Having previously explored the application of the AREA(θ) and rotation barrier as parameters to explain selectivity patterns in the reactions involving the addition of symmetrical nucleophiles to imines,[41] I wished to expand this method to displaced nucleophiles. This particular class of nucleophiles are known to prefer a *Type II* pathway in which the imine adopts a different position inside the catalyst pocket. Since the orientation of the imine dictates which molecular features on the catalyst to be important, I expected the catalyst influence to be different. Recent studies support this hypothesis showing that small AREA(θ) catalysts can lead to high enantioselectivities with *Type I E* reaction pathways but only when combined with displaced nucleophiles (Figure 4.1).[147] Such an observation cannot be explained using the previous model in section 3.2.

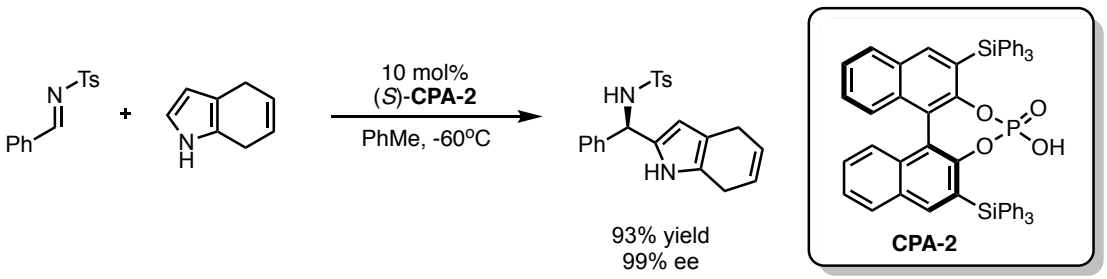

Figure 4.1. Asymmetric Friedel-Crafts reaction proceeding *via* a *Type I E* TS pathway leads to high enantioselectivities with small AREA(θ) catalysts.

Our group has studied the addition of displaced nucleophiles to imines and have determined that the addition of enols and enamides generally proceed *via Type II*, whereas the addition of indoles can be either *Type I*, or *Type II*, in which the preference is modulated by the size of the N-substituent.[37] Our previous study, the transfer hydrogenation of α,β-iminoesters have shown that the inherent steric factors of the reactants dictating the pathway in operation can be outweighed by the catalyst steric environment. The physical underlying basis for catalyst behaviour for this reaction class had yet to be determined.

I wanted to explore the application of my parameters to reactions that proceeded predominantly *via Type II* TS pathways. Developing an improved understanding of the selectivity should not only facilitate a consistent picture into the effect of the 3,3' with all nucleophilic additions to imines but it may also guide catalyst choice for reactions employing complex substrates. To investigate the role of the catalyst in these reactions I choose to study the Friedel-Crafts and addition of enamides as model reactions. These were selected primarily because of the wealth of data that had been complied and the appropriate catalyst screening results were already in place.

The calculations were performed using the general method described previously, in Chapter 3. Free energies in solution were derived from structures optimized in the gas phase at the ONIOM (B3LYP/6-31G**:UFF), level of theory by means of a single point calculation using M06-2X/6-31G** with the polarizable continuum model (PCM) as implemented in the Jaguar program (version 7.9), DCM (probe radius = 2.33 Å) for the Friedel-Crafts study and toluene (probe radius = 2.76 Å) for the addition of enamides, as the solvent.[50] These values were used to correct the Gibbs free energy derived from the ONIOM calculations. The quantitative parameters were calculated as described previously in Chapter 2. Structures are illustrated using CYLview.[196]

4.2 Friedel-Crafts

In 2007, Zhou reported an efficient protocol for the Friedel-Crafts reaction of N-acetyl imines.[28] The catalyst screen showed a similar "Goldilocks" effect, as previously observed with the transfer hydrogenation study in section 3.2, in which the correct catalyst is one that is not too small or too large but somewhere in between (Figure 4.2). Experimentally, it was found that large proximal sterics were required for high levels of enantioselectivity. To understand the reasons for poor selectivity at both ends of the steric spectrum, and the requirement for large proximal sterics, the mechanism was investigated computationally. Transition states for the full catalyst system were located using the general method described above, the results are summarised in Figures 4.3, 4.4 and 4.5.

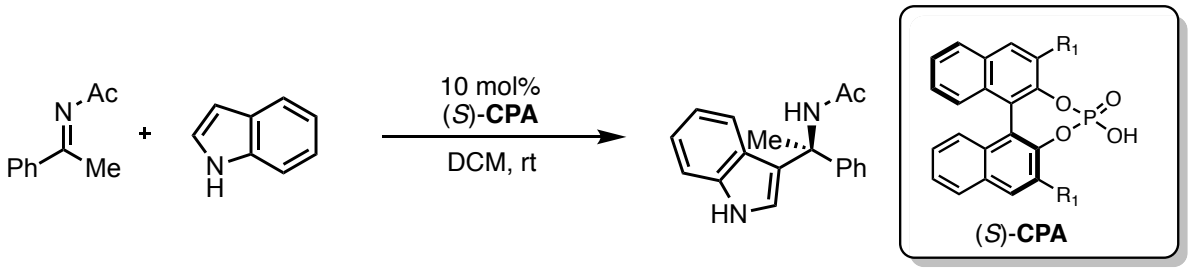

Entry	Catalyst R_1	AREA (θ)	Rotation Barrier (kcal mol^{-1})	ee (%)
1	H	107	0.00	4
2	Ph	70	2.05	32
3	3,5-$(CF_3)_2C_6H_4$	62	2.02	38
4	9-anthryl	61	28.31	66
5	***2,4,6-(^{i}Pr)$_3$C$_6$H$_3$***	***51***	***28.40***	***91***
6	***4-PhC$_6$H$_4$***	***50***	***2.01***	***35***
7	2-naphth	49	2.13	10
8	9-phenanthryl	48	14.45	22
9	3,5-(^{t}Bu)$_2$C$_6$H$_4$	41	2.65	72
10	***SiPh$_3$***	***29***	***1.35***	***25***

Figure 4.2. Effect of 3,3' groups on the enantioselectivity of the Friedel Crafts reaction.

For all catalysts investigated the lowest energy TS pathway was *Type II E*, which is in good agreement with sense of stereoinduction observed by experiment. The *Z* pathways were higher in energy due to the internal steric interactions between the largest substituents. Changing the 3,3' substituents from 2,4,6-triisopropylphenyl (medium AREA(θ)) to $SiPh_3$ (small AREA(θ)) leads to a 1.4 kcal mol^{-1} decrease in energy between the *Type II E* and the *Type I E* TS pathways, which translates experimentally to low levels of enantioselectivity. Visual inspection of the *Type II E* TS in Figures 4.3 and 4.4 shows that the indole pushes towards the imine forcing the benzene into free space, leaving empty space at the back right hand side of the catalyst. The imine N-substitutent is placed in this empty catalyst pocket, with this in combination with a tilted disposition allows the large phenyl group to be placed furthest away from the catalyst bulk. Increasing the sterics remote from the phosphoric acid increases the steric interactions between the N-substituent and the 3,3' group. This leads to a large energetic penalty and increases the energy of the *Type II* TS relative to that of the *Type I* (Figure 4.4). Proximal sterics were determined experimentally to be necessary for efficient stereoinduction, but it was not altogether clear how this catalyst feature imparted such strong enantioselectivity. Calculations on a 4-biphenyl derived phosphoric acid showed that the catalyst created empty space at the front and therefore reduces the effect of the phenyl group leading to a reduction in the energetic preference for the *Type II* TS (Figure 4.5). This serves to explain the discrepancies in selectivity between catalysts with similar distal bulk but varying proximal bulk. This physical factor is not explicitly accounted for by the ligand AREA(θ) but can be described by a proximal bulk steric parameter, such as the rotation barrier.

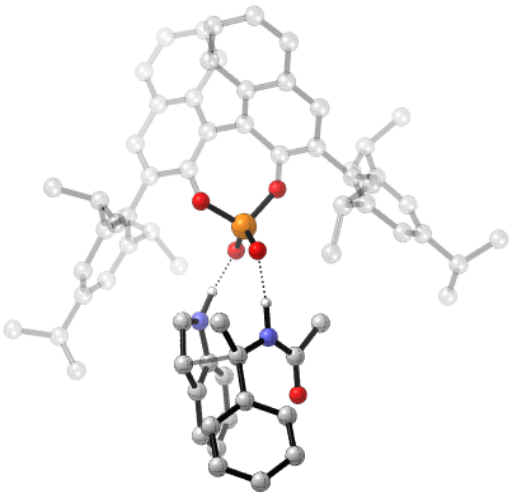

TS21-*Z*: $\Delta\Delta G^{\ddagger}$ = +3.1 kcal mol^{-1}, $\Delta\Delta G_{sol}^{\ddagger}$ = +3.2 kcal mol^{-1}

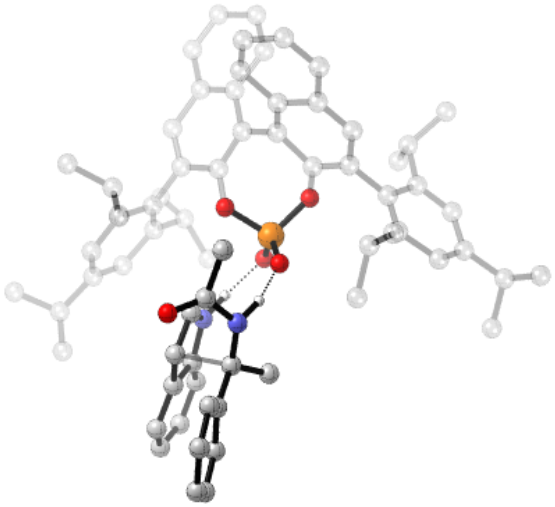

TS22-*Z*: $\Delta\Delta G^{\ddagger}$ = +3.9 kcal mol^{-1}, $\Delta\Delta G_{sol}^{\ddagger}$ = +4.1 kcal mol^{-1}

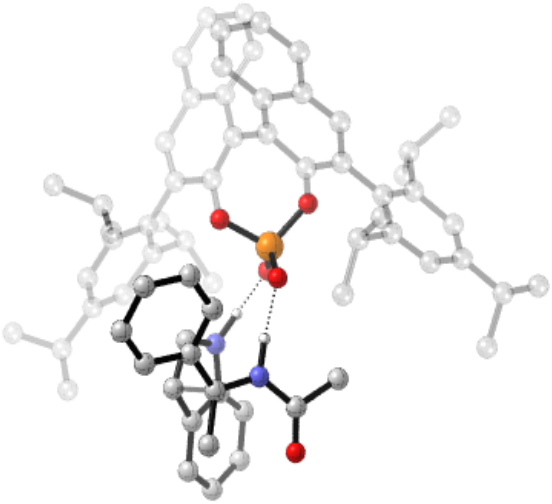

TS21-*E*: $\Delta\Delta G^{\ddagger}$ = 0 kcal mol^{-1}, $\Delta\Delta G_{sol}^{\ddagger}$ = 0 kcal mol^{-1}

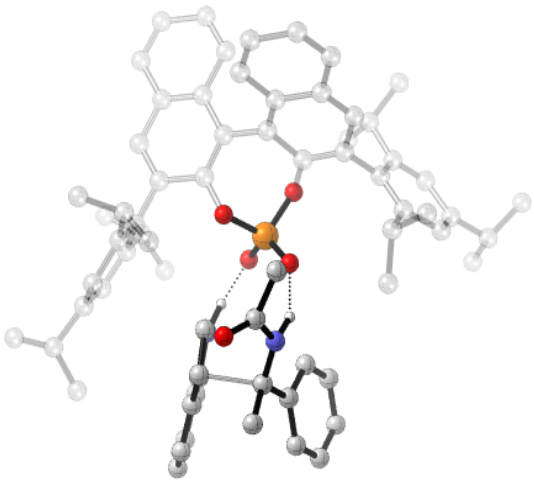

TS22-*E*: $\Delta\Delta G^{\ddagger}$ = +1.3 kcal mol^{-1}, $\Delta\Delta G_{sol}^{\ddagger}$ = +1.7 kcal mol^{-1}

Figure 4.3. Competing TS for the TRIP catalysed Friedel-Crafts. ONIOM (B3LYP/6-31G**:UFF), single-point energy M06-2X/6-31G**. Grayed-out regions were treated with UFF, and the full-colour regions were treated B3LYP/6-31G**.

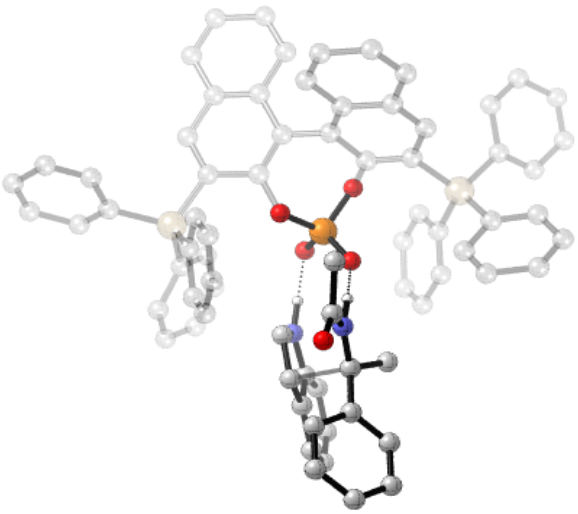

TS24-*Z*: $\Delta\Delta G^{\ddagger}$= +4.5 kcal mol^{-1}, $\Delta\Delta G_{sol}^{\ddagger}$= +3.2 kcal mol^{-1}

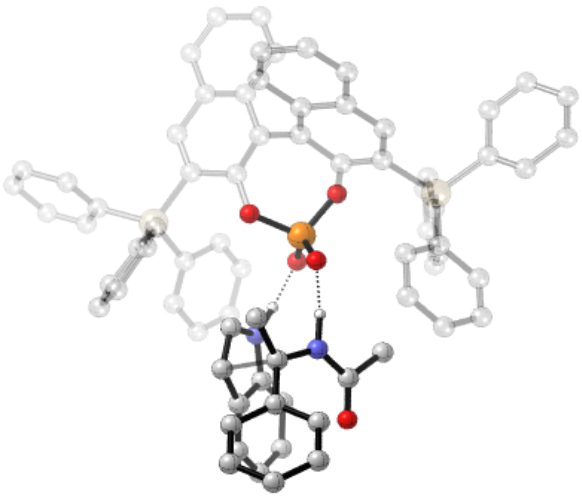

TS23-*Z*: $\Delta\Delta G^{\ddagger}$= +5.8 kcal mol^{-1}, $\Delta\Delta G_{sol}^{\ddagger}$= +5.0 kcal mol^{-1}

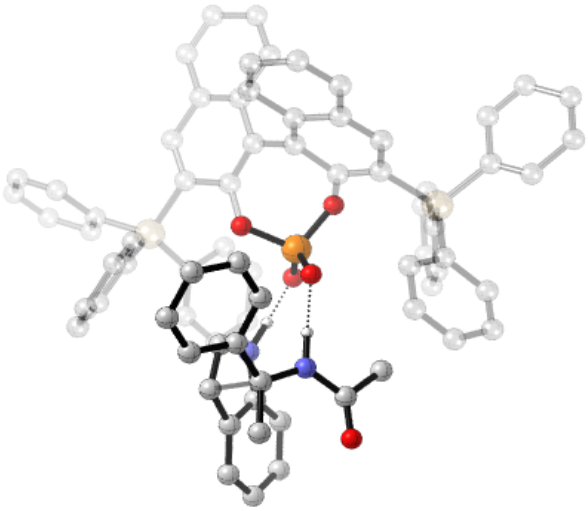

TS23-*E*: $\Delta\Delta G^{\ddagger}$= 0 kcal mol^{-1}, $\Delta\Delta G_{sol}^{\ddagger}$= 0 kcal mol^{-1}

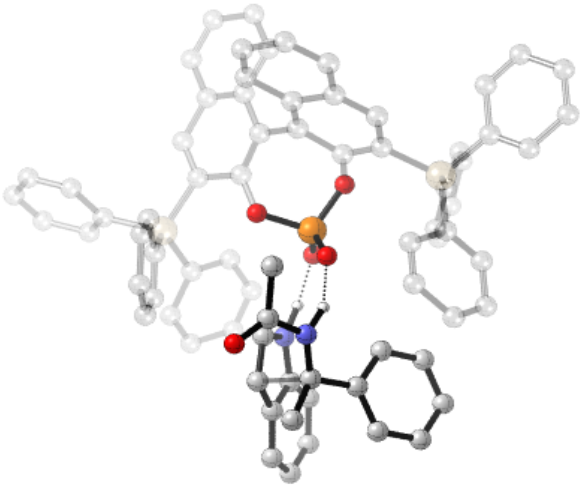

TS24-*E*: $\Delta\Delta G^{\ddagger}$= -0.8 kcal mol^{-1}, $\Delta\Delta G_{sol}^{\ddagger}$= +0.3 kcal mol^{-1}

Figure 4.4. Competing TS for the $SiPh_3$ derived phosphoric acid catalysed Friedel-Crafts. ONIOM (B3LYP/6-31G**:UFF), single-point energy M06-2X/6-31G**. Grayed-out regions were treated with UFF, and the full-colour regions were treated B3LYP/6-31G**.

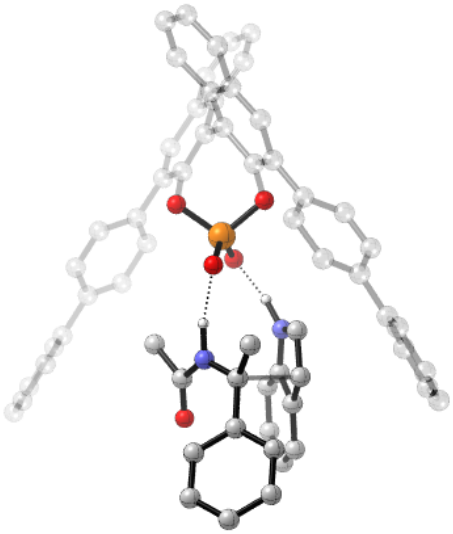

TS26-*Z*: $\Delta\Delta G^{\ddagger}$ = +4.8 kcal mol^{-1}, $\Delta\Delta G_{sol}^{\ddagger}$ = +3.4 kcal mol^{-1}

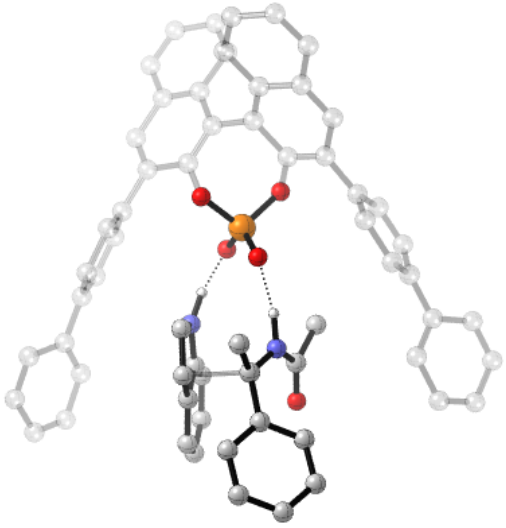

TS25-*Z*: $\Delta\Delta G^{\ddagger}$ = +6.1 kcal mol^{-1}, $\Delta\Delta G_{sol}^{\ddagger}$ = +4.3 kcal mol^{-1}

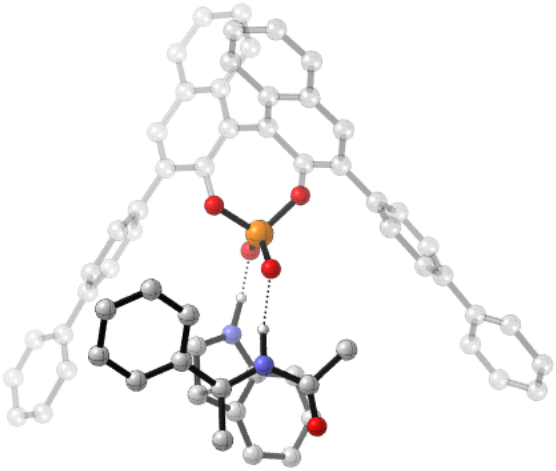

TS25-*E*: $\Delta\Delta G^{\ddagger}$ = 0 kcal mol^{-1}, $\Delta\Delta G_{sol}^{\ddagger}$ = 0 kcal mol^{-1}

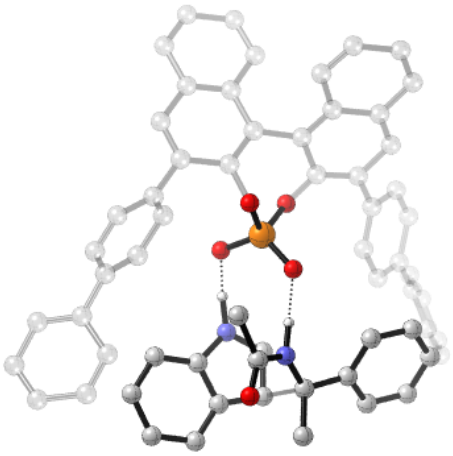

TS26-*E*: $\Delta\Delta G^{\ddagger}$ = +1.8 kcal mol^{-1}, $\Delta\Delta G_{sol}^{\ddagger}$ = +0.8 kcal mol^{-1}

Figure 4.5. Competing TS for the 4-PhC_6H_4 derived phosphoric acid catalysed Friedel-Crafts. ONIOM (B3LYP/6-31G**:UFF), single-point energy M06-2X/6-31G**. Grayed-out regions were treated with UFF, and the full-colour regions were treated B3LYP/6-31G**.

I have summarised the calculations into a simple accessible qualitative model which explains enantioselectivity trends with varying 3,3' substituent (Figure 4.6). This model implies that reactions involving displaced nucleophiles proceeding *via Type II E* pathways will not be suitable for a reaction catalysed by small ligand AREA(θ) catalysts. Such catalysts bias towards a *Type I* transition states leading to little stereoinduction. An optimal catalyst for such a reaction; would be one that is neither too big (raises *Type I* relative to *Type II*), nor too small (cannot differentiate between *Type I* or *Type II*), but somewhere in between. Although small AREA(θ) catalysts will not be selective for *Type II* reactions, they are expected to proceed with high levels of selectivity for *Type I* reaction pathways. Examples where this general trend is observed are given in Table 4.1 in support of the mechanistic model.

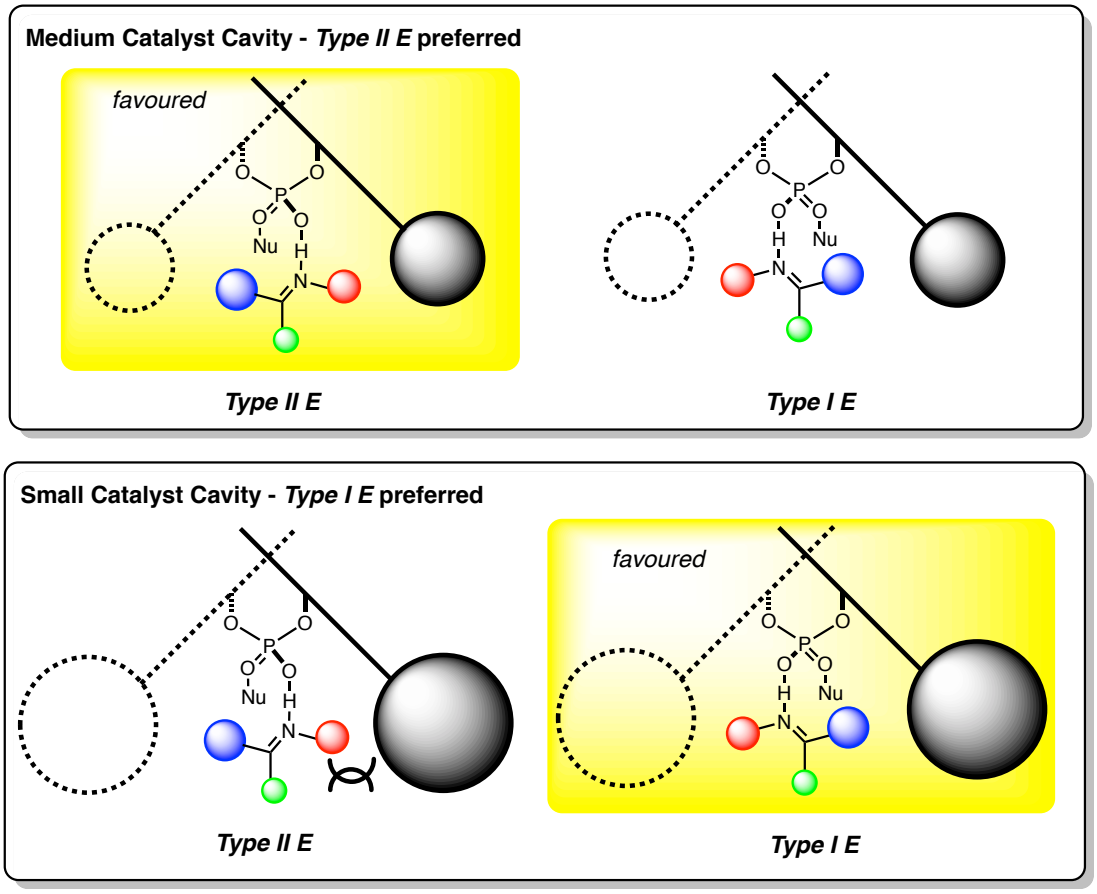

Figure 4.6. Qualitative model describing the preference for *Type I E* transition state with small AREA(θ) catalysts. In the *Type II* conformation, the imine adopts a tilted disposition to minimize steric interactions with the 3,3' groups. Increasing sterics remote from the phosphoric acid increases the interaction between the N-substituent and the 3,3' group.

Table 4.1. Examples of the addition of displaced nucleophiles to imines. For each catalyst classification, I have chosen to compare the best performer from the catalyst screen of a model substrate under the same reaction conditions.

Reaction	Mechanism	AREA(θ) > 70 (%ee)	medium AREA(θ) (%ee)	AREA(θ) < 29 (%ee)
addition of indole[65]	*Type I E*	0	93	73
addition of dihydroindole[147]	*Type I E*	-	97	99
Bignelli[115]	*Type I/II E*	-	80	-96
addition of indole[208]	*Type II E*	-	92	2
addition of enamides[150]	*Type II E*	4	96	9
Povarov[159]	*Type II E*	-	92	27

The model (Figure 4.6) has been validated for acyclic imines in which the small proximal sterics reduce the preference of *Type II* pathways and large remote sterics increase the energy of the *Type II* TS pathways relative to *Type I*. As a means to further probe this model, the influence of proximal and remote sterics on the addition of indoles to cyclic imines was examined. Unlike the addition of symmetrical nucelophiles to cyclic imines proceeding *via Type I* pathways in which the proximal sterics only dictate the level of enantioselectivity to an appreciable extent the model suggests that both steric factors will play a significant role. To this end, I computationally studied the Friedel-Crafts alkylation reaction of indole with racemic spiro indolin-3-ones and show that the same trends from the Friedel-Crafts reaction with acyclic imines can be applied.[209] Catalyst screening results are shown in Figure 4.7 and the results from the calculations can be found in Table 4.2. The routine optimisation table shows a heavy dependence on both proximal and remote sterics on enantioselectivity, in which selective catalysts generally have both, large proximal sterics and small AREA(θ). Calculations have determined the reaction to proceed *via* a *Type I* TS pathway and decreasing the proximal steric profile of the 3,3' substituents decreases the free energy difference between the competing pathways. The model (Figure 4.6) suggests that for reactions involving similar substrates proceeding *via Type II* pathways, small AREA(θ) catalysts will not be selective. A recent study by Ma *et al.* supports this hypothesis in which the authors found that changing the 3,3' group from 2,4,6-triisopropylphenyl (medium AREA(θ)) to $SiPh_3$ (small AREA(θ)) diminished the magnitude of stereoinduction from 78% to 50%.[210]

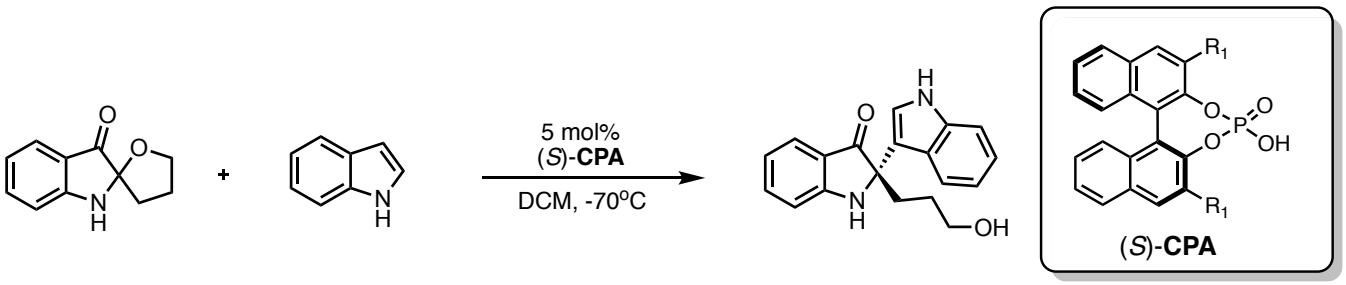

Entry	Catalyst R_1	AREA (θ)	Rotation Barrier (kcal mol^{-1})	ee (%)
1	4-$(NO_2)C_6H_4$	107	0.00	75
2	3,5-$(CF_3)_2C_6H_4$	62	2.02	5
3	1-naphth	62	13.43	77
4	***2,4,6-(^{i}Pr)$_3$C$_6$H$_3$***	***51***	***28.40***	***98***
5	***4-^{t}Bu-2,6-(^{i}Pr)$_2$C$_6$H$_3$***	***51***	***28.18***	***98***
6	***4-PhC$_6$H$_4$***	***50***	***2.01***	***5***
7	***SiPh$_3$***	***29***	***1.35***	***80***

Figure 4.7. Effect of 3,3' groups on the enantioselectivity of the Friedel-Crafts reaction employing cyclic imines.

Table 4.2. Competing TS for the chiral phosphoric acid catalysed addition of indole to cyclic imines. ONIOM (B3LYP/6-31G**:UFF), single-point energy M06-2X/6-31G**.

Mechanism (Catalyst)	$\Delta\Delta G_{sol}^{\ddagger}$
Type I (TRIP), **TS27**	0
Type II (TRIP), **TS28**	+1.7
Type I (4-biphenyl), **TS29**	0
Type II (4-biphenyl), **TS30**	0

4.3 Addition of Enamides

There have been numerous examples of enantioselective additions of enamides to imines. In most cases the effect of the 3,3' groups on enantioselectivity closely mirrors that of the Friedel-Crafts described in section 4.2 and some examples are given in Table 4.1. However, whether the reaction between a displaced nucleophile and an imine proceeding *via* a *Type II* pathway benefits from large or small proximal sterics depends on the size of the displaced nucleophile. In the following reaction reported by Tsogoeva *et al.* both proximal and remote sterics played important stereochemical roles (Figure 4.8).[150] For this particular reaction I observed an inverse relationship between enantioselectivity and the proximal steric profile of the 3,3' substituents.

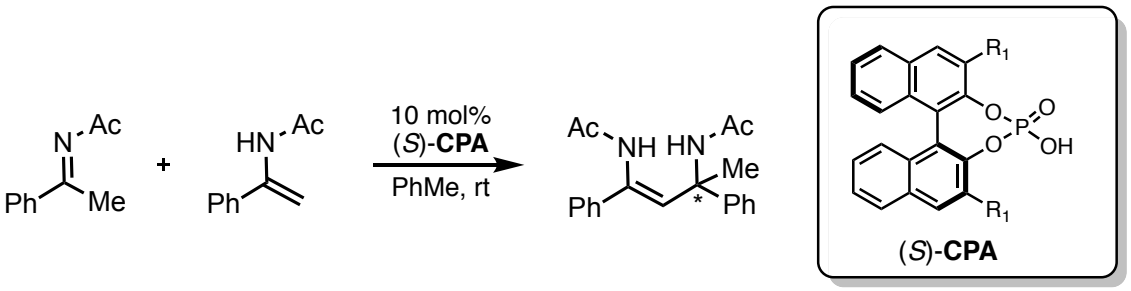

Entry	Catalyst R_1	AREA (θ)	Rotation Barrier (kcal mol^{-1})	ee (%)
1	H	107	0.00	4
2	Ph	70	2.05	56
3	***4-$NO_2C_6H_4$***	***64***	***2.03***	***96***
4	***9-anthryl***	***61***	***28.31***	***25***
5	***$SiPh_3$***	***29***	***1.35***	***9***

Figure 4.8. Effect of 3,3' groups on the enantioselectivity of the addition of enamides to imines. The product stereochemistry was not determined.

Increasing the remote sterics increases the enantioselectivity until a point, which then turns and changes to a decline. Additionally, it was experimentally observed that large proximal sterics was detrimental to the reaction (entry 4). Calculations were performed on three catalysts; 4-$NO_2C_6H_4$, 9-anthryl and $SiPh_3$ derived phosphoric acids to assess the roles of the proximal and remote sterics. The results are summarised in Figures 4.9, 4.10 and 4.11.

The reaction proceeds *via* a *Type II E* pathway and as predicted by the model above (Figure 4.6), increasing the remote sterics by changing the 3,3' from 4-$NO_2C_6H_4$, AREA(64), to $SiPh_3$, AREA(29), increases the energy of the *Type II* pathway relative to the *Type I.* The *Type II E* pathway is now the highest in energy with the reaction proceeding *via Type I Z*, which is in good agreement with the observed stereochemical outcome. This leads to small energy differences between the diastereomeric TS and low levels of enantioselectivity, observing similar trends as with the Friedel-Crafts study. Despite the differing electronic nature between the catalysts, there were no obvious electronic factors attenuating the selectivity. For the 9-anthryl derived phosphoric acid the lowest energy TS was **TS35-*E*** (*Type II E*), in this TS the phenyl substituent on the enamide prefers to be located in the empty catalyst pocket at the front left, this forces the imine to the right hand side of the catalyst. The phenyl substituent of the imine now experiences significant steric interactions with the 3,3' group leading to a large energetic penalty and raising of the *Type II* TS relative to the *Type I*. The small energy difference between the *Type II E* and the *Type I E* (0.4 kcal mol^{-1}) agrees with the poor levels of enantioselectivity observed experimentally (Figure 4.11). I have summarised the calculations into a simple accessible qualitative model which explains enantioselectivity trends with varying 3,3' substituent (Figure 4.12). The calculations suggest that the reason for the enantioselectivity trends with more sterically demanding displaced nucleophiles is a consequence of the size of the substituent attached to the same carbon as the heteroatom that binds to the phosphoryl oxygen of the catalyst. If this substituent is large, the correct catalyst has small proximal sterics; too large raises the energy of *Type II* TS relative to *Type I*. Although, large proximal sterically derived catalysts are predicted not to be selective for reactions involving large displaced nucleophiles, they should proceed with high levels of enantioselectivity with small displaced nucleophiles. Examples of reactions exhibiting this trend are summarized in the Table 4.3**.** In addition, the catalyst screening results not only provide valuable information on the catalyst features required for efficient enantioselectivity but also the TS pathway in operation. When *Type I E* and *Type II E* TS are involved small AREA(θ) catalysts will provide high and low levels of enantioinduction, respectively. This makes the deduction of product stereochemistry possible, which is often not easy to determine without additional experiments.

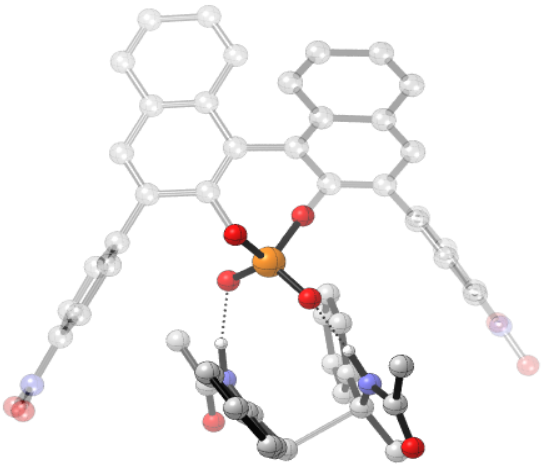

TS32-*E*: $\Delta\Delta G^{\ddagger}$ = +3.2 kcal mol^{-1}, $\Delta\Delta G_{sol}^{\ddagger}$ = +2.6 kcal mol^{-1}

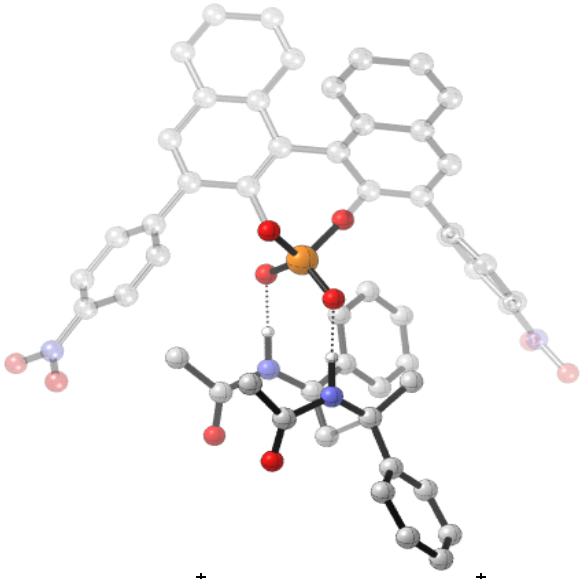

TS32-*Z*: $\Delta\Delta G^{\ddagger}$ = +5.2 kcal mol^{-1}, $\Delta\Delta G_{sol}^{\ddagger}$ = +2.6 kcal mol^{-1}

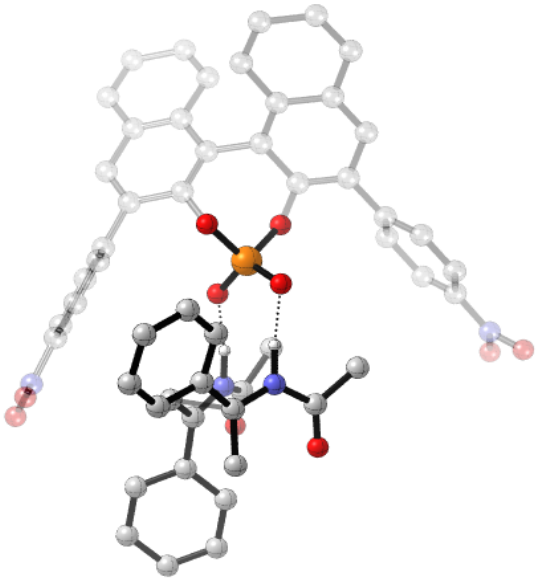

TS31-*E*: $\Delta\Delta G^{\ddagger}$ = 0 kcal mol^{-1}, $\Delta\Delta G_{sol}^{\ddagger}$ = 0 kcal mol^{-1}

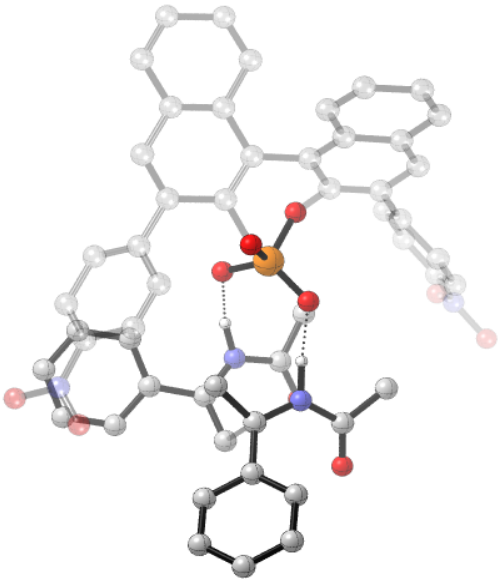

TS31-*Z*: $\Delta\Delta G^{\ddagger}$ = +4.4 kcal mol^{-1}, $\Delta\Delta G_{sol}^{\ddagger}$ = +2.1 kcal mol^{-1}

Figure 4.9. Competing TS for the 4-$NO_2C_6H_4$ derived phosphoric acid catalysed addition of enamides. ONIOM (B3LYP/6-31G**: UFF), single-point energy M06-2X/6-31G**. Grayed-out regions were treated with UFF, and the full-colour regions were treated B3LYP/6-31G**.

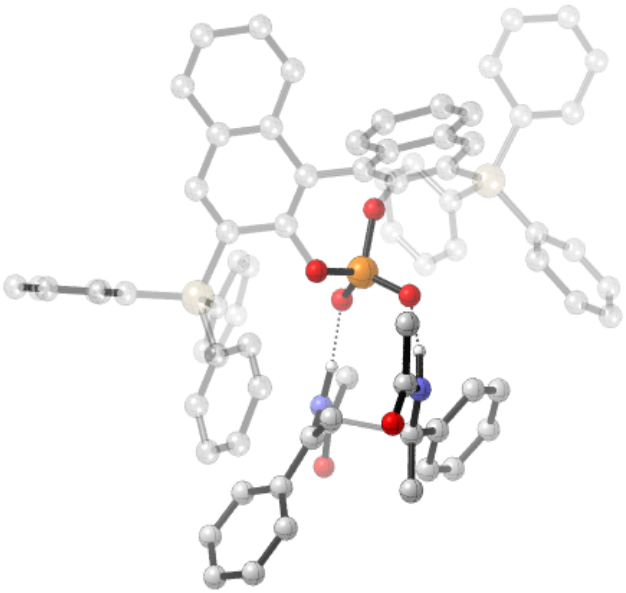

TS34-*E*: $\Delta\Delta G^{\ddagger}$ = +1.7 kcal mol^{-1}, $\Delta\Delta G_{sol}^{\ddagger}$ = +1.7 kcal mol^{-1}

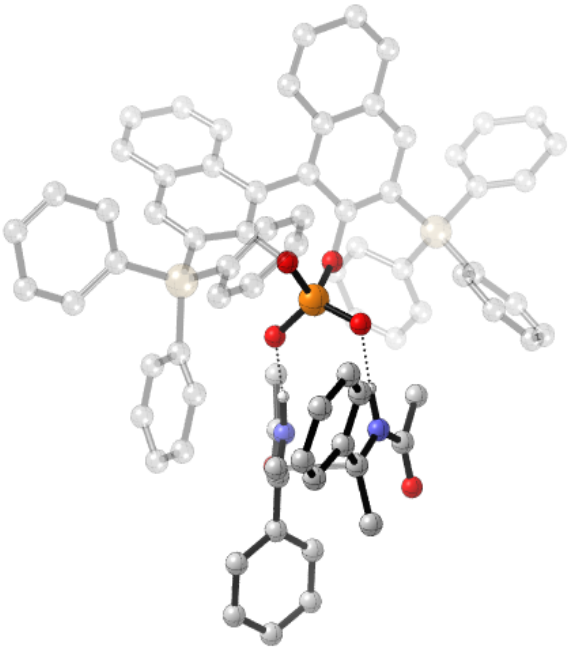

TS33-*E*: $\Delta\Delta G^{\ddagger}$ = +3.2 kcal mol^{-1}, $\Delta\Delta G_{sol}^{\ddagger}$ = +2.6 kcal mol^{-1}

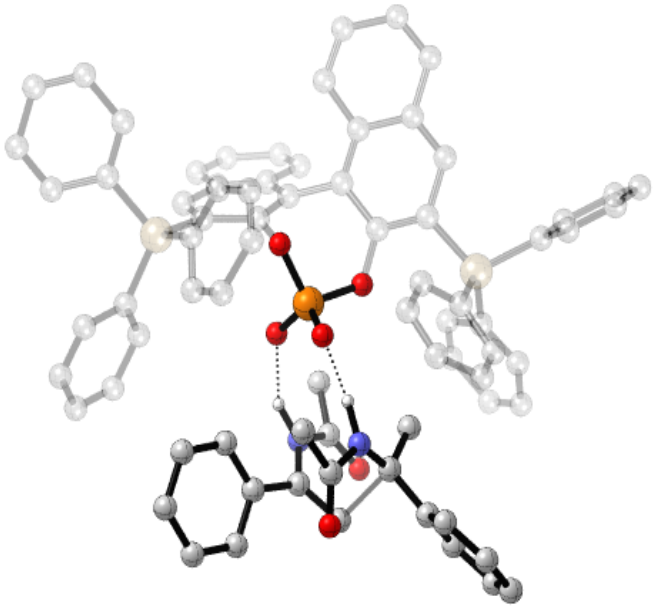

TS34-*Z*: $\Delta\Delta G^{\ddagger}$ = 0 kcal mol^{-1}, $\Delta\Delta G_{sol}^{\ddagger}$ = 0 kcal mol^{-1}

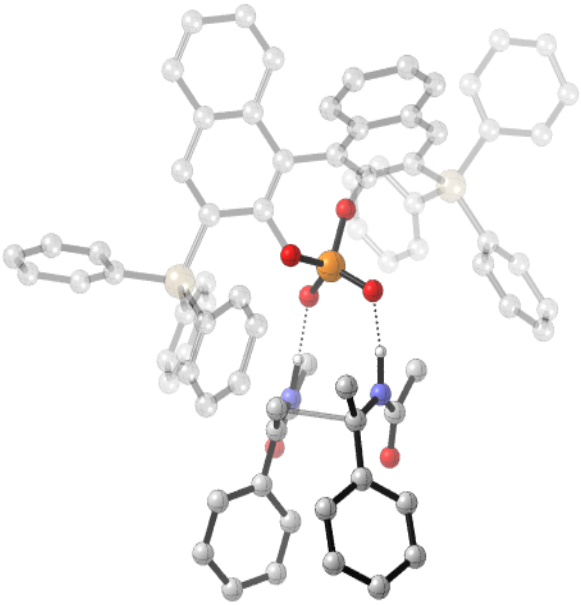

TS33-*Z*: $\Delta\Delta G^{\ddagger}$ = +0.5 kcal mol^{-1}, $\Delta\Delta G_{sol}^{\ddagger}$ = +0.3 kcal mol^{-1}

Figure 4.10. Competing TS for the $SiPh_3$ derived phosphoric acid catalysed addition of enamides. ONIOM (B3LYP/6-31G**: UFF), single-point energy M06-2X/6-31G**. Grayed-out regions were treated with UFF, and the full-colour regions were treated B3LYP/6-31G**.

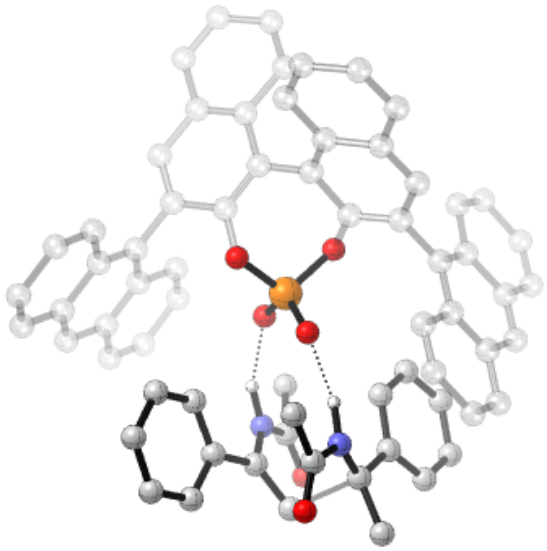

TS36-*E*: $\Delta\Delta G^{\ddagger}$ = -0.9 kcal mol^{-1}, $\Delta\Delta G_{sol}^{\ddagger}$ = +0.4 kcal mol^{-1}

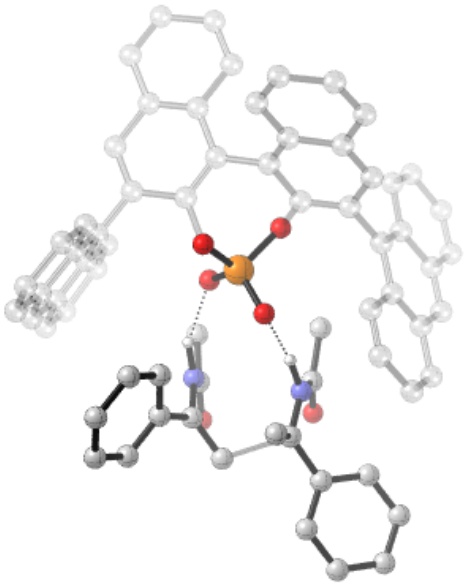

TS35-*Z*: $\Delta\Delta G^{\ddagger}$ = +3.7 kcal mol^{-1}, $\Delta\Delta G_{sol}^{\ddagger}$ = +3.1 kcal mol^{-1}

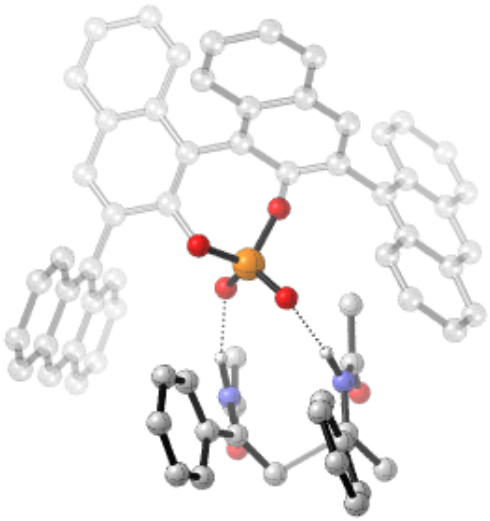

TS35-*E*: $\Delta\Delta G^{\ddagger}$ = 0 kcal mol^{-1}, $\Delta\Delta G_{sol}^{\ddagger}$ = 0 kcal mol^{-1}

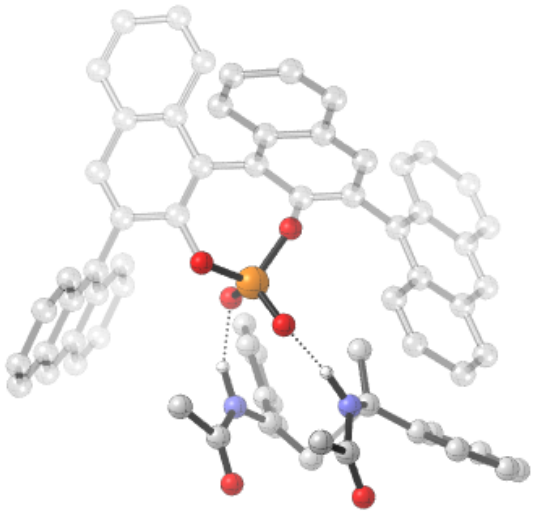

TS36-*Z*: $\Delta\Delta G^{\ddagger}$ = +0.1 kcal mol^{-1}, $\Delta\Delta G_{sol}^{\ddagger}$ = +0.2 kcal mol^{-1}

Figure 4.11. Competing TS for the 9-anthryl derived phosphoric acid catalysed addition of enamides. ONIOM (B3LYP/6-31G**: UFF), single-point energy M06-2X/6-31G**. Grayed-out regions were treated with UFF, and the full-colour regions were treated B3LYP/6-31G**.

.

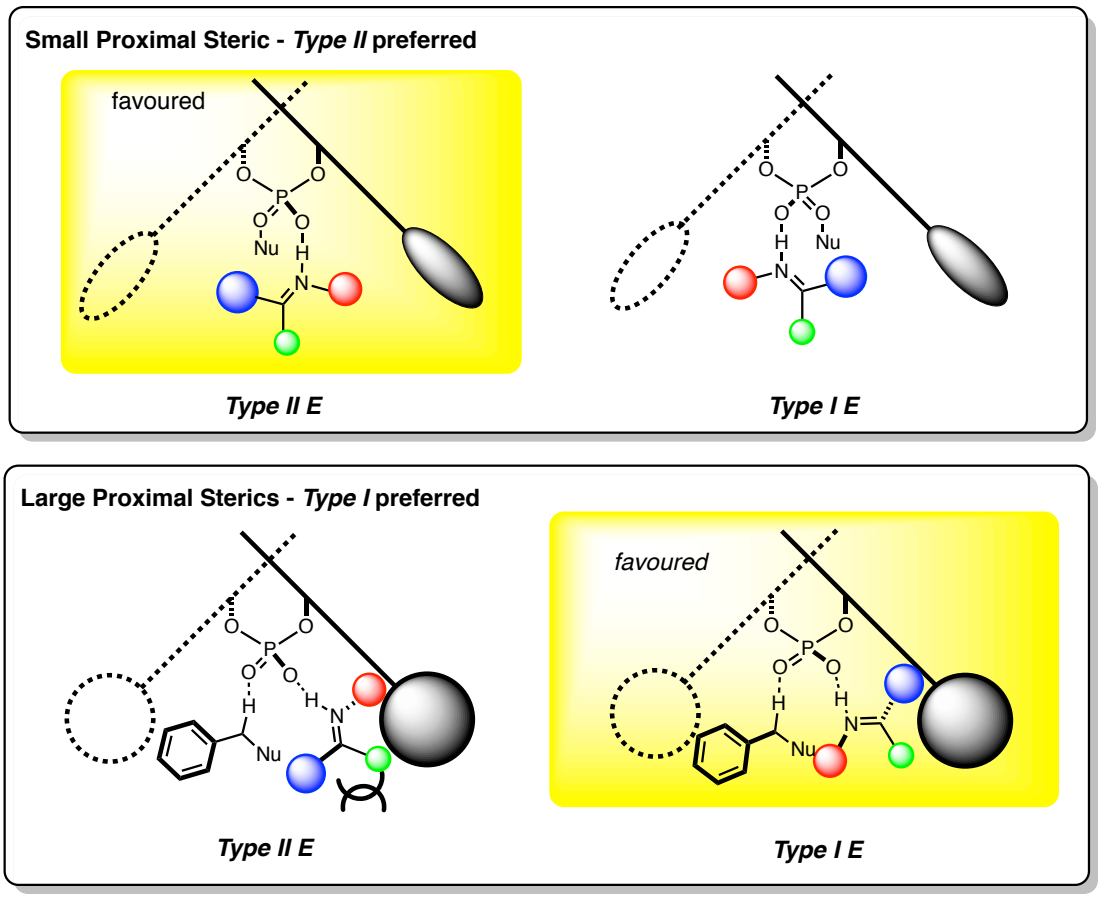

Figure 4.12. Qualitative model describing the preference for *Type I* transition states with large proximal bulk catalysts. The large substituent on the nucleophile prefers to be placed in the empty left hand pocket of the catalyst to minimize steric interactions with the 3,3'. As a consequence the imine adopts a position within the chiral catalyst pocket which is parallel to the 3,3' and so the R group highlighted in blue experiences significant steric interactions with the 3-substituent. The imine rotates 180° about the O-H-N bond, which allows placing the largest substituent furthest away from the catalyst bulk. Decreasing the proximal sterics, decreases the steric interactions between the imine and the 3,3'.

Table 4.3. Examples of the addition of displaced nucleophiles to imines in which the sterics of the nucleophile dictate whether large or small proximal metrics are optimal. All reactions proceed *via Type II E* pathways. For each catalyst classification, I have chosen to compare the best performer from the catalyst screen of a model substrate under the same reaction conditions.

Reaction	Nu Carbon Substituent	Rotation Barrier <3 (ee%)	Medium Rotation Barrier (ee%)	Rotation Barrier >26 (ee%)
addition of enamides[211]	H	79	-	91
Petasis Ferrier[212]	H	-	-	99
addition of vinyl indoles[213]	H	21	54	92
Bignelli[115]	Alkyl	99	64	1
Mannich[214]	Ph	76	51	-

I computationally studied the reaction in Figure 4.8 in which we replaced the phenyl group on the enamide nucleophile with a proton catalysed by a 9-anthryl derived phosphoric acid. I would expect the reaction to proceed *via* a *Type II E* TS pathway and an increase in energies between *Type I* and *Type II* pathways. In line with expectation I found the modification lead to an increase in the *Type I E* and *Type II E* from 0.4 kcal mol^{-1} (Figure 4.11) to +1.4 (Figure 4.13). In **TS37-*E*** (*Type II E*) the phenyl group has more space on the left hand side of the catalyst and so the steric clash between the 9-anthryl group at the 3 position and this substituent is reduced as indicated by comparing the interatomic distances (Figure 4.14). These calculations alongside additional experimental data provide a coherent picture that large groups on the same carbon that binds to the catalyst are not compatible with catalysts with large proximal steric profiles supporting the mechanistic model shown in Figure 4.12.

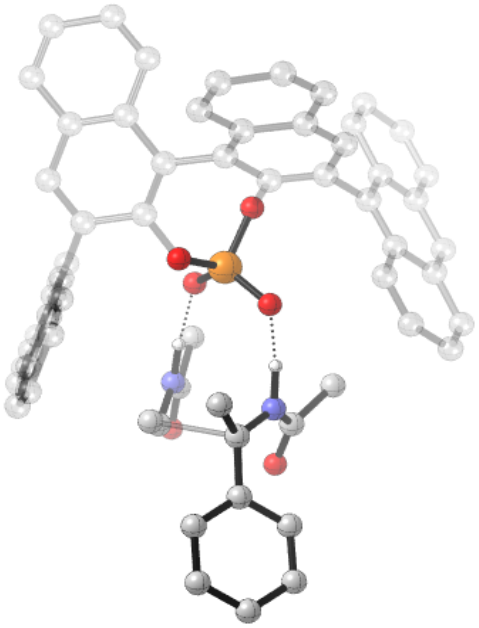

TS37-*Z*: $\Delta\Delta G^{\ddagger}$ = +2.5 kcal mol^{-1}, $\Delta\Delta G_{sol}^{\ddagger}$ = +2.6 kcal mol^{-1}

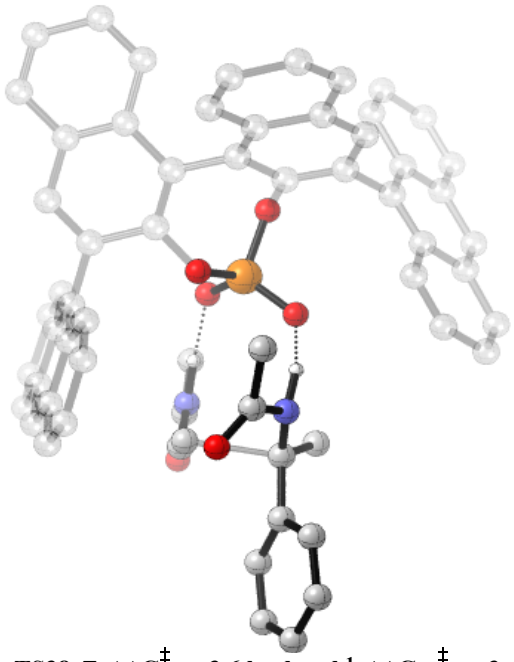

TS38-*Z*: $\Delta\Delta G^{\ddagger}$ = +3.6 kcal mol^{-1}, $\Delta\Delta G_{sol}^{\ddagger}$ = +3.4 kcal mol^{-1}

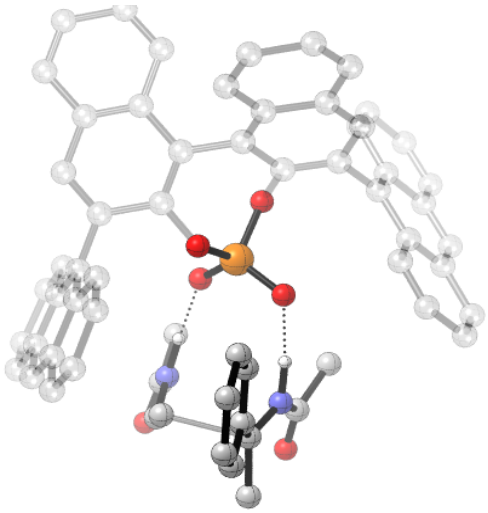

TS37-*E*: $\Delta\Delta G^{\ddagger}$ = 0 kcal mol^{-1}, $\Delta\Delta G_{sol}^{\ddagger}$ = 0 kcal mol^{-1}

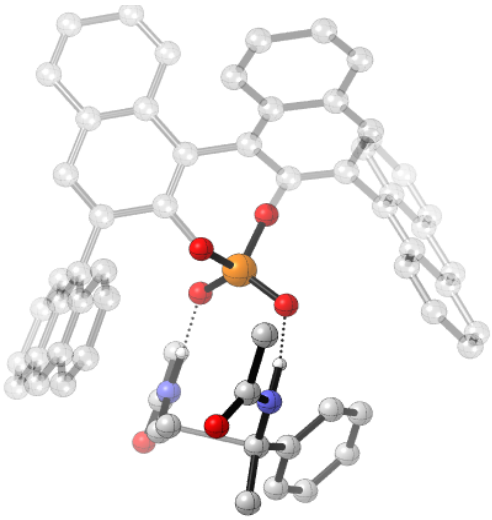

TS38-*E*: $\Delta\Delta G^{\ddagger}$ = +1.1 kcal mol^{-1}, $\Delta\Delta G_{sol}^{\ddagger}$ = +1.4 kcal mol^{-1}

Figure 4.13. Competing TS for the 9-anthryl derived phosphoric acid catalysed addition of enamides. ONIOM (B3LYP/6-31G**: UFF), single-point energy M06-2X/6-31G**. Grayed-out regions were treated with UFF, and the full-colour regions were treated B3LYP/6-31G**.

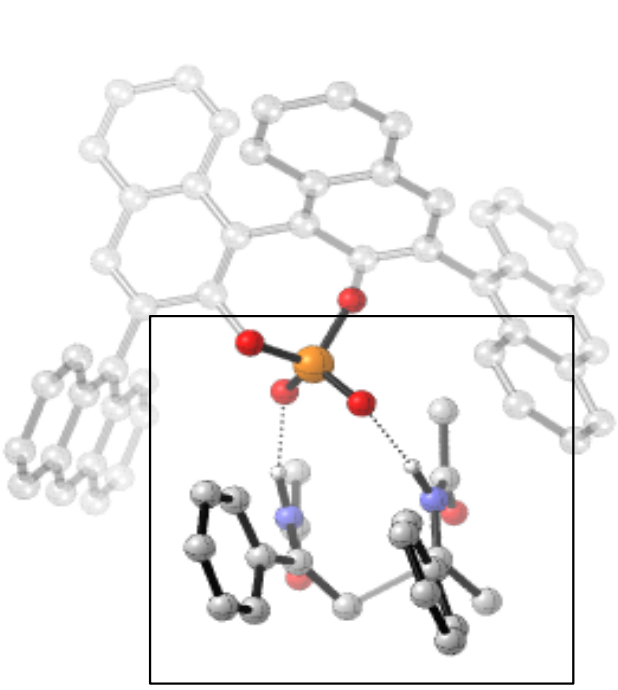

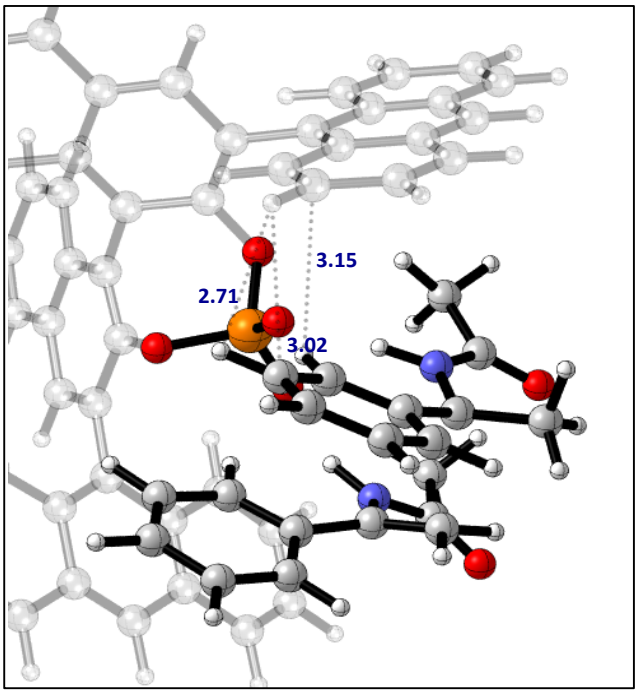

TS35-*E*

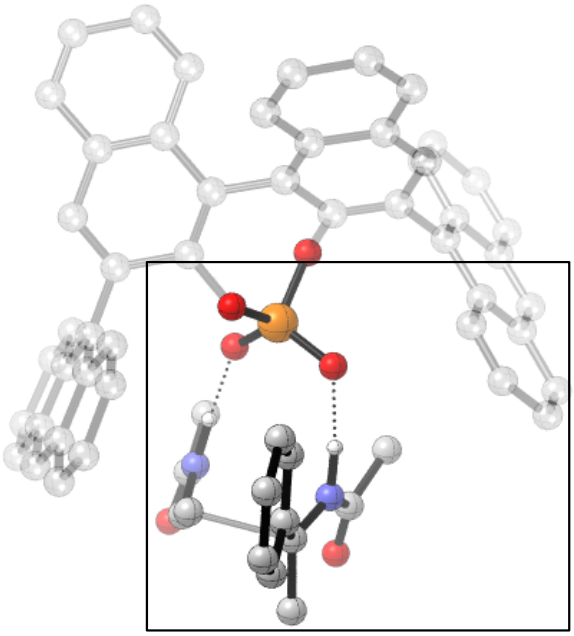

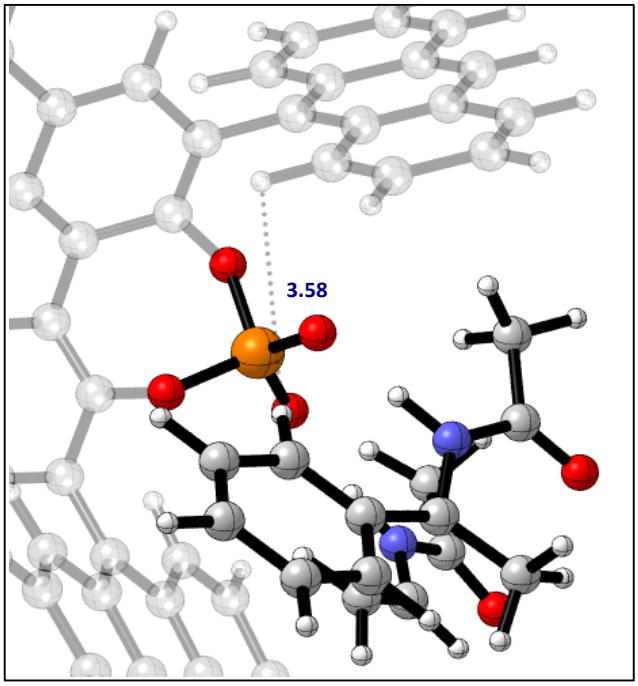

TS37-*E*

Figure 4.14. Comparing the distance of the phenyl C-substituent on the imine to the 9-anthryl group on the catalyst when the nucleophile is changed from large displaced (top) to small displaced (bottom).

4.4 Qualitative Model for Catalyst Choice

By studying a number of reactions for this class, I have been able to observe broad trends. This has provided unprecedented insight into the steric factors that affect the enantioselectivity. Precise tuning of the steric environment of the 3,3' substituent can destabilize particular TS pathways, and by exploiting this finding I was able to construct a simple qualitative model to determine the steric features necessary for efficient stereoinduction (Figure 4.15). The model categorizes all reported imine/nucleophile reactant combinations and provides firstly a starting reference point for the design of selective phosphoric acid catalysed reactions of this type, and secondly the foundations for new selective catalysts. The TS pathway in operation (*Type I/II*, *E/Z*) in combination with the identity of the nucleophile determines which catalysts are selective. The reactants can be combined in different ways leading to eight different outcomes and four different catalyst choices, controlled by the factors listed: size of the *N*-substituent, imine configuration, acyclic or cyclic imine, size of the displaced nucleophile. The reactants follow either right-handed or left-handed pathways depending on the size of *N*-substituent. Reactions with imines bearing large *N*-substituents favor *Type I* pathways; a preference for *E* or *Z* depends on how accessible the configuration is. If the *Z* configuration is energetically inaccessible the reaction proceeds *via* a *Type I E* pathway, the correct catalyst has large proximal sterics and medium AREA(θ).[29,62,104,114b,135-138,155c,201-202, 215 - 220] However, reactions involving displaced nucleophiles the best choice of catalyst has large proximal sterics and small AREA(θ).[19,27,65,145,147,221-226] Higher enantioselectivities with small proximal bulk catalysts are not uncommon with displaced nucleophiles. In these cases the competing *Type II* TS is likely to adopt a tilted disposition meaning the remote sterics are predominantly responsible for the enantioselectivity. For *Type I Z* reactions the correct catalyst is dependent on the nature of the imine and nucleophile. Reactions involving acyclic imines require a catalyst that has large proximal sterics to disfavor *Type II* pathways and small AREA(θ) to disfavor the competing *Type I E* pathway.[31-32,57,63,114b,142-144,227-229] If the imine is cyclic, the optimal catalyst is dependent on the nature of the nucleophile. For symmetrical nucleophiles like Hantzsch esters only proximal sterics affect the TS to an appreciable extent and so the optimal catalyst has large proximal sterics disfavoring the *Type II* competing pathway.[58,114c,141,203-206,230-235] For *Type I* pathways with displaced nucleophiles the competing *Type II* TS arranges the imine towards a tilted disposition due to a greater steric accessibility, as a consequence both proximal and remote sterics play important stereochemical roles. The optimal catalyst has large proximal sterics and small AREA(θ) disfavouring the *Type II* pathway.[114a,209,236-237]

In a similar manner, reactions involving imines with small N-substituents favour *Type II* pathways and can exist as the *E* or *Z* isomers. For *Type II E*, a selective catalyst for such a reaction is one that has medium AREA(θ). However, whether the reaction benefits from large proximal sterics or small depends on the sterics of the nucleophile. For smaller displaced nucleophiles, large proximal sterics are advantageous, disfavouring *Type I E* pathways.[28,149,208,211-213,238-244] However, if the nucleophile is large, small proximal sterics are essential.[26,102,115,150,214] The corresponding *Z* pathway is not known with acyclic imines. Unlike *Type I* reactions involving cyclic substrates and symmetrical nucleophiles in which only proximal sterics had a major influence on stereoselectivity, both proximal and remote sterics will play important stereochemical roles if the reaction proceeds *via* a *Type II* pathway. For such a pathway to be favoured the imine must adopt a tilted disposition regardless whether the nucleophile is symmetrical or displaced and so the correct catalyst has large proximal bulk and medium AREA(θ), showing the same enantioselectivity trends as observed with the Friedel-Crafts study (Figure 4.6).[210,245-247] The only examples of *Type II* reactions using cyclic substrates and displaced nucleophiles employ sterically small nucleophiles such as indoles. Whether the dependence on size of proximal sterics correlates inversely to size of displaced nucleophile as observed with the acyclic imines (Table 4.3) remains an open question but I would expect to observe similar trends.

Although the choice of catalyst depends on the individual substrate combinations the model has supplied some insight into the correct selection of catalyst for a given process and I have included some suggestions. TRIP works well for seven of the eight reaction combinations explaining why it is so general. It should be avoided if the reaction employs large displaced nucleophiles and imines as these generally proceed *via Type II E* pathways. Useful catalysts for this reaction category will contain hydrogens at the 2 and 6 positions of the aromatic ring, for example, phenyl. If TRIP provides less than satisfactory enantioselectivities for reactions requiring large proximal bulk and small AREAs I suggest that the triphenylsilane derived phosphoric acid will be more appropriate.

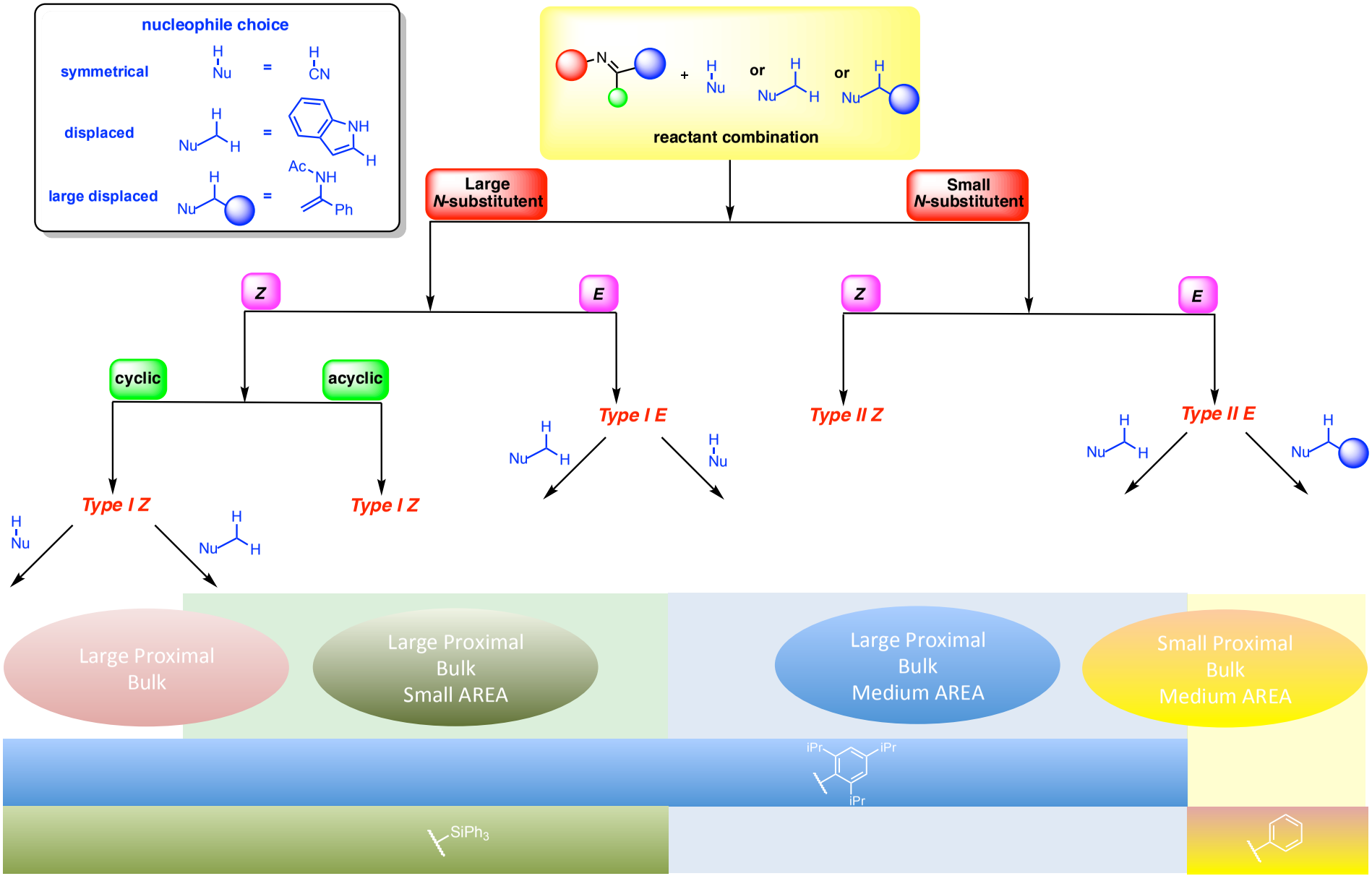

Figure 4.15. Qualitative model for catalyst choice.

4.5 Conclusions

I have computationally explored the 3,3' effect with reactions involving the addition of displaced nucleophiles to imines. My computational studies shows that two models (Figure 4.6 and Figure 4.12) can explain the enantioselectivity in these systems. I have applied these models to explain enantioselectivity trends with similar reactions. Moreover, by virtue of a large-scale data mining process I have developed a general model to guide the best choice of phosphoric acid catalyst for nucleophilic addition to imines. These rules are consistent for all the literature data I have been able to find (seventy-seven papers containing over 1000 examples), explaining enantioselectivity trends with varying 3,3' group and correctively identifying steric features essential for efficient stereoinduction. The literature presented may not be exhaustive but I have yet to find a reaction that does not fit the model. Although some of the pathways have yet to be experimentally explored, extension of the principles presented here will allow the results of any BINOL-phosphoric acid catalysed nucleophilic addition to imines to be predicted. The insights gained in this study can be generalized to countless situations in which the molecular parameters can effectively describe the steric features required for efficient stereoinduction. I expect these computational studies of enantioselectivity will help propel the use of such catalysts in complexity-generating transformations. As a final note, an automated catalyst selection program is currently being developed which will allow selection of the best catalyst from a given input structure and is based on hand written rules. I hope this will increase the model's use within the synthetic community.

Chapter 5

5 New Strategies for the Design of Highly Versatile and Selective Chiral Phosphoric Acids

5.1 Background and Methods

The *de novo* design of chemo-, regio-, and stereo-selective catalysts has been described as the "Holy Grail" for computational chemists and remains a principle challenge in the field of organic synthesis.[153,248] Even in instances where the overall mechanism of a transformation is well understood, the origin of selectivity can remain undetermined. In many cases the key difficulty lies in recognising the influence that catalyst and substrate structural features have on product enantioselectivity, due to interactions at the transition state. This issue, while essential for the rational design of superior catalysts, is intensified in situations where seemingly minor modifications to the catalyst or substrate have a profound, and often non-intuitive influence on enantioselectivity. This phenomenon is common to chiral phosphoric acid catalysis and exemplified by the work presented in Chapters 2, 3 and 4.

Chiral phosphoric acids as catalysts have become popular and while numerous improvements to reaction scope and efficacy were apparent, the design of a new versatile catalyst was lacking. Several modulations of the standard BINOL-derived phosphoric acid have been made and experimentally tested as described in Chapter 1. In most cases only superior enantioselectivities compared to the standard were achieved for isolated examples. Despite the many designs, there has been no catalyst other than TRIP capable of inducing high selectivity for a large range of reactions. The development of a highly versatile and selective catalyst remains a challenge that is largely unmet.

The addition of nucleophiles to imines proceeds *via* a common bifunctional mechanism in which the nucleophile and the electrophile are both activated through hydrogen bonding. Four diastereoisomeric catalyst-substrate complexes are generated, in which the imine can exist as the *E* or *Z* stereoisomers and the imine N-substituent can be rotated away or towards the front of the 3,3' groups. In Chapters 3 and 4, I have studied the effect of catalyst substituents at the 3,3' positions. In most cases the enantioselectivity is dependent on both remote and proximal sterics. The results of high-level QM/MM calculations have been

summarised into a single, simple qualitative model that describes the best choice of catalyst for a particular combination of reactants. TRIP is selective for seven of the eight possible permutations but it fails for reactions proceeding *via Type II E* pathways with large displaced nucleophiles. At this point I questioned "*Is it possible to design a catalyst that is selective for all reactant combinations of interest?"* Such a catalyst could be of enormous importance in this field and may have applications beyond this reaction class. Our detailed mechanistic investigations outline the structural properties that are required for high-levels of stereoinduction, providing hints on what features a versatile catalyst may contain. For most reactions large proximal sterics are required with the exception to one class. "*Is it possible for a single catalyst to have both large and small proximal sterics?"* To achieve this I must develop new design principles. In this regard, C_2 symmetry has been a dominant guiding force in the design of improved ligands for enantioselective-catalysed reactions. Often offering distinct advantages, (1) the presence of a symmetry axis reduces the number of competing diastereomeric reaction pathways, (2) enables a more straightforward analysis of substrate catalyst interactions and (3) simplifies mechanistic and structural studies. The chiral phosphoric acid can be modelled by a quadrant diagram, in which quadrants II and III are equivalently hindered. By making the substituents on the 3 and 3' non-equivalent, I can depict a quadrant diagram that has quadrant II fully blocked and quadrant III partially blocked (Figure 5.1). Judicious choice of different substituents allows the catalyst to exhibit different structural properties on one side than the other. Consequently, the C_1 architecture of the catalyst enables the construction of much more diverse chiral environments than previous catalysts.

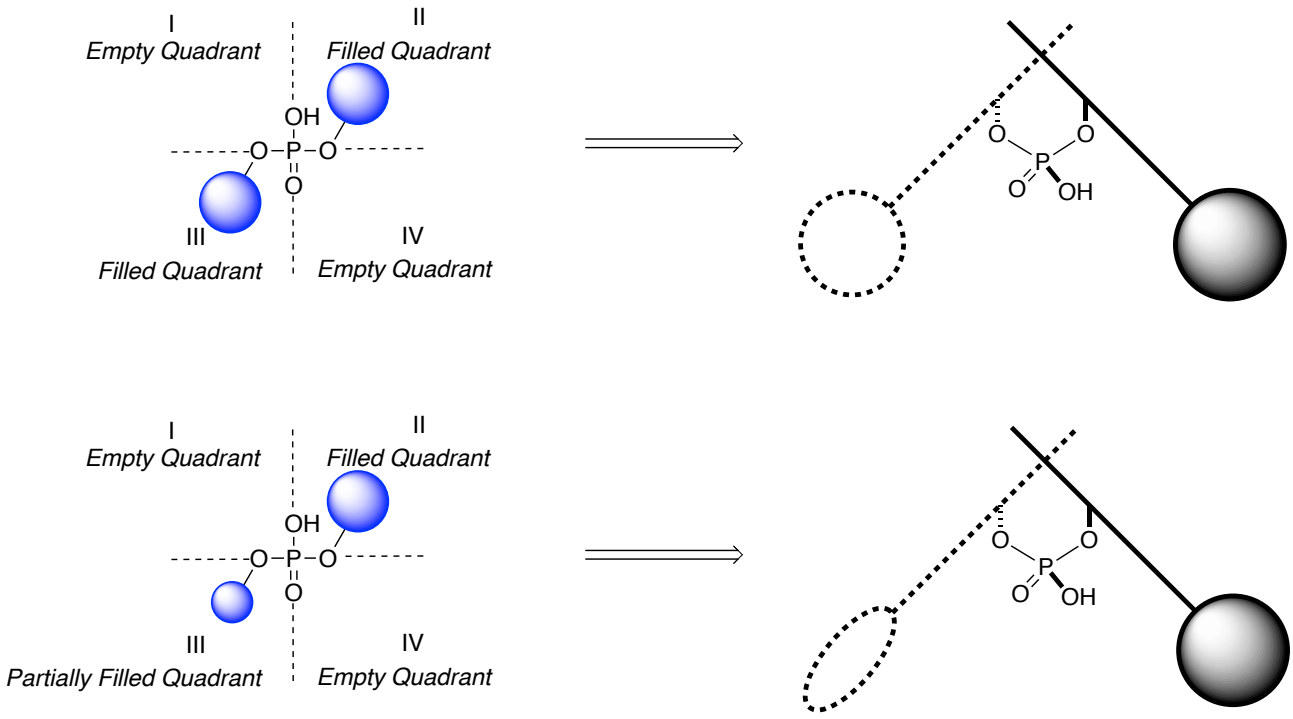

Figure 5.1. Quadrant diagram depicting the steric environment depicted for a C_2 symmetric catalyst (top) and a C_1 symmetric catalyst (bottom).

Given the reasons for poor enantioselectivities with *Type II E* TS pathways and large displaced nucleophiles, I opted to modify TRIP and replace the 3' substituent with a smaller group. Reasoning that this would create more space at the left hand side of the catalyst cavity, allowing accommodation of both, the large displaced nucleophile and the imine. This type of organisational element would avoid a direct steric interaction between the imine C-substituent and the catalyst 3-substituent. Maintaining the rest of TRIP molecular features should allow high enantioselectivies to be achieved with the remaining reactant combinations. Our design principles are outlined in Figure 5.2.

(A) 1nd generation BINOL-derived catalysts

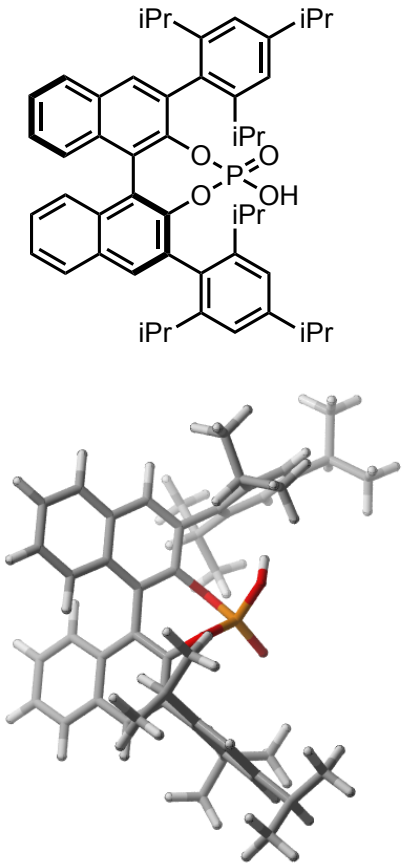

(B) 2nd generation BINOL-derived catalysts

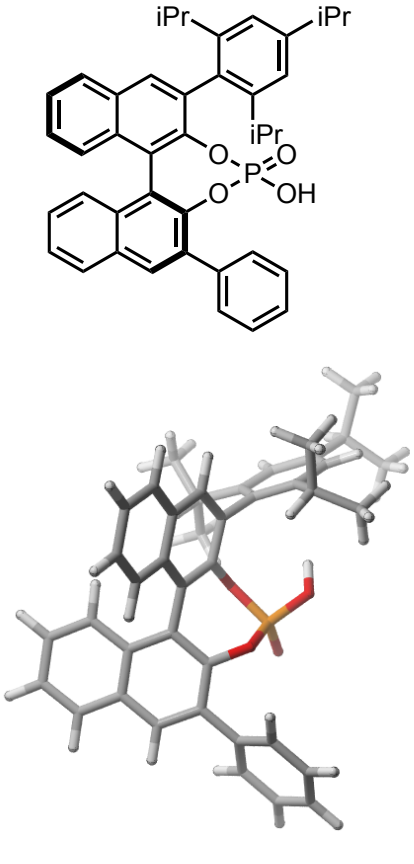

Figure 5.2. Computationally driven design of chiral phosphoric acids. (A) Phosphoric acids have large groups at the 3,3' positions – too large can lead to poor results. (B) More steric bulk on one side of the catalyst than the other is the underlying theme for catalyst improvement.

The positioning of the imine inside the catalyst cavity would not be well determined if the 3' substituent was too small, leading to a number of possible orientations and lack of enantiocontrol. Consequently, it was decided that an aromatic group that had hydrogens at the 2 and 6 positions of the aromatic ring would be most appropriate. To test the degree to which the C_1 symmetric catalyst approaches increased levels of versatility a series of reactions were computationally studied and the levels of enantioinduction predicted, the results are outlined in section 5.2. To my knowledge, the proposed C_1 symmetric catalyst has not been synthesised or explored as an organocatalyst previously.

The calculations were performed using the general method described previously, in Chapter 3. Free energies in solution were derived from structures optimized in the gas phase at the ONIOM (B3LYP/6-31G**:UFF), level of theory by means of a single point calculation using M06-2X/6-31G** with the polarizable continuum model (PCM) as implemented in the Jaguar program (version 7.9), DCM (probe radius = 2.33 Å) for the Friedel-Crafts study involving acyclic imines, toluene (probe radius = 2.76 Å) for the addition of enamides and the Friedel-Crafts involving cyclic imines, benzene (probe radius = 2.33 Å) for the reduction of cyclic imines, diethyl ether (probe radius = 2.60 Å) for the reduction of α,β-imino esters as the solvent.[50] These values were used to correct the Gibbs free energy derived from the ONIOM calculations. Structures are illustrated using CYLview.[196]

5.2 Computational Validation

A variety of diverse reactions were evaluated against the C_1 symmetric catalyst. Although more were investigated, the results can be summarised by discussion of a few representative reactions.

5.2.1 Addition of large displaced nucleophiles to acyclic imines

The addition of large displaced nucleophiles to imines represents a challenging reaction class for catalyst optimisation. The requirements for high levels of enantioselectivity are unique and the most popular catalysts fail to be effective, highlighting the overall difficulty of designing and selecting catalysts for this class of transformations. Experimental studies involving the use of large displaced nucleophiles have helped establish the conceptual foundation of catalyst redesign and therefore represented an ideal class of reaction with which to test my proposal. Our aim was to determine whether appropriate modifications to the catalysts 3' substituent could result in a *Type II E* preference, similar to that observed with proximally small catalysts described in section 4.3. Through thorough mechanistic work, described in the same section, proximally large catalysts are expected to proceed with low levels of enantioinduction. I decided to further investigate the addition of enamides to N-acteyl imines reported by Tsogeva *et al.* with TRIP and the C_1 symmetric catalyst as this would allow accurate determination of the effect of the size of the 3' substituent on reaction pathway choice and efficacy (Figure 5.3).[150] The results are summarised in Figures 5.4 and 5.5.

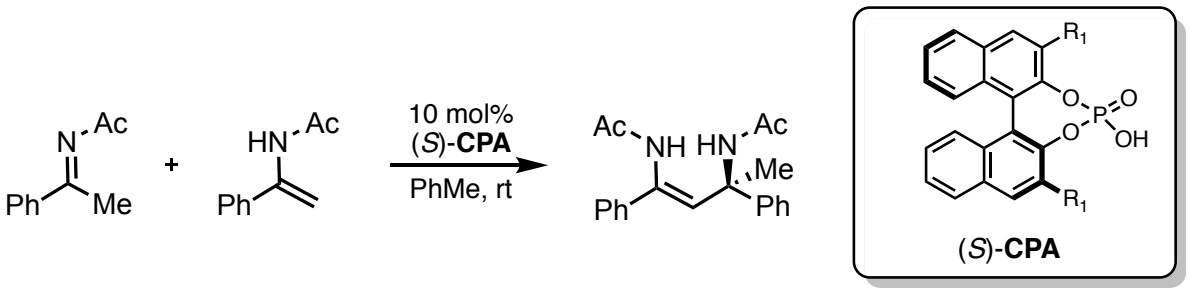

Figure 5.3. Addition of bulky enamides to imines. Through mechanistic work described in section 4.3 I have assigned the configuration at the newly formed stereocenter to be *S*. This has not yet been determined experimentally.

In agreement with expectation, TRIP has computationally been predicted to perform badly, with only a 0.5 kcal mol^{-1} energy difference between TS(*S*) and TS(*R*). This is in contrast to the C_1 symmetric catalyst in which the $\Delta\Delta G^{\ddagger}$ value corresponds to 2.4 kcal mol^{-1} revealing the catalyst to be enantioselective for this transformation. Figure 5.4 shows the qualitative trend is in good agreement with previous analysis. For TRIP, the *Type II* pathways, **TS39-*E*** and **TS39-*Z*** are disfavoured due to increased steric interactions between the reagents and the catalyst 3,3' groups. The steric interactions in the *Type II* pathways are energetically more costly when the 3,3' groups are 2,4,6-triisopropylphenyl in comparison to 9-anthryl explaining the difference in qualitative ordering of the TS between the two. The lowest energy TS pathway is *Type I E* and the directly competing one is that of *Type I Z*. The *Type I Z* places the reagents in their most compact arrangement but minimising the steric interactions between reagents and catalyst is offset by the internal substrate steric interactions present in the imine. Intriguingly, despite increasing the size of the chiral cavity, the lowest energy TS pathway for the C_1 symmetric catalyst is *Type I Z,* **TS42-*Z***. Such a preference can be attributed to the reduction in internal steric substrate interactions which are measured through the dihedral angle defined by CNCC, where the first and last C atoms in the sequence correspond to the acetyl and phenyl carbons, which has increased from 42° in **TS40-*Z*** to 51° in **TS42-*Z*** and this has the effect of pushing the acetyl and phenyl groups further apart. As expected the *Type II E* TS is favoured relative to the *Type I E* which can be attributed to the greater amount of space available in the chiral cavity allowing both, the imine to adopt a tilted disposition and the large nucleophile to fit without significant steric interactions from the catalyst. The *Type I E* and the *Type II Z* are higher in energy as these incur the largest amount of steric interactions with the catalyst. Motivated by these results, I virtually screened the C_1 symmetric catalyst in four additional reactions in which TRIP is predicted to proceed with high levels of stereoinduction.

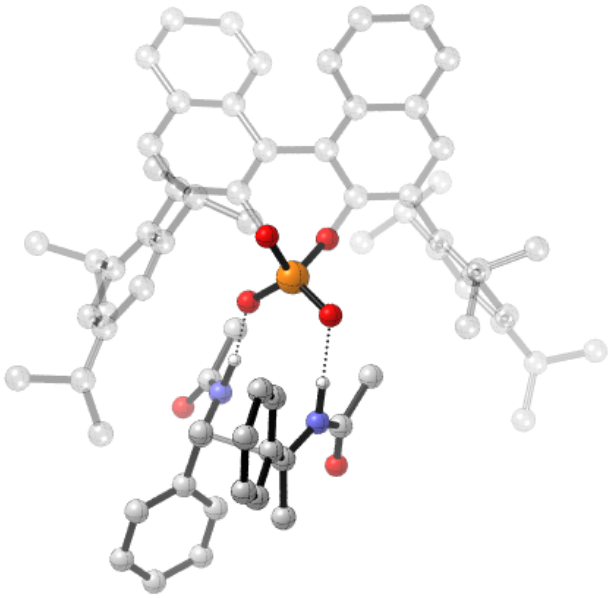

TS39-*E*: $\Delta\Delta G^{\ddagger} = +4.1$ kcal mol^{-1}, $\Delta\Delta G_{sol}^{\ddagger} = +3.8$ kcal mol^{-1}

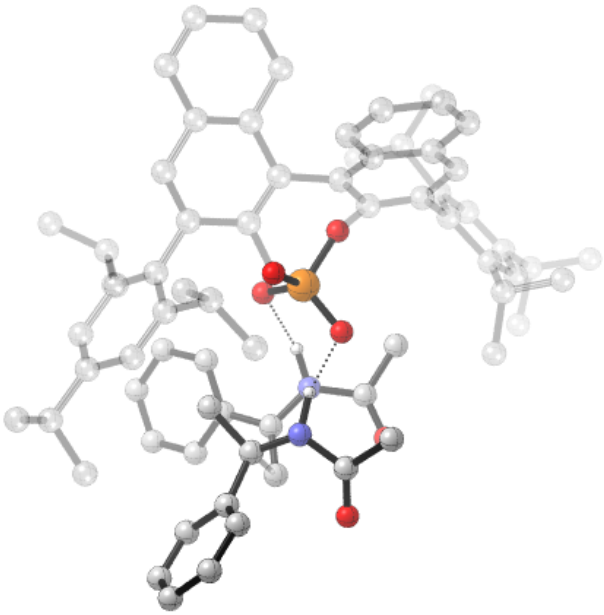

TS39-*Z*: $\Delta\Delta G^{\ddagger} = +7.6$ kcal mol^{-1}, $\Delta\Delta G_{sol}^{\ddagger} = +7.0$ kcal mol^{-1}

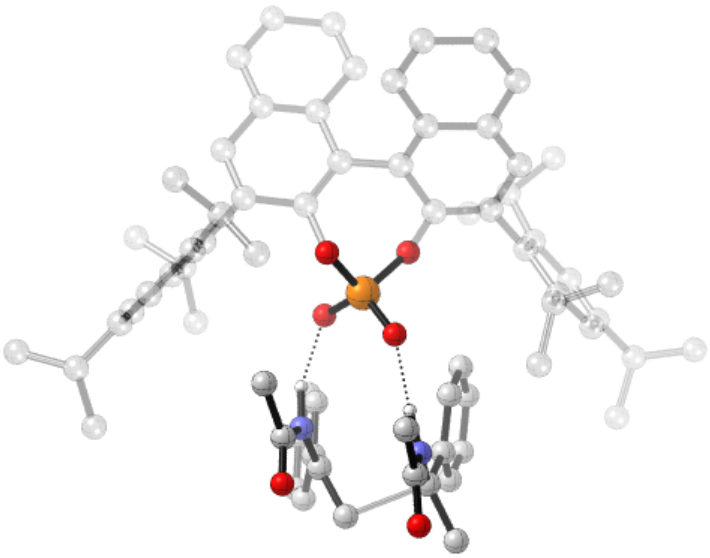

TS40-*E*: $\Delta\Delta G^{\ddagger} = 0$ kcal mol^{-1}, $\Delta\Delta G_{sol}^{\ddagger} = 0$ kcal mol^{-1}

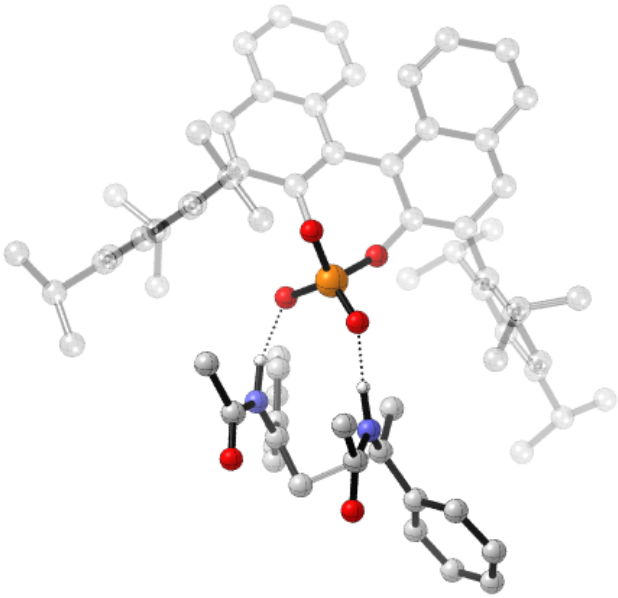

TS40-*Z*: $\Delta\Delta G^{\ddagger} = +1.1$ kcal mol^{-1}, $\Delta\Delta G_{sol}^{\ddagger} = +0.5$ kcal mol^{-1}

Figure 5.4. Competing TS for the TRIP catalysed addition of enamides. ONIOM (B3LYP/6-31G**:UFF), single-point energy M06-2X/6-31G**. Grayed-out regions were treated with UFF, and the full-colour regions were treated B3LYP/6-31G**.

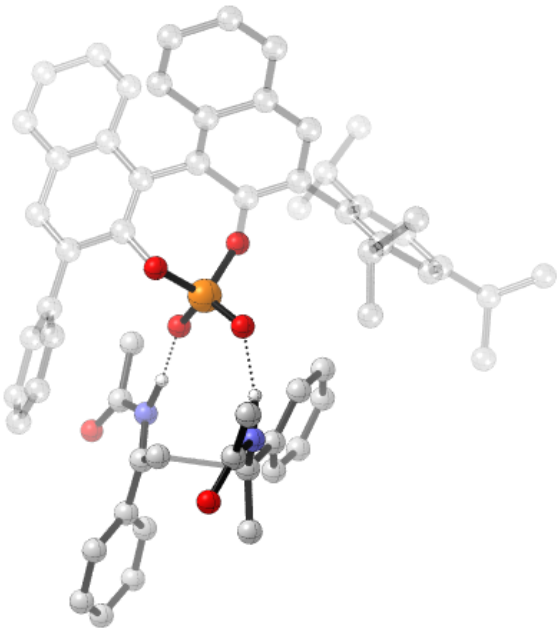

TS42-*E*: $\Delta\Delta G^{\ddagger} = +1.1$ kcal mol^{-1}, $\Delta\Delta G_{sol}^{\ddagger} = +2.4$ kcal mol^{-1}

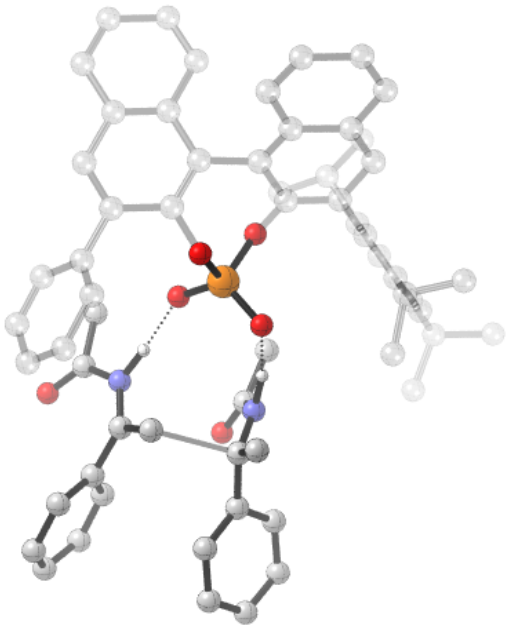

TS41-*Z*: $\Delta\Delta G^{\ddagger} = +2.2$ kcal mol^{-1}, $\Delta\Delta G_{sol}^{\ddagger} = +3.1$ kcal mol^{-1}

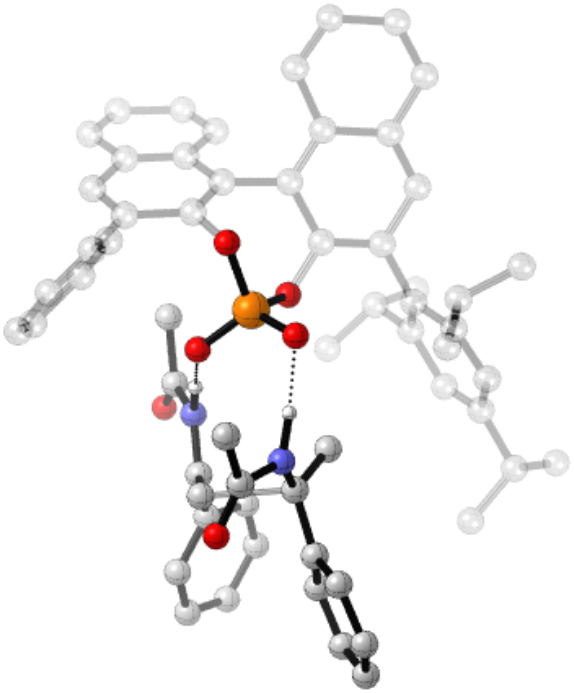

TS42-*Z*: $\Delta\Delta G^{\ddagger} = 0$ kcal mol^{-1}, $\Delta\Delta G_{sol}^{\ddagger} = 0$ kcal mol^{-1}

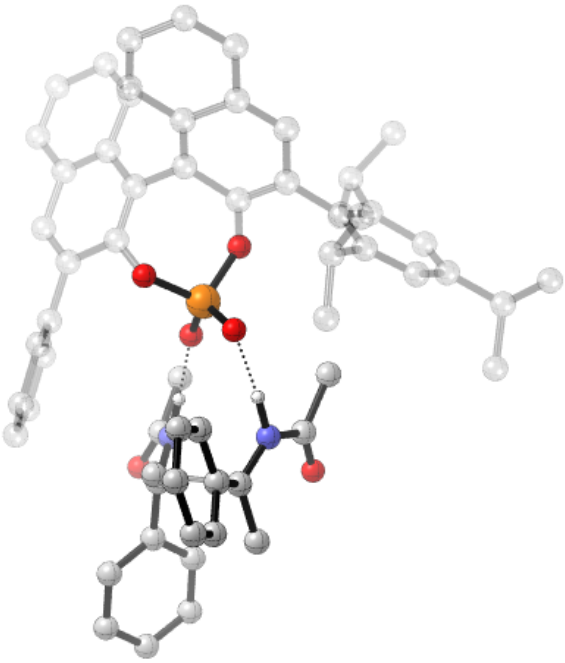

TS41-*E*: $\Delta\Delta G^{\ddagger} = -0.2$ kcal mol^{-1}, $\Delta\Delta G_{sol}^{\ddagger} = +0.9$ kcal mol^{-1}

Figure 5.5. Competing TS for the C_1 symmetric catalysed addition of enamides. ONIOM (B3LYP/6-31G**:UFF), single-point energy M06-2X/6-31G**. Grayed-out regions were treated with UFF, and the full-colour regions were treated B3LYP/6-31G**.

5.2.2 Reduction of cyclic imines

I next investigated the C_1 catalyst in the transfer hydrogenation of cyclic imines (Figure 5.6) and the results are summarised below in Figure 5.7.[141] Experimentally, for this particular example, it was found that proximally small catalysts favour *Type II* pathways and large, *Type I*, as described in Chapter 3. TS analysis revealed that a *Type II* TS was favoured with the C_1 symmetric catalyst and such a preference is due to a combination of steric factors. In the *Type II* TS pathway the Hantzsch ester experiences little steric hindrance from the small phenyl substituent and adopts a position within the catalyst cavity that has the effect of creating empty space at the back of the catalyst which can fit the large cyclic imine *via* a tilted disposition and the n-butyl substituent points towards free space. In the *Type I* TS the Hantzsch ester pushes towards the imine to allow the n-butyl group to fit at the back of the catalyst and this has the effect of forcing the cyclic imine towards the large proximal isopropyl group leading to a large energetic penalty and raising the energy of this pathway relative to the other. The RMSD between the catalyst structures in **TS43** and **TS44**, was calculated to be small, 0.6 Å, differing only in rotation of the 4-isopropyl substituent. This suggests that the catalyst structure does not change from one pathway to the other by a large extent and the 2.7 kcal mol^{-1} energy difference arises mostly from the arrangement of the reagents within the catalyst pocket in support of the above analysis. The C_1 symmetric catalyst is expected to be highly enantioselective for this transformation (>99% ee).

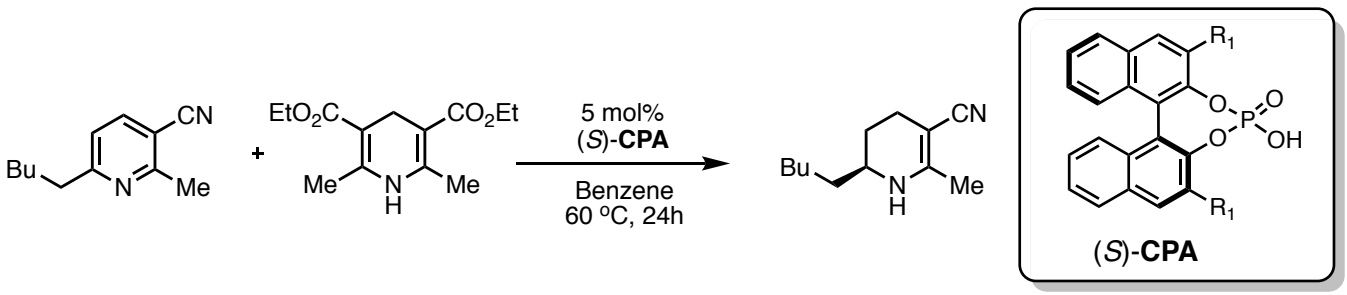

Figure 5.6. Reduction of cyclic imines by Hantzsch esters.

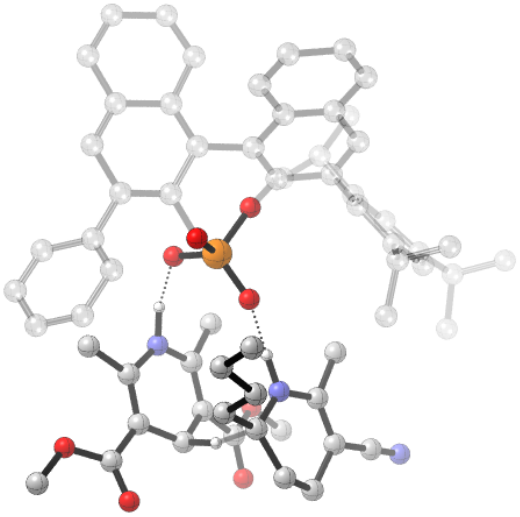

TS43: $\Delta\Delta G^{\ddagger} = 0$ **kcal mol^{-1},** $\Delta\Delta G_{sol}^{\ddagger} = 0$ **kcal mol^{-1}**

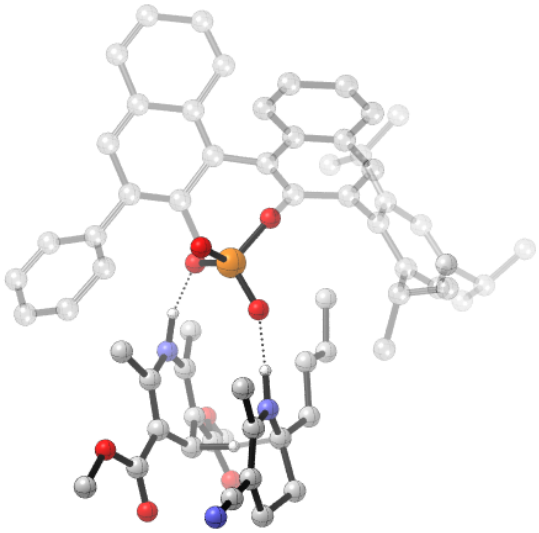

TS44: $\Delta\Delta G^{\ddagger} = +3.4$ **kcal mol^{-1},** $\Delta\Delta G_{sol}^{\ddagger} = +2.9$ **kcal mol^{-1}**

Figure 5.7. Competing TS for the C_1 symmetric catalysed reduction of cyclic imines. ONIOM (B3LYP/6-31G**:UFF), single-point energy M06-2X/6-31G**. Grayed-out regions were treated with UFF, and the full-colour regions were treated B3LYP/6-31G**.

5.2.3 Addition of indole to cyclic imines

In 2014, Maruoka reported an efficient method for the addition of indoles to cyclic imines (Figure 5.8),[247] the sense of stereoinduction is consistent with a *Type II* reaction mechanism which has been computationally verified and the results of which are included in Table 5.1. To determine if the C_1 symmetric catalyst would be enantioselective for such a transformation I studied the enantiodetermining step using the general method. Our calculations suggest that the reaction would proceed *via* a *Type II* reaction pathway as a result of minimal steric interactions between the imine and the 3,3' substituents. Rotating the imine, 180°, with respect to the 3,3' groups, increases the steric interactions between the ester chain and the substituent at the 3 position. This results in lengthening of the hydrogen bond that binds the imine to the catalyst from 1.59 Å to 1.67 Å leading the *Type I* pathway to be higher in energy.

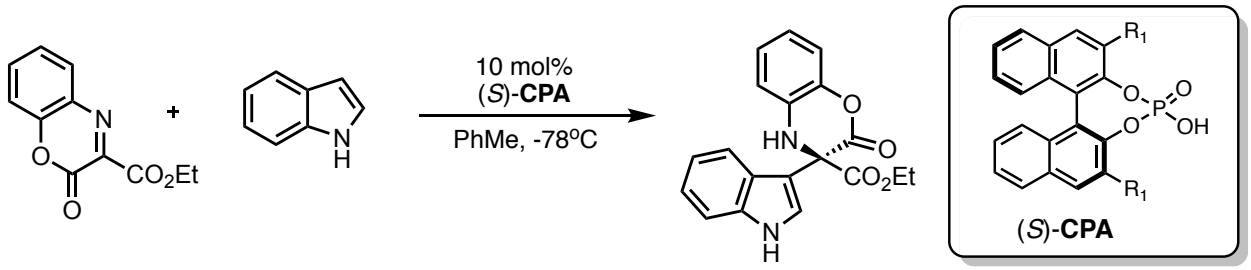

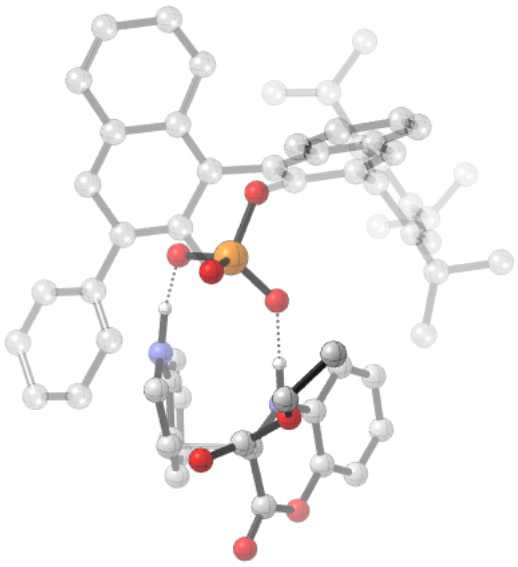

TS45: $\Delta\Delta G^{\ddagger}$ = 0 kcal mol^{-1}, $\Delta\Delta G_{sol}^{\ddagger}$ = 0 kcal mol^{-1}

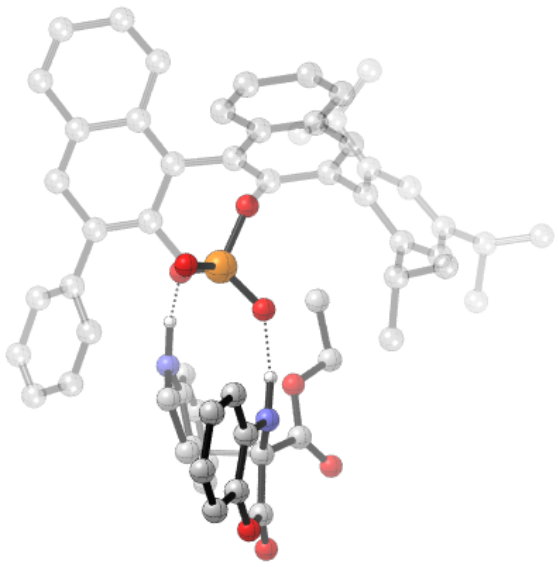

TS46: $\Delta\Delta G^{\ddagger}$ = +3.0 kcal mol^{-1}, $\Delta\Delta G_{sol}^{\ddagger}$ = +2.7 kcal mol^{-1}

Figure 5.8. Reaction scheme and competing TS for the C_1 symmetric catalysed addition of indole to cyclic imines. ONIOM (B3LYP/6-31G**:UFF), single-point energy M06-2X/6-31G**. Grayed-out regions were treated with UFF, and the full-colour regions were treated B3LYP/6-31G**.

Table 5.1. Competing TS for the chiral phosphoric acid catalysed addition of indole to cyclic imines. ONIOM (B3LYP/6-31G**:UFF), single-point energy M06-2X/6-31G**.

Mechanism (Catalyst)	$\Delta\Delta G_{sol}^{\ddagger}$
Type II (C_1 symmetric), **TS45**	0
Type I (C_1 symmetric), **TS46**	+2.7
Type II (Mesityl), **TS47**	0
Type II (Mesityl), **TS48**	+2.5

5.2.4 Addition of indole to acyclic imines

Section 4.2 describes the computational investigation into the effect of the 3,3' substituents on the Friedel-Crafts reaction of indoles and N-acetyl imines proceeding *via* a *Type II* reaction pathway (Figure 5.9).[28] The correct catalyst has both large proximal sterics and medium AREA(θ). The C_1 symmetric catalyst was virtually screened against the reaction conditions outlined by Zhou *et al.* and the results are summarised in Figure 5.10. The favoured reaction pathway, *Type II E*, is maintained with this catalyst and such a preference is attributed to a number of unfavourable steric interactions in the diastereomeric TS. The *Type I Z*, *Type II Z* and *E* pathways are close in energy and disfavoured relative to the *Type I E* by 2.1-2.5 kcal mol^{-1}. The *Type I Z* experiences a significant steric interaction between the methyl group on the imine and the isopropyl group on the catalyst substituent. The steric interaction is reduced in part by increasing the dihedral angle defined by the atoms CNCC, where the first and last C atoms in the sequence correspond to the acetyl and phenyl carbons, to 57° and this rotates the methyl group away from the catalyst. The *Type II Z* TS is more compact to minimise steric interactions between the imine and catalyst reducing the dihedral angle to only 37°, the reduction in steric interaction between the imine and the catalyst is offset by the internal substrate steric interactions. The *Type I E* is higher in energy as the largest imine substituent, the phenyl group, is placed in close proximity to the catalyst 3-substituent. The large energy differences, 2.1 kcal mol^{-1}, between the TS leading to competing products reveal the catalyst to be enantioselective for this reaction, once again, demonstrating the generality of this catalyst.

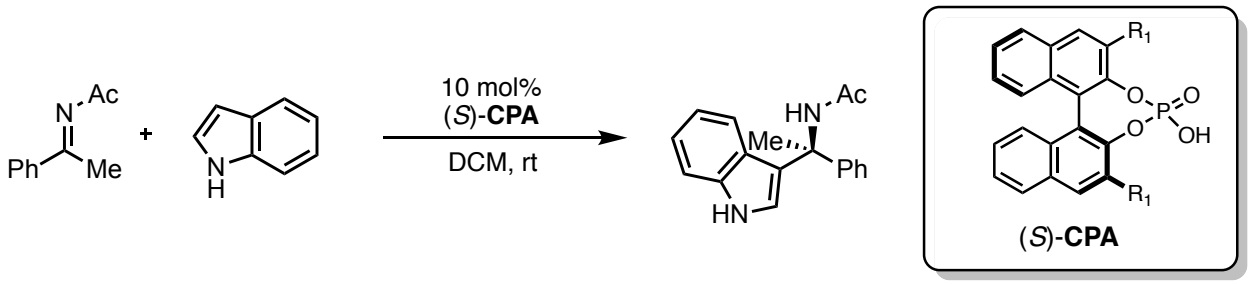

Figure 5.9. Addition of indole to acyclic imines.

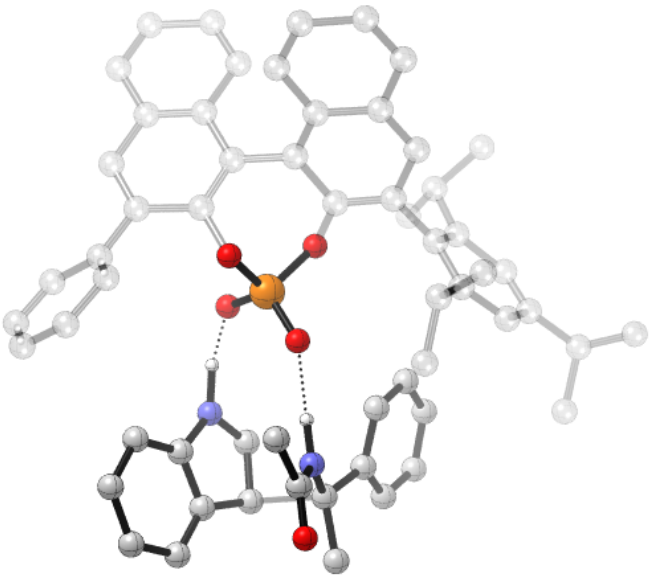

TS50-*E*: $\Delta\Delta G^{\ddagger}$ = +2.8 kcal mol^{-1}, $\Delta\Delta G_{sol}^{\ddagger}$ = +2.2 kcal mol^{-1}

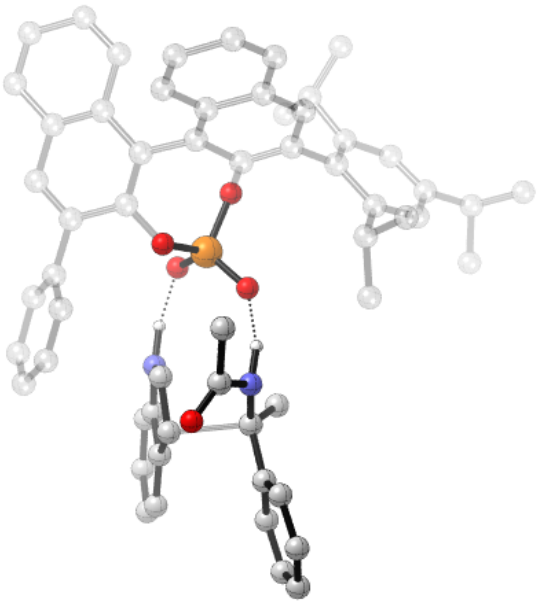

TS50-*Z*: $\Delta\Delta G^{\ddagger}$ = +2.6 kcal mol^{-1}, $\Delta\Delta G_{sol}^{\ddagger}$ = +2.5 kcal mol^{-1}

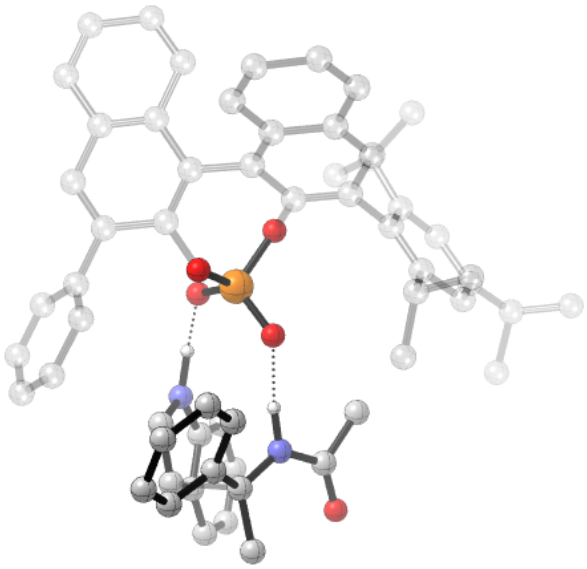

TS49-*E*: $\Delta\Delta G^{\ddagger}$ = 0 kcal mol^{-1}, $\Delta\Delta G_{sol}^{\ddagger}$ = 0 kcal mol^{-1}

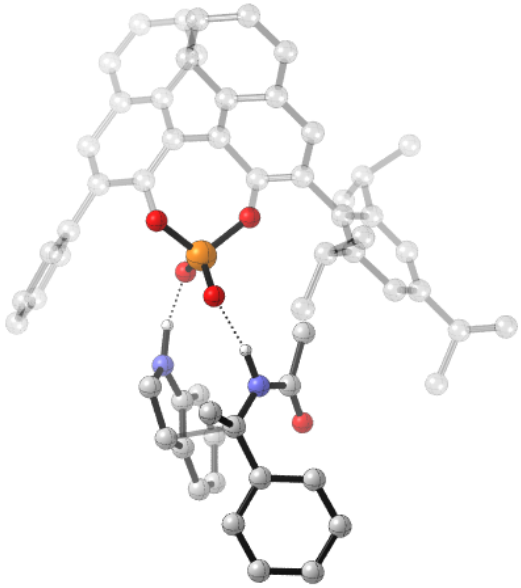

TS49-*Z*: $\Delta\Delta G^{\ddagger}$ = +3.4 kcal mol^{-1}, $\Delta\Delta G_{sol}^{\ddagger}$ = +2.1 kcal mol^{-1}

Figure 5.10. Competing TS for the C_1 symmetric catalysed addition of indole to acyclic imines. ONIOM (B3LYP/6-31G**:UFF), single-point energy M06-2X/6-31G**. Grayed-out regions were treated with UFF, and the full-colour regions were treated B3LYP/6-31G**.

5.2.5 Reduction of acyclic imines

As a final test, the catalyst was screened against the reduction of acyclic imines using a Hantzsch ester (Figure 5.11) in which the pathway *Type I E* or *Type I Z* can be modulated by changing the substituents at the 3,3' positions as described in Section 3.2.[41,114b] The reaction proceeds *via* a *Type II E* pathway (Figure 5.12). This is attributed to the arrangement of reagents inside the catalyst cavity. The Hantzsch ester experiences little steric hindrance from the small phenyl substituent and adopts a position within the catalyst cavity that has the effect of creating empty space at the back of the catalyst in which the large N-substituent can be placed with little steric hindrance. The TS pathway leading to the competing product has been calculated to be +5.4 kcal mol^{-1} and such a large energetic preference originates from increased steric interactions between the large catalyst substituent and the styrene C-substituent. The *Type II Z* TS was calculated to be the highest energy pathway and is due to steric interactions between the proximal isopropyl group and the N-substituent. The imine cannot adopt a tilted disposition to minimise this bad interaction, as this would introduce a secondary steric interaction with the styrene C-substituent and remote isopropyl group.

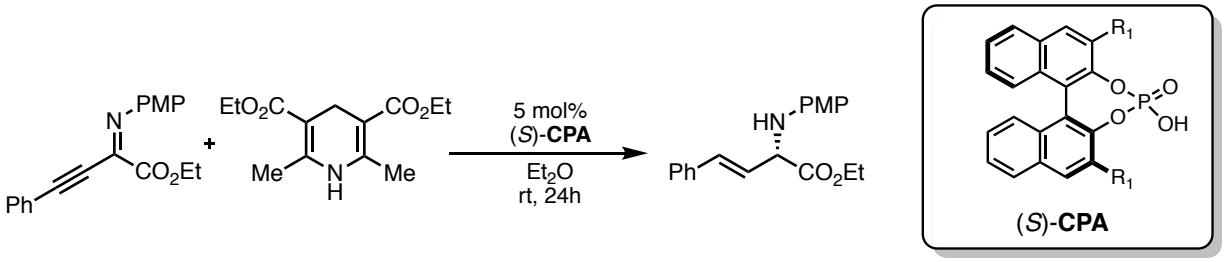

Figure 5.11. Reduction of acyclic imines by Hantzsch esters.

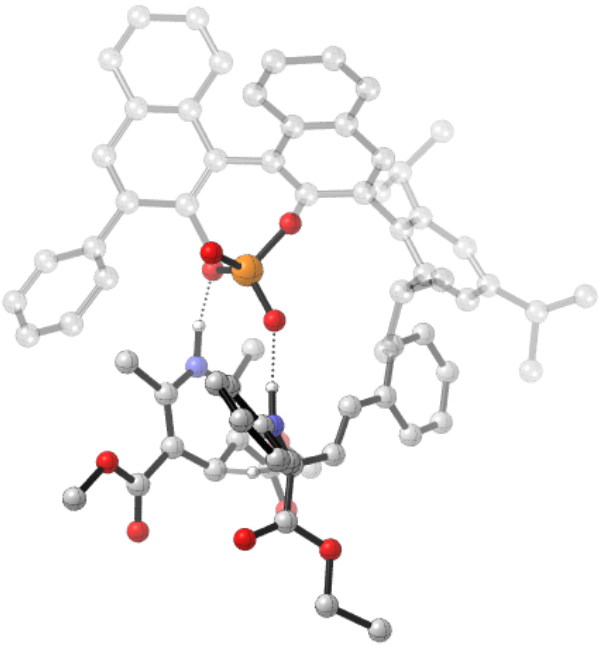

TS52-*E*: $\Delta\Delta G^{\ddagger}$ = +6.2 kcal mol^{-1}, $\Delta\Delta G_{sol}^{\ddagger}$ = +5.4 kcal mol^{-1}

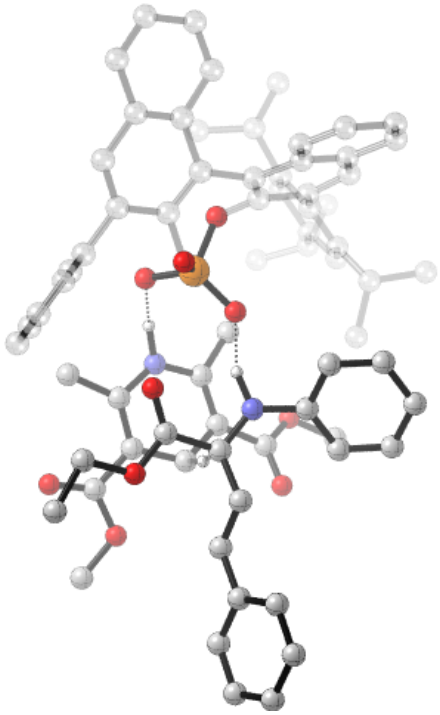

TS51-*Z*: $\Delta\Delta G^{\ddagger}$ = +6.5 kcal mol^{-1}, $\Delta\Delta G_{sol}^{\ddagger}$ = +7.1 kcal mol^{-1}

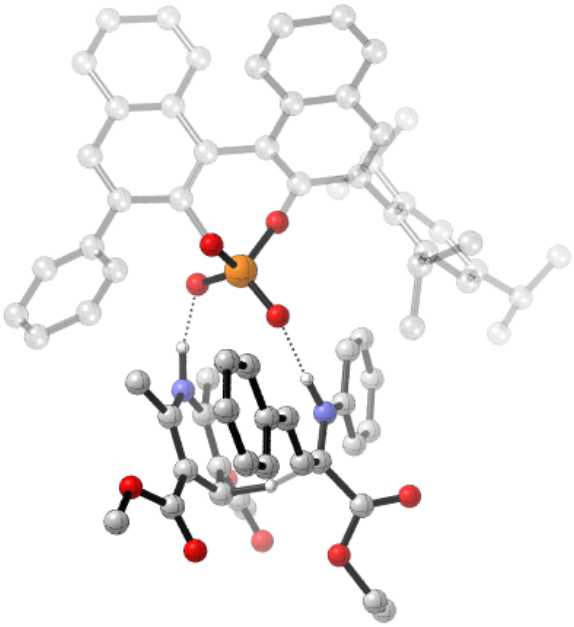

TS52-*E:* $\Delta\Delta G^{\ddagger}$ = 0 kcal mol^{-1}, $\Delta\Delta G_{sol}^{\ddagger}$ = 0 kcal mol^{-1}

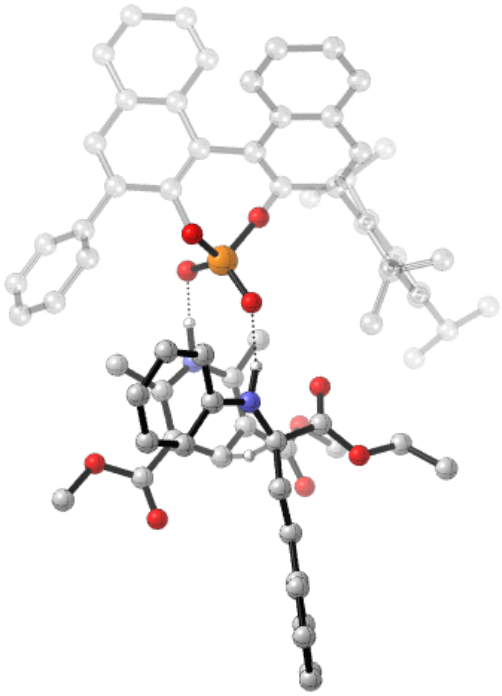

TS52-*Z*: $\Delta\Delta G^{\ddagger}$ = +2.6 kcal mol^{-1}, $\Delta\Delta G_{sol}^{\ddagger}$ = +3.3 kcal mol^{-1}

Figure 5.12. Competing TS for the C_1 symmetric catalysed reduction of acyclic imines. ONIOM (B3LYP/6-31G**:UFF), single-point energy M06-2X/6-31G**. Grayed-out regions were treated with UFF, and the full-colour regions were treated B3LYP/6-31G**.

5.2.6 Summary of catalyst trends

Several broad trends have emerged from the computational data. First the C_1 catalyst exhibits a strong preference for *Type II* reaction pathways with four out of the five reactions proceeding through such. *Type I Z* reactions can be favoured but this may be a consequence of structural peculiarities of the reactant combination. The behaviour with this catalyst is less erratic showing, in these examples, increased consistency in TS pathway choice and less sensitivity towards the sterics of the individual reactant combination, suggesting that the reactions were mainly under catalyst control. This combination is advantageous for both, predicting sense of enantioselectivity and catalyst design. In two of the three reactions, were possible, the two lowest lying TS pathways produced the same enantiomer, which is unique to this catalyst and highly beneficial in terms of enhancing enantioselectivity values. The overall computed enantioselectivites are relatively similar across the five reactions studied (>99%). The impact of the phenyl substituent has been even more intriguing and qualitatively one can understand its effect in terms of biasing all processes towards a *Type II* TS pathway regardless of the reactants employed. To this end, I set out to develop a modular synthesis of the C_1 BINOL-derived chiral phosphoric acid that would allow for the late stage introduction of diversity at the 3' position, enabling the rapid preparation of a library of catalyst from a common intermediate for further evaluation on the effect of the size of this substituent on product ee. The synthesis is outlined in the next section.

5.3 Proposed Synthetic Pathway to the C_1 Symmetric Catalyst

I envisioned that the computationally verified highly versatile C_1 symmetric catalyst could be obtained through a seven step synthetic sequence outlined in Figure 5.13. Starting from (*S*)-BINOL, MOM protection,[249] followed by selective bromination,[250] would provide the coupling handle for the Kumada.[251] Appendage of the large group at the 3-position is followed by a second bromination and coupling,[252] furnishing **12**. The MOM groups are removed *via* acidic hydrolysis and phoshorylation would afford the catalyst, **CPA-20**. These steps have proven to be robust and work for a variety of chiral phosphoric acids varying at the 3,3' position providing evidence for the synthetic viability of the catalyst. Unfortunately due to time constraints the synthesis is only a proposal and is currently being synthesised and tested in the Goodman lab by another member. The anticipated route is modular allowing incorporation of other 3' substituents to investigate experimentally the effect of the size of this substituent on enantioselectivity. The (*R*) enantiomeric series can be accessed in a similar manner. The route appears straightforward and would require only two additional steps in comparison to the synthesis of the traditional C_2 symmetric catalysts.

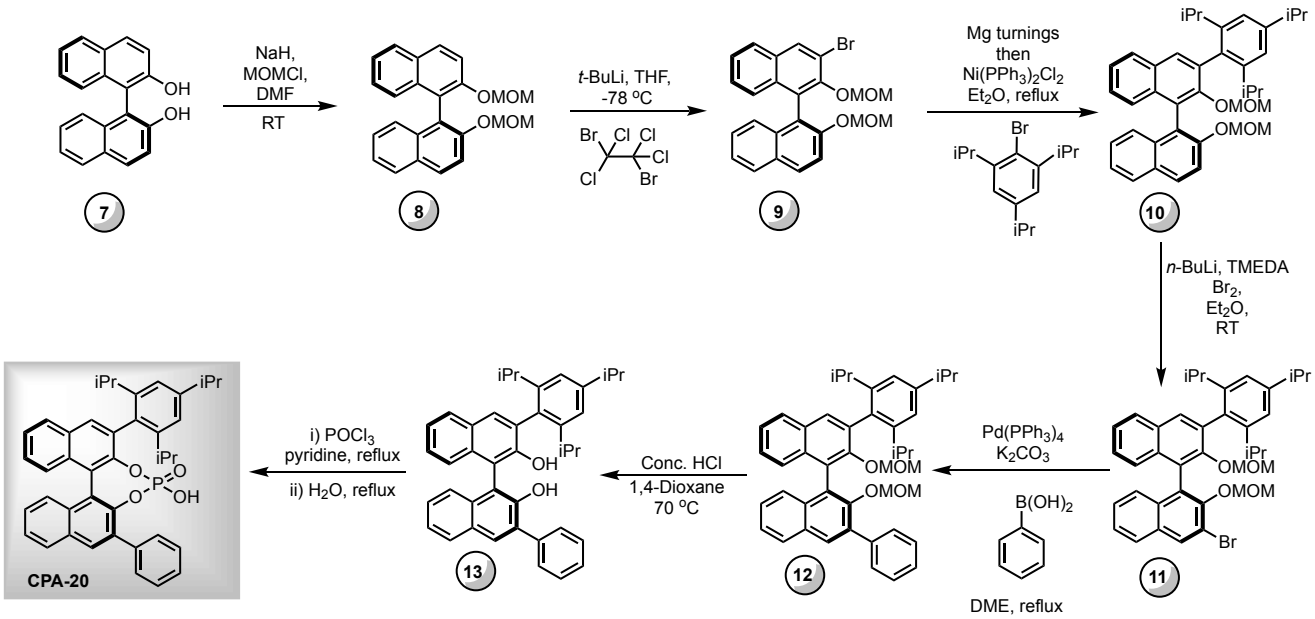

Figure 5.13. Proposed synthetic route to the C_1 symmetric catalyst.

5.4 Conclusions

In this section I proposed a non-intuitive modification of the standard chiral phosphoric acid, incorporating a C_1 symmetric scaffold. By using QM/MM hybrid calculations I have determined that the catalyst is likely to be highly versatile and selective. This is an innovative approach to asymmetric catalyst development in which mechanistic understanding leads experiment, which is extremely rare. Our results suggest that, in addition to being an easily modified catalyst substituent the phenyl serves an organizational function other than simply creating a sterically hindered environment. Such a design principle is conceptually novel. Analysis of the computational data suggested that the modeled reactions were mainly under catalyst control, as substrate features did not affect the enantioselectivity in a considerable, systematic manner. Most notably the catalyst has not been synthesized before but should be through, justification in section 5.3, synthetically viable. The synthesis and testing of this catalyst will be highly useful in assessing the reliability of the present predictions. I believe that the C_1 symmetric catalyst described here presents a second generation of BINOL-derived catalysts. This catalyst is expected to solve the versatility challenge in Brønsted acid catalysis and could also be widely applicable beyond this reaction class.

Chapter 6

6 Transfer Hydrogenation of *ortho*-hydroxyimines

6.1 Background and Methods

Amines are a key feature of many biologically active compounds and methods for the construction of stereogenic carbon-nitrogen bonds have been the focus of a great deal of investigation. The reduction of imines to form amines in an enantioselective fashion through the use of chiral metal catalysts and a hydride source has been studied extensively. A wide variety of metals and chiral ligands have been used but most methods rely on molecular hydrogen, borane or silyl species as a source of hydride. Notable variants of this methodology have been developed through the work of Pflatz,[253] Mukaiyama,[254] and Buchwald.[255] These methods represent significant progress towards a general procedure but suffer from many limitations such as narrow substrate scope and the need for high hydrogen pressures. Furthermore, these methods generally involve the use of transition metal catalysts, which have additional limitations such as air and moisture sensitivity adding a degree of experimental difficulty, as well as cost and toxicity. Current research has focused on developing a general enantioselective reduction procedure using mild, non-toxic reagents through the application of Brønsted acid catalysis.

The effective activation of imines using chiral phosphoric acids led a number of groups to investigate the possibility of performing enantioselective hydride additions to ketimines, which, the addition of nucleophiles had previously, been investigated only on aldimine systems. This strategy proved to be very successful through the work of Rueping,[32] List,[57] and Macmillan.[31] Others have since explored the reaction scope extensively.[114b,135,213,219-220] Mechanistic investigations have found this important class of reactions to proceed *via* a *Type I* bifunctional TS.[20] In 2010 Wang *et al.* reported that the chiral phosphoric acid catalysed transfer hydrogenation of ketimines facilitated by Hantzsch esters could be extended to *ortho*-hydroxybenzophenone-derived substrates to afford the corresponding amines in excellent yield and enantioselectivity (Figure 6.1).[256] Wang suggested a ten membered transition state resembling Akiyama's model,[18,70] with activation of only the imine through protonation and a second hydrogen bonding interaction from the *ortho*-hydroxylaryl

moiety to the P=O of the catalyst. The nucleophile would then be delivered to the most accessible face. Such a model in which only one of the reactants is activated has been found to be higher in energy than compared to those involving bifunctional activation.[25] Despite this, NMR evidence suggested that the phenolic proton was bound to the catalyst.[257] The group also noted that removing the hydroxyl group at the *ortho* position greatly slowed the reaction, supporting the hypothesis of an important productive binding site to the catalyst *via* a hydrogen bond to this position.[258] The uncertainty associated with the mechanism for this important class of substrates makes prediction of the sense of enantioinduction very difficult for novel reactants. No known computational model can explain these experimental observations.

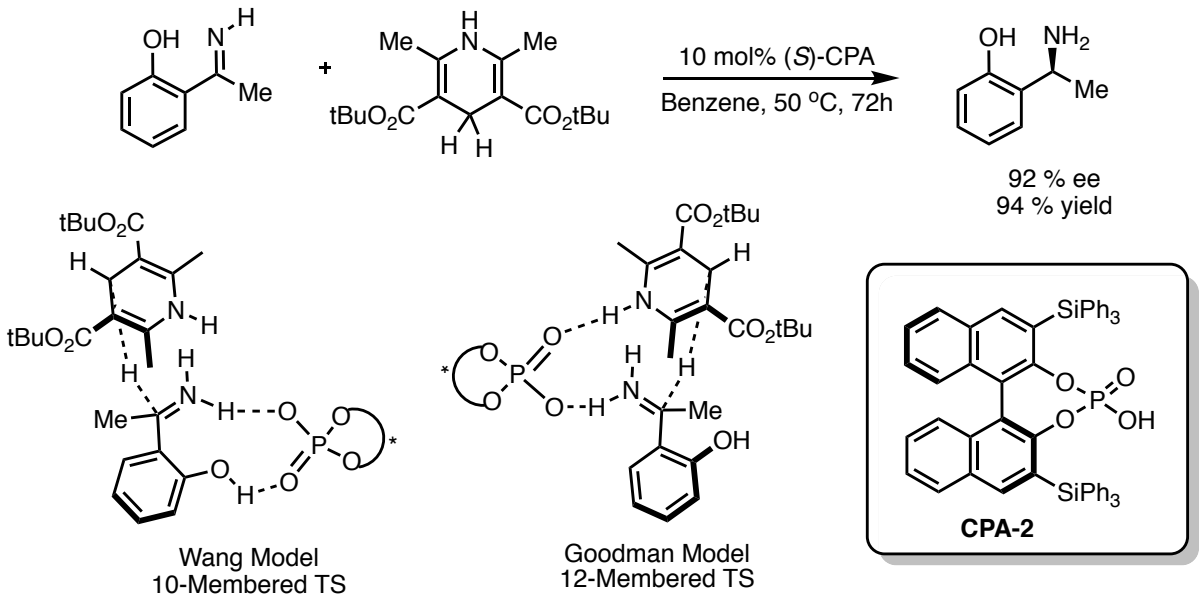

Figure 6.1. Asymmetric transfer hydrogenation of *ortho*-hydroxybenzophenone derived imines.

The preferred reaction pathway was first investigated using buta-1,3-diene-1,4-diol-phosphoric acid as a model for the catalyst, before studying the full molecular system. All reagents and transition states were located first, by a conformational search in MacroModel (version 9.9)[54] using the OPLS-2005 force field.[184-186] Selected conformers within 10 kJ mol^{-1} of the minimum were optimized using the Gaussian 09 (revision D.01).[35] The B3LYP density functional,[43-44] and split-valence polarized 6-31G** basis set,[193-194] were used for all geometry optimizations. Single-point energies were taken using the M06-2X density functional,[46] and 6-31G** basis set. This energy was used to correct the gas-phase energy obtained from the B3LYP calculations. The presence of stationary points along the potential energy surface (PES) was confirmed as being either minima or transition states by the presence of zero or a single imaginary frequency, respectively.

The calculations for the full catalyst system were performed using the general method described previously, in Chapter 3. Free energies in solution were derived from structures optimized in the gas phase at the ONIOM (B3LYP/6-31G**:UFF), level of theory by means of a single point calculation using M06-2X/6-31G** with the polarizable continuum model (PCM) as implemented in the Jaguar program (version 7.9), using benzene (probe radius = 2.60 Å) as the solvent.[50] These values were used to correct the Gibbs free energy derived from the ONIOM calculations. Structures are illustrated using CYLview.[196]

Detailed DFT and ONIOM transition state calculations of this important reaction suggest that the process involves both hydrogen bonding from the hydroxyl group on the imine and the nucleophile's proton to the phosphate catalyst. This mechanistic pathway is lower in energy than the conventional, consistent with the experimentally observed increased rates of reaction with imines that are not derived from *ortho*-hydroxybenzophenone.

6.2 Reaction Mechanism

Investigations of the reaction using the simplified phosphoric acid model, buta-1,3-diene-1,4-diol-phosphoric acid considered three different pathways summarised in Figure 6.2**.** To reduce the computational time slightly, simpler molecules were used: the *tert*-butyl groups of the Hantzsch ester were replaced by methyl. The transition state in which the catalyst establishes two interactions with the imine (Wang's model) leads to *Mechanism H.* The study revealed five unique transition states corresponding to this mechanism. Only the lowest energy TS are shown in Figure 6.2. The catalyst can establish two points of contact to the nitrogen on the imine and the proton on the Hantzsch ester leading to *Mechanism I*. A total of twelve transition states were located, five of these corresponded to *E* imine configuration, the rest, *Z*. These transition states where calculated to be disfavoured relative to *Mechanism J* in which the phosphate catalyst binds to Hantzsch ester and the *ortho*-hydroxyl aryl group. Assuming the reaction is under Curtin-Hammett control, the reaction will proceed *via* the lowest energy TS. **TS55**[259] was found to be the lowest energy and tightest transition state with the shortest hydrogen bonds from imine to catalyst (1.53 Å). This suggests the binding mode change between the imine and the catalyst is due to increased strength of the hydrogen bonding in *Mechanism J* relative to *Mechanism I*. *Mechanism J* is 7.9 kcal mol^{-1} lower in energy than the conventional bifunctional *Mechanism I*, meaning the rate of reaction for these substrates would be expected to be faster. Comparing the $\Delta G^{\ddagger}$ values (quoted relative to infinitely separated reagents) reveals that the rate of reaction for these substrates to be faster, the $\Delta G^{\ddagger}$ value for **TS55** was calculated to be 3.0 kcal mol^{1} which is significantly lower than that obtained for **TS54**, 10.8 kcal mol^{-1}. These calculations are in excellent agreement with the experimental observations as imines that did not have the *ortho*-hydroxyl group to proceed through this lower energy pathway showed no reaction under the same conditions.

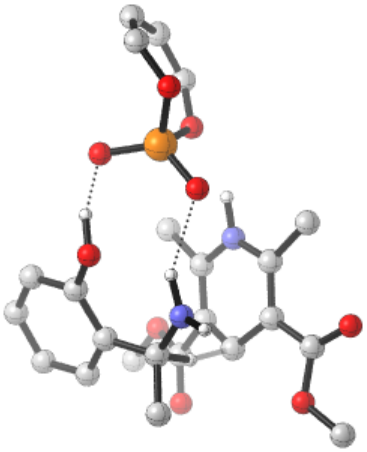

TS53: $\Delta\Delta G^{\ddagger}$ = +10.4 kcal mol^{-1}

Mechanism H

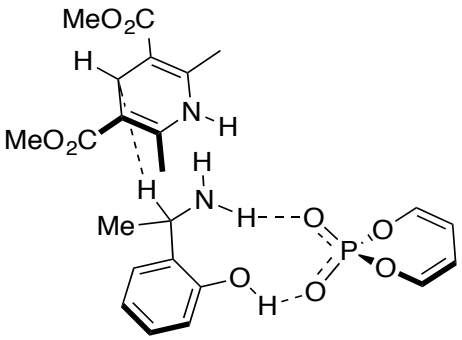

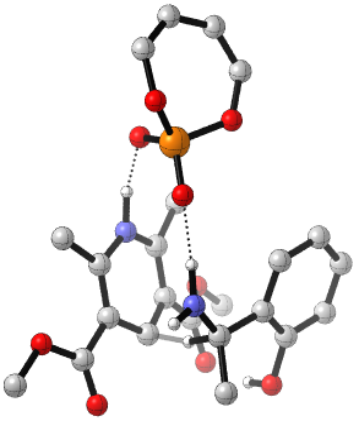

TS54: $\Delta\Delta G^{\ddagger}$ = +7.9 kcal mol^{-1}

Mechanism I

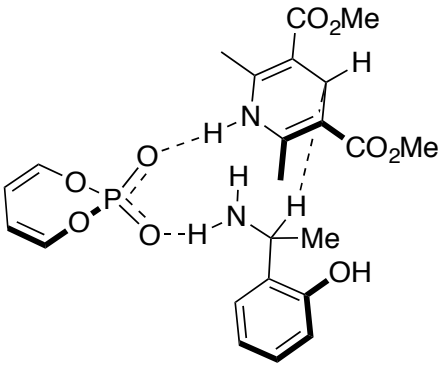

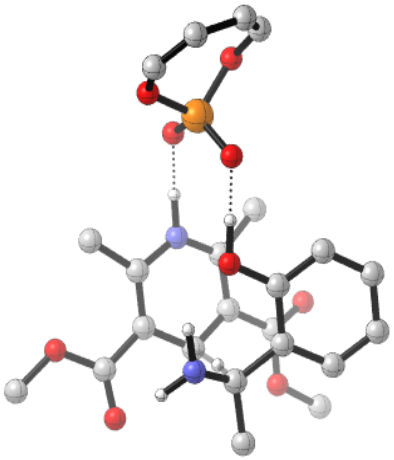

TS55: $\Delta\Delta G^{\ddagger}$ = 0 kcal mol^{-1}

Mechanism J

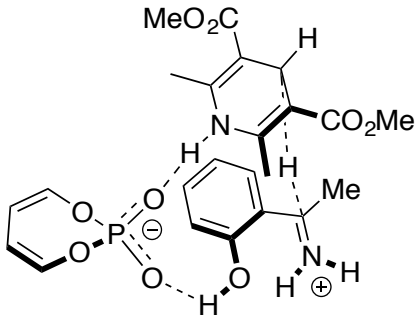

Figure 6.2. Mechanistic proposals and the calculated free energies with the model catalyst. Geometries B3LYP/6-31G**, single-point energy M06-2X/6-31G**.

The reaction is catalysed by phosphoric acids through a proton transfer that activates the imine. This can happen through direct protonation of the imine by the phosphoric acid (**PT2**) or by the hydroxyl group (**PT1**). Our calculations on the model system reveal that the lowest energy pathway is **PT1** and the proton is transferred intramolecularly (Figure 6.3). The protonation pathways **PT1** and **PT2** in which the complex is ternary (Hantzsch ester also coordinating to the catalyst) could not be located. I cannot exclude the possibility of the protonation happening through the ternary complex being correct, but my calculations indicate that the intramolecular proton transfer is most feasible. The barrier, $\Delta G^{\ddagger}$, for protonation in absence of the chiral phosphoric acid was calculated to be 2.8 kcal mol^{-1} and the catalyst lowers this to 0 kcal mol^{-1}.

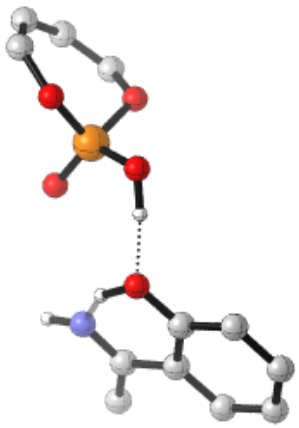

PT1: $\Delta\Delta G^{\ddagger}$ = 0 kcal mol^{-1}, $\Delta\Delta G_{sol}^{\ddagger}$ = 0 kcal mol^{-1}

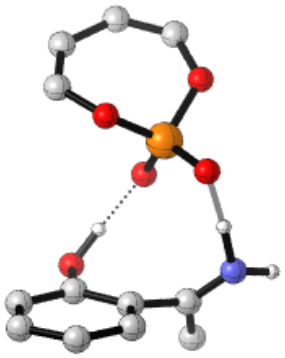

PT2: $\Delta\Delta G^{\ddagger}$ = +2.2 kcal mol^{-1}, $\Delta\Delta G_{sol}^{\ddagger}$ = +1.0 kcal mol^{-1}

Figure 6.3. TS for the protonation of imine catalysed by a model phosphoric acid.

I am, therefore, able to conclude that the reaction proceeds *via* a two-step process. The imine is first activated for nucleophilic attack *via* intramolecular proton transfer from the hydroxyl group on the imine, followed by, hydride addition to the imine facilitated by the chiral phosphoric acid in accordance with *Mechanism J*.

6.3 Origins of Stereoinduction

There are eight reasonable diastereomeric transition states for these reactions, resulting from three mechanisms and a number of different arrangements of the imine. Our model studies allowed us to reduce this number to six, as the energy differences between the bifunctional and dual modes of activation are so large that not even the catalysts steric interactions could change this preference (Figure 6.2). The lowest energy conformations of the diastereoisomeric transition states are shown in Figure 6.4. For each of the bifunctional mechanisms, the *N*-substituent of the imine can be directed away from the front of the 3,3' substituents on the binaphthol ring leading to a *Type I* reaction pathway or towards, *Type II*. Additionally the imine can exist as either the *E* or *Z* isomers for the NH binding mode. The OOH binding mode is restricted to proceed *via* the *E* configuration, geometry optimizations of *Z* TS showed that these structures converged into the dual mode of activation (*Mechanism H*) and were disfavoured by 18.8 kcal mol^{-1} or more relative to **TS58-*E***. Therefore, TS involving the *Z* configuration and this binding mode was not investigated further. Thorough conformational searching of the possible catalyst-substrate conformations located a total of 72 transition states. The calculations suggest that the reaction proceeds *via* an OOH-*Type II E* reaction mechanism, **TS58-*E***. This is favoured relative to the *Type I E*, **TS59-*E***, by 1.9 kcal mol^{-1}, which is in good agreement with the experimentally observed sense of enantioselectivity. The *ortho*-hydroxy aryl group of the imine prefers to be pointed away from the catalyst 3,3' substituents and occupies the free space at the front left hand side of the catalyst. The imine adopts a tilted position, minimising the steric interactions of the *N*-substituent and the 3,3' group. In the *Type I E* TS the aromatic group is orientated towards the back phenyl ring of the $SiPh_3$ 3,3' substituent. This leads to a large energetic penalty and increases the energy of the *Type I E* TS relative to the *Type II E*. The NH *Type II E* TS also avoids the unfavourable steric interactions between the *ortho*-hydoxy group and the 3,3' substituent. However, despite the structural similarities, the NH binding mode was strongly disfavoured confirming the same trends as the model catalyst. The most favourable TS, **TS58-*E*** was the tightest of all the TS with the shortest hydrogen bonds. The strength of the hydrogen bond between **TS58-*E*** and **TS56-*E*** is reduced; the angle of the hydrogen bond deviates modestly away from linearity 176° to 171° and lengthens from 1.48 Å to 1.81 Å. Therefore, the reasons for the large energetic preference of OOH-*Type II E* TS originates from both steric and electronic factors. Relative populations of transition states were predicted at the temperature they were performed from the corrected Gibbs free energy

differences and based on Boltzmann distribution analysis. The computed enantiomeric excess (ee) was 90%, which is very close to the experimental value (92%).

I have summarised the calculations into a qualitative model (Figure 6.5, bottom, the OOH model for *ortho-OH* substrates) to explain and predict the stereochemical outcome in the chiral phosphoric acid catalysed transfer hydrogenations of *ortho*-hydroxy ketimines. The model is built on the OOH-binding mode in which the aromatic substituent is orientated towards the empty pocket of the catalyst. Increasing the sterics remote from the phosphoric acid maximises the steric repulsions between the *ortho*-hydroxy aryl group and the 3,3' substituents in the *Type I E* TS leading to high levels of enantioselectivity.

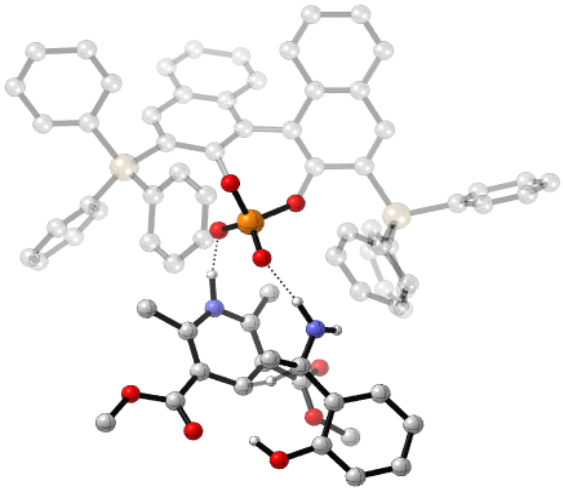

TS56-*Z*: $\Delta\Delta G^{\ddagger}$ = +12.8 kcal mol^{-1}, $\Delta\Delta G_{sol}^{\ddagger}$ = +12.5 kcal mol^{-1}

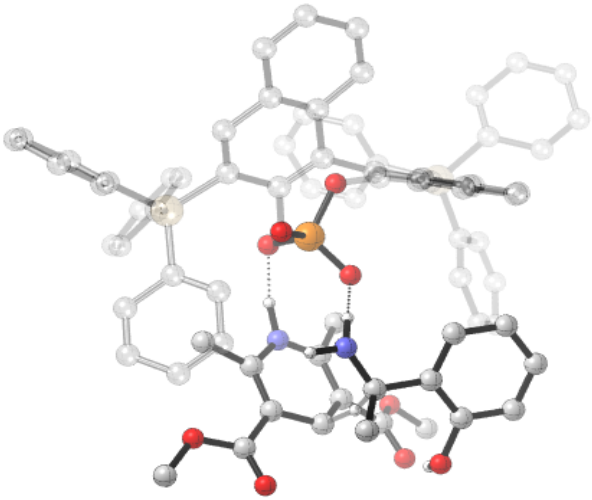

TS57-*E*: $\Delta\Delta G^{\ddagger}$ = +12.9 kcal mol^{-1}, $\Delta\Delta G_{sol}^{\ddagger}$ = +13.1 kcal mol^{-1}

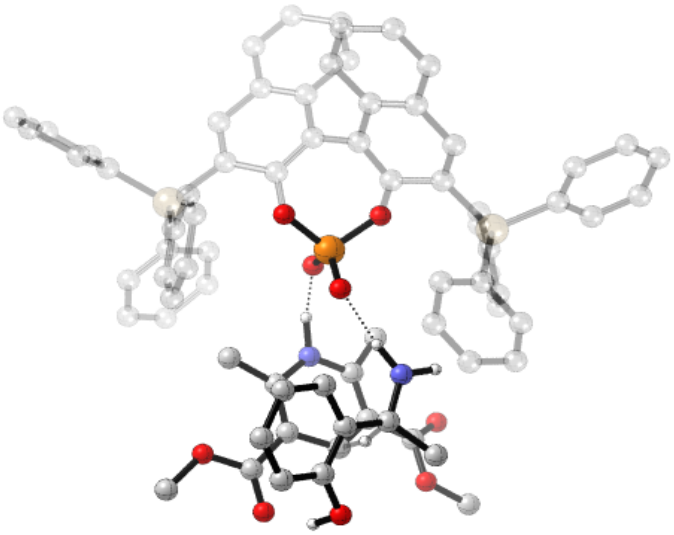

TS56-*E*: $\Delta\Delta G^{\ddagger}$ = +9.5 kcal mol^{-1}, $\Delta\Delta G_{sol}^{\ddagger}$ = +9.9 kcal mol^{-1}

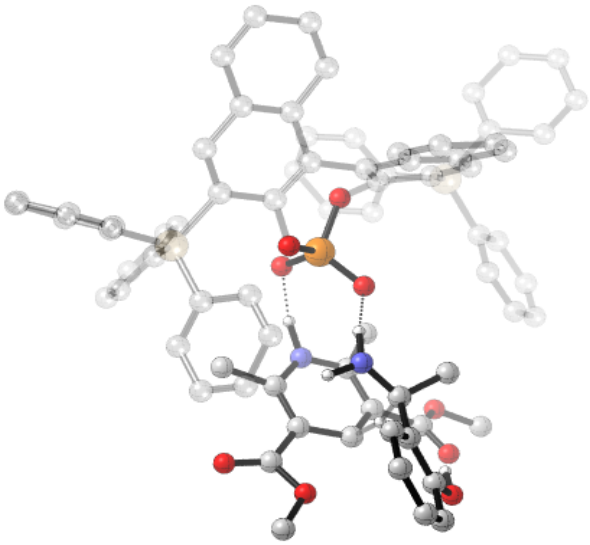

TS57-*Z*: $\Delta\Delta G^{\ddagger}$ = +11.3 kcal mol^{-1}, $\Delta\Delta G_{sol}^{\ddagger}$ = +11.5 kcal mol^{-1}

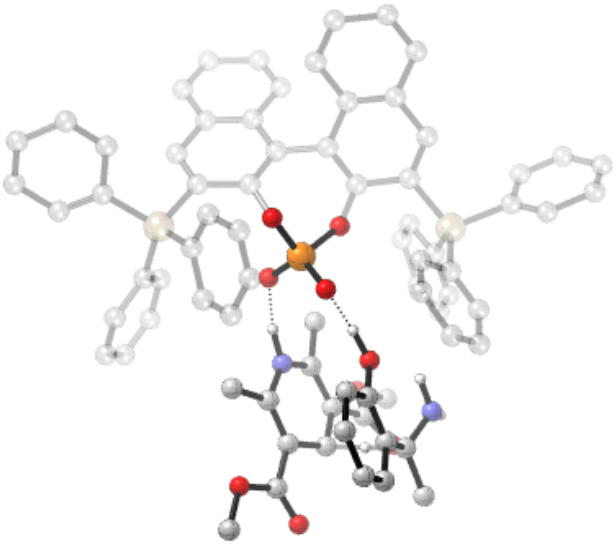

TS58-*E*: $\Delta\Delta G^{\ddagger}$ = 0 kcal mol^{-1}, $\Delta\Delta G_{sol}^{\ddagger}$ = 0 kcal mol^{-1}

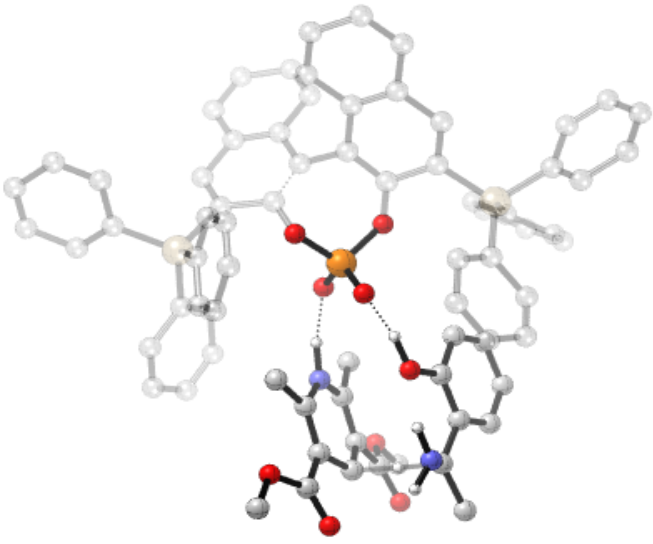

TS59-*E*: $\Delta\Delta G^{\ddagger}$ = +1.9 kcal mol^{-1}, $\Delta\Delta G_{sol}^{\ddagger}$ = +1.4 kcal mol^{-1}

Figure 6.4. Competing TS for the $SiPh_3$ catalysed transfer hydrogenation reaction. ONIOM (B3LYP/6-31G**: UFF), single-point energy M06-2X/6-31G**. Grayed-out regions were treated with UFF, and the full-colour regions were treated B3LYP/6-31G**.

Table 6.1. Interatomic distances for the lowest energy ONIOM TS.

	Interatomic distance (Å)			
	C-H (breaking)	C-H (forming)	NH/OH-O (imine)	NH-O (Hantzsch ester)
TS56-*Z*	1.39	1.34	1.76	1.50
TS57-*E*	1.42	1.32	1.70	1.64
TS56-*E*	1.40	1.32	1.81	1.50
TS57-*Z*	1.37	1.35	1.76	1.59
TS58-*E*	**1.36**	**1.32**	**1.48**	**1.56**
TS59-*E*	1.36	1.33	1.50	1.61

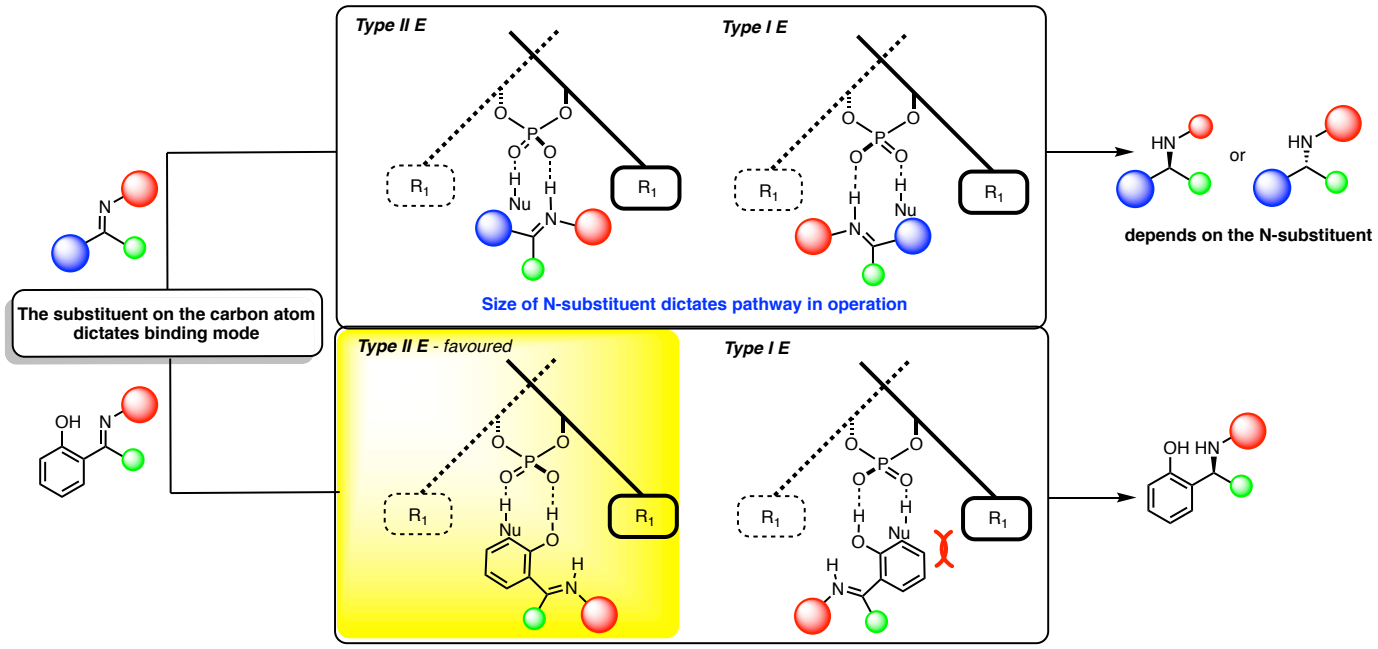

Figure 6.5. Conventional (top) and OOH (*ortho*-OH, bottom) qualitative models for predicting stereoselectivity for nucleophilic additions to imines.

The qualitative OOH model predicts that the introduction of a larger substituent on the nitrogen indicated in red, Figure 6.5, would result in a minimal increase in steric repulsions between this substituent and the 3,3' group. However, the conventional bifunctional model (Figure 6.5**,** top) predicts major steric repulsions and a reaction pathway change from *Type II* to *Type I* as a result. To test this, transition states for a second literature reaction (Figure 6.6),[258] reported by Wang *et al.* in which the H on the nitrogen was replaced by a aromatic moiety were located using ONIOM (B3LYP/6-31G**: UFF), the results are summarized in the Figure 6.7. To simplify my calculations, the aromatic moiety was truncated to a phenyl group; calculations on similar systems have reported this to have a minimal effect on the reaction outcome but would rapidly enhance computational tractability by reducing conformational flexibility.[25,41] According to my calculations OOH-*Type II E* is favoured over OOH-*Type I E* by 2.0 kcal mol^{-1} a value very similar to that calculated for the reduction of NH ketimines. However, for the NH binding mode the lowest energy pathway is now *Type I Z* due to the increased steric interactions between the N-aryl substituent and the 3,3' groups in the *Type II E* TS. The standard bifunctional mechanism predicts a mechanism change where the OOH model does not. The OOH model is consistent with the experimental data.

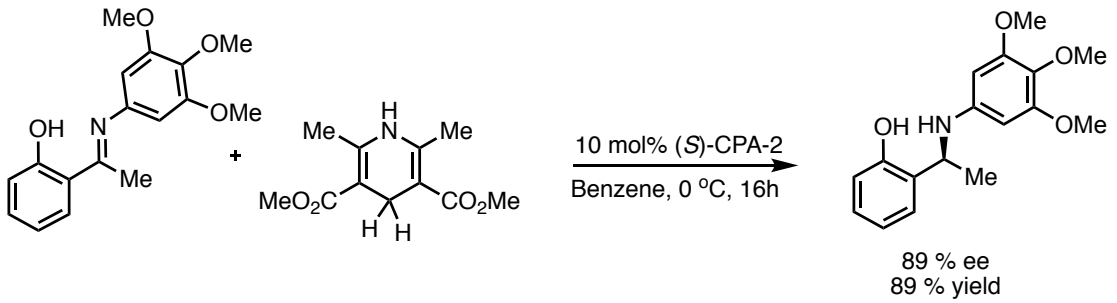

Figure 6.6. Asymmetric transfer hydrogenation of *ortho*-hydroxybenzophenone derived imines with large N-substituents.

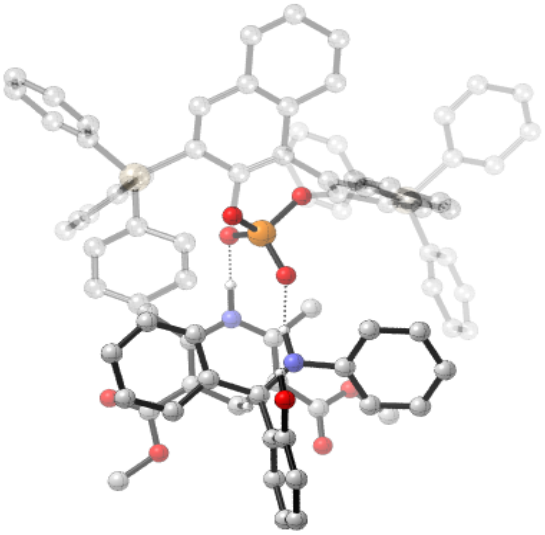

TS60-*Z*: $\Delta\Delta G^{\ddagger}$ = +16.0 kcal mol^{-1}, $\Delta\Delta G_{sol}^{\ddagger}$ = +15.5 kcal mol^{-1}

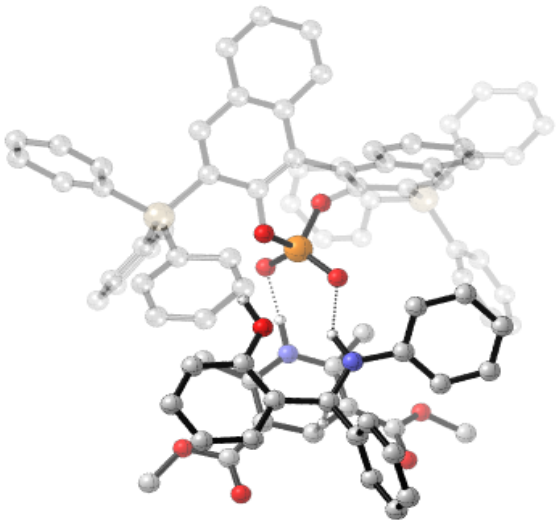

TS60-*E*: $\Delta\Delta G^{\ddagger}$ = +17.3 kcal mol^{-1}, $\Delta\Delta G_{sol}^{\ddagger}$ = +17.4 kcal mol^{-1}

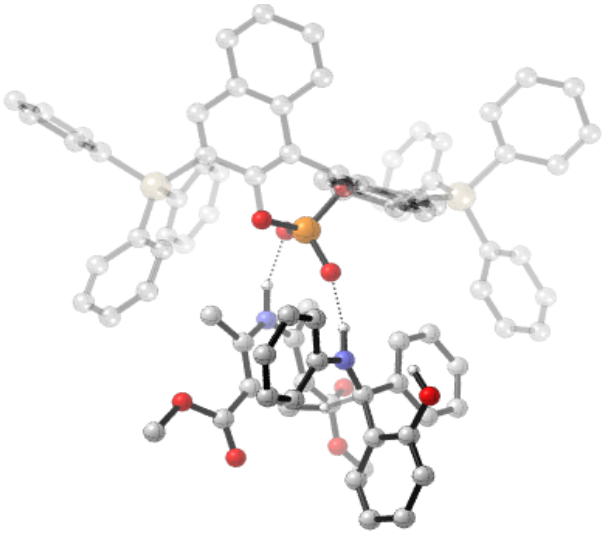

TS61-*Z*: $\Delta\Delta G^{\ddagger}$ = +12.2 kcal mol^{-1}, $\Delta\Delta G_{sol}^{\ddagger}$ = +12.1 kcal mol^{-1}

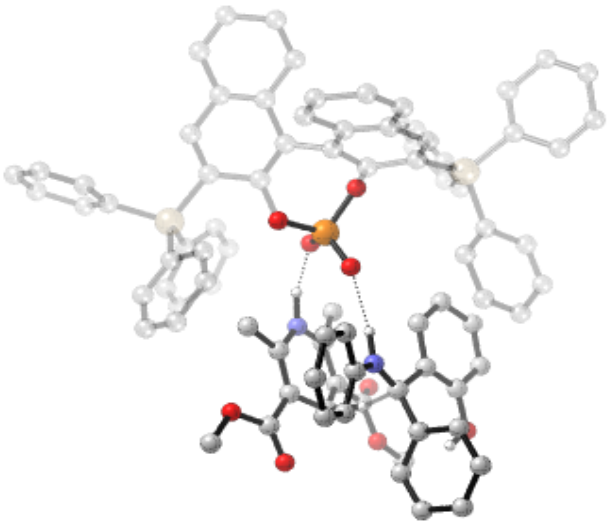

TS61-*E*: $\Delta\Delta G^{\ddagger}$ = +14.7 kcal mol^{-1}, $\Delta\Delta G_{sol}^{\ddagger}$ = +13.9 kcal mol^{-1}

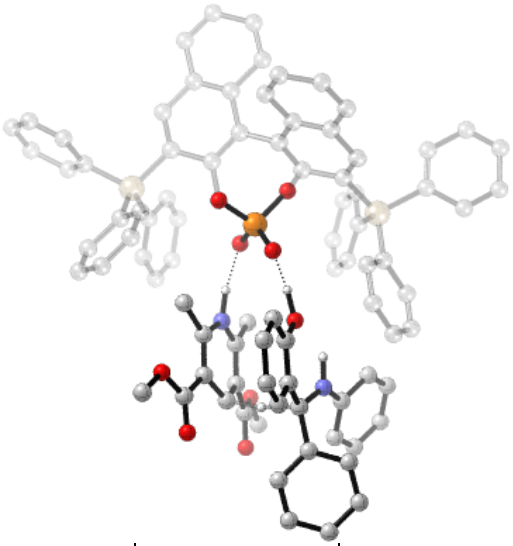

TS62-*E*: $\Delta\Delta G^{\ddagger}$ = 0 kcal mol^{-1}, $\Delta\Delta G_{sol}^{\ddagger}$ = 0 kcal mol^{-1}

TS63-*E*: $\Delta\Delta G^{\ddagger}$ = +2.0 kcal mol^{-1}, $\Delta\Delta G_{sol}^{\ddagger}$ = 1.3 kcal mol^{-1}

Figure 6.7. Competing TS for the $SiPh_3$ catalysed transfer hydrogenation reaction. ONIOM (B3LYP/6-31G**: UFF), single-point energy M06-2X/6-31G**. Grayed-out regions were treated with UFF, and the full-colour regions were treated B3LYP/6-31G**.

6.4 Conclusions

DFT and ONIOM calculations suggest that the phosphoric acid catalysed transfer hydrogenation of imines derived from *ortho*-hydroxybenzophenone involves a bifunctional mechanism in which there are two hydrogen-bonding interactions from reagents to catalyst, one from the *ortho*-hydroxyl group and a second from the nucleophile's proton. This mode of activation is lower in energy than those originally proposed. The hydroxyl group is a key element in dictating reactivity and enantioselectivity. This is an under-appreciated mode of activation achieving faster rates of reaction than the conventional bifunctional mode and these investigations should promote future developments in the field. Our calculations have been summarized into a simple qualitative model (Figure 6.5) that accurately reproduces the experimentally observed sense of enantioinduction for all examples. This model highlights the important steric interactions between substrate and catalyst necessary for efficient stereoinduction.

Chapter 7

7 Origins of Selectivity in Monoactivation Mechanisms

7.1 Background and Methods

Understanding the interaction of catalysts with reagents relies on identifying a small number of catalytic modes of activation. Despite the vast body of literature dedicated to the study of chiral phosphoric acids, defining reactions by mode of activation can be a difficult task, owing to the uncertainties over the exact catalytic mechanisms.[24] The most common scenario is that the chiral phosphoric reacts *via* a bifunctional mechanism, involving both the simultaneous activation of the electrophile and the nucleophile by the catalyst. Such a model, in which the catalyst binds to the nucleophile through it's phosphoryl oxygen, requires an acidic proton for a second hydrogen bonding interaction.[20] Alternatively, if a site of attachment is absent, the reaction can proceed *via* dual or monoactivation mechanisms. Dual activation mechanisms are known to be operational for number of reactions, and Akiyama's Mannich reaction involving silyl enol ethers is an example.[18,70] One common feature of these activation strategies is to coordinate and pre-organise the reactants inside the catalyst through two hydrogen-bonding interactions. However, the pool of potential reactions could be much broader if a specific functionality is not required. Monoactivation mechanisms have been proposed and in each reaction studied so far,[36,38-41,56,70] transition states involving a single interaction from the imine substrate to the catalyst are higher in energy than those involving double coordination. If the reactants lack a second site of interaction, such a mode of activation seems plausible. Despite the risks of the strategy, a number of reactions involving reactants in which a second binding to the catalyst seems mechanistically improbable have shown to be highly enantioselective.[74-83] These mechanistic scenarios are summarised in Figure 7.1. Even with this precedent documenting the synthetic potential of monoactivation mechanisms, only relatively few enantioselective processes capable of proceeding through such have been developed and some are summarised in Table 7.1. The lack of reactions operating under this catalytic mode of action could be due to the reagents binding to only one catalyst site, which leads to highly flexible transition states, which are often not thought to lead to uniformly high levels of enantiomeric excess.[39] This model for activation represents challenges for catalyst design because the relatively well-

understood principles of tuning the catalyst environment developed in the previous chapters can no longer be applied. However, the discovery of catalysts that promote highly enantioselective nucleophilic additions would provide an opportunity to study secondary interactions that are either not present or important in bifunctional activation mechanisms. Ultimately, an understanding of these interactions could be applied to the design of chiral catalysts that interact with other nucleophiles lacking H-bonds.

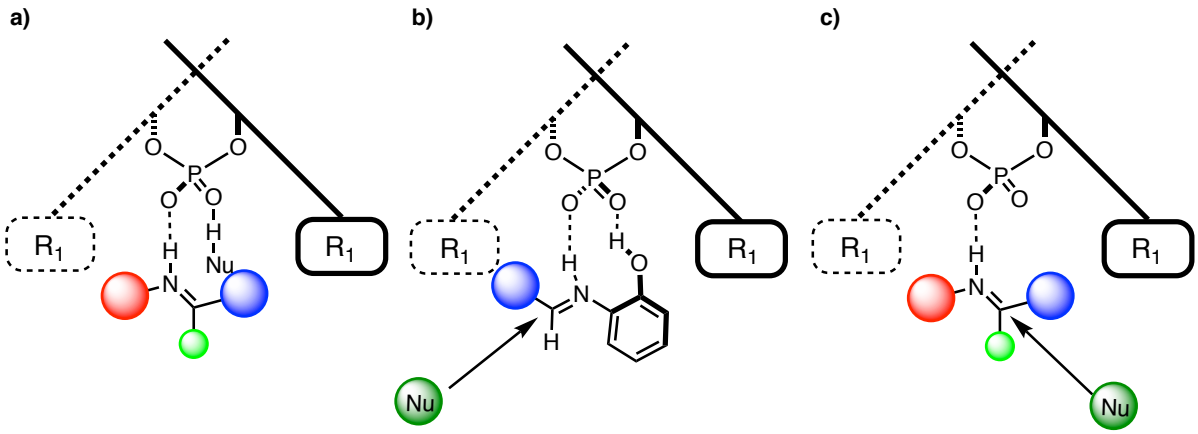

Figure 7.1. Possible modes of activation for phosphoric acid catalysed nucleophilic additions to imines. Transition states (a) and (b) have computationally been verified to be operational, (c) has been calculated to be higher in energy than the two point modes of activation.

Despite the potential importance of monoactivation mechanisms the reasons for such large enantiomeric excesses have not been investigated, making it difficult to predict the stereoselectivity and catalyst requirements for novel reactants. It is probably the flexibility of the systems that makes the computational studies of the key TS, difficult. Such a model has been proposed to explain the enantioselectivity of various Mannich and Friedel-Crafts reactions in which a second binding point from either reactant to the catalyst seems unlikely (Table 7.1).

Table 7.1. Addition of nucleophiles to imines proceeding *via* monoactivation mechanisms. The sense of stereoinduction is based on all reactions catalysed by the same catalyst enantiomer to allow comparison.

Reaction	AREA(θ) > 70 (%ee)	medium AREA(θ) (%ee)	AREA(θ) < 36 (%ee)
addition of silyl dienolates[82]	18	70	-
addition of difluoroenol silylether[81]	-	92	29
addition of vinylketene silyl N,O-acteals[83]	-	75	-90
addition of TBS-protected indoles[77]	-	55	-67
addition of Bn-protected indoles[76]	-	-	-94
addition of furan[75]	-	97	-

Based on X-ray diffraction studies of the imine-catalyst complex, the Schneider group propose a monoactivation model for the addition of silyldienolates, in which the imine is placed in an *E* conformation and the nucleophile approached from the less hindered face, reproducing the sense of stereoinduction observed experimentally.[260] This vinylogous Mannich produces the same sense of stereoinduction as with Akiyama's example,[81] suggesting a similar model could be invoked. In a further example, Schneider showed, that modifying the 3,3' groups can invert the sense of stereoinduction entirely.[83] A similar trend is observed with Friedel-Crafts reactions. While the proposed mechanism accounts for the formation of the major product, it fails to explain the results caused by variations in catalyst. Schneider did not propose an explanation for the inversion of enantioselectivity with change in catalyst structure and Terada suggested that, in his study of the Friedel-Crafts reaction, the inversion was due to the incorporation of the sterically demanding 3,5-dimesityl 3,3' groups blocking one face of nucleophilic approach more than the other.[77] In any case a thorough understanding for the reasons of enantioselectivity is still lacking and could help promote future developments in the field.

I undertook computational studies to explore the reasons for selectivity in monoactivation mechanisms and, to the best of my knowledge, this constitutes the first mechanistic work towards an understanding. Mechanistic insights into these reactions are crucial to the advance of the field from the early proof of concept to a general strategy in stereoselective synthesis.

The calculations were performed using the general method described previously, in Chapter 3. The energy window for conformational sampling was increased from 10 kJ mol^{-1} to 20 kJ mol^{-1} for the Mannich reaction, as I felt an appropriate number of conformers were not generated for the monoactivation mechanisms. Free energies in solution were derived from structures optimized in the gas phase at the ONIOM (B3LYP/6-31G**:UFF), level of theory by means of a single point calculation using M06-2X/6-31G** with the polarizable continuum model (PCM) as implemented in the Jaguar program (version 7.9), toluene (probe radius = 2.76 Å) for the Mannich reaction and DCM (probe radius = 2.33 Å) for the Friedel-Crafts study, as the solvent.[50] These values were used to correct the Gibbs free energy derived from the ONIOM calculations. The quantitative parameters were calculated as described previously in Chapter 2. Structures are illustrated using CYLview.[196]

7.2 Asymmetric Mannich reaction

In 2011, Akiyama reported an efficient method for the preparation of β-amino-α,α-difluoro carbonyl compounds through a chiral phosphoric acid catalysed Mukaiyama Mannich reaction.[81] Despite the importance of the product motif in pharmaceuticals the origins of the asymmetric induction remain unclear.[261] There is an intimate relationship between the substituents distant from the phosphoric acid, quantified by a remote environment angle, AREA(θ), (Figure 7.2) and the selectivity, in which the selectivity increases with decreasing AREA(θ), it then stops and changes to a decline. The break in linearity often frequently seen with similar reactions proceeding *via* a bifunctional mechanism is characteristic of a change in mechanism in the enantiodetermining step. An alternative mechanism, *Mechanism L*, in which the imine establishes two H-bonds with the phosphate catalyst, could explain the decline in stereoinduction with small AREA(θ) catalysts (Figure 7.3). However, this compact arrangement places the imine in an unfavourable *Z* configuration.

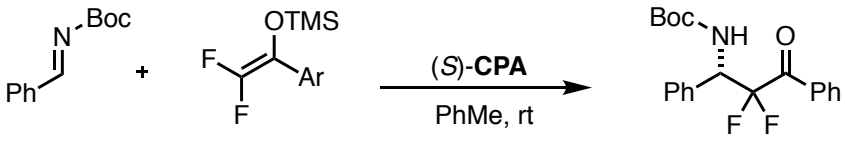

Entry	Catalyst R_1	AREA(θ)	ee%
1	Ph	70	63
2	4-$NO_2C_6H_4$	64	64
3	9-anthryl	61	84
4	TRIP	51	89
5	$SiPh_3$	29	29

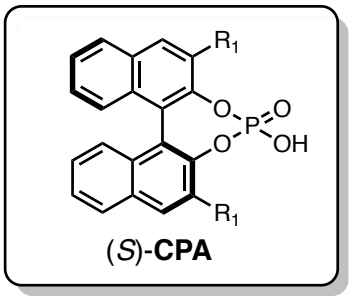

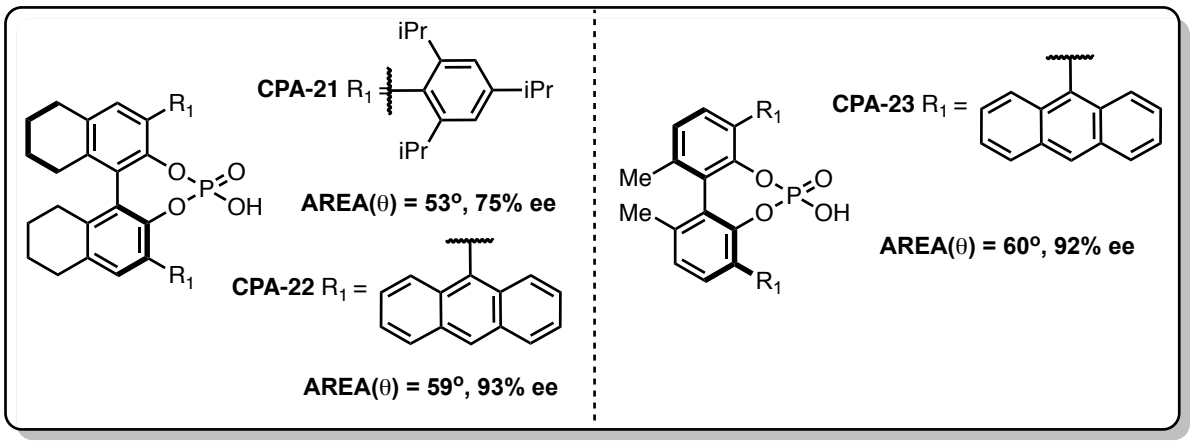

Figure 7.2. Catalyst screening results. Only BINOL derived phosphoric acid are included in the table to allow direct comparison of the effect of the 3,3' group on enantioselectivity. Chiral phosphoric acids with different backbones were tested and have been included for completeness.

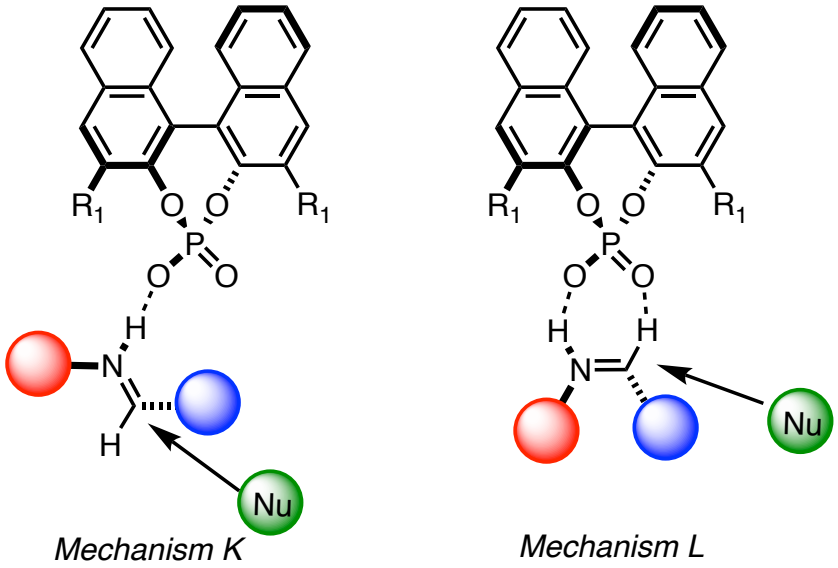

Figure 7.3. Mechanistic hypotheses for the Mannich reaction.

My DFT investigations into the phosphoric acid catalysed Mannich reaction reported by Akiyama *et al*. using a simple achiral model catalyst, buta-1,3-diene-1,4-diol phosphoric acid calculated the dual coordination pathway to be higher in free energy by 3.9 kcal mol^{-1} when evaluated using B3LYP/6-31G**. When the Gibbs energies were corrected by taking a single point calculation using M06-2X/6-31G** the energy difference increased to 6.7 kcal mol^{-1} suggesting that dispersive interactions are significant. Due to the open, flexible nature, 82 unique transition states where located for the mono-coordination pathway. The lowest in energy is shown in Figure 7.4. Although **TS65** features a second hydrogen bonding interaction from the aldimine hydrogen to the phosphoryl oxygen, increased steric interactions between R groups and weakening of the hydrogen bonding from the imine to the catalyst, all contribute to the destabilisation of the *Z* transition state. In addition, **TS64** features a slipped parallel arrangement of the two aryl groups, with an Ar-Ar separation of 3-4 Å, typical for π-π stacking. This stabilising interaction also contributes to the lowering of **TS64**.

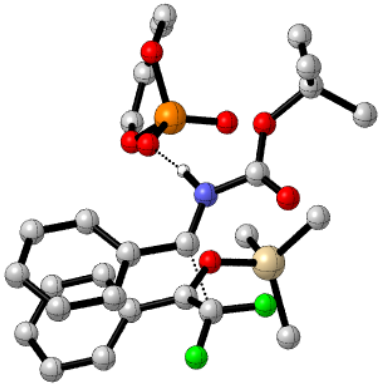

TS64: $\Delta\Delta G^{\ddagger}$ = 0 kcal mol^{-1}

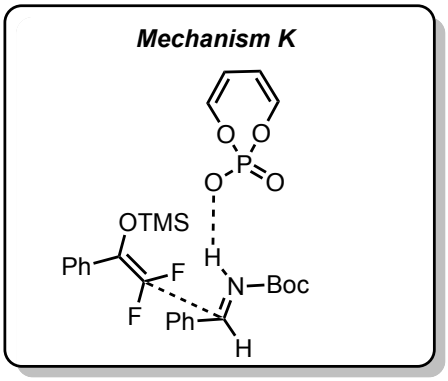

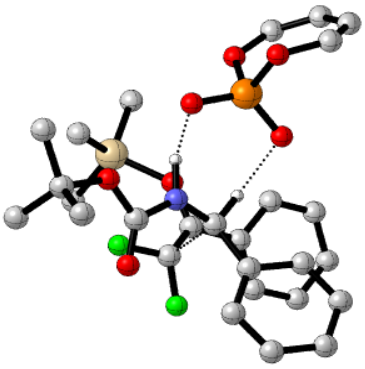

TS65: $\Delta\Delta G^{\ddagger}$ = +6.7 kcal mol^{-1}

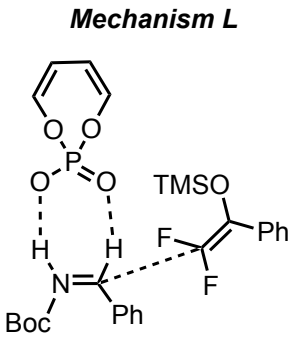

Figure 7.4. Mechanistic hypotheses for the Mannich reaction calculated using the model catalyst. Geometries B3LYP/6-31G**, single-point energy M06-2X/6-31G**.

It is still not altogether clear how a monoactivation mechanism could lead to such high levels of enantioselectivity. Since the imine interacts with the catalyst through the Brønsted acidic site only, its orientation with respect to the catalyst is not fixed. It is expected that conformations leading to the opposite enantiomers will exhibit only small energy differences. Transition states for the full catalyst system were located using ONIOM (B3LYP/6-31G**:UFF). There are six reasonable TS pathways resulting from two different mechanisms, nucleophile approach and orientation of the imine summarised qualitatively in Figure 7.5. The models are shown using the Goodman projection in which the free oxygens are above and below the plane of the paper, each having bulky catalyst substituents on either side. Deprotonation of the phosphoric acid gives a C_2-symmetric structure and so I can arrange the acid catalyst with the OH pointing out of the plane without loss of generality. The imine binds to the Brønsted acidic site and is placed parallel to the 3,3' groups (the bifunctional model places the imine at the front and perpendicular). The nucleophile can approach from the top or the bottom and this forces the imine to occupy the corresponding portion of the chiral cavity. The N-substituent can be pointed towards the front of the catalyst or alternatively it can rotate 180° and point towards the back, below the phosphoryl oxygen,

and depending on these factors the N-substituent can be pointed towards or away from the 3,3' substituent. To be consistent with nomenclature throughout this thesis, TS in which the N-substituent is pointed away from the 3,3' are called *Type I* and towards *Type II*. After a thorough conformational search I identified 167 TS in total and of these the lowest energy are summarised in Figure 7.6**.** The reaction proceeds *via* a monoactivation *E* mechanism in agreement with the calculations using the model catalyst, and the nucleophile approaches from the *Si*-face. Although the *Z* transition states are more compact, the energy required to rotate the phenyl group is greater than the energy of the steric interactions with the 3,3' groups.

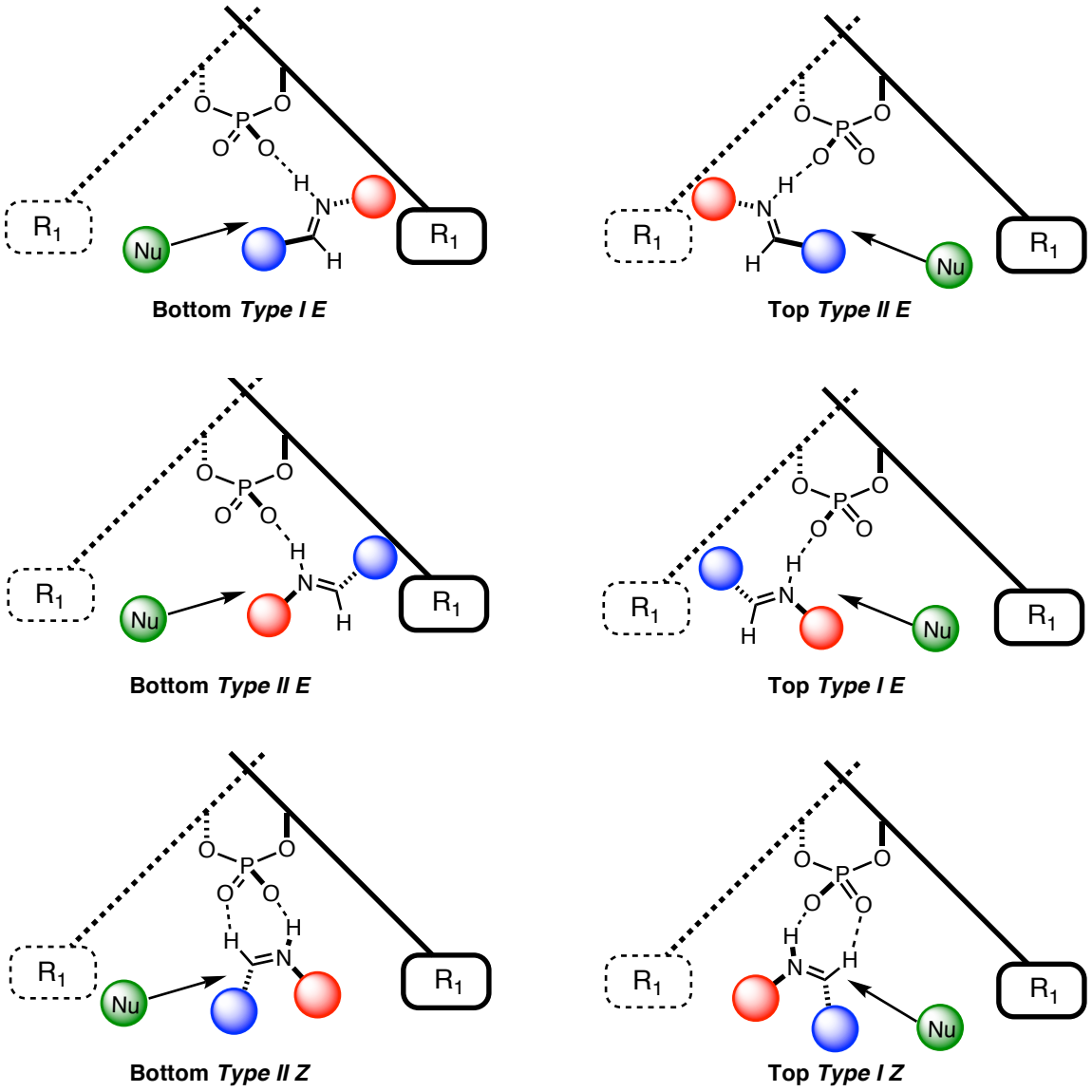

Figure 7.5. Qualitative pictures of plausible TS pathways. The nucleophile can approach from the least hindered side of the catalyst (bottom). However, this would place the imine into the right hand portion of the catalyst cavity, leading to an increase in steric interactions between the imine and the catalyst substituents.

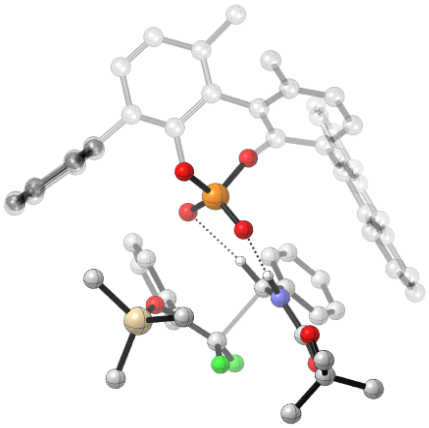

TS66-*Re*: $\Delta\Delta G^{\ddagger} = +10.6$ kcal mol^{-1}, $\Delta\Delta G_{sol}^{\ddagger} = +10.6$ kcal mol^{-1}

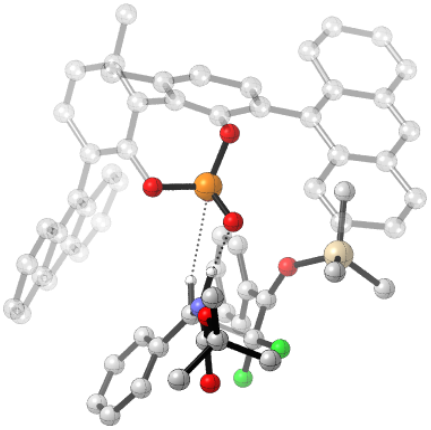

TS67-*Si*: $\Delta\Delta G^{\ddagger} = +11.2$ kcal mol^{-1}, $\Delta\Delta G_{sol}^{\ddagger} = +11.5$ kcal mol^{-1}

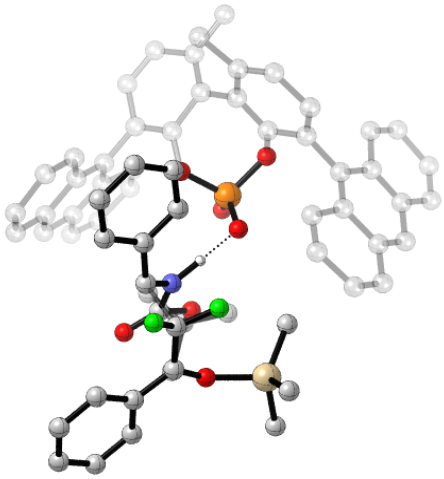

TS69-*Si*: $\Delta\Delta G^{\ddagger} = +5.7$ kcal mol^{-1}, $\Delta\Delta G_{sol}^{\ddagger} = +4.0$ kcal mol^{-1}

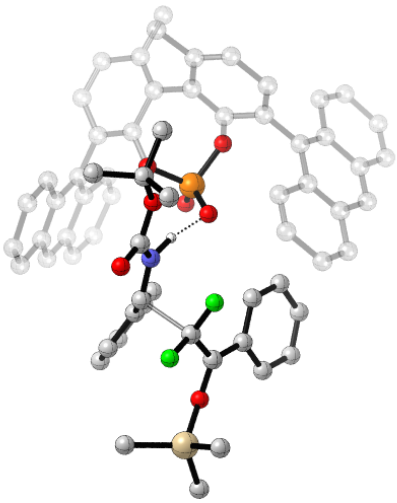

TS69-*Re*: $\Delta\Delta G^{\ddagger} = +8.9$ kcal mol^{-1}, $\Delta\Delta G_{sol}^{\ddagger} = +6.9$ kcal mol^{-1}

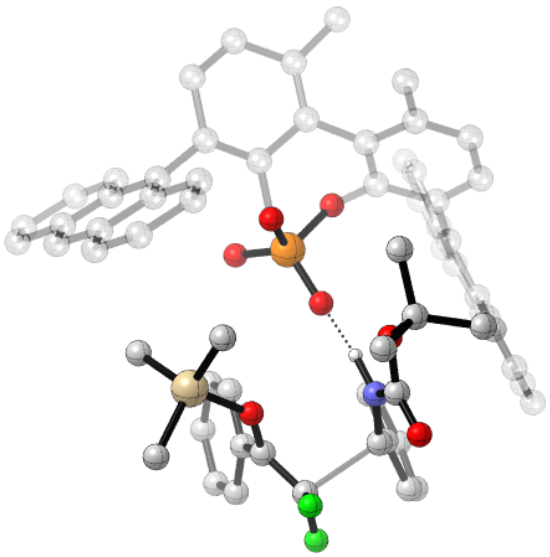

TS68-*Si*: $\Delta\Delta G^{\ddagger} = 0$ kcal mol^{-1}, $\Delta\Delta G_{sol}^{\ddagger} = 0$ kcal mol^{-1}

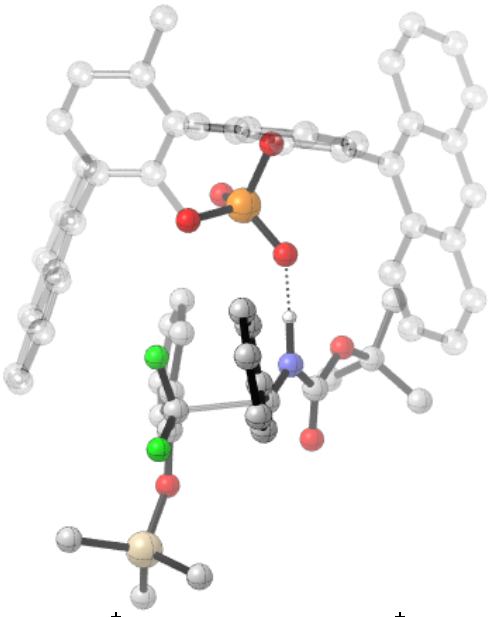

TS68-*Re*: $\Delta\Delta G^{\ddagger} = +2.7$ kcal mol^{-1}, $\Delta\Delta G_{sol}^{\ddagger} = +1.3$ kcal mol^{-1}

Figure 7.6. Competing TS for the 9-anthryl BIPOL-derived catalysed addition of difluoroenol silylether to imines. ONIOM (B3LYP/6-31G**: UFF), single-point energy M06-2X/6-31G**. Grayed-out regions were treated with UFF, and the full-colour regions were treated B3LYP/6-31G**.

For both mechanisms and imine orientations the nucleophile prefers to approach from the least hindered, bottom, side of the catalyst. Approach from the top of the catalyst is higher in energy due to additional steric interactions with the bulky catalyst substituents. The two directly competing transitions states are **TS68-*Si*** and **TS68-*Re*** differing only in the orientation of the N-substituent with respect to the catalyst. **TS68-*Si*** is 1.3 kcal mol^{-1} lower in energy than **TS68-*Re*,** in good agreement with experiment and this is due to both a number of steric and electronic factors. The N-Boc substituent is sterically more demanding than the Ph and so prefers to orientate towards empty space at the front of the catalyst. Rotating the imine 180°, with respect to the hydrogen bond increases the steric interactions between the Boc and the 9-anthryl catalyst substituent. The imine adopts a tilted disposition to minimise this clash but induces a second with the phenyl group and the catalyst backbone. This secondary steric clash decreases the dihedral angle defined by both phenyl groups (described by carbons 2,1,1' and 2', where 2 and 2' are the oxygen bearing carbons) from 60° to 56°. The effect of this is to move the 3 and 3' groups towards the catalyst active site, increasing their interaction with the substrate and the energy of this pathway. **TS68-*Si*** also benefits from a number of non-covalent interactions including a π-stacking interaction between the phenyl group of the imine and the 9-anthryl group of the catalyst and C-H π-interactions between the TMS group of the nucleophile and the 3,3' (Figure 7.7). My calculations suggest that there is a direct steric clash between the catalyst backbone and the phenyl group in the disfavoured TS and increasing the steric demand of the catalyst backbone would result in increased enantioselectivities. To test this mechanistic understanding we re-examined the catalyst screen carried out by the authors and found that replacing BINOL for H_8–BINOL increases the enantioselective effect of the catalyst, suggesting my trend is correct. More importantly, this suggests that BINOL and H_8-BINOL cannot be unified by a single parameter, as the steric differences between the catalyst backbones must be taken into account.

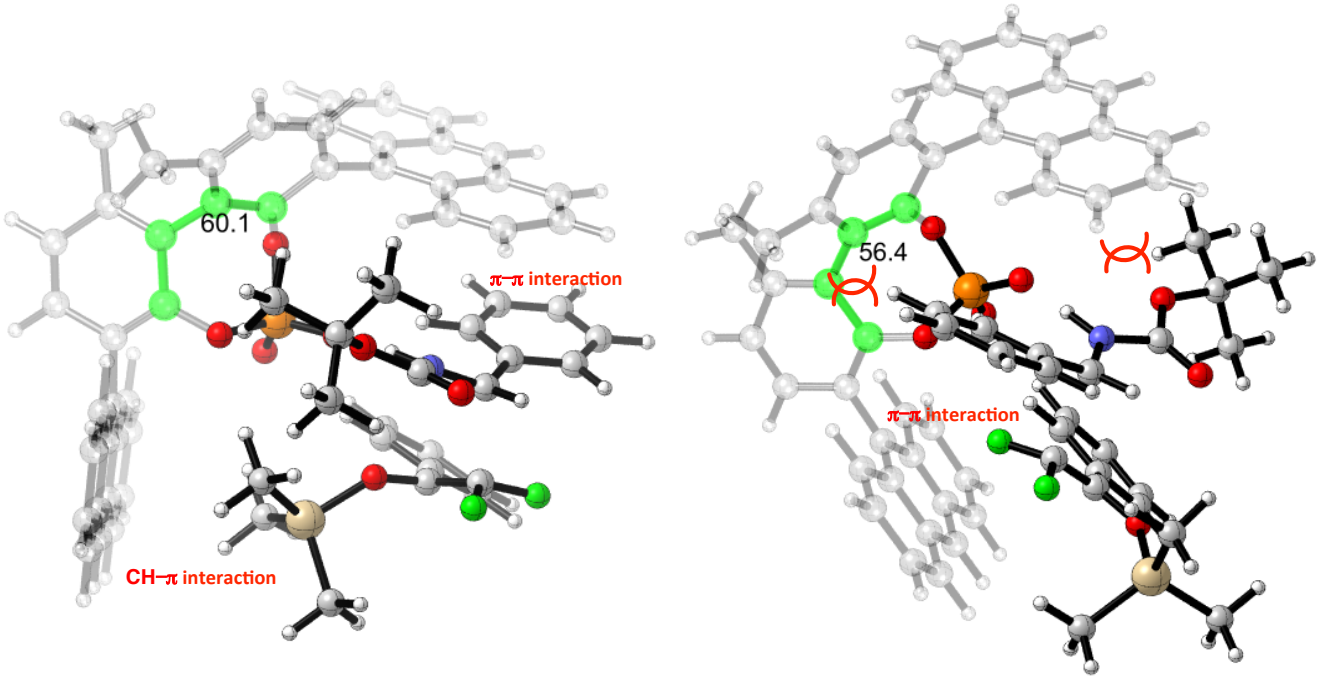

Figure 7.7. In-depth look at the reasons for enantioinduction between competing diastereoisomeric TS.

Increasing the demand of the remote sterics results in a drop in enantioselectivity. It is not altogether clear why this catalyst feature is detrimental to reaction efficacy. We decided to study this using the general method described above (Figure 7.8). After a thorough conformational search consisting of 138 TS, I show that only four of the six viable TS pathways are low in energy. The larger catalyst pocket created by the 9-anthryl allows more conformational flexibility. Interestingly this feature is often thought to be a negative factor in designing enantioselective catalysts; in this specific case it is advantageous. The TS pathways in which the N-Boc was pointed towards the back of the catalyst could not be located *via* a conformational search despite increasing the energy window from 10 to 20 kJ mol^{-1} and were not investigated further. **TS70-*Re*** and **TS71-*Si*** show that this trend is correct with the energy difference to be just 0.2 kcal mol^{-1}, falling from 1.3 kcal mol^{-1}. I found that the increase in the steric profile of the 3,3' substituents raises the energy of the monoactivation mechanisms relative to the dual activation mechanism proceeding through a compact *Z* imine and is rationalized by my qualitative model Figure 7.9. Facilitating the reaction in a medium catalyst cavity results in the *E* configuration being favoured; this configuration reduces the internal substrate steric interactions present in the *Z*. However, as the catalyst cavity decreases, the interaction between the R groups and the 3,3' groups become more energetically costly and raises the energy of the *E* relative to the *Z*.

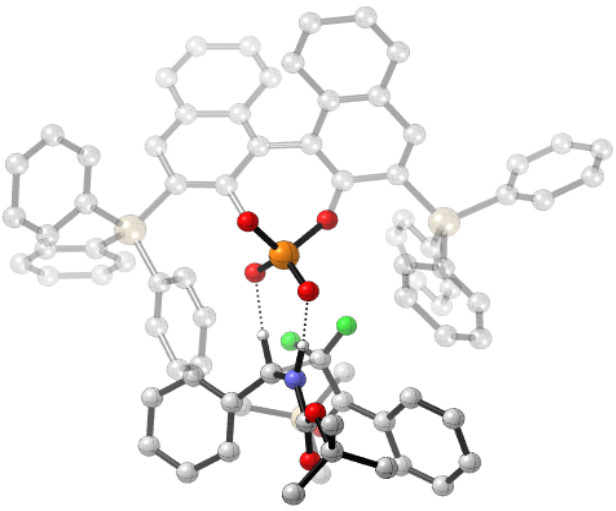

TS71-*Si*: $\Delta\Delta G^{\ddagger}$ = -1.2 kcal mol^{-1}, $\Delta\Delta G_{sol}^{\ddagger}$ = 0 kcal mol^{-1}

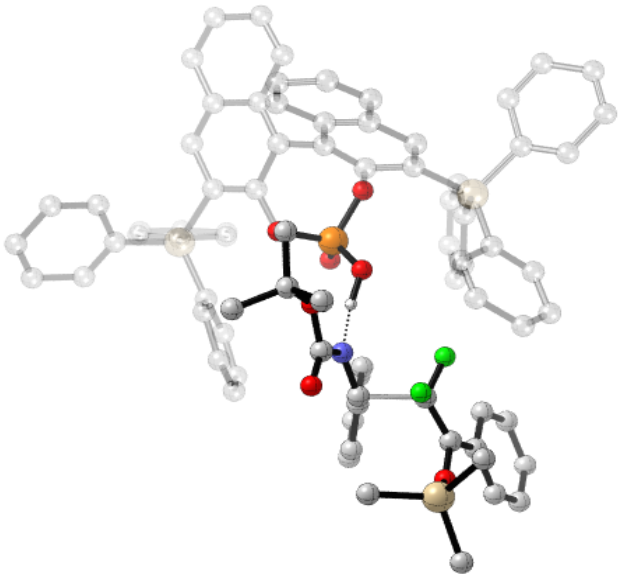

TS73-*Re*: $\Delta\Delta G^{\ddagger}$ = +2.9 kcal mol^{-1}, $\Delta\Delta G_{sol}^{\ddagger}$ = +2.5 kcal mol^{-1}

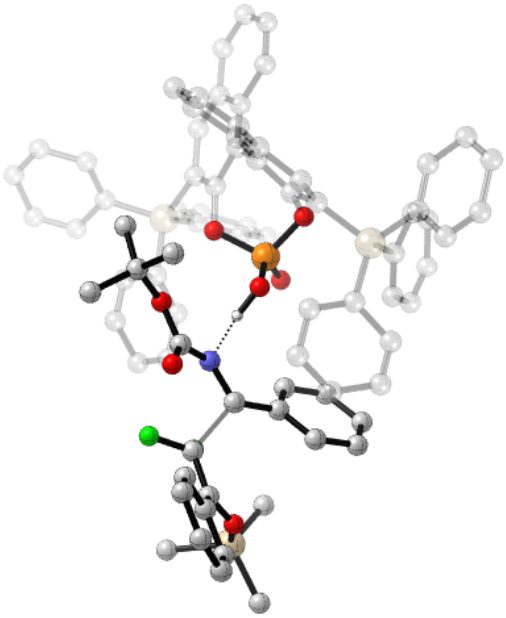

TS72-*Si*: $\Delta\Delta G^{\ddagger}$ = 0 kcal mol^{-1}, $\Delta\Delta G_{sol}^{\ddagger}$ = 0 kcal mol^{-1}

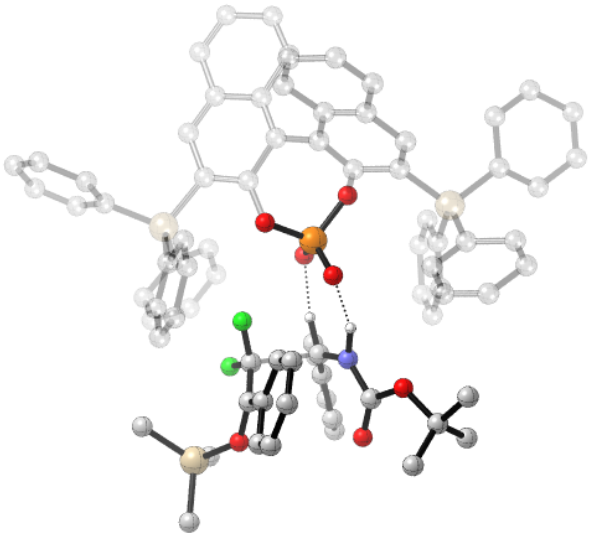

TS70-*Re*: $\Delta\Delta G^{\ddagger}$ = -1.4 kcal mol^{-1}, $\Delta\Delta G_{sol}^{\ddagger}$ = -0.2 kcal mol^{-1}

Figure 7.8. Competing TS for the $SiPh_3$ catalysed addition of difluoroenol silylether to imines. ONIOM (B3LYP/6-31G**: UFF), single-point energy M06-2X/6-31G**. Grayed-out regions were treated with UFF, and the full-colour regions were treated B3LYP/6-31G**.

Solvent effects were shown to have a large impact on the relative free energies of the competing TS that proceeded *via* monoactivation mechanisms (**TS72-*Si*** and **TS73-*Re***). The free energies were calculated to be significantly higher in the gas phase than in solution and this can be attributed to the electron rich nature of the phosphate that is stabilised to a greater extent by solvation than the TS featuring a second hydrogen bond to that position.

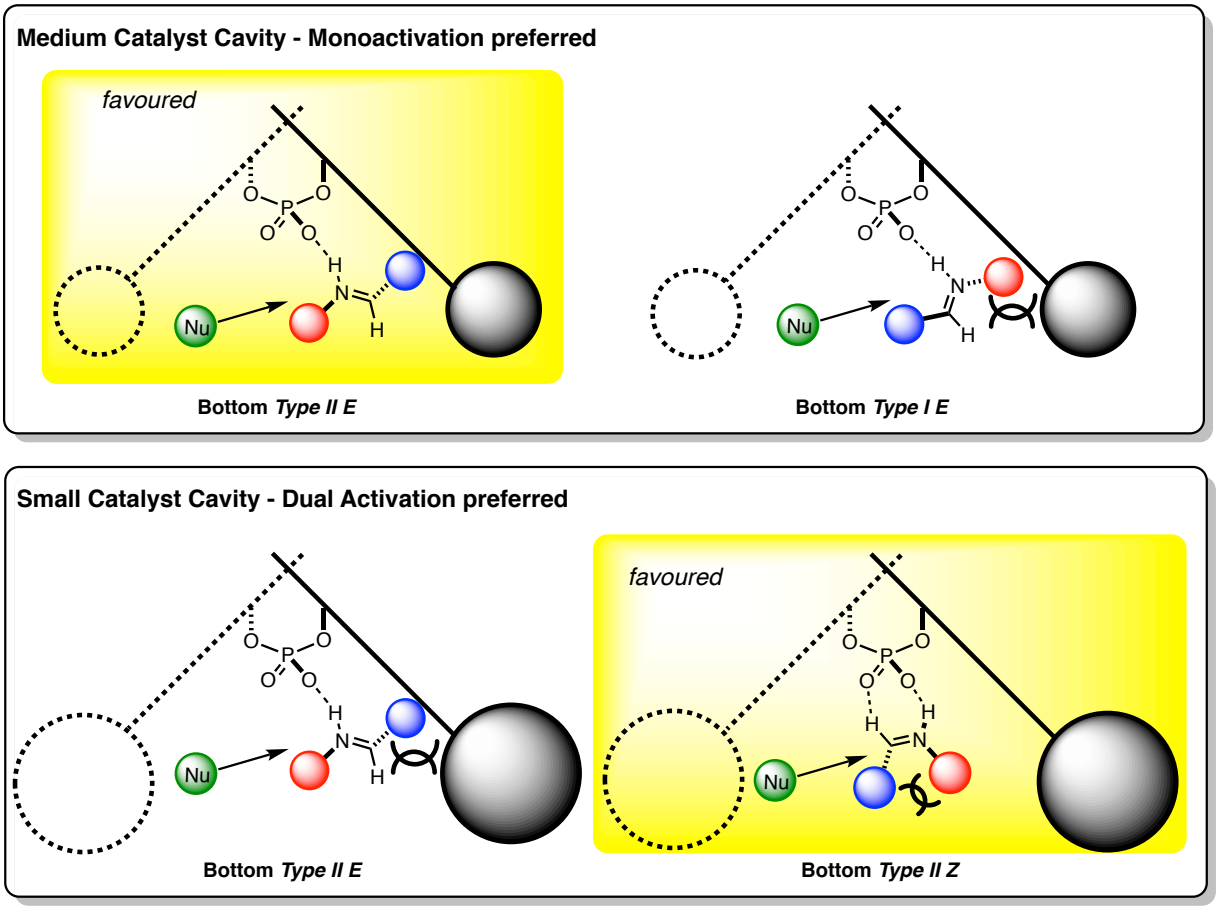

Figure 7.9. Qualitative model describing the preference for *Z* transition state with small ligand angle catalysts. In the *E* configuration, the largest R groups are coplanar and so internal steric interactions are minimized. The *Z* configuration allows placing two groups distant from the majority of the catalyst bulk, but this offset by their proximity to each other.

To summarise this section, the enantioselective origins of the addition of difluoroenol silylether to N-Boc imines has been identified. The experimental enantioselectivity trends are accurately reproduced by comparison of relative free energy differences. To determine if the insights gained in this study are important in similar reactions proceeding *via* monoactivation mechanisms I next studied the Friedel-Crafts reaction reported by Antilla *et al*.

7.3 Asymmetric Friedel-Crafts Reaction

In 2007, Antilla was the first to introduce the addition of protected indoles to imines catalysed by chiral phosphoric acids proceeding *via* a monoactivation mechanism.[78] However, it was not altogether clear why the catalyst achieved such high levels of selectivity (Figure 7.10).

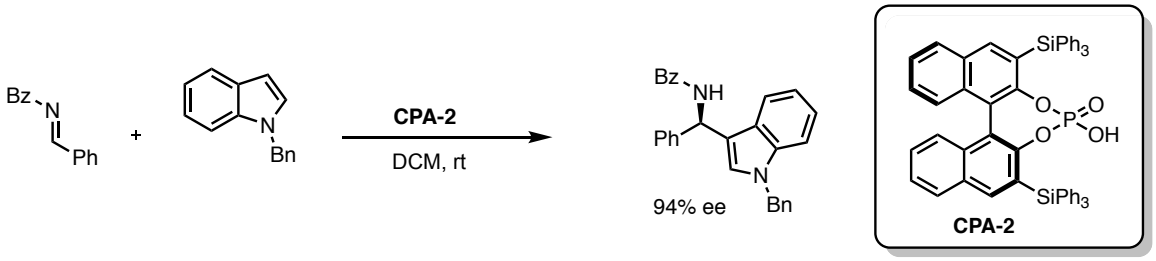

Figure 7.10. Antilla's mono-activated chiral phosphoric acid catalysed Friedel-Crafts reaction.

There are six reasonable TS pathways resulting from two mechanisms, different orientations of the imine and nucleophile approach. In an extensive search of the potential energy surface I found four low energy pathways summarised in Figure 7.11 and show similar trends with the Mannich reaction studied previously. For this reaction, the steric interactions between the imine and the catalyst 3,3' substituent are more relevant than the interactions with the nucleophile, and so nucleophilic approach to the top face is favoured, accounting for the reversal in stereoinduction between the two. This can be attributed to an increase in steric profile of the N-substituent and a decrease in steric bulk surrounding the nucleophilic carbon (the largest nucleophile substituent, benzyl, is further away from the nucleophilic carbon and can rotate away from the catalyst steric bulk). The imine orientates the large benzoyl group away from the front of the 3,3' substituents, the indole approaches from above with the benzyl substituent pointed towards the back of the catalyst and away from the imine. The TS pathway leading to the competing product is 7.4 kcal mol^{-1} higher in energy, which is an overestimation compared to experiment (computed ee > 99 % compared to experimental ee of 94 %). The ONIOM (M06-2X/6-31G**:UFF) method indicates that the discrepancy between calculations and experiment traces back to the UFF component of the optimisation, which overestimates short-range repulsion effects. [262] In **TS76-*Si*** the nucleophile approaches from the bottom forcing the imine to the right hand portion of the catalyst. In this arrangement, the imine experiences a greater steric interaction with the

catalyst. The steric interactions appear not to originate entirely from the substituent at the 3 position and the BINOL backbone plays an important stereochemical role. To test this, the $SiPh_3$ catalyst substituents were replaced by a proton and a single-point energy was taken of the resulting structures without re-optimisation. I found that the energy difference between the competing structures did not change to an appreciable extent with $\Delta\Delta E^{\ddagger}$ dropping from 8.2 kcal mol^{-1} to 6.4 kcal mol^{-1}. Therefore, although the nucleophile approach in the **TS76-*Si*** forces the imine N-substituent towards the majority of the 3,3' steric bulk, the dihedral angle between the binaphthyl backbone and the phenyl group of the $SiPh_3$ substituent, pointing up and out, is small reducing the proximal steric effect of the catalyst. The phenyl group at the back that points down forces the imine away from the catalyst in **TS76-*Si***, and this shift induces a greater steric interaction with the BINOL backbone. This provides insight into why in this case the small AREA catalyst is enantioselective: decreasing the remote steric demands from the catalyst would allow the imine to adjust better inside the catalyst cavity and therefore the steric interactions with the BINOL backbone would be reduced. Showing that the BINOL plays a direct role in stereoinduction rather than the secondary effect of changing the geometry of the chiral cavity, a rationale often invoked. The dual activation pathways are higher in energy due to internal steric repulsion and the preference is less strong in contrast to the previous reaction. Consistent with an increase in energy difference between the *E* and *Z* ground states on comparing N-Boc and N-Benzoyl imines. Decreasing AREA(θ) further would result in a preference for the dual activation mechanism but the precise value depends on the individual substrate combination. These results have been summarised in a simple qualitative model (Figure 7.12).

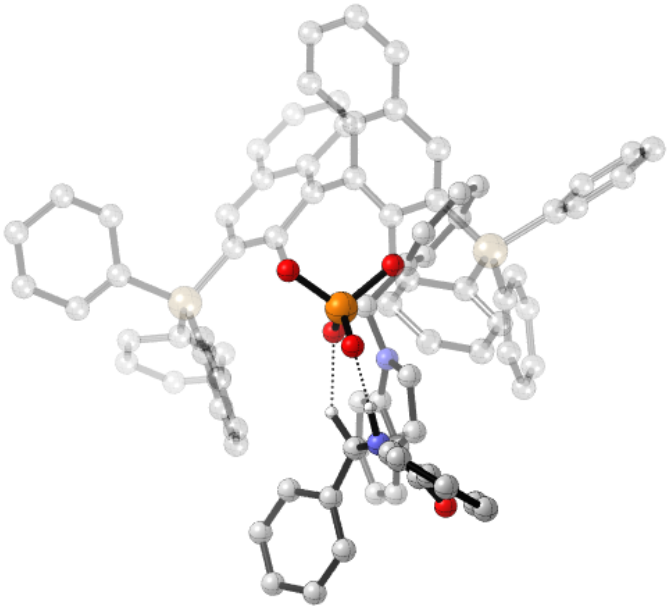

TS75-*Si*: $\Delta\Delta G^{\ddagger}$ = +7.4 kcal mol^{-1}, $\Delta\Delta G_{sol}^{\ddagger}$ = +7.9 kcal mol^{-1}

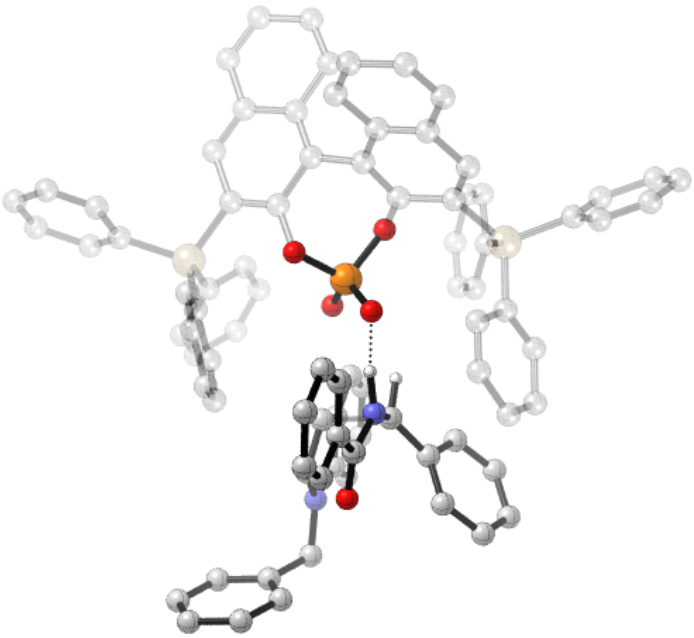

TS74-*Re*: $\Delta\Delta G^{\ddagger}$ = +11.4 kcal mol^{-1}, $\Delta\Delta G_{sol}^{\ddagger}$ = +11.6 kcal mol^{-1}

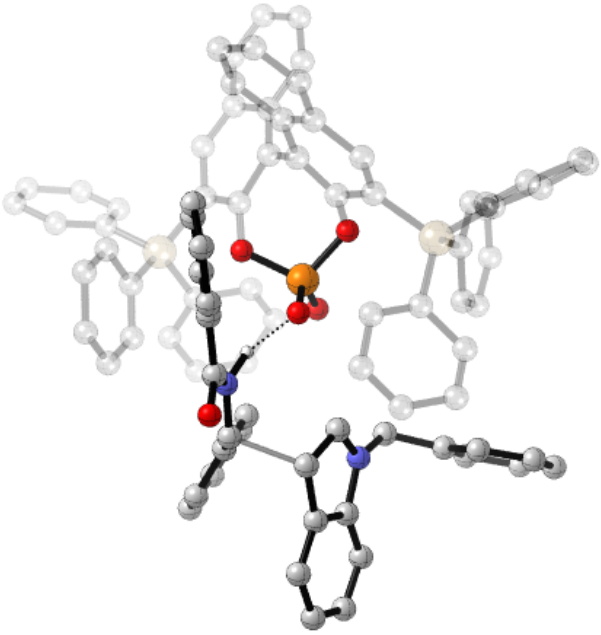

TS77-*Re*: $\Delta\Delta G^{\ddagger}$ = 0 kcal mol^{-1}, $\Delta\Delta G_{sol}^{\ddagger}$ = 0 kcal mol^{-1}

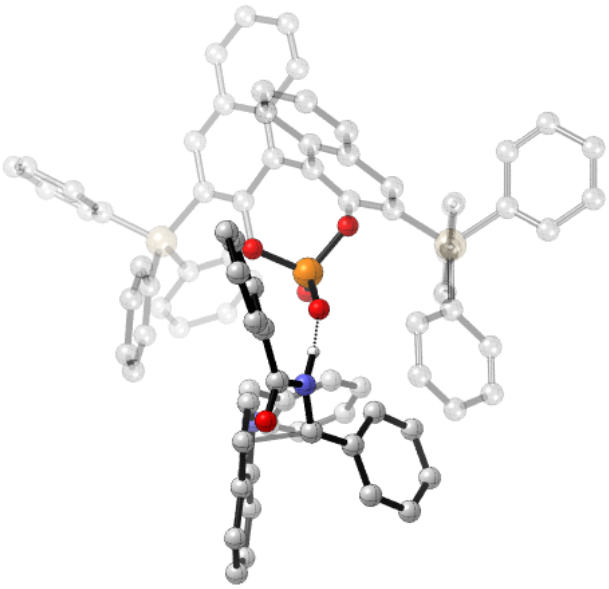

TS76-*Si*: $\Delta\Delta G^{\ddagger}$ = +7.4 kcal mol^{-1}, $\Delta\Delta G_{sol}^{\ddagger}$ = +7.7 kcal mol^{-1}

Figure 7.11. Competing TS for the $SiPh_3$ catalysed Friedel-Crafts. ONIOM (B3LYP/6-31G**:UFF), single-point energy M06-2X/6-31G**. Grayed-out regions were treated with UFF, and the full-colour regions were treated B3LYP/6-31G**.

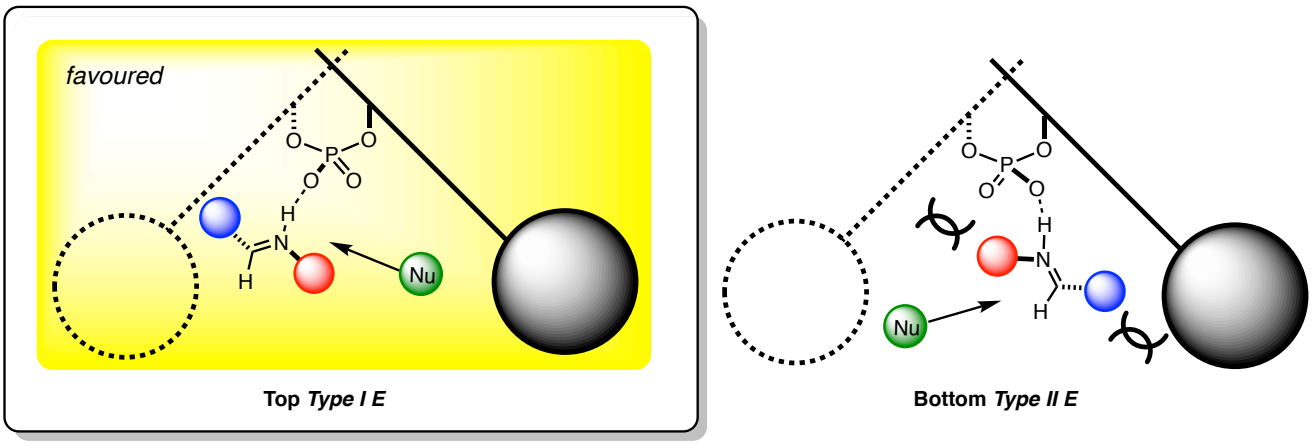

Figure 7.12. Qualitative model describing the origins of enantioselectivity. The Bottom *Type II E* pathway is higher in energy due increased steric interactions between the 3-substituent and the C-substituent, in combination with increased steric interactions with the BINOL backbone and the N-substituent.

7.4 Conclusions

The structure of difluoroenol silylethers and N-protected indoles preclude hydrogen-bonding interactions from the nucleophile to the catalyst, making selective additions challenging. I have investigated and compared reactions proceeding through monoactivation mechanisms. I show that the approach of the nucleophile is dictated by the size of the reactants, and the catalyst 3,3' groups controls both the orientation of the N-substituent and the configuration of the imine (mono or dual activations). Through the use of various techniques, I probed the influence of sterics on the system, and successfully determined a relationship between the remote steric profile of the 3,3' catalyst substituents quantified by AREA(θ) and the level of enantioinduction imparted upon addition.

In my follow up study, I probed the origin of selectivity in Friedel-Crafts reaction and show similar features between the two reactions exist. In both cases the BINOL backbone plays a major stereocontrolling role, offering additional insight into the modification of catalyst architecture on the enantioselectivity.

Chapter 8

8 Silver Phosphate Catalysed Spirocyclisation of Aromatic Ynones

8.1 Background and Methods

Within the broader field of asymmetric catalysis, chiral anion directed catalysis is predicated on the formation of a tight ion pair between the conjugate base and a cationic reaction component. This strategy is in principle general to any situation in which a cationic reagent or reaction intermediate is involved in the enantiodetermining step. Whether the association between the catalyst and substrate is purely electrostatic can lead to some mechanistic uncertainty.[263] Despite this, chiral anion directed catalysis has evolved into a field with numerous reaction classes and catalyst structures having been reported.[264-277]

In 2006, Mayer and List first reported the use of the conjugate base of a chiral phosphoric acid as a chiral anion in catalysis (Figure 8.1).[278] The formation of an ion pair between the achiral iminium and a chiral phosphate enabled a highly enantioselective conjugate reduction of an enone using Hantzsch ester. Since the iminium intermediate is fully substituted, its interaction with the catalyst can only be ionic.

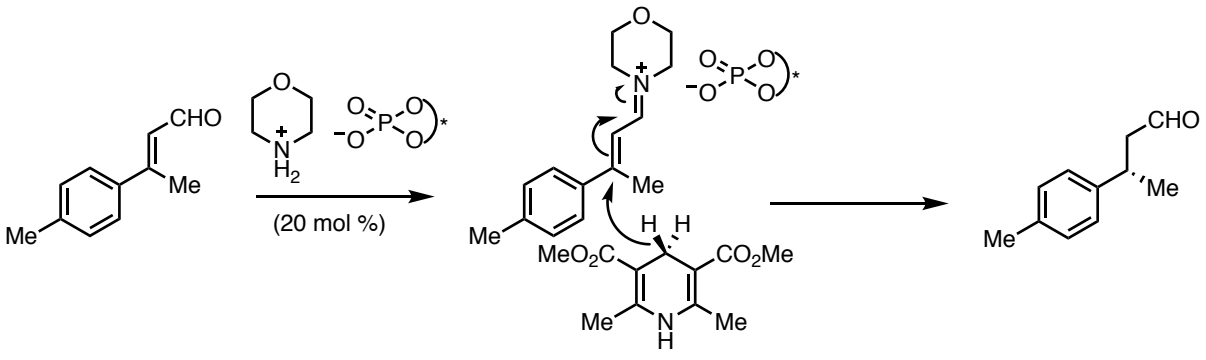

Figure 8.1. List's report of chiral anion catalysis with phosphate anions.

Toste reported in 2007, that transition metal-catalysed reactions could also be rendered highly enantioselective through the action of a chiral phosphate.[279] By combining an achiral cationic Au(I) species with a chiral phosphate, cyclised THF products could be obtained in excellent yields and enantioselectivities (Figure 8.2). This example was particularly noteworthy as the favoured linear geometry of Au(I) complexes makes efficient chiral transfer of chiral information from ligand to substrate challenging.

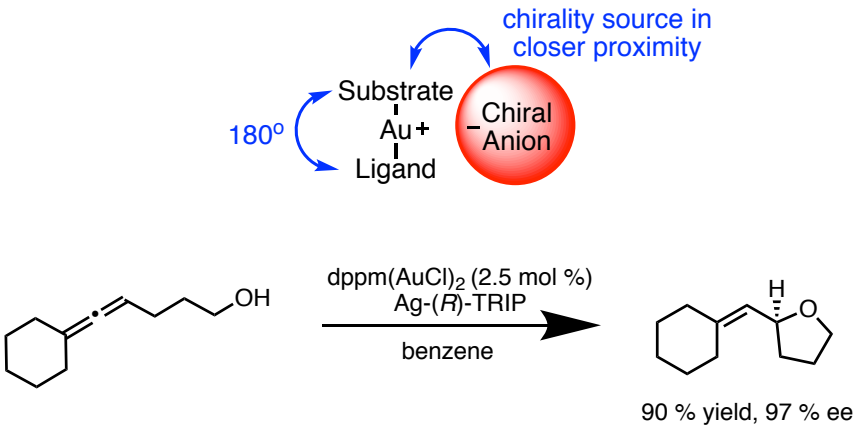

Figure 8.2. Au(I) phosphate catalysed enantioselective hydroalkoxylation.

In 2011, the Toste group extended this idea to enantioselective phase transfer catalysis,[280-281] in which the only previous successful examples involved the use of cationic catalytic species.[282] It was postulated that an insoluble, cationic reagent could be rendered soluble as a result of ion pairing with a lipophilic chiral anion, ensuring that any of the reagent available for subsequent reaction would be in the chiral environment of the catalyst, minimizing an unselective background reaction.[283] This strategy has proved successful for enantioselective halogenations,[284--293] and coupling reactions.[294]

Recently the Taylor group has shown that chiral phosphates could be paired with Ag(I) salts to effect the spirocyclisation of aromatic ynones.[295] The group pursued the same catalyst optimisation strategy that had proved successful for Brønsted acid catalysis, variation of the backbone and 3,3' substituent structure. Despite rigorous empirical screening campaigns only moderate enantioselectivities were obtained (Figure 8.3).

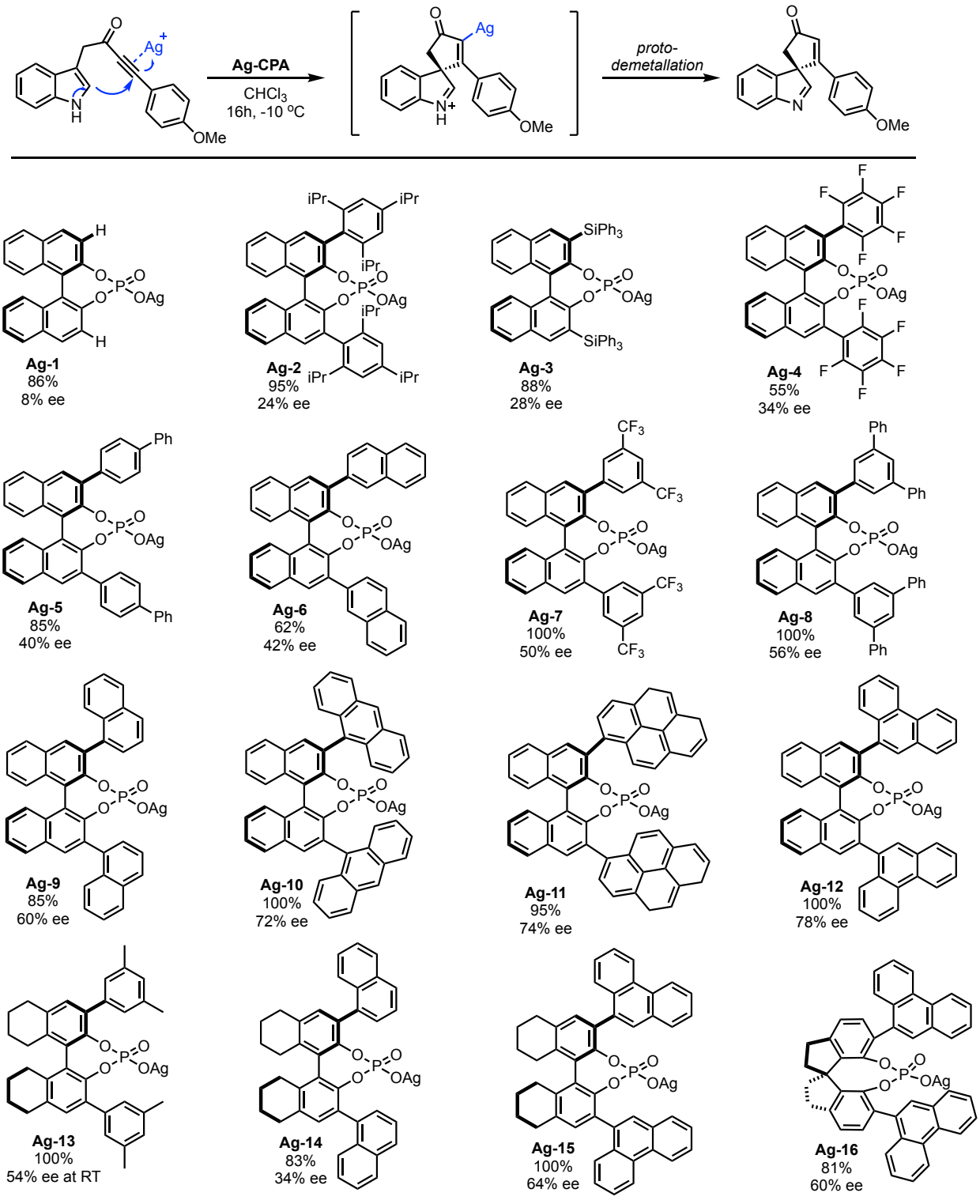

Figure 8.3. Catalyst screening results as reported by Taylor *et al.*

Among the chiral silver phosphates the only clear trend that emerged was that increasing the size of the π-acceptor ligand on the 3,3' substituent increased enantioselectivity but only to an extent (**Ag-9**, **Ag-10**, **Ag-11** and **Ag-12**). Dramatically increasing and decreasing the steric bulk or changing the electronics of the catalysts did not provide a selectivity boost and the enantioselectivities remained consistently poor. Furthermore, enantioselectivity was particularly sensitive to the structure of the aromatic group on the ynone suggesting this was an important structural feature in the TS of the enantiodetermining step. Only modest consistency in enantioselectivity was shown over a small range of ynones (Figure 8.4).

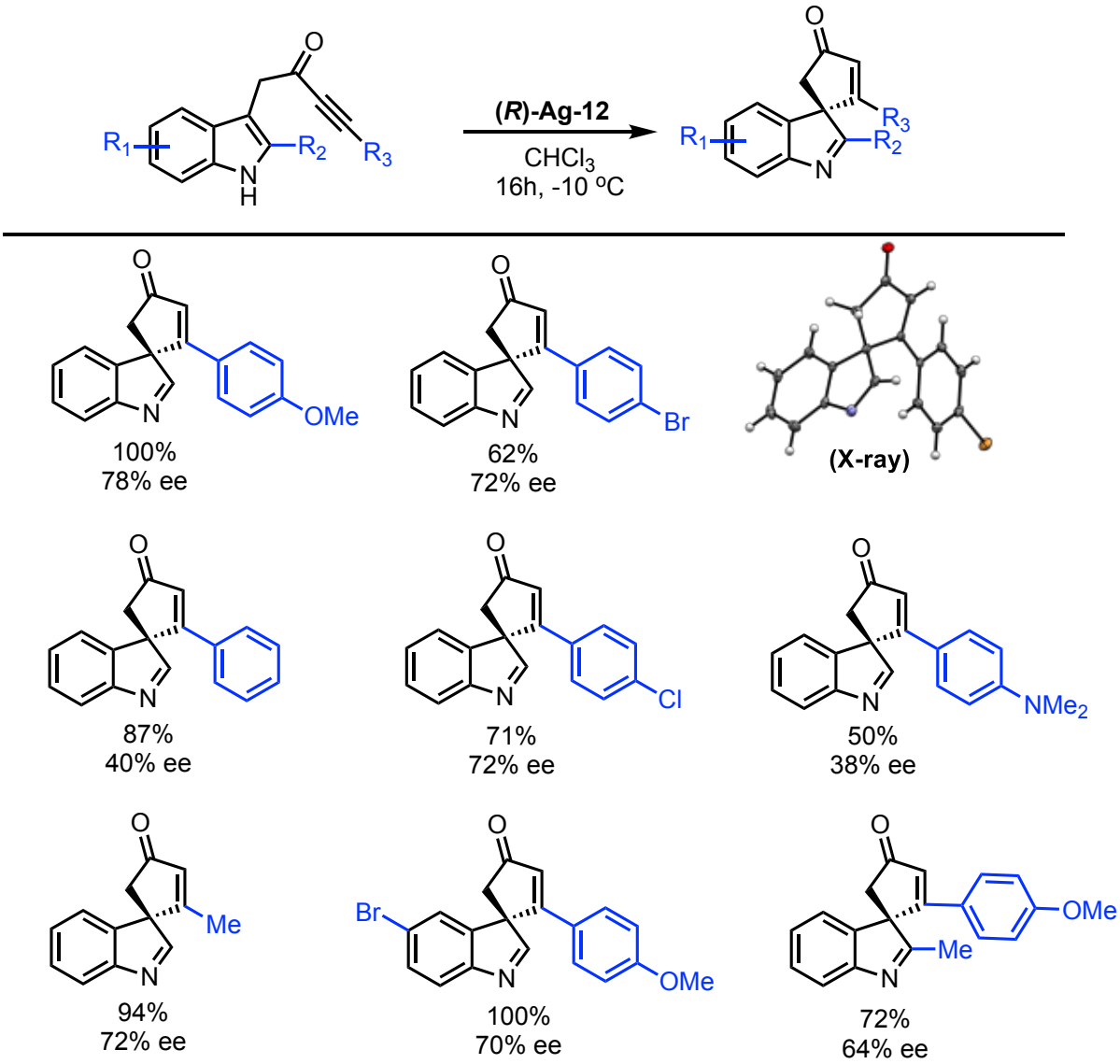

Figure 8.4. Substrate scope.

The origins of the selectivity remain unclear. Taylor and co-workers proposed a model to rationalise selectivity, where the catalyst cavity is envisaged as a grid split into four quadrants of varying steric bulk (Figure 8.5). The reaction is presumed to initiate *via* alkyne coordination to the silver atom in the centre of this cavity and so the stereochemistry is determined by the orientation of the tethered indole, which will favour a conformation that minimises unfavourable steric interactions. This model does not explain the selectivity variation in catalyst nor the dependence of the ynone on stereoinduction. The physical origins of the experimental data was impossible to discern on inspection alone, from this standpoint I was contacted to help with a mechanistic investigation into the reaction with the hope that understanding the reasons for asymmetric induction could be exploited to achieve better enantioselectivities.

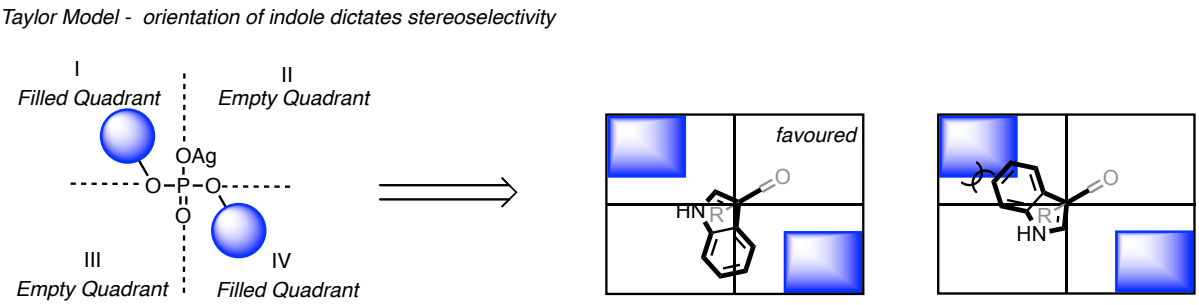

Figure 8.5. Taylor model for rationalising the origin of enantioselectivity.

For the QM/MM hybrid calculations on the full catalyst and reagent system, transition states were located first, by a conformational search in MacroModel (version 9.9)[54] using the OPLS-2005 force field and an acid catalyst as a template.[184-186] The proton of the catalyst was then replaced by a silver atom and selected conformers within 10 kJ mol^{-1} of the minimum were optimized using the ONIOM method implemented in Gaussian 09 (revision D.01).[35]

The B3LYP density functional,[43-44] and LACVP** basis set,[296] were used for the high-layer, and the force field UFF,[195] was used for the low-layer unless stated otherwise. The reactants and the silver phosphate moiety of the catalyst were included in the high-layer, and the remaining regions of the catalyst were treated as the low-layer. The position of the partition within the catalyst was chosen as the silver phosphate binds directly to the reagents, whereas the remaining catalyst acts as steric bulk and can be adequately described by molecular mechanics. All calculations were performed with the (*R*)-catalyst for model consistency with the connectivity shown in the reaction scheme. I use the Kekulé bonding structure for all catalysts ensuring that the connectivity in the catalyst backbone is consistent between the structures allowing for accurate energy and geometry comparisons. Single point energy calculations were performed on the resulting structures using M06 density functional,[46] and the LACVP** basis set, using non-default convergence criteria (fine grid density, ultrafine accuracy level) as implemented in the Jaguar program (version 7.9).[55] This energy was used to correct the gas-phase energy derived from the ONIOM calculations. Free energies in solution were derived from structures optimized in the gas phase at the ONIOM (B3LYP/LACVP**:UFF), level of theory by means of a single point calculation using M06/LACVP** with the polarizable continuum model (PCM) as implemented in the Jaguar program (version 7.9), using chloroform (probe radius = 2.52 Å) as the solvent.[50] These values were used to correct the Gibbs free energy derived from the ONIOM calculations. Structures are illustrated using CYLview.[196]

8.2 Origins of Stereoinduction

8.2.1 Application of ONIOM methods

Chiral phosphoric acids are generally “designed” with large substituents at the 3,3’ with the premise that these groups would occupy chiral space and force the substrate into conformations within the active site that minimize unfavourable steric interactions with catalyst. This conventional strategy has shown to work well as outlined in the preceding chapters. In this case it is clear there was a subtle interplay between the structure of the catalyst and the aromatic group of the ynone, with even minor perturbations to the catalyst or substrate structures often resulting in significant and unpredictable variations in enantioselectivity. This non-intuitive relationship between substrate and catalyst structure coupled with the fact that enantioselectivity could still be improved enticed us to conduct a mechanistic study into the reaction. Reactions with catalysts, **Ag-2**, **3** and **12** were investigated using computational methods and the results are summarised in Figures 8.6 and 8.7. Calculations were performed at the ONIOM(B3LYP/LACVP**:UFF) level followed by single point calculation at the M06 level of theory and the same basis set. Given the computational cost required for the complete catalyst structures and considering that the trends from one catalyst to the next were more important than the absolute value of any one structure, this choice of computational method was deemed acceptable. All catalysts activate the alkyne to nucleophilic attack by coordination. In agreement with experiment, addition to the *Si*-face of the alkene is favoured (**TS78-*Si*, TS79-*Si*** and **TS80-*Si***) and catalyst **Ag-12** is computed to be the most selective. The favoured orientation of the aromatic group in the ynone is important for determining the TS pathway leading to the major enantiomer. In the TS leading to the major enantiomer using **Ag-12** the aromatic group is orientated towards the 9-phenanthryl allowing for π-stacking, **TS80-*Si***. By comparison calculations using **Ag-2** and **3** show that in the favored TS pathway π-stacking is precluded and hence these catalysts are less effective. In these cases the substituent does not possess the optimum geometry to engage in π–stacking interactions. In **TS80-*Re*** the indole tilts to avoid steric interactions with the 3,3’ substituents as such the hydrogen that bonds to the phosphate swaps from N-H to C-H. In the *Re* TS the aromatic group is pointed away from the front of the TS but a combination of increased steric interactions between the indole and the catalyst and decreased π-stacking makes this pathway unfavorable with all catalysts tested.

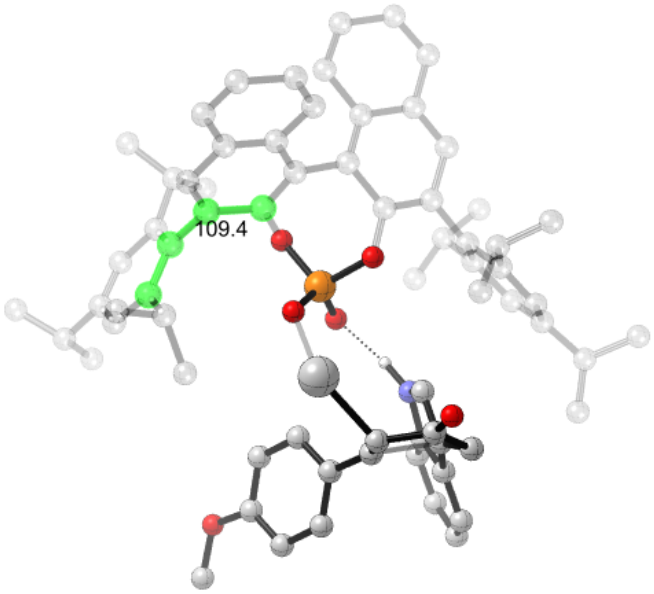

TS78-*Si*: $\Delta\Delta G^{\ddagger}$= 0 kcal mol^{-1}, $\Delta\Delta G_{sol}^{\ddagger}$ = 0 kcal mol^{-1}

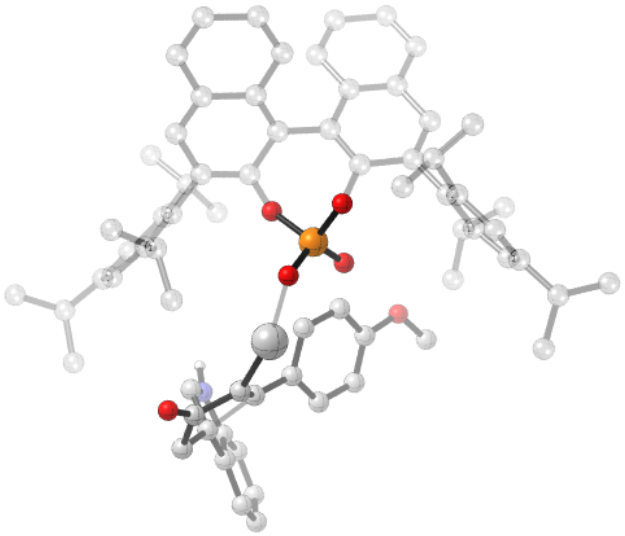

TS78-*Re*: $\Delta\Delta G^{\ddagger}$= +5.3 kcal mol^{-1}, $\Delta\Delta G_{sol}^{\ddagger}$= +0.5 kcal mol^{-1}

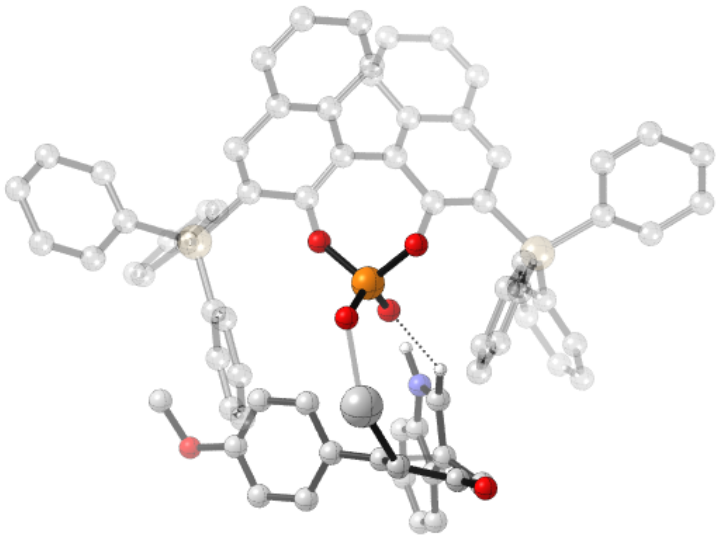

TS79-*Si*: $\Delta\Delta G^{\ddagger}$= 0 kcal mol^{-1}, $\Delta\Delta G_{sol}^{\ddagger}$ = 0 kcal mol^{-1}

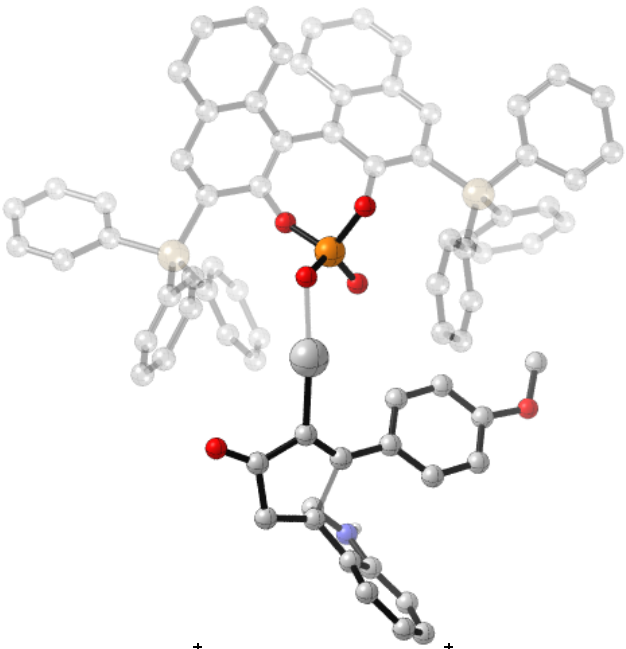

TS79-*Re*: $\Delta\Delta G^{\ddagger}$= +7.3 kcal mol^{-1}, $\Delta\Delta G_{sol}^{\ddagger}$= +0.8 kcal mol^{-1}

Figure 8.6. TS structures for the TRIP and $SiPh_3$ derived silver phosphates. Geometries ONIOM(B3LYP/LACVP**:UFF) followed by single point M06/LACVP **. Grayed-out regions were treated with UFF, and the full-colour regions were treated B3LYP/LACVP**.

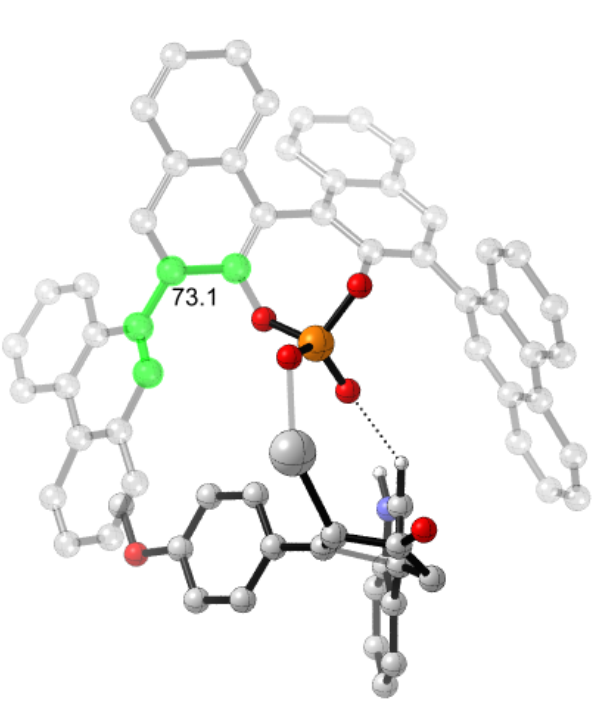

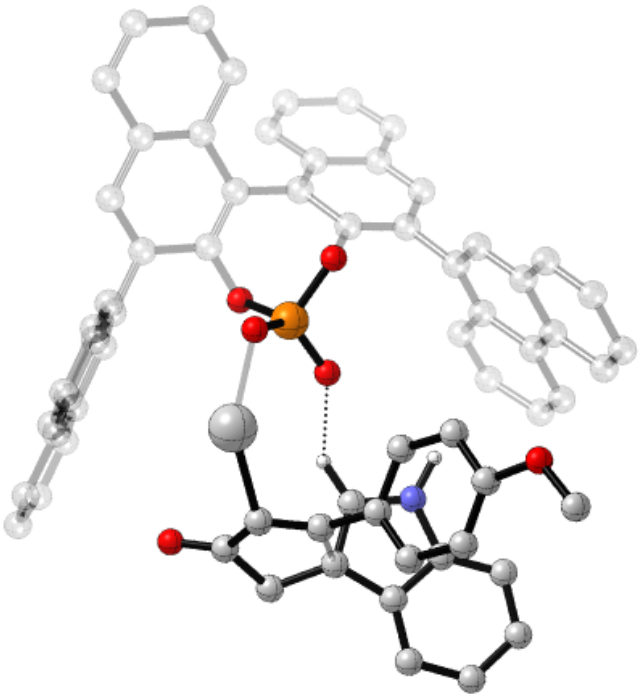

TS80-*Si*: $\Delta\Delta G^{\ddagger}$ = +1.2 kcal mol^{-1}, $\Delta\Delta G_{sol}^{\ddagger}$ = 0 kcal mol^{-1}

TS80-*Re*: $\Delta\Delta G^{\ddagger}$ = 0 kcal mol^{-1}, $\Delta\Delta G_{sol}^{\ddagger}$ = +2.3 kcal mol^{-1}

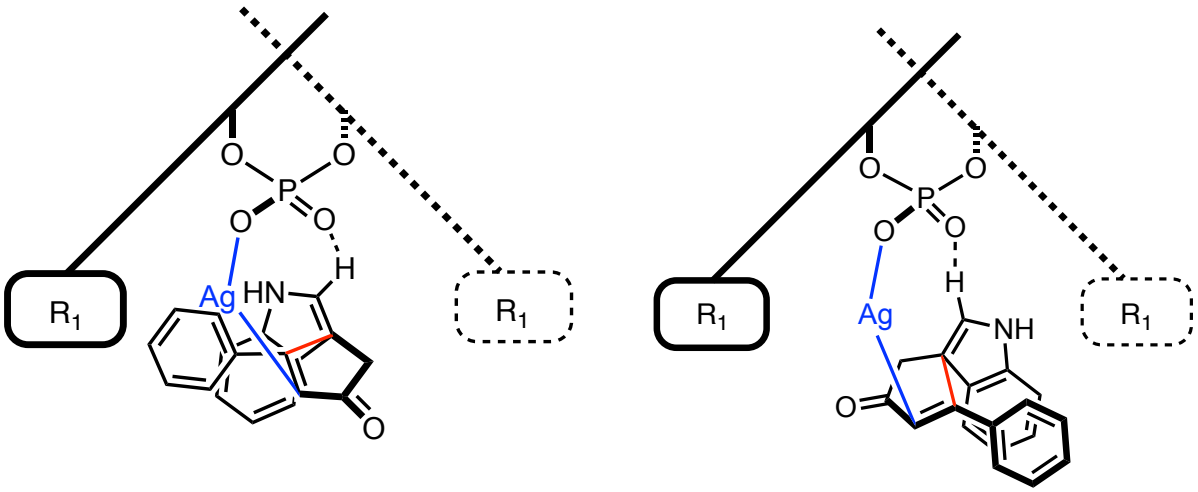

Figure 8.7. TS structures for the 9-phenanthryl derived silver phosphates. Geometries ONIOM(B3LYP/LACVP**:UFF) followed by single point M06/LACVP ** (top). Grayed-out regions were treated with UFF, and the full-colour regions were treated B3LYP/LACVP**. Qualitative model to describe the preference for the *Si* face attack (bottom). In **TS80-*Si*** the aromatic group of ynone points towards the 3,3' group establishing π-interactions. These stabilising interactions are not present **TS80-*Re*** as the aromatic group points towards the empty pocket of the catalyst.

Solvent plays a key role in dictating the selectivity of the reaction. For TRIP and $SiPh_3$ catalysed reactions, in which there is no H-bonding interaction from indole to catalyst, solvent stabilizes the negative charge on the phosphate lowering *Re* relative to *Si*. For the 9-phenanthryl in which H-bonding is established due to the greater steric accessibility, the opposite trend is true and *Si* face addition is lowered relative to *Re*. This is most likely due to the strengthening of the π-interactions through the hydrophobic effect,[297] in which, flat surfaces of aromatic molecules are traditionally considered hydrophobic and the surface area exposed to polar solvent is minimized upon stacking. This highlights the need to rigorously assess solvent effects when computationally investigating competing TS of organometallic reactions. I believed that the torsion angle between the BINOL and the 3,3' substituent reflected the orientation at which the 3' substituent can engage the substrate at the enantiodetermining TS (Figure 8.8). In cases in which the catalyst substituent is favourably positioned to engage the aromatic group during the enantiodetermining TS, a lower energy pathway becomes available which is absent for other catalysts.

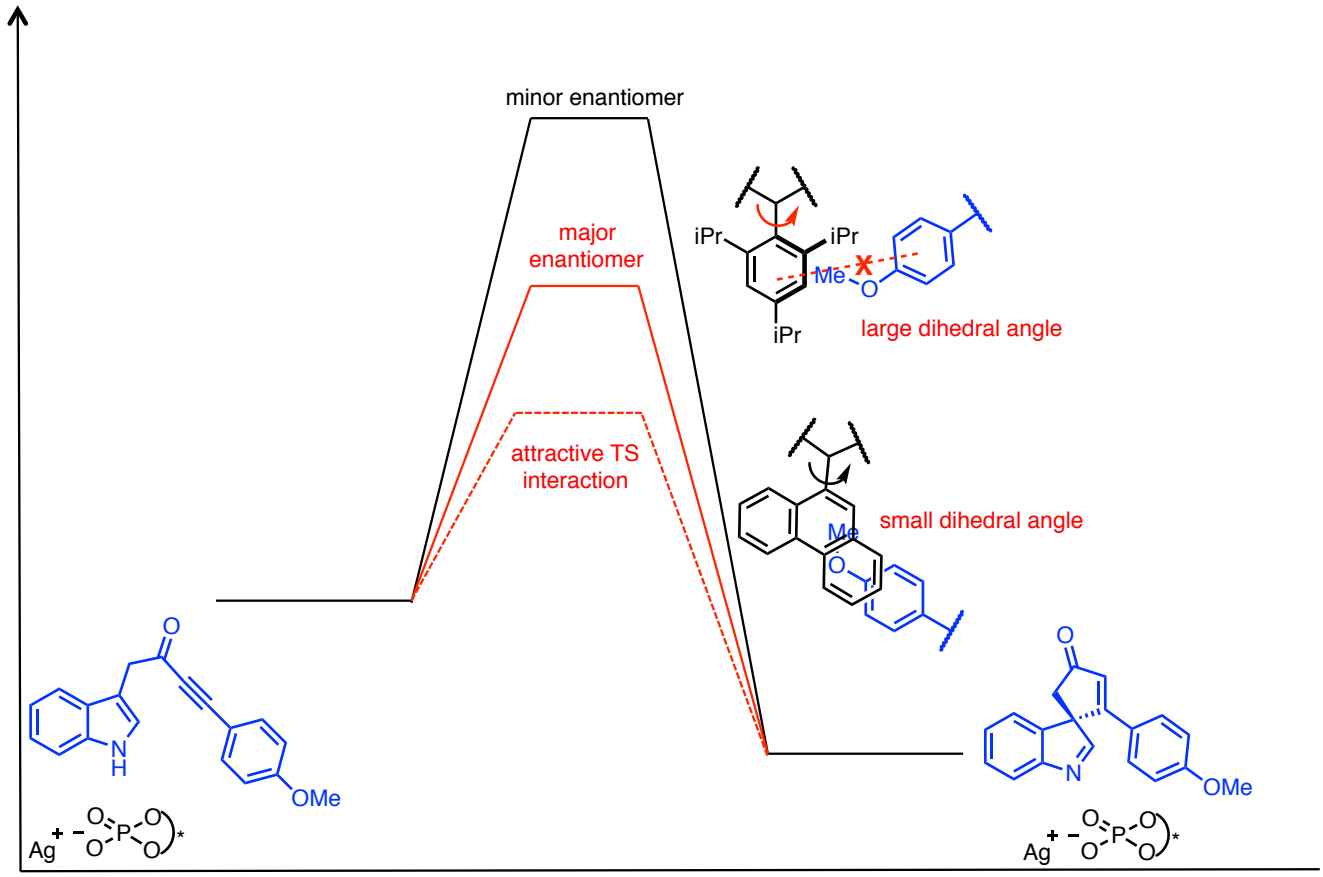

Figure 8.8. Qualitative interpretation of catalyst effect on enantioselectivity.

This view is consistent with a mechanistic picture in which attractive non-covalent interactions stabilise one diastereoisomeric TS, as opposed to the more commonly proposed situation in which steric repulsion selectively disfavours one pathway. Based on my results and those of experiment, the most favourable TS substituent orientation appeared to be with a catalyst with small torsion angles, close to 73°, which leads to higher enantioselectivities. In contrast, catalysts with large torsion angles that did not introduce the proposed directional and steric effects led to diminished enantioselectivities overall.

To direct experimental work, and, therefore, reduce time-consuming experimental screening processes, TS, were located to assess the suitability of different catalysts for the reaction. The expected levels of selectivity were also investigated by comparing the free energies leading to opposite enantiomers to that obtained with the optimal performer. I believed catalysts with unsymmetrical proximal steric bulk would more readily adopt the correct geometry to engage in stacking interactions and opted to include some in the screening process. Despite testing a number of synthetically viable catalysts the predicted enantioselectivities were poor to moderate (Figure 8.9). In light of this failure I decided to modulate the other component of the stacking interaction – the substrate to improve enantioselectivities.

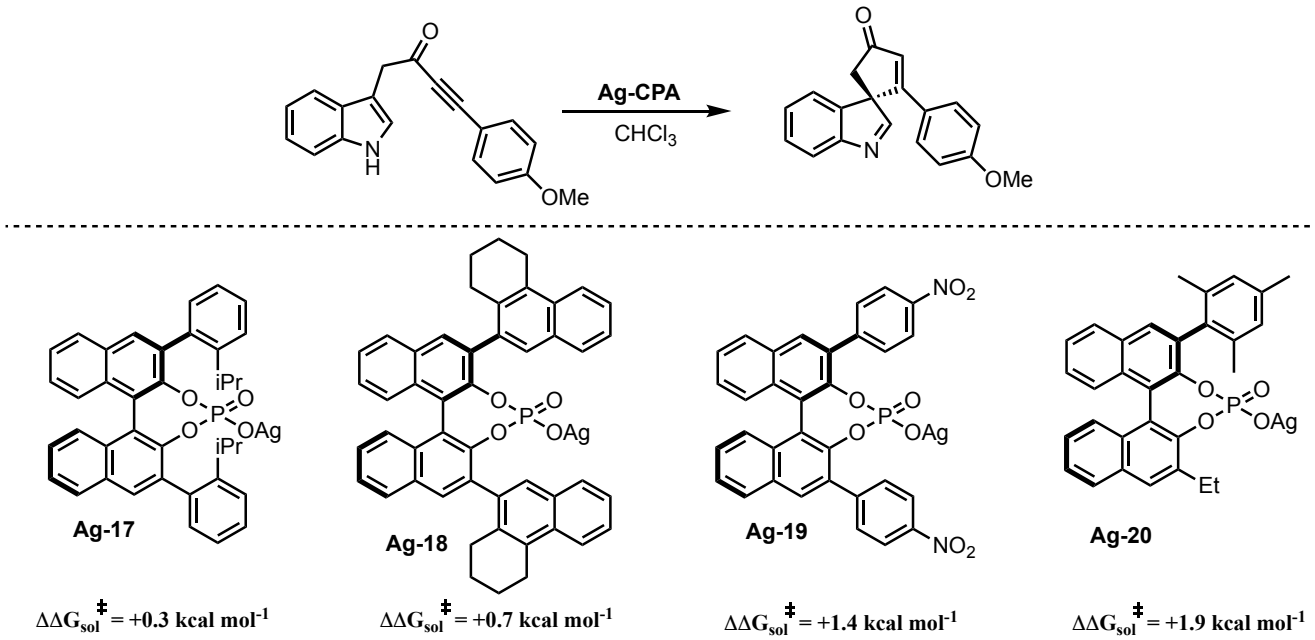

Figure 8.9. Computational catalyst screening results. Energies are quoted relative to *Si* face addition.

8.2.2 Method comparison: ONIOM(B3LYP:UFF) vs B3LYP

In order to test the validity of my results obtained using the ONIOM method, key TS in Figure 8.7 were recalculated. In the interest of computational feasibility the BINOL was truncated to BIPOL. I postulated that such a modification would be minimal, as the substrate did not directly interact with the catalyst backbone. Understanding the form of the potential energy surface (PES) with this simplified system would be useful in determining the accuracy of my method, in addition to highlighting any important interactions for stereoinduction. The lowest recomputed TS leading to competing products are shown in Figure 8.10. The relative energies of the TS between the methods were significantly altered. Addition to the *Si* face is now energetically disfavoured and the reaction is calculated to proceed *via* the alternative TS, **TS81-*Re***. The disagreement of the TS pathway in operation from one method to the other gives us confidence that dispersive interactions are significant stereocontrolling elements and are responsible for the stabilisation of *Si* face addition. The hybrid DFT, B3LYP method, does not capture this effect.

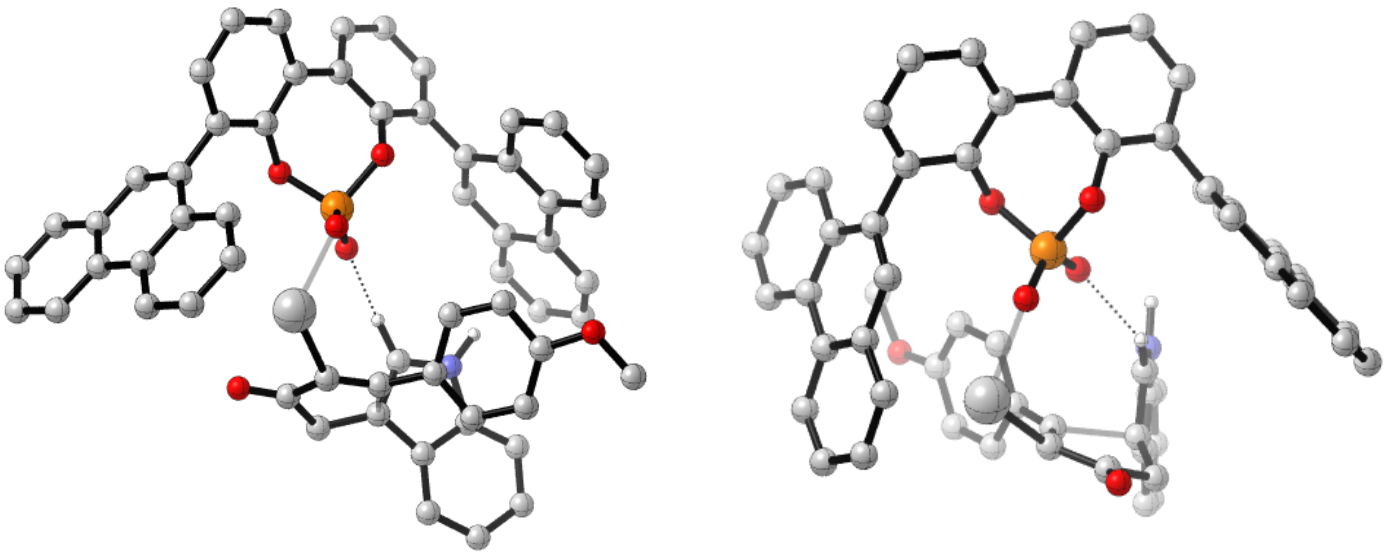

TS81-*Re*: $\Delta\Delta G_{sol}^{\ddagger}$ = 0 kcal mol^{-1} **TS81-*Si*: $\Delta\Delta G_{sol}^{\ddagger}$ = +3.1 kcal mol^{-1}**

Figure 8.10. TS structures for the 9-phenanthryl BIPOL-derived silver phosphate. Geometries B3LYP/LANCVP** followed by single point M06/LACVP**.

8.3 Substrate Effect on Enantioselectivity

There have been numerous studies devoted to understanding the physical origins of substituent effects in tuning the strength of π-π interactions. Until recently, the prevailing viewpoint, initially proposed by Hunter and Sanders,[298] was based on π-polarization. Electron withdrawing substituents were proposed to remove electron density from an arene's π-system *via* π-resonance effects and vice versa for electron donating substituents.[299-305] As such, this model predicts that the interaction between two rings will strengthen with the introducing of an electron withdrawing substituent into one of the partners and the introduction of an electron donating substituent should weaken the interaction by the opposite mechanism. ESP maps have often been employed to support this viewpoint, based on the assumption that the ESP above and below a ring centroid is reflective of its electron density. In recent years, however, the π-polarization model has been a source of controversy.[306-308] High-level computational studies have suggested that the introduction of any substituent donating or withdrawing should increase the strength of the π- π interactions compared with the benzene dimer.[309] The most recent model consistent with the majority of the available data is from Wheeler and Houk, which show that it is the direct interactions between the local C-X/H dipoles of substituted aromatic rings that determine the strength of a π- π interaction.[308,310-317] Viewed from this perspective aromatic rings primarily serve as platforms upon which to place substituents in a spatial arrangement that will either be attractive or repulsive depending on the relative geometries between the interacting dipoles. The direct interaction model also states that the substituent effects should be additive. Correspondingly, I thought that by further substituting the aromatic ynone, appropriately, should enhance the favourable interaction. I anticipated that a TMP group would provide correct requirements for a stronger π-interaction with the 9-phenanthryl catalyst. Indeed when I calculated the corresponding TS the energy difference between the competing pathways increased from 2.3 to 2.9 kcal mol^{-1} (Figure 8.11). The Taylor group evaluated this substrates capacity to obtain improved enantioselectivity experimentally. The computational prediction was verified in practice and the spirocycle was obtained in 90% ee, the highest ee obtained to date. This result supports the claim that the orientation of the phenanthryl ring, coupled with the aromatic substituents, can be strategically manipulated to fine-tune the non-covalent interactions underlying enantioselectivity.

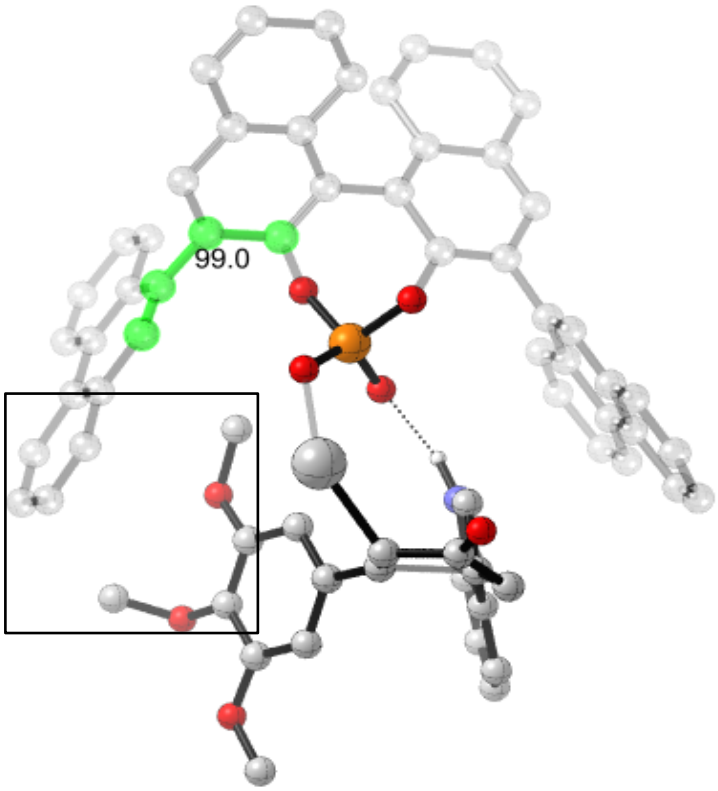

TS82-*Si*: $\Delta\Delta G_{sol}^{\ddagger}$ = 0 kcal mol^{-1}

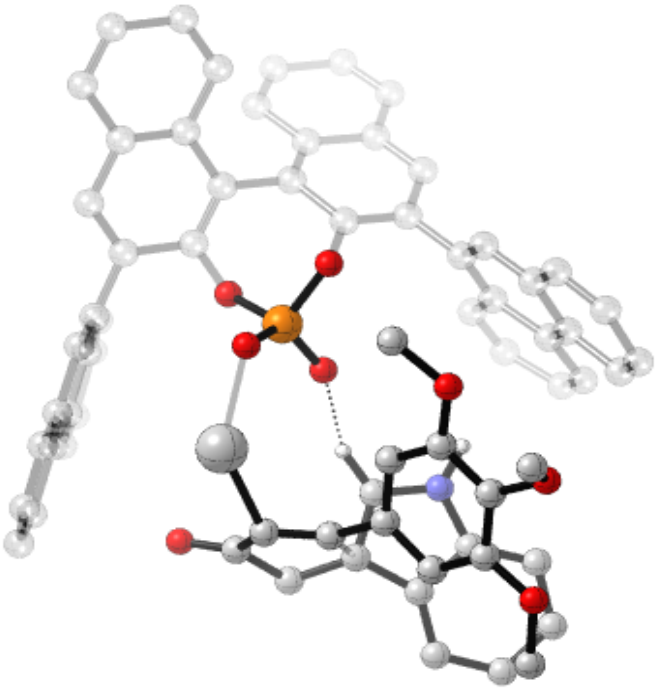

TS82-*Re*: $\Delta\Delta G_{sol}^{\ddagger}$ = +2.9 kcal mol^{-1}

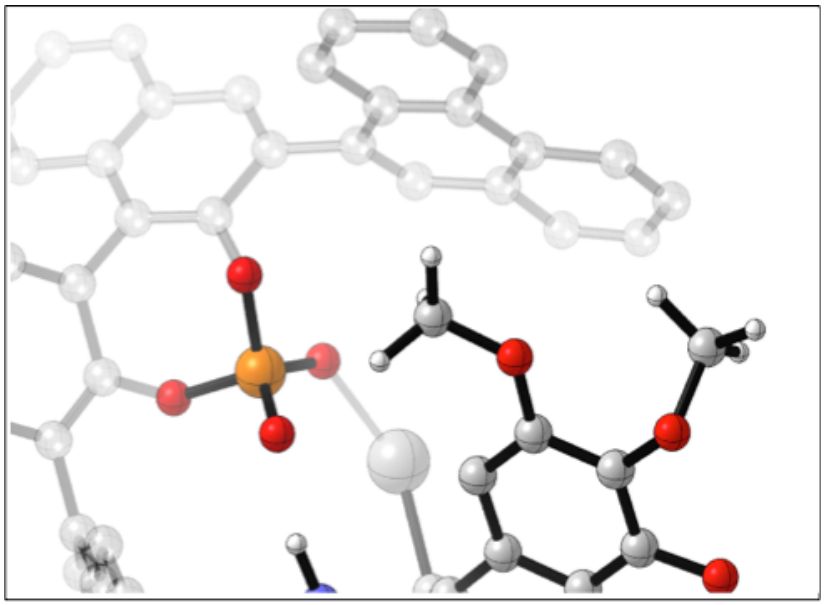

Figure 8.11. TS structures for the 9-phenanthryl derived silver phosphate with the TMP substrate. Geometries ONIOM(B3LYP/LACVP**:UFF) followed by single point M06/LACVP** (top). Grayed-out regions were treated with UFF, and the full-colour regions were treated B3LYP/LACVP**. Increasing the steric bulk of the aromatic group results in an increase in dihedral angle to compensate. Despite this, the introduction of additional C-H groups allows the establishment of additional C-H π-interactions that more than compensates for the diminished π-stacking interactions.

8.4 Redesigning the 3,3' group

Despite obtaining a very positive result, this strategy was not general and in principle was limited to a small subset of highly functionalised ynones. I approached this problem within the framework of my hypothesis that π-interactions are additive and increasing the π-surface area of the 9-phenanthryl group without changing the overall structure may lead to increased favourable interactions. Specifically, I anticipated that a chrysene-derived catalyst could be highly enantioselective and was computationally evaluated using the general method (Figure 8.12).

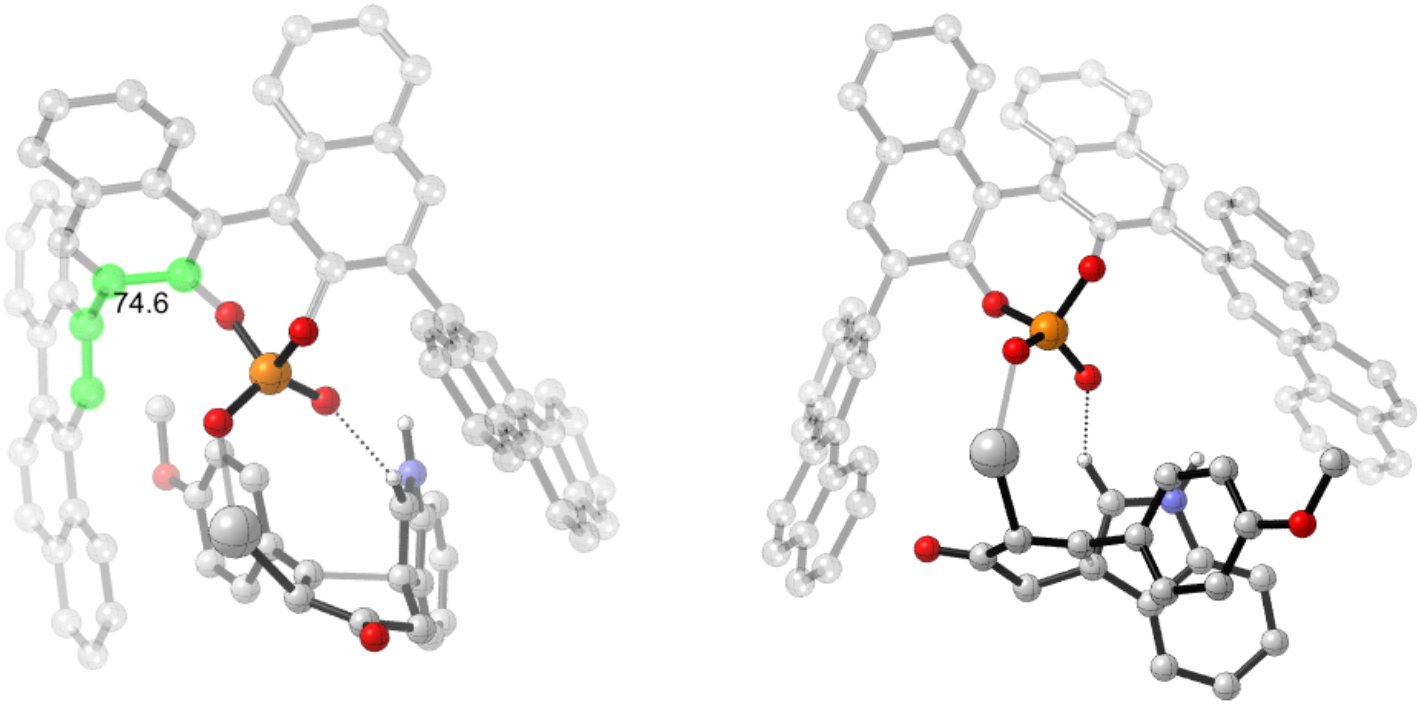

TS83-*Si*: $\Delta\Delta G_{sol}^{\ddagger}$ = 0 kcal mol^{-1} **TS83-*Re*: $\Delta\Delta G_{sol}^{\ddagger}$ = +2.6 kcal mol^{-1}**

Figure 8.12. TS structures for the chrysene derived silver phosphate. Geometries ONIOM(B3LYP/LACVP**:UFF) followed by single point M06/LACVP**. Grayed-out regions were treated with UFF, and the full-colour regions were treated B3LYP/LACVP**.

Computationally the chrysene catalyst is expected to be more selective and the energy gap between the TS leading to competing products increases from 2.3 to 2.6 kcal mol^{-1}. This can be attributed to increased π-stacking interactions between the extended π-surface of the chrysene in comparison with the 9-phenanthryl substituent. Motivated by this result the synthesis and testing of the chrysene catalyst is currently underway.

8.5 Expanding Reaction Scope

I next turned my attention to substrates incorporating pyrrole as the nucleophilic component. When the pyrrole analogue was synthesised and tested in the spirocyclisation reaction similar levels of conversion and enantioselectivity were observed (Figure 8.13).

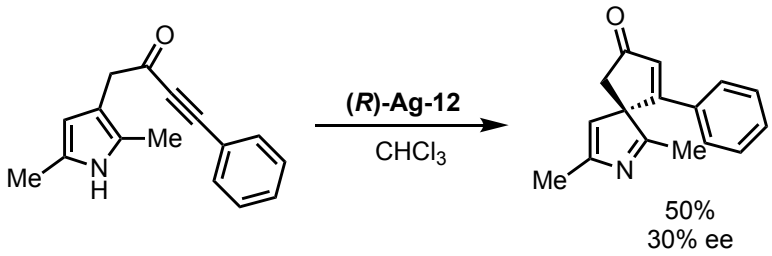

Figure 8.13. Extension of the spirocyclisation methodology to pyrroles.

From the onset it was not immediately obvious to us that the same computational model would be applicable due to the variation in structures. To explore the possibility of extension of the computational model in Figure 8.7, I calculated the TS pathways leading to competing products (Figure 8.14). Interestingly, the substrate takes a similar arrangement within the chiral cavity and the reduction in steric profile of the nucleophilic component allows the pyrrole to tilt towards the 9-phenanthryl without significant steric interactions. The tilted disposition pushes the aromatic group of the ynone in closer proximity to the 9-phenanthryl 3' substituent allowing the establishment of π stacking interactions and a C-H interaction between the phosphoryl oxygen and the methyl group of the pyrrole. Calculations reveal that the pyrrole derived aromatic ynone is expected to perform better, although quantitatively the energy appears to be slightly overestimated, the qualitative agreement from calculation to experiment should follow. Collaborative experimental studies for the verification of this result are underway.

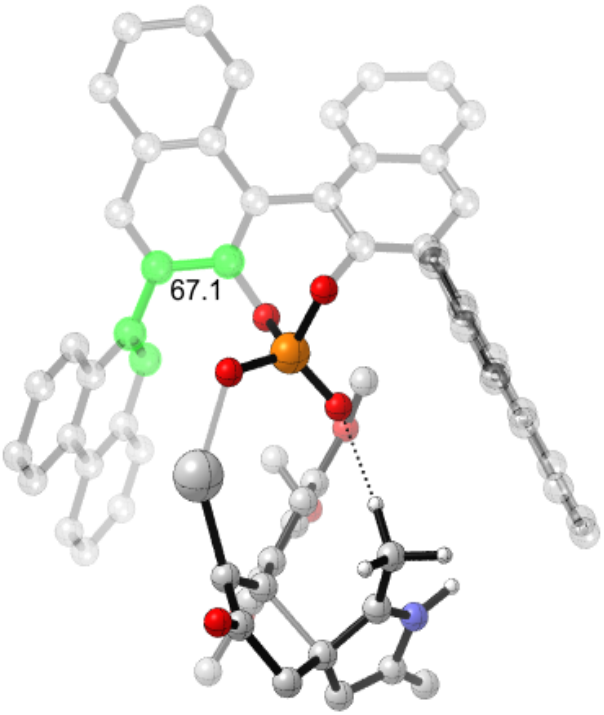

TS84-*Si*: $\Delta\Delta G_{sol}^{\ddagger}$ = 0 kcal mol^{-1}

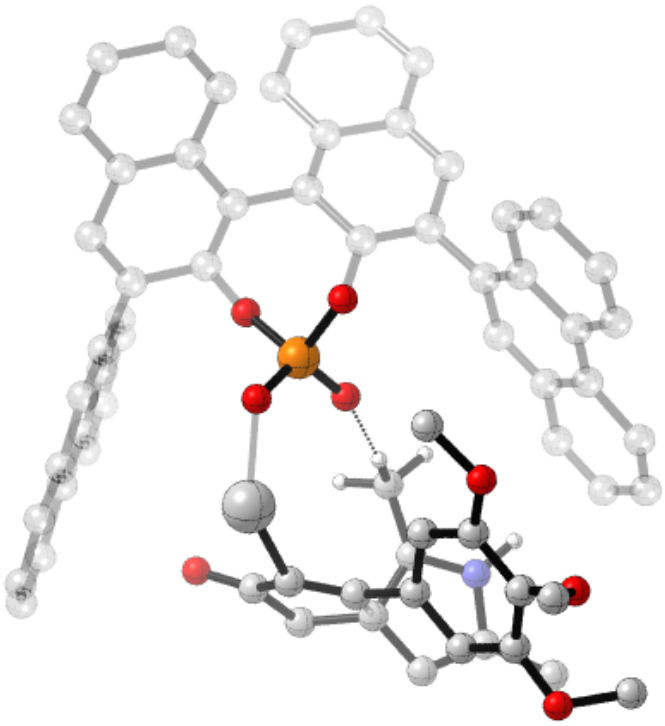

TS84-*Re*: $\Delta\Delta G_{sol}^{\ddagger}$ = +4.4 kcal mol^{-1}

Figure 8.14. TS structures for the 9-phenanthryl derived silver phosphate with the pyrrole substrate. Geometries ONIOM(B3LYP/LACVP**:UFF) followed by single point M06/LACVP**. Grayed-out regions were treated with UFF, and the full-colour regions were treated B3LYP/LACVP**. Decreasing the steric bulk of the nucleophilic component results in greater conformational accessibility inside the chiral cavity. As a result the reagent can tilt towards the 9-phenanthryl 3-substituent allowing the sterically large TMP aromatic group to establish π-stacking interactions as indicated by a small dihedral angle. This is a different scenario to when indole containing substrates are employed, in which the TMP can only establish C-H π-interactions in the *Si*-TS.

8.6 Conclusions

Computations show that phenanthryl catalyst is the most stereoselective because the *Si*-face attack is stabilized by favourable electrostatic interactions between the aromatic group of the ynone and the catalyst 3' substituent. The structure of the aromatic ynone is central to the selectivity of the reaction. Careful modulation of this structural component has rendered the reaction to be highly enantioselective due to increased π–interactions, verified by calculations. These findings will hopefully lead to increased consideration of strategic use of interactions beyond steric repulsion as elements of reaction design. Weak, non-covalent interactions are typically in the energy range required to distinguish a highly enantioselective reaction from its racemic counterpart (2-3 kcal mol^{-1}), providing seemingly endless approaches to rational catalyst design. One of the challenges is that favourable interactions can usually also form with the solvent and so a favourable interaction is not, in itself, important, unless it is stronger than the alternative solvent interactions. The weakly attractive nature of such interactions and their complex geometric requirements render the design of effective catalyst very difficult. It is worth mentioning that no general catalyst emerged during these preliminary scope studies. I believe that different catalysts will provide superior results depending on the substrate employed.

As a collaborative effort I have extended the strategy of chiral phosphate Ag(I) catalysed spirocyclisations beyond indoles as the nucleophilic component. The synthesis of pyrrole compounds is currently underway and should give further insight into the scope of the reaction. Our calculations show that these substrates will undergo the same mechanism and the computational model developed previous is valid. This type of mechanism may be important in other silver phosphate catalysed reactions.

Recapitulation and Conclusions

A trained organic chemist has excellent intuitive skills in anticipating where a particular reaction may occur in a chemical structure and presenting a mechanistic rationale for the observed outcome. However, this skill does not provide a prediction of reaction efficacy. Therefore, the vast majority of time is expended on optimization of reaction conditions. Such a campaign can be highly frustrating in which the chemist investigates, often one at a time, the effect of catalyst and substrate structure, in addition to common reaction parameters (solvent, temperature, time etc.). Most often, the primary reasons for reaction performance is not frequently revealed making hypothesis-driven design and application to complex substrates challenging. A major focus of my research described in this thesis has been to address this considerable challenge by developing a computational tool set capable of predicting and interpreting reaction outcomes.

The most important advance was the discovery and implementation of parameters to describe the steric profile of substituents at the 3 and 3' positions of BINOL-derived chiral phosphoric acids. In this regard, I showed that a combination of, rotation barriers and AREA(θ), as structural descriptors, could be used to investigate the catalyst molecular features required for high levels of stereoselectivity. By focusing on the addition of protic nucleophiles to imines, a simple qualitative model was developed consistent for 77 literature reactions reporting over 1000 transformations, which identifies the catalyst steric features required for efficient enantioselectivity, validated by QM/MM hybrid calculations. This mechanistic understanding allowed the identification of a new, computationally verified, potentially better performing catalyst, which incorporates a non-intuitive C_1 symmetric design.

The transfer hydrogenation of *ortho*-hydroxy imines have also been studied and it has been concluded to proceed *via* an alternative bifunctional mechanism. There are two hydrogen-bonding interactions from reagents to catalyst, one from the *ortho*-hydroxyl group and a second from the nucleophile's proton. This mode of activation is lower in energy than those originally proposed due to the increase in strength of hydrogen bonding interactions between the catalyst and the reagents. An accurate qualitative model was developed which highlighted that large remote steric bulk was an important catalyst feature for efficient

stereoinduction. This study is anticipated to profoundly guide new applications of this catalytic mode of activation in the future.

In a similar theme, the use of AREA(θ) was correlated to enantioselectvity outcomes in nucleophilic additions to imines proceeding *via* monoactivation mechanisms. In sum, the combination of correlations, experimental results and computational characterization of the relevant TS revealed that the nature of the catalyst had a profound effect on the configuration of the imine. For the Mannich reaction, increasing the steric profile of the 3,3' substituents raises the energy of the monoactivation mechanisms, relative to the dual activation mechanism which proceeds through a compact *Z* imine. This distinct shift in mechanism was revealed through changes in slope of the correlation and verified using ONIOM.

Finally, the silver phosphate catalysed spirocyclisication of aromatic ynones was studied using ONIOM methods. Experimentally, the aromatic group on the ynone was determined to be a key stereocontrolling feature, seemingly minor steric and electronic structural perturbations to this functionality, and the catalysts 3,3' substituents had an acute influence on enantioselectivity. This intriguing result suggested that a specific interaction between this substituent and the catalyst was occurring. Calculations have shown the aromatic group of the ynone to be interacting with the 9-phenanthryl catalyst substituent through attractive π-interactions. Exploiting this finding, a highly functionalized aromatic ynone was designed with premise that higher levels of stereoinduction would be achieved. This was verified in practice, obtaining the highest enantioselectivity reported to date for this reaction class, 90% ee. A more interesting aspect of the study is that the catalyst torsion angle in the TS correlates with the enantioselectivity. High enantioselectivites were achieved with catalysts that adopted geometries with small torsion angles. A major limitation of the current system is that only highly functionalized aromatic ynones, have been reported to be effectively used in an enantioselective fashion. To this end, I have designed a novel chrysene substituted catalyst that through increased π-stacking interactions has computationally been determined to be a promising candidate to facilitate the reaction in an enantioselective fashion with substrates containing less functionality at the aromatic substituent.

Collectively the research presented in this thesis demonstrates the complementary manner in which experiment, classical physical organic techniques and high-level calculations can be merged toward a more complete mechanistic assessment. This approach is based on the use of empirical data and information of this sort is often omitted from reports, since only

results leading to the desired outcomes are generally presented and pursued. As the mindset of publishing only the best results changes, such large-scale chemoinformatics investigations will become more apparent in other areas of catalysis.

Bibliography

[1] *Asymmetric Catalysis in Organic Synthesis*; Noyori, R., Ed.; Wiley: New York, 1994.

[2] *Comprehensive Asymmetric Catalysis*; Jacobsen, E. N.; Pfaltz, A.; Yamamoto, H., Eds.; Springer: Heidelberg, 1999.

[3] Knowles, W. S. *Angew. Chem. Int. Ed.* **2002**, *41*, 1999.

[4] Knowles, W. S. *Acc. Chem. Res.* **1983**, *16*, 106.

[5] Noyori, R. *Angew. Chem. Int. Ed.* **2002**, *41*, 2008.

[6] Miyashita, A.; Yasuda, A.; Takaya, H.; Toriumi, K.; Ito, T.; Souchi, T.; Noyori, R. *J. Am. Chem. Soc.* **1980**, *102*, 7932.

[7] Katsuki, T.; Sharpless, K. B. *J. Am. Chem. Soc.* **1980**, *102*, 5974.

[8] Bredig, G.; Friske, P. S. *Bichem. Z.* **1912**, *46*, 7.

[9] List, B.; Lerner, R. A.; Barbas, C. F. *J. Am. Chem. Soc.* **2000**, *122*, 2395.

[10] Corey, E. J.; Xu, F.; Noe, M. C. *J. Am. Chem. Soc.* **1997**, *119*, 12414.

[11] Odonnell, M. J.; Bennett, W. D.; Wu, S. D. *J. Am. Chem. Soc.* **1989**, *111*, 2353.

[12] Ooi, T.; Maruoka, K. *Acc. Chem. Res.* **2004**, *37*, 526.

[13] Maruoka, K.; Ooi, T. *Chem. Rev.* **2003**, *103*, 3013.

[14] Ahrendt, K. A.; Borths, C. J.; MacMillan, D. W. C. *J. Am. Chem. Soc.* **2000**, *122*, 4243.

[15] Sigman, M. S.; Vachal, P.; Jacobsen, E. N. *Angew. Chem. Int. Ed.* **2000**, *39*, 1279.

[16] Huang, Y.; Unni, A. K.; Thadani, A. N.; Rawal, V. H. *Nature* **2003**, *424*, 146.

[17] Yoon, T. P; Jacobsen, E. N. *Science* **2003**, *299*, 1691.

[18] Akiyama, T.; Itoh, J.; Yokota, K.; Fuchibe, K. *Angew. Chem.* **2004**, *116*, 1592.

[19] Uraguchi, D.; Terada, M. *J. Am. Chem. Soc.* **2004**, *126*, 5356.

[20] Reid, J. P.; Simón, L.; Goodman, J. M. *Acc. Chem. Res.* **2016,** *49*, 1029.

[21] Grondal, C.; Jeanty, C.; Enders, D *Nat. Chem.* **2010**, *2*, 167.

[22] Akiyama, T. *Chem Rev.* **2007**, *107,* 5744.

[23] Terada, M. *Synthesis* **2010**, *2010,* 1929.

[24] Parmar, D.; Sugiono, E.; Raja, S.; Rueping, M. *Chem. Rev.* **2014**, *114,* 9047.

[25] Simón, L.; Goodman, J. M. *J. Am. Chem. Soc.* **2008**, *130,* 8741.

[26] Guo, Q.-X.; Liu, H.; Guo, C.; Luo, S.-W.; Gu, Y.; Gong, L.-Z. *J. Am. Chem. Soc.* **2007**, *129*, 3790.

[27] Terada, M.; Machioka, K.; Sorimachi, K. *Angew. Chem., Int. Ed.* **2006**, *45*, 2254.

[28] Jia, Y.-X.; Zhong, J.; Zhu, S.-F.; Zhang, C.-M.; Zhou, Q.-L. *Angew. Chem. Int. Ed*. **2007**, *46*, 5565.

[29] Akiyama, T.; Morita, H.; Itoh, J.; Fuchibe, K. *Org. Lett.* **2005**, *7*, 2583.

[30] Gridnev, I. D.; Kouchi, M.; Sorimachi, K.; Terada, M. *Tetrahedron Lett*. **2007**, *48*, 497.

[31] Storer, R. I.; Carrera, D. E.; Ni, Y.; MacMillan, D. W. C. *J. Am. Chem. Soc*. **2006**, *128*, 84.

[32] Rueping, M.; Sugiono, E.; Azap, C.; Theissmann, T.; Bolte, M. *Org. Lett*. **2005**, *7*, 3781.

[33] Johnson, J. E.; Morales, N. M.; Gorczyca, A. M.; Dolliver, D. D.; McAllister, M. A. *J. Org. Chem.* **2001**, *66*, 7979.

[34] Chung, L. W.; Sameera, W. M. C.; Ramozzi, R.; Page, A. J.; Hatanaka, M.; Petrova, G. P.; Harris, T. V.; Li, X.; Ke, Z., Liu, F.; Li, H.-F.; Ding, L.; Morokuma, K. *Chem. Rev.* **2015**, *115*, 5678.

[35] Frisch, M. J.; *et al.*; *Gaussian 09 Revision D.01*; Gaussian Inc. Wallingford CT 2009.

[36] Simón, L.; Goodman, J. M. *J. Am. Chem. Soc.* **2009**, *131*, 4070.

[37] Simón, L.; Goodman, J. M. *J. Org. Chem.* **2010**, *75,* 589.

[38] Simón, L.; Goodman, J. M. *J. Org. Chem.* **2011**, *76,* 1775.

[39] Grayson, M. N.; Pellegrinet, S. C.; Goodman. *J. Am. Chem. Soc.* **2012**, *134,* 2716.

[40] Overvoorde, L. M.; Grayson, M. N.; Luo, Y.; Goodman, J. M. *J. Org. Chem.* **2015**, *80*, 2634.

[41] Reid, J. P.; Goodman, J. M. *J. Am. Chem. Soc.* **2016**, *138*, 7910.

[42] Paton, R. S.; Goodman, J. M. *J. Chem. Inf. Model*. **2009**, *49*, 944.

[43] Becke, A. D. *Phys. Rev.* A **1998**, *38*, 3098.

[44] Lee, C.; Yang, W.; Parr, R. G. *Phys. Rev. B* **1988**, *37*, 785.

[45] Johnson, E. R.; Mackie, I. D.; DiLabio, G. A. *J. Phys. Org. Chem.* **2009**, *22*, 1127.

[46] Zhao, Y.; Truhlar, D. G. *Theor. Chem. Acc*. **2008**, *120*, 215.

[47] Zhao, Y.; Truhlar, D. G. *Acc. Chem. Res.* **2008**, *41*, 157.

[48] Grimme, S.; Antony, J.; Ehrlich, S.; Krieg, H. *J. Chem. Phys.* **2010**, *132*, 154104.

[49] Tomasi, J.; Mennucci, B.; Cammi, R. *Chem. Rev*. **2005**, *105*, 2999.

[50] Mennucci, B.; Tomasi, J. *J. Chem. Phys.* **1997**, *106*, 5151.

[51] Chang, G.; Guida, W. C.; Still, W. C. *J. Am. Chem. Soc.* **1989**, *111*, 4379.

[52] Schlegel, H. B. *Theor. Chim. Acta* **1984**, 333.

[53] Doney, A. C.; Rooks, B. J.; Lu, T.; Wheeler, S. E. *ACS Catal*. **2016**, *6*, 7948.

[54] MacroModel, version 9.9, Schrodinger, LLC, New York, NY, 2009.

[55] Jaguar, version 7.9, Schrodinger, LLC, New York, NY, 2012.

[56] Marcelli, T.; Hammar, P.; Himo, F. *Chem. Eur. J*. **2008**, *14,* 8562.

[57] Hoffmann, S.; Seayad, A. M.; List, B. *Angew. Chem. Int. Ed.* **2005**, *44,* 7424.

[58] Rueping, M.; Antonchick, A. P.; Theissmann, T. *Angew. Chem. Int. Ed.* **2006**, *45*, 3683.

[59] Shibata, Y.; Yamanaka, M. *J. Org. Chem.* **2013**, *78*, 3731.

[60] Hoffmann, S.; Nicoletti, M.; List, B. *J. Am. Chem. Soc.* **2006**, *128*, 13074.

[61] Marcelli, T.; Hammar, P.; Himo, F. *Adv. Synth. Catal*. **2009**, *351*, 525.

[62] Rueping, M.; Sugiono, E.; Azap, C. *Angew. Chem. Int. Ed*. **2006**, *45*, 2617.

[63] Rueping, M.; Sugiono, E.; Moreth, S. A. *Adv. Synth. Catal.* **2007**, *349*, 759.

[64] Li, J.; Jiang, W.-Y.; Han, K.-L.; He, G.-Z.; Li, C. *J. Org. Chem.* **2003**, *68*, 8786.

[65] Kang, Q.; Zhao, Z.-A.; You, S.-L. *J. Am. Chem. Soc.* **2007**, *129*, 1484.

[66] Greindl, J.; Hioe, J.; Sorgenfrei, N.; Morana, F.; Gschwind, R. M. *J. Am. Chem. Soc.,* **2016**, *138*, 15965.

[67] Akiyama, T.; Morita, H.; Bachu, P.; Mori, K.; Yamanaka, M.; Hirata, T. *Tetrahedron* **2009**, *65*, 4950.

[68] Yamanaka, M.; Hirata, T. *J. Org. Chem.* **2009**, *74*, 3266.

[69] Shi, F.-Q.; Song, B.-A. *Org. Biomol. Chem.* **2009**, *7*, 1292.

[70] Yamanaka, M.; Itoh, J.; Fuchibe, K.; Akiyama, T. *J. Am. Chem. Soc.* **2007,** *129*, 6756.

[71] Itoh, J.; Fuchibe, K.; Akiyama, T. *Angew. Chem. Int. Ed.* **2006**, *45*, 4796.

[72] Akiyama, T.; Morita, H.; Fuchibe, K. *J. Am. Chem. Soc.* **2006**, *128*, 13070.

[73] Akiyama, T.; Honma, Y.; Itoh, J.; Fuchibe, K. *Adv. Synth. Catal.* **2008**, *350*, 399.

[74] Li, G.; Kaplan, M. J.; Wojtas, L.; Antilla, J. C. *Org. Lett.* **2010**, *12*, 1960.

[75] Uraguchi, D.; Sorimachi, K.; Terada, M. *J. Am. Chem. Soc.* **2004**, *126*, 11804.

[76] Rowland, G. B.; Rowland, E. B.; Liang, Y.; Perman, J. A.; Antilla, J. C. *Org. Lett.* **2007**, *9*, 2609.

[77] Terada, M.; Yokoyama, S.; Sorimachi, K.; Uraguchi, D. *Adv. Synth. Catal.* **2007**, *349*, 1863.

[78] Li, G.; Rowland, G. B.; Rowland, E. B.; Antilla, J. C. *Org. Lett.* **2007**, *9*, 4065.

[79] Enders, D.; Seppelt, M.; Beck, T. *Adv. Synth. Catal.* **2010**, *352*, 1413.

[80] Feng, J.; Yan, W.; Wang, D.; Li, P.; Sun, Q.; Wang, R. *Chem. Commun.* **2012**, *48*, 8003.

[81] Kashikura, W.; Mori, K.; Akiyama, T. *Org. Lett.* **2011**, *13*, 1860.

[82] Sickert, M.; Schneider, C. *Angew. Chem. Int Ed.* **2008**, *47*, 3631.

[83] Giera, D. S.; Sickert, M.; Schneider, C. *Org. Lett.* **2008**, *10*, 4259.

[84] Jain, P.; Antilla, J. C. *J. Am. Chem. Soc.* **2010**, *132*, 11884.

[85] Barrio, P; Rodríguez, E; Saito, K; Fustero, S.; Akiyama, T. *Chem. Commun*. **2015**, *51*, 5246.

[86] Rodríguez, E.; Grayson, M. N; Asensio, A.; Barrio, P; Houk, K. N.; Fustero, S. *ACS Catal.* **2016,** *6*, 2506.

[87] Jain, P.; Wang, H.; Houk, K. N.; Antilla, J. C. *Angew. Chem. Int. Ed.* **2012**, *51*, 1391.

[88] Chen, Z.; Wang, B.; Wang, Z.; Zhu, G.; Sun, J. *Angew. Chem. Int. Ed*. **2013**, *52*, 2027.

[89] Wang, Z.; Chen, Z.; Sun, J. *Angew. Chem. Int. Ed*. **2013**, *52*, 6685.

[90] Chen, Z.; Wang, Z.; Sun, J. *Chem. Eur. J.* **2013**, *19*, 8426.

[91] Yang, W.; Sun, J. *Angew. Chem. Int. Ed*. **2016**, *55*, 1868.

[92] Yang, W.; Wang, Z.; Sun, J. *Angew. Chem. Int. Ed.* **2016**, 55, 6954.

[93] Mueller, S.; List, B. *Angew. Chem. Int. Ed.* **2009**, *48*, 9975.

[94] Rueping, M.; Antonchick, A. P. *Angew. Chem. Int. Ed.* **2008**, *47*, 10090.

[95] Liu, W.-J.; Chen, X.-H.; Gong, L.-Z. *Org. Lett.* **2008**, *10*, 5357.

[96] Momiyama, N.; Tabuse, H.; Terada, M. *J. Am. Chem. Soc*. **2009**, *131*, 12882.

[97] Wu, H; Hea, Y.-P.; Shi, F. *Synthesis* **2015**, *47*, 1990.

[98] Zamfir, A.; Schenker, S.; Freund, M.; Tsogoeva, S. B. *Org. Biomol. Chem*. **2010**, *8*, 5262.

[99] Rueping, M.; Kuenkel, A.; Atodiresei, I. *Chem. Soc. Rev.* **2011**, 40, 4539.

[100] Klussmann, M.; Ratjen, L.; Hoffmann, S.; Wakchaure, V.; Goddard, R.; List, B. *Synlett,* **2010**, *14*, 2189.

[101] Clot-Almenara, L.; Rodríguez-Escrich, C.; Osorio-Planes, L.; Pericàs, M. A. *ACS Catal.* **2016,** *6*, 7647.

[102] X.-H. Chen, X.-Y. Xu, H. Liu, L.-F. Cun, L.-Z. Gong, *J. Am. Chem. Soc.* **2006**, *128*, 14802.

[103] T. Akiyama, Y. Saitoh, H. Morita, K. Fuchibe, *Adv. Synth. Catal.* **2005**, *347*, 1523.

[104] Rowland, G. B.; Zhang, H.; Rowland, E. B.; Chennamadhavuni, S.; Wang, Y.; Antilla, J. C. *J. Am. Chem. Soc.* **2005**, *127*, 15696.

[105] Čorić, I.; Müller, S.; List, B. *J. Am. Chem. Soc.* **2010**, *132*, 17370.

[106] Chen, X.-H.; Zhang, W.-Q.; Gong, L.-Z. *J. Am. Chem. Soc.* **2008**, *130*, 5652.

[107] Guo, Q.-S.; Du, D.-M.; Xu, J. *Angew. Chem. Int. Ed.* **2008**, *47*, 759.

[108] Momiyama, N.; Konno, T.; Furiya, Y.; Iwamoto, T.; Terada, M. *J. Am. Chem. Soc.* **2011**, *133*, 19294.

[109] Čorić, I.; List, B. *Nature* **2012**, *483*, 315.

[110] Liao, S.; Čorić, I.; Wang, Q.; List, B.; *J. Am. Chem. Soc.* **2012**, *134,* 10765.

[111] For examples see: (a) Chen, Y.-Y.; Jiang, Y.-J.; Fan, Y.-S.; Sha, D.; Wang, Q.; Zhang, G.; Zheng, L.; Zhang, S. Tetrahedron: Asymmetry, **2012**, *23*, 904. (b) An, D.; Fan, Y.-S.; Gao, Y.; Zhu, Z.-Q.; Zheng, L.-Y.; Zhang, S.-Q. *Eur. J. Org. Chem*. **2014**, 301. (c) Liu, L.; Leutzsch, M.; Zheng, Y.; Alachraf, M. W.; Thiel, W.; List, B. *J. Am. Chem. Soc*. **2015**, *137*, 13268.

[112] Simón, L.; Paton. R. S. *Org. Biomol. Chem*. **2016**, *14*, 3031.

[113] Jindal, G.; Sunoj, R. B. *Angew. Chem. Int. Ed.* **2014**, *53*, 4432.

[114] For examples where large catalysts proceed with reversal in stereoinduction see: (a) Yu, X.; Wang, Y.; Wu, G.; Song, H.; Zhou, Z.; Tang, C. *Eur. J. Org. Chem.* **2011**, 3060. (b) Kang, Q.; Zhao, Z.-A.; You, S.-L. *Org. Lett*. **2008**, *10*, 2031. (c) Rueping, M.; Antonchick, A. P.; Theissmann, T. *Angew. Chem. Int. Ed*. **2006**, *45*, 6751. (d) Gu, Q.; Rong, Z.-Q.; Zheng, C.; You, S.-L. *J. Am. Chem. Soc.* **2010**, *132,* 4056. (e) Feng, J.; Yan, W.; Wang, D.; Li, P.; Sun, Q.; Wang, R. *Chem. Commun.* **2012**, *48*, 8003.

[115] Li, N.; Chen, X.-H.; Song, J.; Luo, S.-W.; Fan, W.; Gong, L.-Z. *J. Am. Chem. Soc*. **2009**, *131*, 15301.

[116] Terada, M.; Yokoyama, S.; Sorimachi, K.; Uraguchi, D. *Adv. Synth. Catal.* **2007**, *349,* 1863.

[117] Seguin, T. J.; Wheeler, S. E. *ACS Catal.* **2016,** *6*, 7222.

[118] Milo, A.; Neel, A. J.; Toste, F. D.; Sigman, M. S. *Science,* **2015**, *347*, 737.

[119] Maity, P.; Pemberton, R. P.; Tantillo, D. J.; Tambar, U. K. *J. Am. Chem. Soc.*, **2013**, *135*, 16380.

[120] Changotra, A.; Das, S.; Sunoj, R. B. *Org. Lett.* **2017,** *19*, 2354.

[121] Rueping, M.; Ieawsuwan, W.; Antonchick, A. P.; Nachtsheim, B. J. *Angew. Chem. Int. Ed.* **2007**, *46*, 2097.

[122] Rueping, M.; Ieawsuwan, W. *Chem. Commun*. **2011**, *47*, 11450.

[123] Yang, M.; Zhao, Y.-M.; Zhang, S.-Y.; Tu, Y.-Q.; Zhang, F.-M. *Chem. Asian J*. **2011**, *6*, 1344.

[124] Nakashima, D.; Yamamoto, H. *J. Am. Chem. Soc.* **2006**, *128*, 9626.

[125] Vellalath, S.; Čorić, I.; List, B. *Angew. Chem. Int. Ed*. **2010**, *49*, 9749.

[126] Cheon, C. H.; Yamamoto, H. *Chem. Commun.* **2011**, *47*, 3043.

[127] Rueping, M.; Nachtsheim, B. J.; Ieawsuwan, W.; Atodiresei, I. *Angew. Chem. Int. Ed.* **2011**, *50*, 6706.

[128] Cheon, C. H.; Yamamoto, H. *J. Am. Chem. Soc.* **2008**, *130*, 9246.

[129] Terada, M.; Sorimachi, K.; Uraguchi, D. *Synlett* **2006**, *2006*, 133.

[130] Pousse, G.; Devineau, A.; Dalla, V.; Humphreys, L.; Lasne, M.-C.; Rouden, J.; Blanchet, J. *Tetrahedron* **2009**, *65*, 10617.

[131] Christ, P.; Lindsay, A. G.; Vormittag, S. S.; Neudoerfl, J.-M.; Berkessel, A.; O'Donoghue, A. C. *Chem. Eur. J.* **2011**, 17, 8524.

[132] Kaupmees, K.; Tolstoluzhsky, N.; Raja, S.; Rueping, M.; Leito, I. *Angew. Chem. Int. Ed*. **2013**, *52*, 11569.

[133] Yang, C.; Xue, X.-S.; Jin, J.-L.; Li, X.; Cheng, J.-P. *J. Org. Chem.* **2013**, *78*, 7076.

[134] Grayson, M. N.; Goodman, J. M. *J. Am. Chem. Soc.* **2013**, *135,* 6142.

[135] Li, G.; Antilla, J. C. *Org. Lett.* **2009**, *11*, 1075.

[136] Zheng, W.; Wojtas, L.; Antilla, J. C. *Angew. Chem. Int. Ed.* **2010**, *49*, 6589.

[137] Li, G.; Fronczek, F. R.; Antilla, J. C. *J. Am. Chem. Soc.* **2008**, *130*, 12216.

[138] Ingle, G. K.; Mormino, M. G.; Wojtas, L.; Antilla, J. C. *Org. Lett*. **2011**, *13*, 4822.

[139] Chen, M.-W.; Chen, Q.-A.; Duan, Y.; Ye, Z.-S.; Zhou, Y.-G. *Chem. Commun*. **2012**, *48*, 1698.

[140] Rueping, M.; Antonchik, A. P.; Theissmann, T. *Angew. Chem. Int. Ed.* **2006**, *45*, 6751.

[141] Rueping, M.; Antonchick, A. P. *Angew. Chem. Int. Ed.* **2007**, *46*, 4562.

[142] Zhu, C.; Akiyama, T. *Org. Lett.* **2009**, *11*, 4180.

[143] Saito, K.; Horiguchi, K.; Shibata, Y.; Yamanaka, M.; Akiyama, T. *Chem. Eur. J.* **2014**, *20*, 7616.

[144] Saito, K.; Akiyama, T. *Chem. Commun*. **2012**, *48*, 4573.

[145] Terada, M.; Sorimachi, K. *J. Am. Chem. Soc.* **2007**, *129*, 292.

[146] Yu, X.; Wang, Y.; Wu, G.; Song, H.; Zhou, Z.; Tang, C. *Eur. J. Org. Chem*. **2011**, *2011*, 3060.

[147] Kang, Q.; Zheng, X.-J.; You, S.-L. *Chem. Eur. J.* **2008**, *14*, 3539.

[148] Terada, M.; Machioka, K.; Sorimachi, K. *J. Am. Chem. Soc.* **2007**, *129*, 10336.

[149] Liu, H.; Dagousset, G.; Masson, G.; Retailleau, P.; Zhu, J. *J. Am. Chem. Soc.* **2009**, *131*, 4598.

[150] Baudequin, C.; Zamfir, A.; Tsogoeva, S. B. *Chem. Commun.* **2008**, 4637.

[151] Mitsumori, S.; Zhang, H.; Cheong, P. H.-Y.; Houk, K. N.; Tanaka, F.; Barbas, C. F. *J. Am. Chem. Soc*. **2006**, *128*, 1040.

[152] Straker, R. N.; Peng, Q.; Mekareeya, A.; Paton, R. S.; Anderson, E. A.: *Nat. Commun.* **2016**, *7*, 10109.

[153] Poree, C.; Schoenebeck, F. *Acc. Chem. Res.* **2017,** *50*, 605.

[154] Sigman, M. S.; Harper, K. C.; Bess, E. N.; Milo, A. *Acc. Chem. Res.,* **2016**, *49*, 1292.

[155] For examples where no reaction is observed for structurally large catalysts see: (a) Saha, S.; Schneider, C. *Chem. Eur. J.* **2015**, 21, 2348. (b) Lu, M.; Lu, Y.; Zhu, D.; Zeng, X.; Li, X.; Zhong, G. *Angew. Chem. Int. Ed*. **2010**, 49, 8588. (c) Wen, W.; Zheng, Y.; Li-Yu, P.; Li-Na, F.; Qi-Xang, G. *Org. Lett.* **2015**, 17, 3922.

[156] Harper, K. C.; Bess, E. N.; Sigman, M. S. *Nat. Chem.* **2012**, 4, 366.

[157] Harper, K.; Sigman, M. S. *J. Org. Chem.* **2013**, 78, 2813.

[158] Hansch, C.; Leo, A. Exploring QSAR: Fundatmentals and Applications in Chemistry and Biology; American Chemical Society: Washington, DC, 1995.

[159] Taft, R. W. *J. Am. Chem. Soc.* **1952**, *74*, 3120.

[160] Taft, R. W. *J. Am. Chem. Soc.* **1953**, *75*, 4538.

[161] Charton, M. *J. Org. Chem.* **1976**, *41*, 2217.

[162] Charton, M. *J. Am. Chem. Soc.* **1975**, 97, 3691.

[163] Charton, M*. J. Am. Chem. Soc.* **1975**, *97*, 3694.

[164] Charton, M. *J. Am. Chem. Soc.* **1975**, *97*, 1552.

[165] Hansch, C.; Leo, A.; Taft, R. W. *Chem. Rev.* **1991**, *91*, 165.

[166] Winstein, S.; Holness, N. J. *J. Am. Chem. Soc*. **1955**, *77*, 5562.

[167] Bott, G.; Field, L. D.; Sternhell, S. *J. Am. Chem. Soc*. **1980**, *102*, 5618.

[168] Adams, R.; Yuan, H. C*. Chem. Rev.* **1933**, *12,* 261.

[169] Tolman, C. A. *J. Am. Chem. Soc.* **1970**, *92*, 2956.

[170] Tolman, C. A. *Chem. Rev.* **1977**, *77*, 313.

[171] Hillier, A. C.; Sommer, W. J.; Yong, B. S; Petersen, J. L. Cavallo, L.; Nolan, S. P. *Organometallics*, **2003**, *22*, 4322.

[172] Harper, K. C.; Sigman, M. S. *Science,* **2011**, *333*, 1875.

[173] Gustafson, J. L.; Sigman, M. S.; Miller, S. J.; *Org. Lett*. **2010**, *12*, 2794.

[174] Verloop, A.; Tipker, J. *Pharmacochem. Libr.* **1987**, *10*, 97.

[175] Bess, E. N.; Bischoff, A. J.; Sigman, M. S. *Proc. Nat. Acad. Sci.*, **2014**, *111*, 14698.

[176] Milo, A.; Neel, A. J.; Toste, F. D.; Sigman, M. S. *Science* **2015**, *347*, 737.

[177] Bess, E. N.; Guptill, D. M.; Davies, H. M. L.; Sigman, M. S. *Chem. Sci*. **2015**, 6, 3057.

[178] Mougel, V.; Santiago, C. B.; Zhizhko, P. A.; Bess, E. N.; Varga, J.; Frater, G.; Sigman, M. S.; Copéret, C. *J. Am. Chem. Soc*. **2015**, 137, 6699.

[179] Zhang, C.; Santiago, C. B.; Kou, L.; Sigman, M. S. *J. Am. Chem. Soc*., **2015**, 137, 7290.

[180] Zhang, C.; Santiago, C. B.; Crawford, J. M.; Sigman, M. S. *J. Am. Chem. Soc*. **2015**, *137*, 15668.

[181] Neel, A. J.; Milo, A.; Sigman, M. S.; Toste, F. D. *J. Am. Chem. Soc*. **2016**, *138*, 3863.

[182] Niemeyer, Z.; Milo, A.; Hickey, D. P.; Sigman, M. S. *Nat. Chem*. **2016**, *8*, 610.

[183] Chen, Z.-M.; Hilton, M. J.; Sigman, M. S. *J. Am. Chem. Soc*. **2016**, 138, 11461.

[184] Kaminski, G.A.; Friesner, R. A.; Tirado-Rives, J.; Jorgensen, E. *J. Phys. Chem. B.* **2001**, 105, 6474.

[185] Jorgensen, W. L.; Maxwell, D. S.; Tirado-Rives, J. *J. Am. Chem. Soc.* **1996**, *118*, 11225.

[186] Jorgensen, W. L; Tirado-Rives, J. *J. Am. Chem. Soc.* **1988**, 110, 1657..

[187] González, A. Z.; Benitez, D. Tkatchouk, E.; Goddard, W. A.; Toste, F. D. *J. Am. Chem. Soc.* **2011**, *133*, 550.

[188] Champagne, P. A.; Houk, K. N. *J. Am. Chem. Soc.* **2016***, 138,* 12356.

[189] Müller, S.; Webber, M. J.; List, B. *J. Am. Chem. Soc.* **2011**, *133*, 18534.

[190] Guo, C.; Song, J.; Huang, J.-Z.; Chen, P.-H.; Luo, S.-W.; Gong, L.-Z. *Angew. Chem. Int. Ed.* **2012**, 51, 1046.

[191] Wanner, M. J.; Claveau, E.; van Maarseveen, J. H.; Hiemstra, H. *Chem. Eur. J.* **2011**, 17, 13680.

[192] Zhang, Z.; Antilla, J. C. *Angew. Chem. Int. Ed.* **2012**, *51*, 11778.

[193] Krishnan, R.; Binkley, J. S.; Seeger, R.; Pople, J. A. *J. Chem. Phys.* **1980**, *72*, 650.

[194] Gill, P. M. W.; Johnson, B. G.; Pople, J. A.; Frisch, M. J. *Chem. Phys. Lett.* **1992**, *197*, 499.

[195] Rappe, A. K.; Casewit, C. J.; Colwell, K. S.; Goddard, W. A.; Skiff, W. M. *J. Am. Chem. Soc.* **1992**, *114*, 10024.

[196] CYL view, 1.0b; Legault, C. Y., Université de Sherbrooke, 2009.

[197] Schreck, J. O. *J. Chem. Ed.* **1971**, *48*, 103.

[198] Jaffé, H. H. *Chem. Rev.* **1953**, *53*, 191.

[199] Richard, J. P.; Jencks, W. P. *J. Am. Chem. Soc.* **1982**, *104*, 4689.

[200] Wodrich, M. D.; Corminboeuf, C.; Schleyer, P. v. R. *Org. Lett*. **2006**, *8*, 3631.

[201] Zhang, H; Wen, H.; Gan, L. Peng, Y. *Org. Lett.* **2012,** *14,* 2126.

[202] Zeng, X.; Zeng, X.; Xu, Z.; Lu, M.; Zhong, G. *Org. Lett.* **2009,** *11,* 3036.

[203] Aillerie, A.; Gosset, C.; Dumont, C.; Skrzypczak, V.; Champetter, P.; Pellegrini, S.; Bousquet, T.; Pélinski, L. *RSC Adv*. **2016**, *6*, 54185.

[204] Rueping, M.; Brinkmann, C.; Antonchick, P.; Atodiresei, I. *Org. Lett.* **2010,** *12,* 4604.

[205] Rueping, M.; Tato, F.; Schoepke, F. R. *Chem. Eur. J.* **2010**, *16*, 2688.

[206] Guo, R.-N.; Chen, Z.-P.; Cai X.-F.; Zhou, Y.-G. *Synthesis* **2014**, *46*, 2751.

[207] Monaco, M. R.; Properzi, R.; List, B. *Synlett*, **2016**, *27*, 591.

[208] Husmann, R.; Sugiono, E.; Mersmann, S.; Raabe, G.; Rueping, M.; Bolm, C. *Org. Lett.* **2011,** *13,* 1044.

[209] Yin, Q.; You, S.-L. *Chem. Sci*. **2011**, *2*, 1344.

[210] Zhang, K.-F.; Nie, J.; Guo, R.; Zheng, Y.; Ma, J.-A. *Adv. Synth. Catal.* **2013**, *355*, 3497.

[211] Terada, M.; Machioka, K.; Sorimachi, K.; *Angew. Chem. Int. Ed.* **2009**, *48*, 2553.

[212] Terada, M.; Komuro, T.; Toda, Y.; Korenaga, T. *J. Am. Chem. Soc.* **2014**, *136*, 7044.

[213] Xue, J.-H.; Shi, M.; Yu, F.; Li, X.-Y.; Ren, W.; Fu, L.-N.; Guo Q.-X. *Org. Lett.* **2016**, *18*, 3874.

[214] Rueping, M.; Sugiono, E.; Schoepke, F. R. *Synlett* **2007**, *9*, 1441.

[215] Liang, Y.; Rowland, E. B.; Rowland, G. B.; Perman, J. A.; Antilla, J. C. *Chem. Comm.* **2007**, 4477.

[216] Uraguchi, D.; Sorimachi, K.; Terada, M. *J. Am. Chem. Soc.* **2005**, *127*, 9360.

[217] Akiyama, T.; Suzuki, T.; Mori, K. *Org. Lett. 11*, **2009**, 2445.

[218] Zhu, C.; Akiyama, T. *Adv. Synth. Catal.* **2010**, *352*, 1846.

[219] Kang, Q.; Zhao, Z.-A.; You, S.-L. *Adv. Synth. Catal.* **2007**, *349*, 1657.

[220] Li, G.; Liang, Y.; Antilla, J. C. *J. Am. Chem. Soc.* **2007**, *129*, 5830.

[221] Xu, F.; Huang, D.; Han, C.; Shen, W.; Lin, X.; Wang, Y. *J. Org. Chem*. **2010**, *75*, 8677.

[222] Xing, C.-H.; Liao, Y.-X.; Ng, J.; Hu, Q.-S. *J. Org. Chem*. **2011**, *76*, 4125.

[223] Nakamura, S.; Sakurai, Y.; Nakashima, H.; Shibata, N.; Toru, T. *Synlett* **2009**,*10*, 1639.

[224] Ávila, E. P.; Justo, R. M. S.; Gonçalves, V. P.; Pereira, A. A.; Diniz, R.; Amarante, G. W. *J. Org. Chem*. **2015**, *80*, 590.

[225] Kikuchi, J.; Momiyama, N.; Terada, M. *Org. Lett.* **2016**, *18*, 2521.

[226] Terada, M.; Tanaka, H.; Sorimachi, K. *Synlett* **2008**, *11*, 1661.

[227] Heseler, A.; Kato, M.; Mori, K.; Akiyama, T. *Angew. Chem. Int. Ed.* **2011**, *50*, 8180.

[228] Kim, K.-H.; Lee, C.-Y.; Cheon, C.-H. *J. Org. Chem.* **2015**, *80*, 6367.

[229] Sakamoto, T.; Mori, K.; Akiyama, T. *Org. Lett*. **2012**, *14*, 3312.

[230] Rueping, M.; Stoeckel, M.; Sugiono, E.; Theissmann, T. *Tetrahedron* **2010,** *66,* 6565.

[231] Zhou, J.; Zhang, Q.-F.; Zhao, W.H.; Jiang, Q.-F. *Org. Biomol. Chem.* **2016**, *14*, 6937.

[232] Metallinos, C.; Barrett, F. B.; Xu, S.; *Synlett* **2008**, *5*, 720.

[233] Rueping, M.; Antonchick, A. P.; *Angew. Chem. Int. Ed.* **2008**, *47*, 5836.

[234] Cai, X.-F.; Chen, M.-W.; Ye, Z.-S.; Guo, R.-N.; Shi, L.; Li, Y.-Q.; Zhou, Y.-G. -*Chem. Asian J.* **2013**, *8*, 1381.

[235] Cai, X.-F.; Guo, R.-N.; Feng, G.-S.; Wu, B.; Zhou, Y.-G.; *Org. Lett*. **2014**, *16*, 2680.

[236] Zhao, Y.; Wang, Y.; Zhao, J. *Tetrahedron Lett.* **2017,** *58*, 213.

[237] Rueping, M.; Raja, S.; Núñez, A. *Adv. Synth. Catal.* **2011**, *353*, 563.

[238] Terada, M.; Toda, Y. *J. Am. Chem. Soc.* **2009,** *131*, 6354.

[239] Dagousset, G.; Drouet, F.; Masson, G.; Zhu, J. *Org. Lett.* **2009**, *11*, 5546.

[240] Lin, J.-H.; Zong, G.; Du, R.-B.; Xiao, J.-C.; Liu, S. *Chem. Commun*. **2012,** *48*, 7738.

[241] Brioche, J.; Courant, T.; Alcaraz, L.; Stocks, M.; Furber, M.; Zhu, J.; Masson, G. *Adv. Synth. Catal.* **2014**, *356*, 1719.

[242] Richmond, E.; Khan, I. U.; Moran, J. *Chem. Eur. J.* **2016**, *22*, 12274.

[243] Dagousset, G.; Erb, W.; Zhu, J.; Masson, G. *Org. Lett.* **2014**, *16*, 2554.

[244] Dagousset, G.; Zhu, J.; Masson, G. *J. Am. Chem. Soc.* **2011**, *133*, 14804.

[245] Suć, J.; Dokli, I.; Gredičak, M. *Chem. Commun.* **2016**, *52*, 2071.

[246] Unhale, R. A.; Molleti, N.; Rana, N. K.; Dhanasekaran, S.; Bhandary, S.; Singh, V. K. *Tetrahedron Lett.* **2017**, *58,* 145.

[247] Kano, T.; Takechi, R.; Kobayashi, R.; Maruoka, K.; *Org. Biomol. Chem.* **2014**, *12*, 724.

[248] Peng, Q.; Duarte, F.; Paton, R. S. *Chem. Soc. Rev.* **2016**, *45*, 6093.

[249] Kobayashi, S.; Kusakabe, K.; Komiyama, S.; Ishitani, H. *J. Org. Chem.* **1999**, *64*, 4220.

[250] Li, Y.; Li, Q. *Org. Lett.* **2012**, *14*, 4362.

[251] Romanov-Michailidis, F.; Guénée, L.; Alexakis, A. *Angew. Chem. Int. Ed.* **2013**, *52*, 9266.

[252] Hatano, M; Ikeno, T.; Matsumura, T.; Torii, S.; Ishihara, K. *Adv. Synth. Catal.* **2008**, *350,* 1776.

[253] Schnider, P.; Koch, G; Prétot, R.; Wang, G; Bohnen, F. M; Kruger, C; Pfaltz, A. *Chem. Eur. J.* **1997**, *3*, 887.

[254] Sugi, K. D.; Nagata, T.; Yamada, T.; Mukaiyama, T. *Chem. Lett.* **1997**, 493.

[255] Verdaguer, X.; Lange, U. E. W.; Reding, M. T.; Buchwald, S. L. *J. Am. Chem. Soc.* **1996**, *118*, 6784.

[256] Nguyen, T. B.; Bousserouel, H.; Wang, Q.; Guéritte, F. *Org. Lett.* **2010**, *12*, 4705.

[257] Nguyen, T. B.; Wang, Q.; Guéritte, F. *Chem. Eur. J.* **2011**, *17*, 9576.

[258] Nguyen, T. B.; Bousserouel, H.; Wang, Q.; Guéritte, F. *Adv. Synth. Catal.* **2011**, *353*, 257.

[259] I have drawn the TS as aromatic but other resonance structures are possible.

[260] Sickert, M.; Abels, F.; Lang, M.; Sieler, J.; Birkemeyer, C.; Schneider, C. *Chem. Eur. J.* **2010**, *16*, 2806.

[261] Tozer, M. J.; Herpin, T. F. *Tetrahedron* **1996**, 52, 8619.

[262] Zgarbova, M.; Otyepka, M.; Sponer, J.; Hobza, P.; Jurecka, P. *Phys. Chem. Chem. Phys.* **2010**, *12*, 10476.

[263] Fleischmann, M.; Drettwan, D.; Sugiono, E.; Rueping, M.; Gschwind, R. M. *Angew. Chem. Int. Ed.* **2011**, *50*, 6364.

[264] Phipps, R. J.; Hamilton, G. L.; Toste, F. D. *Nat. Chem.* **2012**, *4*, 603.

[265] Mahlau, M.; List, B. *Angew. Chem. Int. Ed.* **2013**, *52*, 518.

[266] Brak, K.; Jacobsen, E. N. *Angew. Chem. Int. Ed.* **2013**, *52*, 534.

[267] Mukherjee, S.; List, B. *J. Am. Chem. Soc.* **2007**, *129*, 11336.

[268] Rueping, M.; Antonchick, A. P.; Brinkmann, C. *Angew. Chem. Int. Ed.* **2007**, *46*, 6903.

[269] Liao, S.; List, B. *Angew. Chem. Int. Ed.* **2010**, *49*, 628.

[270] Jiang, G.; Halder, R.; Fang, Y.; List, B. *Angew. Chem. Int. Ed.* **2011**, *50*, 9752.

[271] Rauniyar, V.; Wang, Z. J.; Burks, H. E.; Toste, F. D. *J. Am. Chem. Soc.* **2011**, *133*, 8486.

[272] Chai, Z.; Rainey, T. J. *J. Am. Chem. Soc.* **2012**, *134*, 3615.

[273] Zbieg, J. R.; Yamaguchi, E.; McInturff, E. L.; Krische, M. J. *Science* **2012**, *336*, 324.

[274] Ohmatsu, K.; Ito, M.; Kunieda, T.; Ooi, T. *Nat. Chem.* **2012**, *4*, 473.

[275] Wang, X.; List, B. *Angew. Chem. Int. Ed.* **2008**, *47*, 1119.

[276] Hamilton, G. L.; Kanai, T.; Toste, F. D. *J. Am. Chem. Soc.* **2008**, *130*, 14984.

[277] Rueping, M.; Uria, U.; Lin, M.-Y.; Atodiresei, I. *J. Am. Chem. Soc.* **2011**, *133*, 3732.

[278] Mayer, S.; List, B. *Angew. Chem. Int. Ed.* **2006**, *45*, 4193.

[279] Hamilton, G. L.; Kang, E. J.; Mba, M.; Toste, F. D. *Science* **2007**, *317*, 496.

[280] Shirakawa, S.; Maruoka, K. *Angew. Chem. Int. Ed.* **2013**, *52*, 4312.

[281] Tan, J.; Yasuda, N. *Org. Process Res. Dev.* **2015**.

[282] Hughes, D. L.; Dolling, U. H.; Ryan, K. M.; Schoenewaldt, E. F.; Grabowski, E. J. J. *J. Org. Chem.* **1987**, *52*, 4745.

[283] Rauniyar, V.; Lackner, A. D.; Hamilton, G. L.; Toste, F. D. *Science* **2011**, *334*, 1681.

[284] Phipps, R. J.; Hiramatsu, K.; Toste, F. D. *J. Am. Chem. Soc.* **2012**, *134*, 8376.

[285] Wang, Y.-M.; Wu, J.; Hoong, C.; Rauniyar, V.; Toste, F. D. *J. Am. Chem. Soc.* **2012**, *134*, 12928.

[286] Honjo, T.; Phipps, R. J.; Rauniyar, V.; Toste, F. D. *Angew. Chem. Int. Ed.* **2012**, *51*, 9684.

[287] Phipps, R. J.; Toste, F. D. *J. Am. Chem. Soc.* **2013**, *135*, 1268.

[288] Shunatona, H. P.; Früh, N.; Wang, Y.-M.; Rauniyar, V.; Toste, F. D. *Angew. Chem. Int. Ed.* **2013**, *52*, 7724.

[289] Wu, J.; Wang, Y.-M.; Drljevic, A.; Rauniyar, V.; Phipps, R. J.; Toste, F. D. *Proc. Natl. Acad. Sci.* **2013**, *110*, 13729.

[290] Yang, X.; Phipps, R. J.; Toste, F. D. *J. Am. Chem. Soc.* **2014**, *136*, 5225.

[291] Liu, H.; Jiang, G.; Pan, X.; Wan, X.; Lai, Y.; Ma, D.; Xie, W. *Org. Lett.* **2014**, *16*, 1908.

[292] Romanov-Michailidis, F.; Guénée, L.; Alexakis, A. *Org. Lett.* **2013**, *15*, 5890.

[293] Romanov-Michailidis, F.; Pupier, M.; Guénée, L.; Alexakis, A. *Chem. Commun.* **2014**, *50*, 13461.

[294] Avila, C. M.; Patel, J. S.; Reddi, Y.; Saito, M.; Nelson, H. M.; Shunatona, H. P.; Sigman, M. S.; Sunoj, R. B.; Toste, F. D. *Angew. Chem. Int. Ed.* **2017**, *56*, 5806.

[295] James, M. J.; Cuthbertson, J. D.; O'Brien, P. A.; Taylor, R. J. K.; Unsworth, W. P. *Angew. Chem. Int. Ed.* **2015**, *54*, 7640.

[296] Hay, P. J.; Wadt, W. R. *J. Chem. Phys*. **1985**, *82*, 270.

[297] Cubberley, M. S.; Iverson, B. L. *J. Am. Chem. Soc.* **2001,** *123,* 7560.

[298] Hunter, C. A.; Sanders, J. K. M. *J. Am. Chem. Soc.* **1990**, *112*, 5525.

[299] Hunter, C. A.; Low, C. M. R.; Vinter, J. G.; Zonta, C. *J. Am. Chem. Soc.* **2003**, *125*, 9936.

[300] Cockroft, S. L.; Hunter, C. A.; Lawson, K. R.; Perkins, J.; Urch, C. J. *J. Am. Chem. Soc.* **2005**, *127*, 8594.

[301] Cockroft, S. L.; Hunter, C. A. *Chem. Commun.* **2006**, 36, 3806.

[302] Cozzi, F.; Cinquini, M.; Annunziata, R.; Dwyer, T.; Siegel, J. S. *J. Am. Chem. Soc.* **1992**, *114*, 5729.

[303] Cozzi, F.; Cinquini, M.; Annuziata, R.; Siegel, J. S. *J. Am. Chem. Soc.* **1993**, *115*, 5330.

[304] Cozzi, F.; Ponzini, F.; Annunziata, R.; Cinquini, M.; Siegel, J. S. *Angew. Chem. Int. Ed. Engl.* **1995**, *34*, 1019.

[305] Cozzi, F.; Annunziata, R.; Benaglia, M.; Cinquini, M.; Raimondi, L.; Baldridge, K. K.; Siegel, J. S. *Org. Biomol. Chem.* **2003**, *1*, 157.

[306] Martinez, C. R.; Iverson, B. L. *Chem. Sci.* **2012**, *3*, 2191.

[307] Grimme, S. *Angew. Chem. Int. Ed.* **2008**, *47*, 3430.

[308] Bloom, J. W. G.; Wheeler, S. E. *Angew. Chem. Int. Ed.* **2011**, *50*, 7847.

[309] Sinnokrot, M. O.; Sherrill, C. D. *J. Am. Chem. Soc.* **2004**, *126*, 7690.

[310] Raju, R. K.; Bloom, J. W. G.; An, Y.; Wheeler, S. E. *ChemPhysChem* **2011**, *12*, 3116.

[311] Wheeler, S. E.; Bloom, J. W. G. *J. Phys. Chem. A* **2014**, *118*, 6133.

[312] Wheeler, S. E.; Houk, K. N. *J. Am. Chem. Soc.* **2008**, *130*, 10854.

[313] Wheeler, S. E.; Houk, K. N. *Mol. Phys.* **2009**, *107*, 749.

[314] Wheeler, S. E.; Houk, K. N. *J. Chem. Theory Comput.* **2009**, *5*, 2301.

[315] Wheeler, S. E. *J. Am. Chem. Soc.* **2011**, *133*, 10262.

[316] Raju, R. K.; Bloom, J. W. G.; Wheeler, S. E. *J. Chem. Theory Comput.* **2013**, *9*, 3479.

[317] Wheeler, S. E. *Acc. Chem. Res.* **2013**, *46*, 1029.

Appendix

Basis Sets

6-31G	Pople split valence basis set with six primitive Gaussians for the contracted core functions.
6-31G(d)	Includes a set of d functions on heavy atoms.
6-31G(d,p)	As above with the inclusion a set of p functions on hydrogens.
LACVP	Combination of the 6-31G with the LANL2DZ effective core basis set. Atoms H to Ar are described with 6-31G basis set, while heavier atoms are described by the LANL2DZ basis set.
LANL2DZ	LANL basis set for which fourth row elements are handled using a nonrelativistic [Ar] 18-electron core and a relativistic [Kr] 36-electron core with double split valence function for fifth row elements.

Density Functionals

B3LYP	Becke's three parameter functional with Lee-Yang-parr correlation.
M06-2X	Minnesota 06 meta exchange-correlation functional by Truhlar which contains twice the amount of nonlocal exchange (2X) as M06; it is parameterised for nonmetals only and has 54% HF exchange. It is a hybrid meta-generalised gradient approximation (GGA) exchange functional.
M06	Minnesota 06 meta exchange-correlation functional by Truhlar; it is parameterized for both transition metals and nonmetals, and has 27% HF exchange.

Solvation Model

PCM — The polarisable continuum model is an implicit solvation model in which the solute charge distribution is described as being inside a cavity that displaces an otherwise homogeneous dielectric medium. The Poisson equation is valid for situations where a polarisable medium responds linearly to an embedded charge and expresses the electrostatic potential as a function of charge density and dielectric constant. The molecular cavity is described by the molecular surface and the solute charge it distributed onto grid points on this surface.

Computational Methods Development

Throughout the course of the investigations described in the thesis two programs were written using Python, a programming language, with the purpose of simplifying steric parameter calculation described in Chapter 2. In this section I describe how each program works.

AREA(θ)

The program for the automated calculation of AREA(θ) relies on generating two vectors from the phosphorous, one to the midpoint of the binaphthyl oxygens(**o**) and the second to the center of an atom on the catalyst 3,3' substituents(**c**). By calculating the length and dot product, AREA(θ) can be determined using the cosine equation.

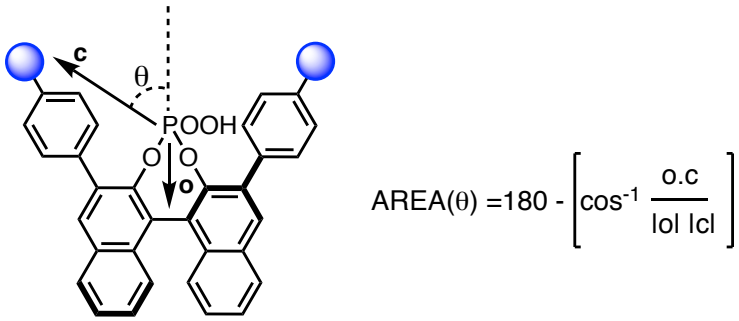

Figure A.1. Calculation of AREA(θ).

Catalyst Volume

In Chapter 2 it was discovered that both proximal and remote sterics played important stereochemical roles. To simplify analysis a complete steric description of the 3,3' groups was sought. One option is to calculate the volume of the catalyst cavity created by the binaphthyl rings and constrained by the 3,3' substituents. The program for the calculation of

catalyst volume relies on being able to generate, locate and sum a number of point probes. Point probes can be generated easily, but if I am going to be able to uncover useful information about the volume properties of systems, I must be able to determine if the point probe is inside the cavity of the catalyst system of interest.

The position of the point probe can be determined by constructing hypothetical lines from the center of one atom on the 3-substituent to another on the 3' using x, y and z coordinates. The distance from the point probe to the line is calculated and a distance cut-off of 0.5 Å selected. From this, the point probe is determined to be either in or outside the catalyst cavity. Summation of the point probes is representative of the volume. These techniques were incorporated into a program written in Python.

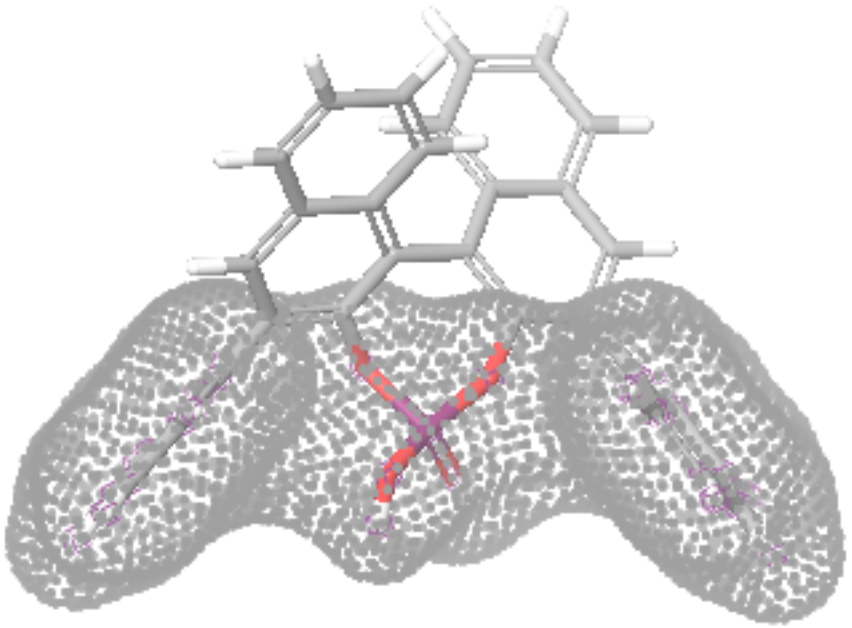

Figure A.2. Qualitative picture describing the volume calculation. Point probes indicated in gray, are generated and determined whether to be either inside or outside the catalyst cavity. Summation of point probes inside the catalyst cavity is representative of the volume. (*R*)-Ph substituted CPA is shown in a wire-frame model as an example. Structure is illustrated using Maestro.

Computational Data

All energies and Gibbs free energies in this section are given in Hartrees (H); imaginary frequencies are given in cm^{-1}. The lowest energy conformer for each TS is presented followed by data for additional conformations considered.

Appendix to Chapter 3

Figure 3.5.

Structure	M06-2X derived free energy	M06-2X derived free energy in solution	Imaginary Frequency
TS1-*Z*	-4264.207320	-4264.225888	-950.53
	-4264.203685	-4264.221676	-953.39
	-4264.203480	-4264.221686	-956.36
	-4264.196029	-4264.215192	-895.79
	-4264.199579	-4264.218054	-944.85
	-4264.196599	-4264.215772	-882.54
	-4264.204201	-4264.221911	-979.76
	-4264.205199	-4264.223087	-1001.36
	-4264.203394	-4264.221613	-967.60
	-4264.204720	-4264.222946	-985.73
	-4264.205310	-4264.223332	-999.16
	-4264.204183	-4264.222026	-978.34
	-4264.206072	-4264.224532	-956.99
	-4264.204173	-4264.222051	-978.23
	-4264.204445	-4264.223148	-971.63
	-4264.199392	-4264.217915	-862.21
	-4264.198370	-4264.216744	-926.90
	-4264.196452	-4264.216615	-914.52
	-4264.203221	-4264.221608	-929.78
	-4264.201531	-4264.220807	-929.77
	-4264.198419	-4264.216842	-926.93
	-4264.197306	-4264.216128	-895.46
	-4264.196165	-4264.216459	-908.17
	-4264.203584	-4264.221981	-930.59
	-4264.197289	-4264.216083	-895.44
	-4264.204177	-4264.221910	-979.72
	-4264.203563	-4264.221918	-930.61
	-4264.197431	-4264.215236	-876.71
	-4264.204935	-4264.222914	-981.70
TS1-*E*	-4264.205817	-4264.228042	-1074.97
	-4264.203133	-4264.223452	-993.13

	-4264.204021	-4264.224440	-981.48
	-4264.205013	-4264.226206	-984.70
	-4264.205061	-4264.226281	-984.74
	-4264.202418	-4264.222800	-986.48
	-4264.201794	-4264.222588	-962.55
	-4264.204428	-4264.225986	-941.60
	-4264.204401	-4264.226054	-941.33
	-4264.202843	-4264.224302	-927.72
	-4264.205067	-4264.226199	-984.74
	-4264.194827	-4264.217094	-1070.69
	-4264.202786	-4264.223064	-993.04
	-4264.201784	-4264.222223	-985.41
	-4264.205050	-4264.226269	-984.82
	-4264.204923	-4264.226286	-936.43
	-4264.196559	-4264.216033	-978.05
	-4264.196944	-4264.216761	-980.16
	-4264.204583	-4264.225686	-953.82
	-4264.205100	-4264.226316	-984.71
	-4264.196881	-4264.216733	-980.16
	-4264.202693	-4264.223089	-986.38
	-4264.198239	-4264.218841	-951.93
	-4264.204850	-4264.226295	-936.41
TS2-*Z*	-4264.215925	-4264.236788	-893.28
	-4264.204524	-4264.223228	-967.65
	-4264.200387	-4264.217741	-928.83
	-4264.202110	-4264.220047	-942.86
	-4264.210556	-4264.228992	-953.24
	-4264.198986	-4264.216552	-949.02
	-4264.215548	-4264.234526	-897.06
	-4264.198771	-4264.217129	-923.89
	-4264.207557	-4264.226138	-943.97
	-4264.200141	-4264.219463	-958.10
	-4264.207809	-4264.226429	-910.96
	-4264.215607	-4264.234721	-898.37
	-4264.197192	-4264.215719	-961.75
	-4264.203812	-4264.221515	-992.61
	-4264.210610	-4264.229053	-953.16
	-4264.205971	-4264.224932	-954.99
	-4264.207819	-4264.226458	-910.87
	-4264.205256	-4264.224102	-892.31
	-4264.204282	-4264.223098	-890.41
	-4264.204975	-4264.223848	-941.52
	-4264.215530	-4264.234546	-897.09
	-4264.197224	-4264.215741	-961.83
	-4264.199491	-4264.217077	-988.54

	-4264.199466	-4264.217111	-988.56
	-4264.202664	-4264.219946	-950.78
	-4264.200695	-4264.218504	-978.02
	-4264.206710	-4264.225179	-914.29
	-4264.203507	-4264.222420	-897.29
	-4264.203536	-4264.222442	-897.39
	-4264.214338	-4264.233304	-920.24
	-4264.199988	-4264.218009	-951.81
	-4264.211594	-4264.231564	-891.02
	-4264.205993	-4264.224970	-954.92
	-4264.203116	-4264.221701	-913.58
	-4264.198392	-4264.216360	-973.15
	-4264.207790	-4264.226721	-962.40
	-4264.200116	-4264.218642	-920.92
	-4264.210574	-4264.229069	-953.24
	-4264.200014	-4264.217855	-951.85
	-4264.208865	-4264.227465	-915.74
	-4264.208265	-4264.227579	-931.84
	-4264.206000	-4264.224984	-955.03
	-4264.202565	-4264.219752	-950.83
	-4264.202143	-4264.220112	-942.73
TS2-*E*	-4264.220997	-4264.242302	-930.63
	-4264.214438	-4264.234344	-976.65
	-4264.214403	-4264.234358	-978.22
	-4264.220599	-4264.240843	-974.54
	-4264.214492	-4264.234255	-969.12
	-4264.219640	-4264.240135	-973.44
	-4264.214545	-4264.234276	-969.06
	-4264.209917	-4264.230906	-938.45
	-4264.214777	-4264.234898	-994.76
	-4264.210702	-4264.230801	-983.68
	-4264.215029	-4264.234844	-989.36
	-4264.214430	-4264.234383	-978.06
	-4264.213837	-4264.234275	-990.36
	-4264.219722	-4264.239726	-982.25
	-4264.213838	-4264.233797	-989.17
	-4264.214221	-4264.234176	-988.72
	-4264.214830	-4264.234212	-979.61
	-4264.220314	-4264.241233	-930.79

Figure 3.6.

Structure	M06-2X derived free energy	M06-2X derived free energy in solution	Imaginary Frequency
TS3-*Z*	-5062.168944	-5062.195728	-998.59
	-5062.162896	-5062.189822	-985.53
	-5062.165928	-5062.192767	-997.98
	-5062.165556	-5062.192134	-998.27
	-5062.161424	-5062.188877	-989.92
	-5062.164072	-5062.191163	-985.82
	-5062.165771	-5062.192732	-991.01
	-5062.162738	-5062.189561	-983.19
	-5062.165894	-5062.193104	-1003.79
	-5062.165995	-5062.193006	-999.80
	-5062.165865	-5062.192688	-998.03
TS3-*E*	-5062.164792	-5062.192706	-996.94
	-5062.163818	-5062.191245	-985.34
	-5062.163423	-5062.190545	-983.30
	-5062.162417	-5062.189802	-983.51
	-5062.164129	-5062.191457	-984.94
	-5062.164033	-5062.192143	-986.06
	-5062.164215	-5062.191516	-984.87
	-5062.163279	-5062.191579	-961.99
	-5062.155508	-5062.182301	-1062.38
	-5062.154328	-5062.180916	-1069.68
	-5062.161781	-5062.189668	-997.13
	-5062.162650	-5062.190247	-1000.33
	-5062.163070	-5062.190882	-962.59
	-5062.163295	-5062.191733	-965.68
	-5062.162443	-5062.190247	-995.71
	-5062.161805	-5062.189692	-997.28
	-5062.162055	-5062.190174	-960.14
	-5062.152750	-5062.179117	-1049.53
	-5062.160484	-5062.188639	-957.13
	-5062.150836	-5062.176737	-1053.81
	-5062.163100	-5062.191126	-964.45
	-5062.162247	-5062.190223	-1005.63
	-5062.162491	-5062.190337	-1000.61
TS4-*Z*	-5062.181985	-5062.208505	-943.04
	-5062.177028	-5062.203673	-949.08
	-5062.173102	-5062.200287	-909.22
	-5062.171527	-5062.198143	-999.65
	-5062.172295	-5062.199536	-912.68
	-5062.180747	-5062.207277	-943.26
	-5062.174424	-5062.201309	-904.39
	-5062.171681	-5062.198731	-935.82

-

	-5062.176441	-5062.203567	-909.53
	-5062.180744	-5062.207273	-943.03
	-5062.180100	-5062.207345	-910.52
	-5062.176798	-5062.203130	-939.55
	-5062.172060	-5062.199233	-910.85
	-5062.172064	-5062.199234	-910.88
	-5062.170095	-5062.196526	-873.27
	-5062.178453	-5062.204739	-938.64
	-5062.170924	-5062.197384	-891.94
	-5062.168606	-5062.197767	-946.67
	-5062.181085	-5062.207019	-973.92
	-5062.173132	-5062.200063	-936.19
	-5062.175631	-5062.202782	-911.67
	-5062.176986	-5062.203150	-975.03
	-5062.175416	-5062.202479	-910.45
TS4-*E*	-5062.181192	-5062.209646	-792.12
	-5062.167096	-5062.193131	-991.37
	-5062.178908	-5062.206291	-894.10
	-5062.177864	-5062.205138	-883.06
	-5062.167302	-5062.192730	-980.97
	-5062.180909	-5062.207477	-904.71
	-5062.178774	-5062.205213	-899.77
	-5062.167256	-5062.192696	-981.17
	-5062.180893	-5062.207470	-904.44
	-5062.178828	-5062.205274	-899.80
	-5062.179377	-5062.206352	-904.04
	-5062.162929	-5062.189114	-996.18
	-5062.162501	-5062.188631	-1002.01
	-5062.165839	-5062.191950	-1006.16
	-5062.164705	-5062.193234	-914.96
	-5062.179519	-5062.208089	-796.08
	-5062.177485	-5062.205557	-850.49
	-5062.163938	-5062.191703	-933.62
	-5062.177713	-5062.205681	-929.60
	-5062.165147	-5062.191275	-992.18
	-5062.161194	-5062.189796	-917.04
	-5062.165069	-5062.191187	-992.10
	-5062.177046	-5062.203319	-918.13
	-5062.180195	-5062.207698	-911.10
	-5062.160300	-5062.188214	-945.87
	-5062.173208	-5062.199745	-981.49
	-5062.175393	-5062.203437	-848.87
	-5062.176274	-5062.204472	-847.69
	-5062.177015	-5062.203291	-918.33
	-5062.177833	-5062.205804	-927.22
	-5062.168368	-5062.194828	-938.08

-

	-5062.165340	-5062.191706	-936.17
	-5062.162674	-5062.188591	-952.76
	-5062.173174	-5062.199995	-974.07
	-5062.177200	-5062.203907	-919.10

Table 3.1

Structure	M06-2X derived free energy	M06-2X derived free energy in solution	Imaginary Frequency
TS1-*Z*	-4264.203426	-4264.221631	-879.92
TS1-*E*	-4264.195164	-4264.215779	-949.49
TS2-*Z*	-4264.212694	-4264.232912	-883.82
TS2-*E*	-4264.220035	-4264.240953	-929.68
TS3-*Z*	-5062.165409	-5062.190499	-919.66
TS3-*E*	-5062.162667	-5062.189772	-901.86
TS4-*Z*	-5062.174173	-5062.200283	-883.02
TS4-*E*	-5062.169616	-5062.197613	-877.14

Figure 3.10.

Structure	M06-2X derived free energy	M06-2X derived free energy in solution	Imaginary Frequency
TS5	-3194.529235	-3194.547535	-561.47
	-3194.525381	-3194.543426	-789.60
	-3194.522691	-3194.541226	-803.70
	-3194.526415	-3194.544745	-570.73
	-3194.528707	-3194.547054	-556.39
	-3194.526658	-3194.545044	-583.91
	-3194.527173	-3194.545561	-586.93
	-3194.526177	-3194.544512	-570.52
	-3194.528695	-3194.547042	-558.84
	-3194.528887	-3194.547243	-558.53
	-3194.526080	-3194.544407	-573.23
TS6	-3194.523722	-3194.541356	-651.01
	-3194.523618	-3194.541252	-655.29
	-3194.523522	-3194.541152	-656.06
	-3194.520606	-3194.539433	-775.21
	-3194.520587	-3194.539459	-774.68
	-3194.520621	-3194.539477	-775.19
	-3194.520623	-3194.539501	-774.25
	-3194.520589	-3194.539450	-776.07
	-3194.520559	-3194.539409	-774.55
	-3194.520145	-3194.539106	-715.73
	-3194.520616	-3194.539493	-774.77

	-3194.520629	-3194.539485	-775.77
	-3194.519022	-3194.537205	-801.28
	-3194.519228	-3194.537425	-803.14
	-3194.519786	-3194.537969	-805.53
	-3194.515251	-3194.533484	-818.01
	-3194.519219	-3194.537425	-804.30
	-3194.519867	-3194.538048	-801.55
	-3194.520556	-3194.539707	-682.63
	-3194.520753	-3194.539788	-747.81
	-3194.516193	-3194.534366	-649.90
	-3194.516318	-3194.534472	-647.34
	-3194.516153	-3194.534301	-645.57
	-3194.516116	-3194.534265	-648.03
TS7	-3808.641262	-3808.659631	-718.29
	-3808.639053	-3808.657591	-639.47
	-3808.630910	-3808.649786	-668.42
	-3808.631054	-3808.649982	-662.41
	-3808.639572	-3808.658117	-616.87
	-3808.641248	-3808.659617	-722.35
	-3808.641173	-3808.659503	-712.03
	-3808.636871	-3808.655935	-699.39
	-3808.630706	-3808.649241	-667.22
	-3808.630694	-3808.649210	-657.02
	-3808.639151	-3808.659073	-762.72
	-3808.629221	-3808.649367	-620.12
TS8	-3808.635721	-3808.653842	-831.11
	-3808.632295	-3808.651936	-835.47
	-3808.635553	-3808.653746	-824.39

Figure 3.11.

Structure	M06-2X derived free energy	M06-2X derived free energy in solution	Imaginary Frequency
TS9	-3501.590140	-3501.608475	-715.42
	-3501.589858	-3501.608223	-742.43
	-3501.589854	-3501.608162	-713.79
	-3501.590099	-3501.608434	-723.61
	-3501.590069	-3501.608373	-718.30
	-3501.589951	-3501.608010	-710.69
	-3501.589868	-3501.608171	-721.40
	-3501.589993	-3501.608288	-724.70
	-3501.590117	-3501.608442	-720.37
	-3501.583198	-3501.602379	-706.70
	-3501.586821	-3501.605793	-667.19
	-3501.582999	-3501.602161	-707.57

	-3501.583724	-3501.602832	-714.17
	-3501.579070	-3501.598432	-598.66
	-3501.579017	-3501.598363	-592.72
TS10	-3501.590113	-3501.609791	-775.60
	-3501.579223	-3501.601584	-595.99
	-3501.579492	-3501.598871	-600.29
	-3501.579026	-3501.598356	-591.43
	-3501.579166	-3501.598504	-595.90
	-3501.579059	-3501.598362	-593.39
	-3501.578973	-3501.598323	-588.39
	-3501.580893	-3501.600593	-899.76
	-3501.589824	-3501.609501	-788.27
TS11	-3808.657496	-3808.677416	-709.76
	-3808.657375	-3808.677296	-722.49
	-3808.657320	-3808.677200	-719.94
	-3808.657211	-3808.677096	-719.27
	-3808.657417	-3808.677331	-711.10
	-3808.657274	-3808.677190	-716.51
	-3808.657274	-3808.677219	-709.49
	-3808.657021	-3808.676937	-709.37
	-3808.657381	-3808.677316	-714.99
	-3808.657214	-3808.677089	-709.86
	-3808.657057	-3808.676952	-711.44
	-3808.657270	-3808.677199	-712.91
	-3808.651813	-3808.671555	-754.91
	-3808.651824	-3808.671540	-731.43
	-3808.651750	-3808.671467	-719.67
	-3808.651830	-3808.671568	-732.26
	-3808.651780	-3808.671504	-732.56
	-3808.650908	-3808.670854	-706.47
	-3808.650894	-3808.670722	-715.55
	-3808.652114	-3808.672212	-666.92
TS12	-3808.658381	-3808.678998	-835.29
	-3808.657946	-3808.677874	-816.09
	-3808.658557	-3808.678547	-800.88
	-3808.658148	-3808.678083	-824.47
	-3808.655580	-3808.676050	-789.66
	-3808.656097	-3808.676444	-793.04
	-3808.655600	-3808.675937	-776.66

Table 3.3

Structure	M06-2X derived free energy	M06-2X derived free energy in solution	Imaginary Frequency
TS5	-3194.525539	-3194.543357	-695.33
TS6	-3194.524425	-3194.540870	-931.73
TS7	-3808.640362	-3808.658459	-813.60
TS8	-3808.634659	-3808.652268	-959.83
TS9	-3501.588406	-3501.606264	-885.07
TS10	-3501.587545	-3501.606568	-866.58
TS11	-3808.656012	-3808.675381	-851.90
TS12	-3808.654263	-3808.674165	-900.45

Figure 3.13.

Structure	M06-2X derived free energy	M06-2X derived free energy in solution	Imaginary Frequency
TS13	-3690.833034	-3690.852152	-636.55
	-3690.826225	-3690.845647	-614.51
	-3690.834609	-3690.852039	-623.84
	-3690.827620	-3690.846548	-615.91
	-3690.831014	-3690.850518	-624.20
	-3690.825954	-3690.846312	-582.16
TS14	-3690.833665	-3690.855100	-750.84
	-3690.833424	-3690.854840	-765.11
	-3690.826245	-3690.846947	-713.16
TS15	-3704.927061	-3704.942714	-719.50
	-3704.926101	-3704.942212	-722.05
	-3704.926262	-3704.942414	-721.72
	-3704.920582	-3704.936570	-720.97
	-3704.912693	-3704.928750	-706.08
	-3704.919503	-3704.935110	-570.52
	-3704.919973	-3704.936820	-687.43
	-3704.924887	-3704.941996	-704.41
TS16	-3704.923144	-3704.938776	-698.42
	-3704.922399	-3704.937901	-806.40
	-3704.922526	-3704.937912	-797.76
	-3704.922810	-3704.938348	-689.19
	-3704.922703	-3704.938324	-683.56
	-3704.922486	-3704.938110	-799.40
	-3704.920460	-3704.936527	-799.98
	-3704.920988	-3704.936953	-801.27
	-3704.920938	-3704.936964	-796.16

Figure 3.15.

Structure	M06-2X derived free energy	M06-2X derived free energy in solution	Imaginary Frequency
TS17-*Z*	-4431.320404	-4431.333640	-97.54
	-4431.319881	-4431.333154	-101.31
	-4431.317691	-4431.330876	-111.05
	-4431.318640	-4431.331969	-108.93
	-4431.318479	-4431.331449	-113.04
TS17-*E*	-4431.325972	-4431.338608	-116.00
	-4431.324853	-4431.336883	-90.80
	-4431.324943	-4431.337240	-78.75
	-4431.321819	-4431.334390	-61.19
	-4431.322592	-4431.334999	-102.84
	-4431.324039	-4431.337047	-97.74
	-4431.322516	-4431.334413	-81.33
	-4431.326766	-4431.338452	-109.99
	-4431.324849	-4431.336639	-103.16
	-4431.317553	-4431.328346	-101.57
	-4431.325957	-4431.337568	-108.59
	-4431.326086	-4431.337693	-108.38
	-4431.315594	-4431.302251	-98.61
TS18-*Z*	-4431.319768	-4431.333052	-95.89
	-4431.317544	-4431.330694	-113.49
	-4431.319251	-4431.332324	-109.45
	-4431.316538	-4431.329672	-108.64
	-4431.315374	-4431.328429	-125.48
TS18-*E*	-4431.327453	-4431.338787	-73.28
	-4431.326799	-4431.338443	-91.65
	-4431.323779	-4431.335083	-77.73
	-4431.322155	-4431.333397	-55.63
	-4431.323633	-4431.334986	-79.06
	-4431.322039	-4431.333306	-54.54
	-4431.320885	-4431.331686	-90.42
	-4431.320485	-4431.331394	-90.18
	-4431.317921	-4431.329369	-79.05
	-4431.318869	-4431.330225	-86.63
	-4431.319461	-4431.330908	-88.10

Figure 3.16.

Structure	M06-2X derived free energy	M06-2X derived free energy in solution	Imaginary Frequency
TS19-*Z*	-3790.421924	-3790.430612	-119.40
	-3790.421310	-3790.430236	-118.19
	-3769.414858	-3769.423669	-92.21
	-3790.416256	-3790.429403	-104.75
	-3790.417191	-3790.430199	-105.15
	-3790.420390	-3790.429523	-118.97
	-3790.420583	-3790.429708	-119.30
	-3790.420595	-3790.429535	-120.02
	-3790.414388	-3790.428220	-106.87
	-3790.421484	-3790.430150	-119.37
	-3790.420970	-3790.429039	-85.86
	-3790.414889	-3790.423361	-98.13
TS19-*E*	-3790.421014	-3790.428710	-106.13
	-3790.416886	-3790.425504	-98.31
	-3790.418725	-3790.426648	-97.49
	-3790.415876	-3790.424707	-103.23
TS20-*Z*	-3790.418769	-3790.427132	-103.33
	-3790.412418	-3790.422400	-111.02
	-3790.410300	-3790.419507	-73.34
	-3790.412777	-3790.421453	-88.31
	-3790.411636	-3790.420071	-87.54
	-3790.410169	-3790.418372	-74.87
	-3790.412987	-3790.421860	-91.09
	-3790.413428	-3790.422233	-96.59
	-3790.415975	-3790.424392	-100.52
	-3790.416618	-3790.425276	-104.46
	-3790.408930	-3790.418980	-107.17
	-3790.416231	-3790.424973	-105.10
	-3790.412058	-3790.420546	-90.78
	-3790.417241	-3790.425204	-75.94
	-3790.407109	-3790.416548	-74.33
	-3790.407612	-3790.417344	-76.78
	-3790.415296	-3790.424009	-88.38
	-3790.416664	-3790.425103	-103.05
	-3790.419002	-3790.427003	-114.28
TS20-*E*	-3790.426324	-3790.434143	-105.82
	-3791.416494	-3791.424794	-63.62
	-3790.426360	-3790.434084	-106.80
	-3790.426054	-3790.434091	-106.50
	-3790.422469	-3790.431041	-87.89
	-3790.416673	-3790.425239	-71.59

	-3790.421397	-3790.429653	-92.57
	-3790.412076	-3790.420360	-69.53
	-3790.421527	-3790.429811	-94.62
	-3790.416995	-3790.425234	-98.72

Appendix to Chapter 4

Figure 4.3.

Structure	M06-2X derived free energy	M06-2X derived free energy in solution	Imaginary Frequency
TS21-*Z*	-3461.010619	-3461.034457	-256.31
	-3461.003149	-3461.025360	-273.30
	-3461.002346	-3461.024665	-271.43
	-3460.998015	-3461.020301	-266.71
	-3460.999817	-3461.021195	-275.23
	-3460.999577	-3461.021097	-277.18
	-3460.998654	-3461.020285	-275.01
	-3460.999002	-3461.021550	-272.86
	-3461.003679	-3461.025911	-274.59
	-3461.010923	-3461.033189	-251.69
	-3461.011009	-3461.033500	-254.63
	-3461.011067	-3461.033542	-255.24
	-3461.010846	-3461.033108	-249.48
	-3461.011867	-3461.034084	-252.56
	-3461.010667	-3461.033246	-254.07
	-3460.999542	-3461.021124	-277.22
	-3461.009550	-3461.031875	-254.13
	-3461.010621	-3461.032946	-249.37
TS21-*E*	-3461.015501	-3461.039551	-262.04
	-3461.008790	-3461.031887	-278.14
	-3461.008386	-3461.031301	-277.13
	-3461.016632	-3461.038579	-261.41
	-3461.008330	-3461.031235	-276.16
	-3461.015885	-3461.038486	-264.35
	-3461.007592	-3461.028971	-276.36
	-3461.014925	-3461.037353	-256.75
	-3461.015713	-3461.038111	-260.98
	-3461.015153	-3461.037458	-263.81
	-3461.016149	-3461.038748	-268.27
	-3461.014875	-3461.037482	-252.80
	-3461.013545	-3461.035514	-265.32
	-3461.012782	-3461.034064	-265.41
	-3461.014766	-3461.039222	-258.50
	-3461.015626	-3461.038208	-261.48

	-3461.014900	-3461.036899	-255.99
	-3461.016197	-3461.038375	-268.10
	-3460.999663	-3461.022919	-277.66
TS22-*Z*	-3461.009308	-3461.033004	-256.49
	-3461.008150	-3461.031723	-255.90
	-3461.008821	-3461.032059	-254.85
	-3461.008667	-3461.032257	-253.42
	-3461.005378	-3461.031037	-269.90
	-3461.005255	-3461.031349	-272.87
	-3461.004960	-3461.030548	-269.68
	-3461.002175	-3461.025785	-276.34
	-3461.004750	-3461.027542	-288.27
	-3461.007545	-3461.030226	-244.53
	-3461.008613	-3461.029954	-246.37
	-3461.002084	-3461.025693	-277.20
	-3461.002156	-3461.025718	-275.96
	-3461.002680	-3461.026528	-279.25
	-3460.999348	-3461.021393	-290.79
	-3461.008905	-3461.032217	-249.16
	-3461.002322	-3461.025880	-276.95
	-3461.002693	-3461.026739	-280.13
	-3461.000629	-3461.025920	-272.49
TS22-*E*	-3461.013360	-3461.036811	-256.19
	-3461.012412	-3461.035795	-302.75
	-3461.012380	-3461.035104	-251.24
	-3461.009211	-3461.030094	-252.06
	-3461.002945	-3461.024832	-279.22
	-3461.003596	-3461.025676	-277.59
	-3461.003234	-3461.025411	-277.18
	-3461.009584	-3461.032883	-282.98

Figure 4.4.

Structure	M06-2X derived free energy	M06-2X derived free energy in solution	Imaginary Frequency
TS23-*Z*	-4258.971725	-4259.004456	-247.70
	-4258.966756	-4258.997383	-261.89
	-4258.970392	-4259.002560	-250.00
	-4258.963782	-4258.994121	-246.64
	-4258.965486	-4258.999083	-271.25
	-4258.967897	-4258.998040	-250.50
	-4258.964104	-4258.998003	-246.97
	-4258.963475	-4258.993029	-246.48
	-4258.972089	-4259.004328	-249.26
	-4258.963925	-4258.996166	-244.79

	-4258.971543	-4259.004206	-248.45
TS23-*E*	-4258.980985	-4259.012376	-265.35
	-4258.978080	-4259.009481	-266.58
	-4258.977826	-4259.008547	-269.93
	-4258.967326	-4258.997887	-248.26
	-4258.976328	-4259.007458	-270.86
	-4258.977092	-4259.007735	-269.06
	-4258.978427	-4259.012257	-270.24
	-4258.976846	-4259.007461	-267.96
	-4258.970464	-4259.000532	-258.04
	-4258.973676	-4259.007495	-271.40
	-4258.965976	-4258.996621	-249.13
TS24-*Z*	-4258.973813	-4259.007267	-273.52
	-4258.972960	-4259.003744	-254.23
	-4258.971041	-4259.002412	-241.04
	-4258.971961	-4259.004452	-279.68
	-4258.970670	-4259.001320	-252.72
	-4258.955429	-4258.988652	-241.38
	-4258.972657	-4259.003208	-255.18
	-4258.968238	-4258.998679	-267.18
	-4258.971845	-4259.002536	-251.02
	-4258.975638	-4259.005990	-255.76
	-4258.972478	-4259.003608	-254.15
	-4258.974123	-4259.005752	-239.99
	-4258.970725	-4259.002012	-256.33
	-4258.970281	-4259.000995	-255.30
	-4258.971824	-4259.002421	-252.44
	-4258.973297	-4259.004042	-256.36
	-4258.972749	-4259.003480	-253.46
TS24-*E*	-4258.982253	-4259.011949	-265.54
	-4258.981559	-4259.011132	-262.98
	-4258.973909	-4259.003283	-274.65
	-4258.979344	-4259.009270	-266.04
	-4258.981109	-4259.009558	-269.43
	-4258.975620	-4259.004657	-276.05
	-4258.981886	-4259.011552	-263.95
	-4258.976994	-4259.005092	-273.96

Figure 4.5.

Structure	M06-2X derived free energy	M06-2X derived free energy in solution	Imaginary Frequency
TS25-*Z*	-3215.928014	-3215.965673	-250.32
	-3215.923163	-3215.960681	-276.35
	-3215.921753	-3215.959430	-279.55
	-3215.914507	-3215.949609	-271.21
	-3215.926802	-3215.963927	-243.79
	-3215.918726	-3215.956045	-276.15
	-3215.914084	-3215.948291	-268.73
	-3215.917262	-3215.954817	-277.34
	-3215.920485	-3215.958961	-276.35
	-3215.919660	-3215.958108	-274.92
TS25-*E*	-3215.937736	-3215.972448	-279.18
	-3215.936002	-3215.971086	-259.41
	-3215.936968	-3215.971544	-271.07
	-3215.936459	-3215.970810	-268.84
	-3215.936045	-3215.970462	-267.32
	-3215.937553	-3215.972447	-283.10
	-3215.934744	-3215.970333	-264.41
TS26-*Z*	-3215.930159	-3215.967012	-259.09
	-3215.917196	-3215.953309	-277.54
	-3215.917205	-3215.954203	-284.50
	-3215.923465	-3215.960552	-273.51
	-3215.918023	-3215.955703	-272.39
	-3215.930974	-3215.966067	-251.22
	-3215.929400	-3215.965012	-256.45
	-3215.917161	-3215.955492	-275.84
	-3215.922523	-3215.958623	-277.57
	-3215.929205	-3215.964232	-253.28
	-3215.929621	-3215.964628	-253.06
	-3215.917263	-3215.955845	-274.30
	-3215.923125	-3215.958182	-275.41
	-3215.923274	-3215.958375	-277.13
	-3215.923397	-3215.954842	-264.99
	-3215.925179	-3215.957403	-262.24
	-3215.926149	-3215.959471	-274.11
	-3215.929318	-3215.964787	-254.56
	-3215.925774	-3215.960581	-244.88
	-3215.928753	-3215.963167	-253.59
	-3215.922888	-3215.959309	-271.11
	-3215.925132	-3215.956794	-263.22
	-3215.924910	-3215.956620	-269.05
	-3215.927865	-3215.963801	-261.00
	-3215.929366	-3215.964845	-255.04

	-3215.925813	-3215.960633	-245.28
	-3215.928719	-3215.964301	-248.84
	-3215.930593	-3215.965367	-252.65
	-3215.930019	-3215.964961	-254.31
TS26-*E*	-3215.934929	-3215.971268	-264.00
	-3215.928063	-3215.963653	-282.98
	-3215.935045	-3215.970998	-263.49
	-3215.928610	-3215.963974	-281.68
	-3215.933450	-3215.967762	-264.27
	-3215.933252	-3215.970443	-265.17
	-3215.933505	-3215.968144	-262.24
	-3215.927521	-3215.963086	-281.20
	-3215.935790	-3215.969728	-261.22
	-3215.933627	-3215.971228	-266.76
	-3215.935199	-3215.970116	-261.33
	-3215.933241	-3215.967033	-253.75
	-3215.933067	-3215.966614	-254.80
	-3215.934033	-3215.967704	-258.61
	-3215.932414	-3215.968034	-265.17
	-3215.933403	-3215.968200	-262.01
	-3215.931112	-3215.964636	-245.49
	-3215.933273	-3215.967093	-245.41
	-3215.931153	-3215.965741	-260.56

Table 4.2.

Structure	M06-2X derived free energy	M06-2X derived free energy in solution	Imaginary Frequency
TS27	-3574.284355	-3574.308210	-228.76
	-3574.284216	-3574.308007	-230.61
	-3574.282248	-3574.293637	-231.66
	-3574.282977	-3574.294365	-233.87
	-3574.282979	-3574.306811	-237.70
	-3574.282869	-3574.306701	-237.34
	-3574.282317	-3574.293735	-231.40
	-3574.273413	-3574.301554	-238.85
	-3574.266159	-3574.279355	-237.41
	-3574.276223	-3574.299859	-242.59
	-3574.274576	-3574.300033	-248.51
	-3574.283001	-3574.306907	-232.40
	-3574.281988	-3574.306625	-242.48
TS28	-3574.280913	-3574.305460	-244.38
	-3574.278028	-3574.302354	-276.00
	-3574.278219	-3574.302352	-279.88
	-3574.278115	-3574.302836	-269.13
		-	

	-3574.274915	-3574.304369	-239.12
	-3574.275959	-3574.275959	-273.02
	-3574.276382	-3574.287686	-251.39
	-3574.276614	-3574.302180	-245.12
	-3574.275900	-3574.289347	-234.27
	-3574.275562	-3574.299790	-251.29
	-3574.275611	-3574.304607	-226.49
	-3574.274708	-3574.302586	-233.17
	-3574.276575	-3574.287647	-243.50
	-3574.276251	-3574.288057	-243.17
	-3574.276374	-3574.301650	-245.77
	-3574.276220	-3574.301815	-244.67
TS29	-3329.202950	-3329.237972	-233.31
	-3329.202963	-3329.237227	-233.85
	-3329.202890	-3329.237900	-233.11
	-3329.203178	-3329.237468	-234.64
TS30	-3329.197559	-3329.237965	-267.34
	-3329.197473	-3329.237923	-267.32
	-3329.195789	-3329.235807	-284.75
	-3329.194346	-3329.235253	-273.33
	-3329.193901	-3329.236284	-273.07
	-3329.193749	-3329.235371	-261.23
	-3329.193698	-3329.235348	-261.63

Figure 4.9.

Structure	M06-2X derived free energy	M06-2X derived free energy in solution	Imaginary Frequency
TS31-*Z*	-3316.663390	-3316.689204	-241.69
	-3316.658813	-3316.684303	-287.06
	-3316.658355	-3316.683446	-254.76
	-3316.662038	-3316.687022	-257.14
	-3316.658513	-3316.683966	-286.46
	-3316.652425	-3316.676822	-280.50
	-3316.659060	-3316.684423	-235.88
TS31-*E*	-3316.670324	-3316.692600	-208.75
	-3316.661711	-3316.685663	-245.22
	-3316.660599	-3316.684090	-258.20
	-3316.664245	-3316.687253	-254.05
	-3316.653939	-3316.678357	-297.60
	-3316.660043	-3316.684834	-254.28
	-3316.664247	-3316.687106	-252.00
	-3316.660536	-3316.684021	-259.22
TS32-*Z*	-3316.662067	-3316.688388	-214.55
	-3316.658652	-3316.682974	-260.41

	-3316.656598	-3316.678580	-259.84
	-3316.639535	-3316.665163	-348.37
	-3316.640280	-3316.665860	-353.55
	-3316.663483	-3316.686863	-257.43
	-3316.658901	-3316.681125	-282.73
	-3316.659512	-3316.684216	-257.67
	-3316.655780	-3316.678458	-278.68
	-3316.645667	-3316.670477	-274.73
	-3316.644954	-3316.669715	-274.54
	-3316.658599	-3316.681151	-281.97
	-3316.654091	-3316.677284	-263.25
	-3316.655695	-3316.678400	-279.32
	-3316.658666	-3316.681415	-267.86
TS32-*E*	-3316.665299	-3316.688535	-253.13
	-3316.662141	-3316.685585	257.98
	-3316.653979	-3316.677748	-259.32
	-3316.661855	-3316.683783	-284.19
	-3316.662260	-3316.685007	-271.98
	-3316.655093	-3316.678719	-271.22

Figure 4.10.

Structure	M06-2X derived free energy	M06-2X derived free energy in solution	Imaginary Frequency
TS33-*Z*	-4412.704122	-4412.721398	-217.46
	-4412.698447	-4412.716330	-255.51
	-4412.692741	-4412.709760	-244.38
	-4412.693064	-4412.711171	-253.46
	-4412.693390	-4412.711843	-250.50
	-4412.697997	-4412.715986	-256.87
	-4412.702946	-4412.720329	-201.64
	-4412.684819	-4412.702157	-241.88
	-4412.694786	-4412.712160	-208.32
	-4412.696859	-4412.714792	-259.47
	-4412.693341	-4412.711101	-194.25
	-4412.692658	-4412.710648	-257.31
	-4412.704010	-4412.721162	-218.56
TS33-*E*	-4412.702132	-4412.719161	-223.49
	-4412.700651	-4412.717581	-246.05
	-4412.700136	-4412.717201	-242.86
	-4412.700654	-4412.717879	-246.23
	-4412.700267	-4412.717434	-270.05
	-4412.696742	-4412.714145	-247.20
	-4412.700538	-4412.717673	-227.25
	-4412.694456	-4412.712497	-282.32

	-4412.696514	-4412.714981	-265.55
	-4412.693960	-4412.711113	-248.11
	-4412.696459	-4412.715983	-245.62
	-4412.701702	-4412.718733	-228.83
TS34-*Z*	-4412.704864	-4412.721814	-236.41
	-4412.70123	-4412.718787	-241.98
	-4412.691522	-4412.707983	-291.18
	-4412.691728	-4412.708561	-274.74
	-4412.701187	-4412.718643	-274.32
	-4412.697185	-4412.713548	-253.71
	-4412.698193	-4412.706125	-262.32
	-4412.70201	-4412.720173	-233.62
	-4412.692704	-4412.710570	-265.73
	-4412.698994	-4412.716455	-266.72
	-4412.694507	-4412.711398	-229.63
	-4412.700135	-4412.717570	-267.05
	-4412.696217	-4412.714177	-264.59
TS34-*E*	-4412.703274	-4412.720214	-288.56
	-4412.702269	-4412.719445	-276.33
	-4412.702187	-4412.719026	-273.09
	-4412.694753	-4412.711395	-264.31
	-4412.701950	-4412.719016	-270.47
	-4412.690889	-4412.707563	-264.31

Figure 4.11.

Structure	M06-2X derived free energy	M06-2X derived free energy in solution	Imaginary Frequency
TS35-*Z*	-3522.025866	-3522.044371	-256.17
	-3522.027572	-3522.043544	-223.53
	-3522.022198	-3522.040427	-293.84
	-3522.022355	-3521.040627	-295.22
	-3522.025376	-3522.042234	-197.56
	-3522.024434	-3522.043002	-238.07
	-3522.009685	-3522.028709	-300.45
	-3522.020196	-3521.037972	-272.77
	-3522.016773	-3522.033828	-269.64
	-3522.026348	-3522.043705	-200.21
	-3522.018760	-3522.037033	-290.34
	-3522.016567	-3522.034110	-282.44
TS35-*E*	-3522.031715	-3522.049343	-243.02
	-3522.026410	-3522.042679	-312.17
	-3522.029698	-3522.046707	-230.84
	-3522.028344	-3522.045642	-270.90
	-3522.027475	-3522.044255	-319.85
	-		

TS36-*Z*	-3522.031515	-3522.049036	-255.24
	-3522.031847	-3522.047508	-216.12
	-3522.025056	-3522.041971	-263.79
	-3522.013841	-3522.032072	-270.14
	-3522.024336	-3522.042666	-286.02
	-3522.022580	-3522.039817	-283.32
	-3522.024469	-3522.039737	-279.40
	-3522.018427	-3522.035906	-261.15
	-3522.022855	-3522.040259	-182.69
	-3522.018430	-3522.034356	-265.57
	-3522.026895	-3522.045171	-281.19
	-3522.022706	-3522.040507	-256.10
TS36-*E*	-3522.033080	-3522.048641	-273.76
	-3522.025725	-3521.042319	-281.92
	-3522.026770	-3522.042922	-263.19
	-3522.025699	-3522.042346	-282.11
	-3522.026972	-3522.043100	-264.24

Figure 4.13.

Structure	M06-2X derived free energy	M06-2X derived free energy in solution	Imaginary Frequency
TS37-*Z*	-3291.139216	-3291.156191	-206.02
	-3291.136321	-3291.154010	-271.19
	-3291.136217	-3291.153799	-270.38
	-3291.138603	-3291.156047	-288.53
	-3291.137983	-3291.155458	-286.47
	-3291.138969	-3291.155839	-202.87
TS37-*E*	-3291.143258	-3291.160276	-239.70
	-3291.140892	-3291.157388	-271.56
	-3291.141430	-3291.157143	-235.76
	-3291.142363	-3291.159682	-220.12
TS38-*Z*	-3291.137587	-3291.154887	-224.49
	-3291.137284	-3291.154659	-222.00
	-3291.137422	-3291.154836	-226.44
	-3291.137578	-3291.154883	-224.64
	-3291.137283	-3291.154586	-226.17
	-3291.137077	-3291.154400	-219.15
	-3291.130222	-3291.147467	-250.99
	-3291.130374	-3291.147630	-249.26
TS38-*E*	-3291.141561	-3291.158061	-272.20
	-3291.141088	-3291.157464	-271.46
	-3291.139239	-3291.155690	-256.90

Appendix to Chapter 5

Figure 5.4.

Structure	M06-2X derived free energy	M06-2X derived free energy in solution	Imaginary Frequency
TS39-*Z*	-3614.735072	-3614.747798	-256.09
	-3614.731247	-3614.742730	-287.73
	-3614.734020	-3614.746946	-258.26
	-3614.732828	-3614.745750	-262.29
	-3614.733414	-3614.746289	-261.28
	-3614.735065	-3614.747667	-255.32
	-3614.733906	-3614.746729	-258.45
	-3614.731239	-3614.743845	-278.16
	-3614.731672	-3614.744472	-283.71
	-3614.731610	-3614.744263	-285.11
	-3614.731631	-3614.744244	-284.52
	-3614.731483	-3614.744171	-282.93
TS39-*E*	-3614.740700	-3614.752893	-274.60
	-3614.739444	-3614.751236	-237.43
	-3614.739656	-3614.751524	-240.04
	-3614.739584	-3614.751447	-238.90
	-3614.740616	-3614.752792	-265.47
TS40-*Z*	-3614.745475	-3614.758121	-241.90
	-3614.731812	-3614.743303	-290.25
	-3614.729001	-3614.739962	-298.17
	-3614.728881	-3614.739849	-295.31
	-3614.729213	-3614.740311	-298.87
	-3614.745252	-3614.757799	-242.31
	-3614.742633	-3614.755498	-270.94
	-3614.745281	-3614.757866	-243.76
	-3614.745322	-3614.757904	-243.16
TS40-*E*	-3614.747175	-3614.758918	-263.70
	-3614.735256	-3614.746796	-247.12
	-3614.739500	-3614.750855	-283.09
	-3614.737139	-3614.748451	-294.32
	-3614.737044	-3614.748531	-270.13

Figure 5.5.

Structure	M06-2X derived free energy	M06-2X derived free energy in solution	Imaginary Frequency
TS41-*Z*	-3261.327345	-3261.341303	-235.82
	-3261.325316	-3261.339798	-245.58
	-3261.323925	-3261.339059	-299.44

	-3261.325929	-3261.340358	-252.22
	-3261.320890	-3261.334136	-246.88
	-3261.314433	-3261.329272	-299.51
	-3261.320526	-3261.333786	-246.69
	-3261.319929	-3261.333320	-248.56
	-3261.314165	-3261.329028	-302.25
	-3261.320213	-3261.333612	-247.84
	-3261.313674	-3261.327739	-300.75
	-3261.321287	-3261.334342	-254.15
	-3261.325167	-3261.339315	-252.11
	-3261.315353	-3261.327965	-268.67
	-3261.326177	-3261.341023	-240.05
	-3261.323540	-3261.338341	-242.45
TS41-*E*	-3261.331240	-3261.344852	-262.77
	-3261.328337	-3261.341640	-235.33
	-3261.314047	-3261.327889	-298.90
	-3361.329612	-3261.343291	-266.32
	-3261.317776	-3261.331996	-284.64
	-3261.330170	-3261.334027	-251.32
	-3261.317981	-3261.332538	-260.37
	-3261.330262	-3261.343756	-250.33
	-3261.318345	-3261.332050	-257.48
	-3261.319488	-3261.333967	-256.35
	-3261.327600	-3261.341564	-238.69
	-3261.316027	-3261.330956	-262.71
	-3261.323686	-3261.337135	-271.38
	-3261.316613	-3261.330858	-277.68
TS42-*Z*	-3261.330844	-3261.346285	-258.98
	-3261.318970	-3261.333111	-261.49
	-3261.319053	-3261.333460	-264.59
	-3261.323131	-3261.341520	-236.14
	-3261.329806	-3261.345503	-246.73
	-3261.330048	-3261.346232	-243.12
	-3261.317181	-3261.331010	-285.48
	-3261.323900	-3261.339424	-292.95
	-3261.311274	-3261.326649	-334.55
	-3261.329193	-3261.345055	-245.28
	-3261.316431	-3261.330205	-282.58
	-3261.307525	-3261.324672	-272.13
	-3261.322333	-3261.335837	-268.34
TS42-*E*	-3261.329082	-3261.342466	-262.48
	-3261.328129	-3261.341678	-265.68

Figure 5.7.

Structure	M06-2X derived free energy	M06-2X derived free energy in solution	Imaginary Frequency
TS43	-3547.935862	-3547.952515	-594.09
	-3547.930021	-3547.946907	-798.31
	-3547.935522	-3547.952257	-594.56
	-3547.935651	-3547.952275	-604.41
	-3547.930499	-3547.947105	-794.17
TS44	-3547.930424	-3547.947927	-736.60
	-3547.924992	-3547.941816	-777.97
	-3547.925005	-3547.941842	-787.73
	-3547.925020	-3547.941880	-791.29
	-3547.925909	-3547.942569	-772.25
	-3547.930247	-3547.947792	-743.71
	-3547.929969	-3547.947441	-747.36
	-3547.929861	-3547.947368	-750.31
	-3547.928210	-3547.944525	-828.40
	-3547.928222	-3547.944500	-833.34
	-3547.928454	-3547.944787	-826.78
	-3547.928127	-3547.944389	-830.65
	-3547.925656	-3547.942913	-760.95
	-3547.929261	-3547.946321	-774.63

Figure 5.8.

Structure	M06-2X derived free energy	M06-2X derived free energy in solution	Imaginary Frequency
TS45	-3370.099065	-3370.113536	-200.22
	-3370.097296	-3370.111956	-217.89
	-3370.097333	-3370.111971	-218.05
	-3370.097446	-3370.112016	-218.71
	-3370.097112	-3370.111773	-217.21
	-3370.094963	-3370.109579	-218.94
	-3370.098511	-3370.108470	-200.14
	-3370.098124	-3370.112577	-200.27
	-3370.098695	-3370.113179	-197.60
	-3370.095183	-3370.109835	-220.15
	-3370.095258	-3370.109852	-220.30
	-3370.094903	-3370.109535	-218.32
TS46	-3370.094211	-3370.109173	-247.93
	-3370.093856	-3370.108943	-254.05
	-3370.093907	-3370.108902	-248.06
	-3370.093191	-3370.108517	-226.43

Table 5.1.

Structure	M06-2X derived free energy	M06-2X derived free energy in solution	Imaginary Frequency
TS47	-3252.311178	-3252.326357	-203.15
	-3252.301239	-3252.315667	-175.50
TS48	-3252.308761	-3252.322345	-235.91
	-3252.306836	-3252.322204	-231.45
	-3252.306092	-3252.321674	-234.15

Figure 5.10.

Structure	M06-2X derived free energy	M06-2X derived free energy in solution	Imaginary Frequency
TS49-*Z*	-3107.596624	-3107.626472	-254.31
	-3107.586239	-3107.617473	-280.38
	-3107.586514	-3107.614367	-238.13
	-3107.586546	-3107.614551	-239.98
	-3107.586270	-3107.617559	-281.49
	-3107.586524	-3107.614439	-238.48
	-3107.586497	-3107.614503	-241.83
	-3107.592635	-3107.623195	-272.83
	-3107.596119	-3107.625976	-254.11
	-3107.596208	-3107.625954	-253.41
	-3107.596451	-3107.626305	-254.81
TS49-*E*	-3107.602073	-3107.629840	-272.79
	-3107.601534	-3107.629092	-269.47
	-3107.601900	-3107.629747	-271.41
	-3107.601509	-3107.629035	-269.83
	-3107.601477	-3107.629101	-268.98
	-3107.601664	-3107.629270	-271.33
	-3107.602018	-3107.629578	-274.55
	-3107.601691	-3107.629502	-269.69
	-3107.600955	-3107.628160	-266.58
	-3107.582989	-3107.610055	-257.59
TS50-*Z*	-3107.597887	-3107.625863	-258.90
	-3107.597132	-3107.624874	-254.86
	-3107.596235	-3107.624462	-256.29
	-3107.596889	-3107.624688	-256.34
	-3107.596494	-3107.624676	-257.39
	-3107.591356	-3107.618779	-263.45
	-3107.590857	-3107.618511	-261.80
	-3107.591489	-3107.618817	-264.16
	-3107.590884	-3107.618114	-261.00
	-3107.591290	-3107.618581	-262.35

	-3107.590058	-3107.619391	-235.61
	-3107.590328	-3107.619836	-239.46
	-3107.585587	-3107.614737	-266.59
	-3107.586419	-3107.612936	-273.18
	-3107.586670	-3107.613203	-275.48
	-3107.596525	-3107.624595	-261.21
TS50-*E*	-3107.597667	-3107.626260	-289.79
	-3107.597487	-3107.626147	-294.85
	-3107.597394	-3107.626006	-297.07
	-3107.597376	-3107.626063	-297.27
	-3107.597524	-3107.626122	-292.63
	-3107.597512	-3107.626153	-295.34
	-3107.597480	-3107.626149	-295.37
	-3107.597430	-3107.626035	-296.22
	-3107.597476	-3107.626117	-295.64
	-3107.597552	-3107.626201	-292.64
	-3107.597376	-3107.626079	-295.45
	-3107.597912	-3107.623757	-261.53
	-3107.597103	-3107.625715	-291.86
	-3107.596884	-3107.622351	-259.22

Figure 5.12.

Structure	M06-2X derived free energy	M06-2X derived free energy in solution	Imaginary Frequency
TS51-*Z*	-3910.793803	-3910.817439	-920.75
	-3910.792124	-3910.815379	-948.83
	-3910.792340	-3910.815625	-952.95
	-3910.792800	-3910.816026	-962.34
	-3910.792610	-3910.815838	-958.50
	-3910.786806	-3910.810286	-878.46
	-3910.786823	-3910.810374	-869.25
	-3910.786897	-3910.810423	-885.57
	-3910.787299	-3910.811580	-912.87
	-3910.787332	-3910.811735	-909.05
	-3910.789686	-3910.813455	-878.19
	-3910.789643	-3910.812837	-879.84
	-3910.793186	-3910.816452	-908.93
	-3910.793213	-3910.816800	-902.06
TS51-*E*	-3910.804213	-3910.828778	-975.79
	-3910.803984	-3910.828556	-964.29
	-3910.804207	-3910.828703	-973.30
	-3910.804111	-3910.828613	-968.93
	-3910.803852	-3910.828435	-963.85
	-3910.803945	-3910.828510	-970.77

	-3910.804134	-3910.828698	-974.07
	-3910.803881	-3910.828461	-981.52
	-3910.798155	-3910.822005	-1003.31
	-3910.797851	-3910.821696	-1003.94
	-3910.797956	-3910.821831	-1000.69
	-3910.797917	-3910.821722	-999.36
	-3910.797468	-3910.820578	-998.80
	-3910.796952	-3910.822317	-957.84
	-3910.796387	-3910.821603	-953.55
	-3910.797441	-3910.818702	-989.66
	-3910.800803	-3910.822018	-991.97
	-3910.798119	-3910.819324	-991.84
	-3910.801864	-3910.828400	-907.22
	-3910.801633	-3910.828191	-904.22
	-3910.788303	-3910.813293	-872.74
TS52-*Z*	-3910.800042	-3910.823545	-975.53
	-3910.800362	-3910.822870	-852.28
	-3910.795978	-3910.819144	-956.50
	-3910.800404	-3910.822630	-853.31
	-3910.795629	-3910.819485	-945.34
	-3910.799006	-3910.822402	-972.83
	-3910.794102	-3910.817681	-924.98
	-3910.794172	-3910.817706	-932.15
	-3910.794060	-3910.817469	-903.45
	-3910.793717	-3910.816921	-893.14
	-3910.794074	-3910.817450	-909.05
	-3910.793939	-3910.817288	-898.42
	-3910.795825	-3910.819084	-955.48
	-3910.796944	-3910.820066	-959.29
TS52-*E*	-3910.794324	-3910.820124	-986.07
	-3910.794020	-3910.819841	-983.94
	-3910.794232	-3910.820015	-986.86
	-3910.793570	-3910.819379	-981.44
	-3910.793573	-3910.819283	-985.25
	-3910.794140	-3910.819935	-983.67
	-3910.793945	-3910.819731	-984.92
	-3910.794244	-3910.820075	-987.65
	-3910.793724	-3910.819653	-989.45
	-3910.794144	-3910.820032	-987.44
	-3910.794176	-3910.820004	-988.88
	-3910.787012	-3910.811030	-627.62
	-3910.787108	-3910.811181	-620.72
	-3910.787003	-3910.811066	-628.59
	-3910.787077	-3910.811141	-626.32
	-3910.787068	-3910.811124	-615.18
	-3910.787111	-3910.811231	-617.39

-

	-3910.794690	-3910.820278	-927.06
	-3910.794785	-3910.820435	-927.27
	-3910.793978	-3910.819295	-924.26
	-3910.787565	-3910.811503	-956.47
	-3910.794611	-3910.820210	-934.84

Appendix to Chapter 6

Figure 6.2.

Structure	B3LYP free energy	M06-2X derived free energy	Imaginary Frequency
TS53	-2021.445237	-2020.729720	-761.42
	-2021.415341	-2020.695682	-306.23
	-2021.415339	-2020.695678	-306.08
	-2021.415339	-2020.695690	-306.19
	-2021.411895	-2020.691943	-285.76
	-2021.413566	-2020.693977	-280.46
	-2021.413577	-2020.693990	-280.92
	-2021.415343	-2020.695700	-306.28
	-2021.426340	-2020.706510	-742.80
	-2021.426354	-2020.706523	-742.80
	-2021.426339	-2020.706509	-742.78
	-2021.425467	-2020.704460	-764.38
TS54-*E*	-2021.451587	-2020.733701	-829.57
	-2021.451585	-2020.733693	-829.50
	-2021.451590	-2020.733695	-829.58
	-2021.451579	-2020.733683	-829.57
	-2021.451574	-2020.733668	-829.54
	-2021.451587	-2020.733699	-829.57
	-2021.451570	-2020.733672	-829.60
	-2021.446481	-2020.726082	-813.44
	-2021.446481	-2020.726077	-813.41
	-2021.452747	-2020.733086	-844.19
	-2021.452746	-2020.733071	-844.19
	-2021.452747	-2020.733072	-844.19
	-2021.446478	-2020.726048	-813.20
	-2021.451578	-2020.731906	-787.87
	-2021.452513	-2020.732353	-844.09
	-2021.452514	-2020.732354	-844.12
	-2021.452716	-2020.733211	-820.51
TS54-*Z*	-2021.885009	-2020.733064	-884.58
	-2021.885009	-2020.733051	-884.56
	-2021.885009	-2020.733059	-884.55
	-2021.885009	-2020.733063	-884.58

	-2021.885009	-2020.733058	-884.61
	-2021.885009	-2020.733055	-884.56
	-2021.885009	-2020.733057	-884.52
	-2021.885009	-2020.733060	-884.51
	-2021.885009	-2020.733048	-884.51
	-2021.885009	-2020.733052	-884.52
	-2021.876616	-2020.724939	-887.61
	-2021.883476	-2020.729364	-645.14
	-2021.883476	-2020.729368	-645.14
	-2021.883476	-2020.729361	-645.02
	-2021.883476	-2020.729360	-645.30
	-2021.883476	-2020.729366	-645.18
	-2021.882880	-2020.729810	-720.52
	-2021.882880	-2020.729803	-720.46
	-2021.882880	-2020.729800	-720.52
	-2021.882880	-2020.729798	-720.50
	-2021.882880	-2020.729828	-720.29
	-2021.883015	-2020.728912	-700.54
	-2021.880968	-2020.727120	-698.69
	-2021.880887	-2020.726443	-664.61
	-2021.880887	-2020.726447	-664.61
	-2021.873473	-2020.717391	-866.67
	-2021.873473	-2020.717386	-866.68
	-2021.878551	-2020.723662	-732.56
TS55	-2021.466982	-2020.746243	-764.21
	-2021.449707	-2020.731851	-682.76
	-2021.466459	-2020.745669	-733.78
	-2021.466456	-2020.745657	-733.65
	-2021.466456	-2020.745655	-733.69
	-2021.449706	-2020.731844	-682.55
	-2021.449725	-2020.732051	-715.06
	-2021.466520	-2020.745739	-761.42
	-2021.449727	-2020.732057	-715.52

Figure 6.3.

Structure	B3LYP free energy	M06-2X derived free energy	M06-2X derived free energy in solution	Imaginary Frequency
PT1	-1237.809521	-1237.406021	-1237.419009	-793.21
	-1237.806956	-1237.402467	-1237.417849	-1018.00
	-1237.809352	-1237.404378	-1237.418361	-1027.87
	-1237.809341	-1237.405929	-1237.418976	-779.26
PT2	-1237.800497	-1237.402541	-1237.417473	-65.01

Figure 6.4.

Structure	M06-2X derived free energy	M06-2X derived free energy in solution	Imaginary Frequency
TS56-*Z*	-4601.397990	-4601.415476	-865.40
	-4601.395000	-4601.413360	-755.51
	-4601.395472	-4601.414129	-777.06
	-4601.395722	-4601.413999	-787.28
	-4601.393563	-4601.411427	-862.81
	-4601.387155	-4601.405910	-917.23
	-4601.387381	-4601.406287	-916.76
	-4601.388068	-4601.405014	-655.62
	-4601.395436	-4601.412417	-866.14
	-4601.384124	-4601.405282	-880.94
	-4601.393530	-4601.410797	-744.45
TS56-*E*	-4601.403198	-4601.419580	-825.60
	-4601.397602	-4601.414807	-887.65
	-4601.398462	-4601.415507	-882.72
	-4601.398563	-4601.415660	-793.30
	-4601.398778	-4601.415989	-888.19
	-4601.394409	-4601.411563	-802.12
	-4601.399489	-4601.416789	-886.47
	-4601.393526	-4601.409896	-823.58
	-4601.397375	-4601.414184	-900.79
	-4601.391700	-4601.408816	-777.62
	-4601.395809	-4601.413499	-874.42
	-4601.399184	-4601.416253	-787.90
	-4601.401282	-4601.418356	-792.77
	-4601.394818	-4601.414060	-850.40
	-4601.397752	-4601.414318	-836.78
	-4601.395544	-4601.412242	-818.67
	-4601.391918	-4601.409806	-861.46
	-4601.399013	-4601.415887	-897.16
	-4601.400675	-4601.417795	-796.63
TS57-*Z*	-4601.400364	-4601.417016	-894.32
	-4601.389665	-4601.407430	-693.03
	-4601.396005	-4601.412990	-895.44
	-4601.389885	-4601.407443	-677.71
	-4601.385785	-4601.403564	-710.74
	-4601.394204	-4601.411499	-906.81
	-4601.392668	-4601.410575	-876.09
	-4061.396230	-4061.413128	-898.22
	-4601.393194	-4601.410871	-865.57
	-4601.390600	-4601.408729	-920.22
	-4601.379678	-4601.399710	-864.64

	-4601.389118	-4601.407006	-874.09
	-4601.398576	-4601.415469	-939.58
	-4601.390013	-4601.407796	-883.08
	-4601.390936	-4601.409891	-657.01
	-4601.394138	-4601.411404	-903.61
	-4601.396481	-4601.415025	-764.90
	-4601.386416	-4601.404094	-919.31
TS57-*E*	-4601.397735	-4601.414528	-867.84
	-4601.392706	-4601.409224	-898.01
	-4601.387724	-4601.404373	-899.58
	-4601.393090	-4601.409608	-942.61
TS58-*E*	-4601.418309	-4601.435352	-771.73
	-4601.418230	-4601.435231	-774.45
	-4601.409971	-4601.426910	-794.20
	-4601.411663	-4601.428597	-758.77
TS59-*E*	-4601.415225	-4601.433118	-783.16
	-4601.411439	-4601.430373	-750.98
	-4601.415121	-4601.433061	-785.21
	-4601.415146	-4601.433031	-786.61
	-4601.415196	-4601.433087	-786.93
	-4601.414873	-4601.432962	-788.72
	-4601.414567	-4601.432676	-791.83
	-4601.414669	-4601.432765	-791.57
	-4601.414644	-4601.432815	-790.92
	-4601.414940	-4601.432934	-789.86
OOH-*Type II Z*	-4601.380958	-4601.399433	-924.58
OOH-*Type I Z*	-4601.388414	-4601.406026	-941.59
	-4601.383601	-4601.401342	-995.10
	-4601.383391	-4601.401080	-993.89
	-4601.381945	-4601.399685	-969.23

Figure 6.7.

Structure	M06-2X derived free energy	M06-2X derived free energy in solution	Imaginary Frequency
TS60-*Z*	-5023.892161	-5023.910490	-967.44
	-5023.886206	-5023.904672	-990.73
	-5023.886691	-5023.905153	-991.24
	-5023.886605	-5023.905084	-994.56
	-5023.890134	-5023.908446	-949.76
	-5023.889153	-5023.907299	-948.42
	-5023.887358	-5023.905121	-1068.40
TS60-*E*	-5023.890010	-5023.907395	-1066.15
	-5023.884630	-5023.902407	-1059.89
	-5023.884879	-5023.902642	-1057.73

	-5023.884617	-5023.902443	-1057.60
	-5023.889940	-5023.907244	-1063.40
	-5023.887400	-5023.905086	-1075.75
	-5023.882132	-5023.900745	-1031.11
	-5023.861031	-5023.878473	-920.04
TS61-*Z*	-5023.898096	-5023.915832	-1002.79
	-5023.896330	-5023.914159	-989.29
	-5023.895974	-5023.913763	-995.96
	-5023.897735	-5023.915497	-1001.19
	-5023.897975	-5023.915195	-1139.61
	-5023.898169	-5023.915427	-1135.80
	-5023.897956	-5023.915207	-1132.78
	-5023.890415	-5023.908294	-1121.06
	-5023.890091	-5023.907953	-1135.20
	-5023.890238	-5023.908116	-1125.70
	-5023.890408	-5023.908312	-1121.67
	-5023.890376	-5023.908256	-1121.18
	-5023.891739	-5023.909754	-1024.14
	-5023.890943	-5023.908883	-1027.02
	-5023.895784	-5023.913076	-1120.47
	-5023.896389	-5023.913749	-1143.12
	-5023.898026	-5023.915361	-1125.08
	-5023.895931	-5023.913399	-1129.43
	-5023.897049	-5023.914672	-997.61
	-5023.897056	-5023.914666	-992.25
	-5023.895992	-5023.913617	-989.23
TS61-*E*	-5023.894199	-5023.913005	-978.69
	-5023.892667	-5023.910367	-1060.03
	-5023.892658	-5023.910372	-1061.24
	-5023.891879	-5063.909659	-1044.02
	-5023.885989	-5023.903565	-1121.78
	-5023.892549	-5023.910250	-1067.53
	-5023.894652	-5023.912270	-1069.26
	-5023.887706	-5023.905752	-1049.48
	-5023.887008	-5023.904491	-1123.26
	-5023.865089	-5023.883063	-910.16
	-5023.865624	-5023.883544	-898.13
	-5023.881682	-5023.899471	-1143.25
	-5023.881697	-5023.899465	-1145.54
	-5023.892145	-5023.909810	-1058.63
	-5023.891990	-5023.909525	-1048.87
	-5023.892404	-5023.910131	-1061.72
	-5023.892803	-5023.910602	-956.43
TS62-*E*	-5023.917585	-5023.935180	-1070.60
	-5023.886858	-5023.904098	-1128.45
	-5023.915796	-5023.933430	-1041.64

	-5023.884454	-5023.901532	-1124.04
	-5023.914809	-5023.932541	-1065.02
TS63-*E*	-5023.914410	-5023.933177	-1039.63
	-5023.911415	-5023.930253	-1019.30
	-5023.911488	-5023.930374	-1020.36
	-5023.911612	-5023.930512	-1020.92
	-5023.896456	-5023.913867	-1098.31
OOH-*Type II Z*	-5023.863942	-5023.884257	-1059.74
	-5023.856278	-5023.878037	-988.41
OOH-*Type I Z*	-5023.894756	-5023.912640	-994.35
	-2289.648868	-5023.910932	-986.16
	-5023.888658	-5023.908366	-1012.48
	-5023.864808	-5023.886517	-1050.98

Appendix to Chapter 7

Figure 7.4.

Structure	B3LYP free energy	M06-2X derived free energy	Imaginary Frequency
TS64	-2460.851147	-2460.028720	-334.54
	-2460.846778	-2460.019446	-316.65
	-2460.846779	-2460.019446	-316.64
	-2460.846778	-2460.019447	-316.65
	-2460.844892	-2460.017862	-353.04
	-2460.849448	-2460.020272	-366.19
	-2460.843141	-2460.015747	-373.70
	-2460.843142	-2460.015751	-373.69
	-2460.843141	-2460.015763	-373.70
	-2460.843950	-2460.016673	-367.60
	-2460.843947	-2460.016685	-367.62
	-2460.842276	-2460.014852	-333.92
	-2460.842064	-2460.014408	-337.17
	-2460.846265	-2460.017745	-370.26
	-2460.846782	-2460.018447	-376.74
	-2460.848435	-2460.020739	-365.99
	-2460.843142	-2460.015770	-373.70
	-2460.843142	-2460.015763	-373.70
	-2460.843937	-2460.016661	-367.57
	-2460.849450	-2460.020275	-366.18
	-2460.846934	-2460.022802	-355.86
	-2460.846937	-2460.022821	-355.89
	-2460.846777	-2460.019441	-316.60
	-2460.848075	-2460.020392	-370.08
	-2460.843010	-2460.016418	-390.47

-2460.848926	-2460.022294	-357.43
-2460.846280	-2460.019472	-386.61
-2460.846281	-2460.019482	-386.61
-2460.847078	-2460.017138	-381.80
-2460.845548	-2460.019598	-382.67
-2460.852532	-2460.028247	-357.29
-2460.852535	-2460.028267	-357.30
-2460.846933	-2460.022823	-355.93
-2460.844593	-2460.018338	-388.96
-2460.844869	-2460.016762	-387.03
-2460.851142	-2460.028713	-334.51
-2460.842914	-2460.017399	-401.29
-2460.846277	-2460.019462	-386.70
-2460.842973	-2460.016378	-390.39
-2460.843003	-2460.016429	-390.59
-2460.848095	-2460.020815	-374.45
-2460.848043	-2460.020352	-370.12
-2460.841991	-2460.018532	-373.27
-2460.846035	-2460.021212	-383.88
-2460.844593	-2460.018346	-388.97
-2460.843197	-2460.019447	-361.47
-2460.846253	-2460.017731	-370.25
-2460.842911	-2460.017409	-401.24
-2460.844587	-2460.018330	-388.97
-2460.838945	-2460.011132	-411.21
-2460.846259	-2460.017735	-370.27
-2460.852535	-2460.028251	-357.25
-2460.847374	-2460.024414	-343.87
-2460.842356	-2460.015247	-387.11
-2460.842358	-2460.015250	-387.10
-2460.842351	-2460.015254	-387.10
-2460.848359	-2460.022977	-361.73
-2460.848064	-2460.024116	-350.68
-2460.842351	-2460.015259	-387.10
-2460.846929	-2460.022800	-355.90
-2460.847140	-2460.022741	-352.40
-2460.846031	-2460.021220	-383.91
-2460.842561	-2460.016573	-360.63
-2460.851799	-2460.028265	-356.23
-2460.846777	-2460.019434	-316.61
-2460.846778	-2460.019442	-316.64
-2460.852532	-2460.028262	-357.28
-2460.852539	-2460.028275	-357.31
-2460.845748	-2460.018488	-383.36
-2460.847144	-2460.022745	-352.43
-2460.847139	-2460.022739	-352.37

-

	-2460.851148	-2460.028710	-334.54
	-2460.848430	2461.011132	-366.05
	-2460.851143	-2460.028712	-334.52
	-2460.846925	-2460.022800	-355.92
	-2460.848295	-2460.025545	-351.28
	-2460.852538	-2460.028255	-357.29
	-2460.843948	-2460.016669	-367.59
	-2460.851793	-2460.028250	-356.28
	-2460.852513	-2460.028247	-357.26
	-2460.851146	-2460.028718	-334.54
	-2460.848927	-2460.022275	-357.42
TS65	-2460.844959	-2460.018014	-354.21
	-2460.844772	-2460.017009	-349.35
	-2460.844960	-2460.017998	-354.21
	-2460.844772	-2460.017027	-349.36
	-2460.841106	-2460.015805	-366.66
	-2460.840708	-2460.015434	-366.16
	-2460.844959	-2460.018012	-354.22
	-2460.844767	-2460.017015	-349.34
	-2460.844960	-2460.018002	-354.21
	-2460.844960	-2460.017997	-354.22
	-2460.844960	-2460.018007	-354.22

Figure 7.6.

Structure	M06-2X derived free energy	M06-2X derived free energy in solution	Imaginary Frequency
TS66-*Re*	-3921.480051	-3921.494298	-323.28
	-3921.474437	-3921.486519	-363.71
	-3921.476031	-3921.487869	-374.20
	-3921.474456	-3921.486590	-363.72
	-3921.475068	-3921.488239	-353.68
	-3921.475249	-3921.488283	-348.11
	-3921.476034	-3921.487857	-374.19
	-3921.476962	-3921.489045	-370.09
	-3921.477191	-3921.491448	-369.77
	-3921.474451	-3921.486560	-363.70
	-3921.471139	-3921.487843	-388.65
	-3921.467618	-3921.482872	-382.55
	-3921.477138	-3921.491407	-369.90
	-3921.474984	-3921.488252	-353.21
	-3921.476888	-3921.489082	-369.30
	-3921.473825	-3921.488739	-376.37
	-3921.475921	-3921.487795	-373.91
	-3921.481427	-3921.493152	-321.36

	-3921.481508	-3921.493129	-321.32
	-3921.465541	-3921.489922	-376.73
	-3921.473097	-3921.489670	-387.76
	-3921.474045	-3921.488837	-378.04
	-3921.472348	-3921.489015	-387.32
	-3921.474299	-3921.489319	-378.27
	-3921.470527	-3921.483212	-378.02
	-3921.474027	-3921.488685	-378.04
	-3921.477312	-3921.491226	-369.64
	-3921.477147	-3921.491453	-369.66
	-3921.477943	-3921.492029	-340.47
	-3921.465553	-3921.480943	-376.71
	-3921.477868	-3921.491956	-340.45
	-3921.470735	-3921.484347	-374.34
	-3921.471176	-3921.483913	-377.73
	-3921.471189	-3921.483903	-377.71
	-3921.472401	-3921.489065	-387.32
	-3921.470590	-3921.483469	-376.16
	-3921.471165	-3921.483718	-377.72
	-3921.472394	-3921.489038	-387.32
	-3921.477894	-3921.491879	-340.43
	-3921.464233	-3921.478485	-361.14
	-3921.475324	-3921.488332	-347.96
	-3921.477907	-3921.492002	-340.43
	-3921.480018	-3921.494153	-323.32
	-3921.472233	-3921.487301	-383.64
	-3921.473764	-3921.488665	-376.38
	-3921.464182	-3921.478438	-361.15
	-3921.473794	-3921.488687	-376.43
	-3921.472374	-3921.489027	-387.29
	-3921.473810	-3921.488702	-376.38
	-3921.473822	-3921.488729	-376.40
TS67-*Si*	-3921.479148	-3921.492894	-364.46
	-3921.464564	-3921.478789	-401.36
	-3921.467796	-3921.480420	-357.68
	-3921.474329	-3921.489286	-422.48
	-3921.477572	-3921.489442	-339.89
	-3921.466591	-3921.482568	-380.52
	-3921.477553	-3921.489442	-339.91
	-3921.470215	-3921.483636	-364.71
	-3921.470566	-3921.482632	-374.31
	-3921.466198	-3921.478052	-387.26
	-3921.474536	-3921.488045	-399.50
	-3921.470637	-3921.484075	-375.87
	-3921.466468	-3921.479504	-388.38
	-3921.465293	-3921.479054	-404.98

-3921.477039	-3921.489048	-352.06
-3921.477057	-3921.489075	-352.06
-3921.466143	-3921.478004	-387.34
-3921.467772	-3921.483967	-388.77
-3921.465300	-3921.479058	-404.98
-3921.473794	-3921.486891	-383.96
-3921.473822	-3921.486870	-383.98
-3921.473281	-3921.486084	-397.60
-3921.474535	-3921.486576	-350.60
-3921.474947	-3921.489321	-380.30
-3921.479131	-3921.492817	-363.30
-3921.473835	-3921.485568	-367.88
-3921.478251	-3921.492235	-361.05
-3921.474473	-3921.489311	-421.28
-3921.474437	-3921.489269	-421.28
-3921.473827	-3921.486855	-384.00
-3921.470610	-3921.482682	-374.20
-3921.463162	-3921.475394	-374.08
-3921.473957	-3921.488782	-377.26
-3921.465295	-3921.479053	-404.99
-3921.465294	-3921.479054	-405.02
-3921.476444	-3921.490006	-355.40
-3921.466895	-3921.478297	-391.25
-3921.470380	-3921.485101	-379.07
-3921.465279	-3921.479030	-404.98
-3921.464032	-3921.477859	-403.88
-3921.467755	-3921.482533	-398.02
-3921.467723	-3921.483901	-388.71
-3921.475738	-3921.489954	-379.31
-3921.467047	-3921.480386	-355.98
-3921.466379	-3921.481535	-411.65
-3921.470592	-3921.482665	-374.16
-3921.475755	-3921.489968	-379.32
-3921.463562	-3921.475197	-374.84
-3921.476831	-3921.491666	-400.17
-3921.463517	-3921.475144	-374.84
-3921.475910	-3921.488788	-413.16
-3921.472061	-3921.483910	-370.05
-3921.476315	-3921.489568	-408.43
-3921.470462	-3921.482267	-372.18
-3921.470533	-3921.482607	-374.20
-3921.478745	-3921.491841	-413.36
-3921.474399	-3921.489228	-421.29
-3921.476445	-3921.490007	-355.35
-3921.464417	-3921.476401	-390.79
-3921.463041	-3921.475884	-387.76

	-3921.474621	-3921.488382	-399.52
	-3921.472208	-3921.486443	-410.13
	-3921.474606	-3921.488582	-395.17
	-3921.473480	-3921.487343	-398.35
	-3921.468829	-3921.483795	-397.18
	-3921.471041	-3921.485454	-378.54
	-3921.475124	-3921.487835	-365.10
	-3921.471703	-3921.485878	-409.32
	-3921.469897	-3921.486200	-387.52
	-3921.473843	-3921.486938	-383.97
	-3921.473872	-3921.486907	-383.97
	-3921.475105	-3921.487803	-364.96
	-3921.474839	-3921.488678	-399.65
	-3921.477039	-3921.489844	-341.11
	-3921.477436	-3921.489246	-341.69
	-3921.467086	-3921.478405	-390.88
	-3921.478764	-3921.491389	-333.14
	-3921.465299	-3921.479069	-405.00
	-3921.477022	-3921.489836	-341.08
	-3921.473848	-3921.486924	-383.95
	-3921.477044	-3921.489865	-341.14
	-3921.472220	-3921.486456	-410.14
	-3921.473661	-3921.486559	-383.68
	-3921.467817	-3921.484009	-388.72
	-3921.463068	-3921.476891	-404.64
	-3921.477511	-3921.489372	-339.86
	-3921.470771	-3921.483651	-376.61
TS68-*Si*	-3921.511202	-3921.511202	-348.96
	-3921.494751	-3921.506633	-371.14
	-3921.492259	-3921.498654	-385.67
TS68-*Re*	-3921.492722	-3921.509155	-374.01
	-3921.485138	-3921.501756	-397.40
TS69-*Si*	-3921.487968	-3921.504900	-388.58
	-3921.488418	-3921.496585	-391.03
	-3921.488603	-3921.497052	-387.91
	-3921.479319	-3921.497505	-341.09
	-3921.487959	-3921.496351	-388.59
	-3921.487080	-3921.503632	-387.04
	-3921.476753	-3921.493926	-361.14
	-3921.482538	-3921.498593	-368.07
	-3921.471790	-3921.488943	-413.32
	-3921.478438	-3921.496208	-344.37
	-3921.484403	-3921.499977	-367.27
	-3921.480396	-3921.498656	-397.30
	-3921.476405	-3921.494811	-406.89
	-3921.479565	-3921.498332	-393.22

	-3921.479197	-3921.496774	-393.75
	-3921.476920	-3921.494819	-405.95
	-3921.476307	-3921.493604	-400.59
	-3921.479410	-3921.497967	-393.01
TS69-*Re*	-3921.482857	-3921.500171	-396.84
	-3921.477588	-3921.492116	-386.43
	-3921.478023	-3921.492224	-404.50
	-3921.479809	-3921.494260	-386.49
	-3921.479818	-3921.495360	-358.67
	-3921.476605	-3921.491587	-366.56
	-3921.480026	-3921.498094	-405.34

Figure 7.8.

Structure	M06-2X derived free energy	M06-2X derived free energy in solution	Imaginary Frequency
TS70-*Re*	-5040.679267	-5040.693968	-376.23
	-5040.679252	-5040.693950	-376.16
	-5040.679224	-5040.693927	-376.23
	-5040.662069	-5040.676088	-342.79
	-5040.652696	-5040.666728	-355.75
	-5040.655778	-5040.672244	-417.56
	-5040.651783	-5040.668883	-355.31
	-5040.671088	-5040.686672	-380.97
	-5040.666443	-5040.680681	-347.55
	-5040.660526	-5040.675567	-367.31
	-5040.677242	-5040.692967	-383.19
	-5040.668993	-5040.683848	-390.98
	-5040.665652	-5040.681559	-382.10
	-5040.677454	-5040.693100	-382.63
	-5040.665035	-5040.680755	-382.06
	-5040.665028	-5040.680750	-382.06
	-5040.671238	-5040.688249	-374.33
	-5040.666234	-5040.680669	-348.65
	-5040.657940	-5040.673847	-382.98
	-5040.666903	-5040.683152	-367.78
	-5040.665152	-5040.679532	-417.38
	-5040.672684	-5040.687012	-347.08
	-5040.666636	-5040.682285	-383.94
	-5040.677171	-5040.692893	-383.13
	-5040.643523	-5040.659425	-427.82
	-5040.664671	-5040.679745	-393.22
	-5040.662704	-5040.678711	-385.84
	-5040.659974	-5040.677145	-400.16
TS71-*Si*	-5040.678879	-5040.693616	-387.36

-5040.660314	-5040.674127	-370.49
-5040.660855	-5040.676751	-386.20
-5040.670497	-5040.683960	-407.85
-5040.672106	-5040.686434	-383.96
-5040.647755	-5040.660676	-352.32
-5040.667530	-5040.679842	-373.66
-5040.670542	-5040.683996	-407.84
-5040.666961	-5040.679346	-373.13
-5040.660974	-5040.676386	-408.95
-5040.668596	-5040.683127	-403.03
-5040.670139	-5040.684762	-405.90
-5040.662370	-5040.677214	-410.28
-5040.649125	-5040.664980	-361.93
-5040.666231	-5040.678255	-357.01
-5040.667554	-5040.680879	-407.05
-5040.669183	-5040.681600	-399.50
-5040.673562	-5040.686932	-414.45
-5040.670499	-5040.683947	-407.83
-5040.668262	-5040.684833	-411.88
-5040.667323	-5040.679681	-372.55
-5040.657735	-5040.672250	-359.28
-5040.668234	-5040.684111	-411.88
-5040.670117	-5040.684572	-400.56
-5040.668469	-5040.684290	-395.31
-5040.668832	-5040.685659	-382.00
-5040.660524	-5040.676128	-387.27
-5040.671250	-5040.686221	-394.02
-5040.671006	-5040.687741	-382.01
-5040.663160	-5040.677125	-357.40
-5040.658631	-5040.673223	-363.42
-5040.670990	-5040.687370	-384.41
-5040.670132	-5040.684583	-400.60
-5040.665886	-5040.681299	-407.42
-5040.673128	-5040.688054	-403.86
-5040.665002	-5040.680807	-394.85
-5040.672113	-5040.686783	-393.29
-5040.673164	-5040.689103	-396.14
-5040.672988	-5040.687931	-395.41
-5040.669590	-5040.686120	-384.61
-5040.670916	-5040.687277	-384.41
-5040.763805	-5040.777265	-370.66
-5040.668221	-5040.684102	-411.87
-5040.660487	-5040.677322	-382.23
-5040.666083	-5040.680061	-357.00
-5040.667408	-5040.681659	-375.58
-5040.672782	-5040.688669	-389.50

	-5040.670564	-5040.685899	-407.93
	-5040.664778	-5040.678714	-356.87
	-5040.666058	-5040.681889	-394.79
	-5040.666745	-5040.682535	-395.60
	-5040.667705	-5040.682145	-400.14
TS72-*Si*	-5040.676977	-5040.693667	-371.53
	-5040.673535	-5040.687814	-441.48
	-5040.662447	-5040.679461	-410.57
	-5040.675009	-5040.690593	-430.75
	-5040.673049	-5040.687121	-441.71
	-5040.662323	-5040.679348	-438.40
	-5040.673584	-5040.687875	-441.46
	-5040.668171	-5040.684857	-412.09
	-5040.665932	-5040.682999	-333.61
	-5040.673696	-5040.687929	-411.22
	-5040.668097	-5040.685157	-340.57
	-5040.670122	-5040.687022	-363.97
	-5040.665872	-5040.682684	-410.57
	-5040.662010	-5040.677636	-427.16
	-5040.675562	-5040.691772	-366.73
	-5040.667163	-5040.684200	-407.39
	-5040.673707	-5040.687918	-411.71
	-5040.673206	-5040.687510	-433.85
	-5040.676724	-5040.693450	-372.48
	-5040.667848	-5040.684257	-362.14
	-5040.672350	-5040.686320	-432.98
	-5040.665721	-5040.682541	-410.48
	-5040.668033	-5040.684111	-358.33
	-5040.667364	-5040.684200	-339.98
	-5040.673373	-5040.688651	-417.36
	-5040.669467	-5040.687099	-352.59
	-5040.670409	-5040.686634	-361.69
TS73-*Re*	-5040.672416	-5040.689644	-379.88
	-5040.670161	-5040.685860	-401.48
	-5040.664777	-5040.680535	-389.99
	-5040.669896	-5040.686920	-396.57
	-5040.673664	-5040.689327	-408.77
	-5040.669886	-5040.686529	-350.52
	-5040.676390	-5040.690783	-436.45
	-5040.675856	-5040.690037	-440.03
	-5040.668160	-5040.684909	-320.35
	-5040.667431	-5040.683730	-397.65
	-5040.666480	-5040.683268	-308.35
	-5040.672210	-5040.688301	-394.39
	-5040.667509	-5040.686187	-376.04
	-5040.669886	-5040.686971	-310.10

	-5040.666936	-5040.683327	-373.08
	-5040.671560	-5040.686851	-350.84
	-5040.666097	-5040.682859	-373.68
	-5040.667029	-5040.683515	-374.07
	-5040.668695	-5040.684413	-347.07
	-5040.661059	-5040.677498	-265.74
	-5040.671714	-5040.689025	-188.97
	-5040.670579	-5040.686787	-332.21
	-5040.670963	-5040.688293	-377.91
	-5040.655647	-5040.672087	-365.78
	-5040.665811	-5040.681668	-372.91
	-5040.673183	-5040.687484	-422.11
	-5040.670275	-5040.689253	-375.38
	-5040.672548	-5040.687832	-368.63
	-5040.670463	-5040.687372	-374.65
	-5040.670176	-5040.685077	-218.65
	-5040.664011	-5040.681300	-440.65

Figure 7.11.

Structure	M06-2X derived free energy	M06-2X derived free energy in solution	Imaginary Frequency
TS74-*Re*	-4681.467580	-4681.500172	-244.79
	-4681.456927	-4681.491596	-292.88
	-4681.463589	-4681.495176	-278.33
	-4681.464361	-4681.495570	-224.97
	-4681.465173	-4681.497291	-262.45
	-4681.468362	-4681.499477	-246.32
	-4681.446480	-4681.482404	-299.15
	-4681.462645	-4681.493177	-225.07
	-4681.456077	-4681.490509	-292.81
	-4681.461953	-4681.495020	-278.39
	-4681.466451	-4681.497910	-225.49
TS75-*Si*	-4681.473890	-4681.506082	-256.81
	-4681.453303	-4681.485985	-289.86
	-4681.473283	-4681.505502	-252.90
	-4681.471445	-4681.503620	-256.50
	-4681.468275	-4681.499804	-250.22
	-4681.456223	-4681.488816	-275.42
	-4681.460094	-4681.494792	-297.53
	-4681.467488	-4681.499809	-256.04
	-4681.475024	-4681.506051	-249.59
	-4681.470364	-4681.501528	-250.70
	-4681.470858	-4681.502871	-250.47
	-4681.468843	-4681.501152	-256.02

	-4681.453631	-4681.485335	-265.16
	-4681.473251	-4681.504456	-250.30
	-4681.465949	-4681.498525	-287.21
	-4681.452796	-4681.488108	-298.84
	-4681.472405	-4681.504196	-246.59
	-4681.462552	-4681.494964	-252.71
	-4681.468418	-4681.499948	-250.20
	-4681.467137	-4681.497172	-244.38
	-4681.451170	-4681.485069	-291.75
	-4681.452808	-4681.487386	-300.54
	-4681.470861	-4681.502880	-250.46
TS76-*Si*	-4681.473838	-4681.506412	-253.11
	-4681.448924	-4681.482871	-267.09
	-4681.452424	-4681.486684	-272.08
	-4681.444886	-4681.478325	-289.97
	-4681.445634	-4681.481570	-289.24
	-4681.443225	-4681.476745	-320.57
	-4681.440805	-4681.479125	-317.15
	-4681.454472	-4681.492735	-322.29
	-4681.464995	-4681.496391	-236.80
	-4681.461498	-4681.494857	-282.09
	-4681.455395	-4681.493297	-324.39
	-4681.463509	-4681.501179	-310.78
	-4681.454035	-4681.489870	-314.36
	-4681.464481	-4681.497979	-238.48
	-4681.454802	-4681.492867	-322.25
TS77-*Re*	-4681.485672	-4681.518688	-252.39
	-4681.470979	-4681.504517	-257.66
	-4681.484013	-4681.517711	-248.87
	-4681.468527	-4681.500851	-229.99
	-4681.454963	-4681.488511	-253.35
	-4681.458600	-4681.496630	-303.95
	-4681.484009	-4681.518355	-254.69
	-4681.481478	-4681.514905	-252.86
	-4681.459724	-4681.496451	-288.34
	-4681.478999	-4681.512790	-287.91
	-4681.457681	-4681.490019	-221.36
	-4681.484027	-4681.518191	-251.42
	-4681.456295	-4681.489715	-257.88

Appendix to Chapter 8

Figure 8.6.

Structure	M06 derived free energy	M06 derived free energy in solution	Imaginary Frequency
TS78-*Si*	-3661.940009	-3661.965404	-307.16
	-3661.937026	-3661.960387	-314.34
	-3661.937447	-3661.961651	-313.93
	-3661.940504	-3661.963482	-305.46
	-3661.938997	-3661.961911	-302.38
	-3661.917050	-3661.942803	-322.42
TS78-*Re*	-3661.931529	-3661.964559	-235.69
	-3661.933922	-3661.960363	-301.76
	-3661.930951	-3661.957599	-300.40
	-3661.932241	-3661.959268	-296.32
	-3661.932092	-3661.959226	-296.70
	-3661.934045	-3661.960360	-315.37
	-3661.934296	-3661.956784	-315.41
	-3661.931448	-3661.952980	-318.00
	-3661.932648	-3661.957388	-298.88
	-3661.934129	-3661.957358	-293.49
	-3661.932677	-3661.955707	-320.61
	-3661.931510	-3661.957717	-312.95
	-3661.929118	-3661.956507	-306.68
	-3661.931617	-3661.955023	-298.52
	-3661.933507	-3661.956844	-323.67
TS79-*Si*	-4459.795068	-4459.825511	-298.33
	-4459.794103	-4459.823655	-305.76
	-4459.794525	-4459.824582	-301.33
	-4459.779354	-4459.810506	-322.55
	-4459.776526	-4459.804609	-311.41
	-4459.783247	-4459.815258	-271.55
	-4459.779225	-4459.807356	-312.31
	-4459.787610	-4459.818857	-305.41
	-4459.782142	-4459.813193	-317.30
	-4459.783083	-4459.813412	-313.50
	-4459.752842	-4459.780652	-298.16
	-4459.769799	-4459.797990	-308.63
	-4459.770728	-4459.798907	-310.11
TS79-*Re*	-4459.783487	-4459.824228	-201.21
	-4459.780932	-4459.808796	-314.62
	-4459.776369	-4459.803878	-314.85
	-4459.781840	-4459.810747	-300.69

Figure 8.7.

Structure	M06 derived free energy	M06 derived free energy in solution	Imaginary Frequency
TS80-*Si*	-3569.210338	-3569.246437	-294.32
	-3568.210770	-3568.245906	-281.19
	-3569.211180	-3569.243107	-311.24
	-3569.210894	-3569.246429	-298.56
	-3569.206226	-3569.240551	-309.66
	-3569.206915	-3569.240881	-308.79
	-3569.206132	-3569.240870	-308.94
	-3569.209301	-3569.242060	-309.34
	-3569.209240	-3569.242046	-313.20
	-3569.206798	-3569.240984	-297.91
	-3569.207309	-3569.241547	-308.25
	-3569.209254	-3569.242010	-312.48
TS80-*Re*	-3569.212276	-3569.242696	-294.22
	-3569.206573	-3569.237602	-306.56
	-3569.204332	-3569.237070	-298.39
	-3569.212057	-3569.241716	-295.41
	-3569.208196	-3569.239487	-306.28
	-3569.208544	-3569.241298	-298.82
	-3569.207762	-3569.239821	-298.07
	-3569.207480	-3569.239326	-307.16

Figure 8.9.

Structure	M06 derived free energy	M06 derived free energy in solution	Imaginary Frequency
Ag-17-*Si*	-3190.870834	-3190.899266	-304.78
	-3190.864696	-3190.892991	-311.63
	-3190.866276	-3190.897023	-293.13
	-3190.867732	-3190.896668	-301.20
	-3190.867016	-3190.898148	-291.49
	-3190.867740	-3190.897884	-310.97
	-3190.866900	-3190.896551	-290.45
	-3190.866793	-3190.896722	-287.97
	-3190.866116	-3190.895065	-309.91
	-3190.864249	-3190.894815	-296.04
	-3190.866247	-3190.896911	-293.68
	-3190.864862	-3190.896071	-295.32
	-3190.870719	-3190.899125	-306.96
	-3190.864414	-3190.895706	-292.05
	-3190.869898	-3190.898438	-303.60
	-3190.870596	-3190.899021	-308.61

	-3190.860247	-3190.889804	-315.73
	-3190.864893	-3190.896244	-288.08
	-3190.866159	-3190.896899	-293.93
	-3190.863618	-3190.894394	-292.36
	-3190.864529	-3190.895282	-294.97
	-3190.864729	-3190.895758	-292.08
	-3190.866406	-3190.897072	-294.48
Ag-17-*Re*	-3190.871467	-3190.899810	-295.33
	-3190.867653	-3190.896096	-290.27
	-3190.871556	-3190.899774	-294.89
	-3190.866115	-3190.895013	-316.18
	-3190.864178	-3190.892789	-285.64
	-3190.870119	-3190.897980	-294.81
	-3190.864821	-3190.893803	-295.45
	-3190.864059	-3190.893143	-315.95
	-3190.868949	-3190.897388	-296.04
	-3190.866424	-3190.895096	-297.00
	-3190.861663	-3190.891136	-317.10
	-3190.869575	-3190.897493	-295.57
	-3190.862442	-3190.891448	-315.29
	-3190.863384	-3190.892724	-317.16
Ag-18-*Si*	-3573.960770	-3573.991013	-312.60
	-3573.961976	-3573.990656	-314.08
	-3573.961280	-3573.989827	-312.66
	-3573.957438	-3573.986598	-313.68
	-3573.960555	-3573.990156	-305.15
	-3573.955426	-3573.984876	-307.62
	-3573.959765	-3573.988863	-313.37
	-3573.957959	-3573.987245	-313.52
	-3573.958363	-3573.987272	-305.88
	-3573.959993	-3573.986922	-303.75
	-3573.959141	-3573.989136	-309.47
	-3573.962120	-3573.990983	-311.73
	-3573.961997	-3573.990651	-312.93
	-3573.960697	-3573.990620	-310.76
Ag-18-*Re*	-3573.963468	-3573.989823	-289.62
	-3573.960408	-3573.988193	-292.15
	-3573.954645	-3573.984918	-308.22
	-3573.958988	-3573.988603	-297.15
	-3573.955007	-3573.985653	-307.62
	-3573.954655	-3573.985437	-309.15
	-3573.956149	-3573.985179	-313.35
	-3573.954617	-3573.985488	-307.45
Ag-19-*Si*	-3364.091741	-3364.139456	-297.14
	-3364.059258	-3364.106364	-298.41
	-3364.060086	-3364.107765	-295.85

	-3364.060060	-3364.107664	-294.68
	-3364.060474	-3364.107857	-297.29
	-3364.092191	-3364.139453	-299.92
Ag-19-*Re*	-3364.093139	-3364.137187	-297.32
	-3364.061382	-3364.105844	-298.52
	-3364.064272	-3364.107670	-295.95
	-3364.064444	-3364.107486	-296.08
	-3364.057206	-3364.102791	-294.73
	-3364.063713	-3364.106770	-296.23
	-3364.063770	-3364.106848	-296.22
	-3364.056153	-3364.101946	-295.94
	-3364.063768	-3364.107041	-296.33
Ag-20-*Si*	-2920.839317	-2920.880091	-220.52
	-2920.841649	-2920.874497	-300.27
	-2920.844258	-2920.873197	-313.60
	-2920.843814	-2920.876628	-300.86
	-2920.843032	-2920.876678	-293.64
	-2920.844986	-2920.874147	-314.58
	-2920.843315	-2920.876852	-293.66
	-2920.842817	-2920.876859	-295.94
	-2920.844745	-2920.874382	-314.18
	-2920.846005	-2920.875540	-312.34
	-2920.844211	-2920.873127	-313.66
	-2920.841620	-2920.874339	-301.38
	-2920.844256	-2920.874040	-313.10
	-2920.844179	-2920.873113	-314.18
	-2920.843617	-2920.872851	-314.66
Ag-20-*Re*	-2920.845852	-2920.877137	-294.16
	-2920.843160	-2920.873293	-300.76
	-2920.846041	-2920.876992	-295.25

Figure 8.10.

Structure	M06 derived free energy	M06 derived free energy in solution	Imaginary Frequency
TS81-*Si*	-3262.426284	-3262.456717	-302.41
	-3262.426285	-3262.456714	-302.41
	-3262.417999	-3262.453875	-293.17
	-3262.417534	-3262.455016	-294.22
	-3262.418002	-3262.453876	-293.17
	-3262.417996	-3262.453866	-293.17
	-3262.417302	-3262.453826	-295.33
	-3262.417297	-3262.453823	-295.33
	-3262.417278	-3262.453818	-295.32
TS81-*Re*	-3262.428184	-3262.461631	-293.15

	-3262.426754	-3262.459293	-288.87
	-3262.428390	-3262.461395	-298.09
	-3262.428394	-3262.461399	-298.09
	-3262.428523	-3262.461271	-294.55
	-3262.428327	-3262.461072	-296.48
	-3262.426731	-3262.459629	-286.18

Figure 8.11.

Structure	M06 derived free energy	M06 derived free energy in solution	Imaginary Frequency
TS82-*Si*	-3798.074326	-3798.109558	-313.04
	-3798.072804	-3798.104391	-314.37
	-3798.074452	-3798.104962	-314.82
	-3798.073726	-3798.104145	-314.58
	-3798.076451	-3798.107785	-309.43
	-3798.074773	-3798.108679	-296.19
	-3798.073099	-3798.108390	-288.74
	-3798.075040	-3798.109128	-313.41
	-3798.074149	-3798.105276	-308.15
	-3798.069709	-3798.102452	-293.87
	-3798.067886	-3798.099397	-296.66
	-3798.074426	-3798.106804	-309.43
	-3798.061047	-3798.095108	-309.01
	-3798.072837	-3798.108842	-296.98
	-3798.073836	-3798.104439	-309.26
	-3798.073159	-3798.102583	-307.33
	-3798.073268	-3798.102467	-310.13
	-3798.073517	-3798.104295	-310.37
	-3798.072716	-3798.102264	-308.97
	-3798.073302	-3798.102795	-310.39
	-3798.071311	-3798.106004	-309.87
	-3798.072114	-3798.103553	-306.87
	-3798.072805	-3798.103030	-307.49
	-3798.069614	-3798.105196	-310.52
	-3798.073591	-3798.105819	-310.24
	-3798.070184	-3798.105901	-311.95
TS82-*Re*	-3798.077301	-3798.104995	-284.24
	-3798.076628	-3798.104116	-283.26
	-3798.073737	-3798.099988	-274.21
	-3798.070156	-3798.101674	-291.03
	-3798.071174	-3798.101574	-287.21
	-3798.076276	-3798.104292	-285.41
	-3798.043608	-3798.076855	-282.39
	-3798.068595	-3798.100100	-276.10

Figure 8.12.

Structure	M06 derived free energy	M06 derived free energy in solution	Imaginary Frequency
TS83-*Si*	-3876.156988	-3876.192569	-291.03
	-3876.153439	-3876.188261	-301.18
	-3876.153423	-3876.188272	-301.55
	-3876.154080	-3876.189110	-311.03
	-3876.153459	-3876.188068	-302.25
	-2876.156298	-3876.191038	-305.24
	-3876.153877	-3876.188801	-309.55
	-3876.154260	-3876.188862	-304.68
	-3876.151911	-3876.184181	-312.06
	-3876.153778	-3876.187143	-308.84
	-3876.148427	-3876.183211	-294.32
	-3876.155671	-3876.190807	-305.55
	-3876.138018	-3876.168882	-313.65
TS83-*Re*	-3876.155975	-3876.188416	-289.38
	-3876.145528	-3876.178539	-316.50
	-3876.145843	-3876.178908	-315.01
	-3876.145420	-3876.178256	-317.32
	-3876.142106	-3876.176086	-309.90

Figure 8.14.

Structure	M06 derived free energy	M06 derived free energy in solution	Imaginary Frequency
TS84-*Si*	-3723.121120	-3723.154701	-270.63
	-3723.117783	-3723.149638	-262.14
	-3723.121292	-3723.154651	-274.85
	-3723.117151	-3723.153196	-273.81
	-3723.120169	-3723.154454	-272.39
	-3723.121889	-3723.154524	-277.60
	-3723.121688	-3723.154866	-271.15
	-3723.120494	-3723.153358	-268.40
	-3723.119631	-3723.153601	-274.49
	-3723.116930	-3723.151415	-278.02
	-3723.115738	-3723.147110	-279.14
	-3723.115317	-3723.149948	-289.42
	-3723.117244	-3723.151989	-261.29
TS84-*Re*	-3723.114480	-3723.147671	-267.20
	-3723.082892	-3723.113559	-294.11
	-3723.097752	-3723.130607	-275.66
	-3723.111172	-3723.144003	-270.95
	-3723.104012	-3723.136687	-283.76